UNIVERSITY OF CALIFORNIA SAN DIEGO

The Properties and Evolution of Star Forming Regions Over Cosmic Time

A dissertation submitted in partial satisfaction of the
requirements for the degree Doctor of Philosophy

in

Physics

by

Maren Cosens

Committee in charge:

Professor Shelley A. Wright, Chair
Professor Alison Coil
Professor James Day
Professor Dusan Keres
Professor Karin Sandstrom

2022

The Dissertation of Maren Cosens is approved, and it is acceptable in quality and form for publication on microfilm and electronically.

University of California San Diego

2022

DEDICATION

To Jordan, my extremely supportive partner and pandemic office-mate

TABLE OF CONTENTS

LIST OF FIGURES

LIST OF TABLES

ACKNOWLEDGEMENTS

First off, I would like to thank Professor Shelley A. Wright for being such a fantastic advisor and mentor these past 6 years. Your guidance has helped me to become a better and more confident scientist and instrumentalist. An especially big thank you for always caring about the well being of your students. My first year at UCSD especially would have been much more stressful without your support as I dealt with unexpected health issues.

Thank you to the entire OIR Lab group, both past and present. I have been incredibly fortunate to have the chance to work with such a wonderful group of people and I have learned so much from each of you. Especially when I first arrived, the senior members of the lab — Greg Walth, Andrey Vayner, and Jerome Maire — not only made me feel welcome, but were instrumental in helping me grow as a scientist.

I would like to thank my cohort of physics graduate students; especially during the first few years. The first year courses and qualifying exam were often a grind, but one made easier by your support and camaraderie. Thank you to the entire CASS community; I've enjoyed many lunches on the balcony, Friday afternoon BASH's, and just the general sense of welcome within this community.

I would also like to thank all of my collaborators. I have been very fortunate to work with and learn from a wonderful group of scientists and engineers over the past six years.

Thank you to my parents, Doug and Terry Cosens, for everything you've done for me throughout my life. Thank you for your love and support, and instilling the work ethic and love of science that has helped me get where I am today. And an extra big thank you for being willing to drop everything to come to San Diego and help me when I was diagnosed with cancer. There's no way I would have been able to continue with grad school during the treatment without your incredible physical and emotional support.

Thank you to Jordan Runco, my wonderful fiancé and best friend. I'm so glad we got to go through our PhD programs at the same time. Thank you for always supporting me and believing in me even when I doubted myself. I can't imagine being stuck in our apartment / office without you

the last couple years; thank you for helping me keep my sanity and work life balance. Our cat, Obi, gets some credit for that too since it is physically impossible to either over sleep or work through dinner time with that little fur-ball around.

Chapter 2, in full, is a reprint of the material as it appears in The Astrophysical Journal 2018. Cosens, M., Wright, S. A., Mieda, E., Murray, N., Armus, L., Do, T., Larkin, J. E., Larson, K., Martinez, G., Walth, G., and Vayner, A, *The Astrophysical Journal*, 869, 11, 2018. The dissertation author was the primary investigator and author of this paper.

Chapter 3, in full, is a reprint of the material as it appears in The Astrophysical Journal 2022. Cosens, M., Wright, Murray, N., Armus, L., Sandstrom, K., Do, T., Larson, K., Martinez, G., Sabhlok, S., Vayner, A., and Wiley, J., *The Astrophysical Journal*, 929, 74, 2022. The dissertation author was the primary investigator and author of this paper.

Chapter 4, in part, is a reprint of the material as it appears in the Proceedings of the SPIE 2020. Cosens, M., Wright, S. A., Arriaga, P., Brown, A., Fitzgerald, M., Jones, T., Kassis, M., Kress, E., Kupke, R., Larkin, J. E., Lyke, J., Wang, E., Wiley, J., & Yeh, S, *Proceedings of the SPIE*, 114474X, 2020. The dissertation author was the primary investigator and author of this paper.

Chapter 5, in full, is material in preparation for publication in the Proceedings of the SPIE 2022. Cosens, M., Wright, S. A., Brown, A., Fitzgerald, M., Johnson, C., Jones, T., Kassis, M., Kress, E., Kupke, R., Larkin, J. E., Magnone, K., McGurk, R., Rundquist, N., Sohn, J., Wang, E., Wiley, J., & Yeh, S, "Liger at Keck Observatory: Imager Detector and IFS Pick-off Mirror Assembly", *Proceedings of the SPIE*, *in prep*. The dissertation author is the primary investigator and author of this paper.

Figure 1.1 is reproduced from Allington-Smith (2006) with permission from Elsevier.

The data presented herein were obtained at the W. M. Keck Observatory, which is operated as a scientific partnership among the California Institute of Technology, the University of California and the National Aeronautics and Space Administration. The Observatory was made possible by the generous financial support of the W. M. Keck Foundation. I want to thank the Observatory staff for their help in obtaining and reducing the observations in this thesis. I also wish to recognize

and acknowledge the very significant cultural role and reverence that the summit of Maunakea has always had within the indigenous Hawaiian community. I have been most fortunate to have the opportunity to conduct observations from this mountain.

VITA

2013	Undergraduate Teaching Assistant, Department of Chemistry and Biochemistry, California State Polytechnic University, San Luis Obispo
2014-2016	Student Researcher, Physics Department, California State Polytechnic University, San Luis Obispo
2016	B. S. in Mechanical Engineering *cum laude*, California State Polytechnic University, San Luis Obispo
2016,2019	Graduate Teaching Assistant, Physics Department, University of California, San Diego
2016-2022	Graduate Student Researcher, Physics Department, University of California, San Diego
2022	Ph. D. in Physics, University of California, San Diego

PUBLICATIONS

Cosens, M., Wright, S. A., Brown, A., Fitzgerald, M., Johnson, C., Jones, T., Kassis, M., Kress, E., Kupke, R., Larkin, J. E., Magnone, K., McGurk, R., Rundquist, N., Sohn, J., Wang, E., Wiley, J., & Yeh, S, "Liger at Keck Observatory: Imager Detector and IFS Pick-off Mirror Assembly", *Proceedings of the SPIE*, *in prep*

Cosens, M., Wright, S. A., Murray, N., Armus, L., Sandstrom, K., Do, T., Larson, K., Martinez, G., Sabhlok, S., Vayner, A., & Wiley, J., "Kinematics and Feedback in H II Regions in the Dwarf Starburst Galaxy IC 10", *The Astrophysical Journal*, 929, 74, 2022

Cosens, M., Wright, S. A., Arriaga, P., Brown, A., Fitzgerald, M., Jones, T., Kassis, M., Kress, E., Kupke, R., Larkin, J. E., Lyke, J., Wang, E., Wiley, J., & Yeh, S, "Liger for Next-Generation Keck AO: Filter Wheel and Pupil Design", *Proceedings of the SPIE*, 11447, 114474X, 2020

Cosens, M., Wright, S. A., Mieda, E., Murray, N., Armus, L., Do, T., Larkin, J. E., Larson, K., Martinez, G., Walth, G., & Vayner, A, "Size-Luminosity Scaling Relations of Local and Distant Star-forming Regions", *The Astrophysical Journal*, 869, 11, 2018.

Cosens, M., Maire, J., Wright, S. A., Antonio, F., Aronson, M., Chaim-Weismann, S. A., Drake, F. D.,Horowitz, P., Howard, A. W., Raffanti, R., Siemion, A. P. V., Stone, R. P. S., Treffers, R. R., Uttamchandani, A., & Werthimer, D, "Panoramic Optical and Near-Infrared SETI Instrument: Prototype Design and Testing", *Proceedings of the SPIE*, 107025H, 2018

ABSTRACT OF THE DISSERTATION

The Properties and Evolution of Star Forming Regions Over Cosmic Time

by

Maren Cosens

Doctor of Philosophy in Physics

University of California San Diego, 2022

Professor Shelley A. Wright, Chair

Star formation is key to the regulation of galactic environments. Studying the sites of ongoing star formation is therefore critical to understanding the evolution of galaxies over cosmic time. Integral Field Spectrographs (IFS) have allowed astronomers to probe the dynamical processes of galaxies at high redshift, z$\sim$1-3, revealing unique kiloparsec-scale "clumps" of star formation. The relationships between clump size, luminosity, and velocity dispersion are particularly important to understanding clump formation and evolution. These relationships have been measured in a variety of studies but disagreement remains about their nature and possible evolution with redshift.

To investigate the cause of these differences, I collected a comprehensive sample of clump observations across redshifts and developed a Bayesian Markov Chain Monte Carlo fitting routine to robustly explore the scaling relationships of star-forming regions. There is evidence of a break

into two clump populations based on their star formation rate surface density with differences in slope due to either the formation mode or geometry of the clump and host galaxy disk, but there is added uncertainty from limited observations at small clump sizes.

To address this limitation, I observed a sample of compact H II regions in the local starburst galaxy, IC 10, with the Keck Cosmic Web Imager IFS at the W. M. Keck Observatory. I found these H II regions are offset to higher luminosity and velocity dispersion for a given size. These H II regions do not appear to be virialized, and instead show evidence that they are young and expanding. Even in the most compact H II regions, warm gas pressure from photoinization heating provides the dominant contribution to outward pressure and expansion.

Improvements in instrumentation are also key to improving studies of the characteristics and evolution of star-forming regions, as well as many other astronomical objects. Liger, an adaptive optics fed IFS and imager for Keck Observatory, will provide improvements in resolution, field of view, and wavelength coverage compared to current instruments. I have developed the mechanical design of three major components of the Liger imager and sequential spectrograph: the filter wheel; selectable cold pupil stop; and mounting stage for the imager detector and IFS pick-off mirrors.

Chapter 1

Introduction

The first galaxies are thought to have formed in the first few hundred million years after the Big Bang when the Universe was only a small fraction of it's current age. The Universe at this time was a vastly different environment than the present day; most heavy elements had not yet been formed and the universe was in a period known as the "dark ages" with opaque neutral gas filling the spaces between the islands of young stars and newly forming galaxies. These early galaxies looked far different than what we observe in the current universe, and yet, they evolved over the last $\sim$13 billion years into the elliptical and spiral galaxies of the present day — including our own Milky Way galaxy — through processes like mergers and accretion of gas from the circum- and intergalactic medium to form stars. To understand the environment of the current universe we must observe both local galaxies as well their precursors at earlier cosmic times. Due to the finite speed of light, when we observe distant galaxies we observe them as they were in the past, providing a window into our universe's history.

One of the key ways in which galaxies have evolved is through the formation of new generations of stars which produce heavy elements, changing the chemical composition of the galaxy, and inputting massive amounts of energy into the surrounding gas — a process known as "feedback". Feedback can be both positive and negative. In the cases of positive feedback, areas of higher density and turbulence are produced which can trigger additional star formation. However, negative feedback from star formation is thought to be one of the main mechanisms to halt further star formation and expel material from the region or even the galaxy. Therefore, studying the

progression of star formation is critical to understanding the regulation of galactic environments and the evolution of galaxies over cosmic time (e.g., Hopkins et al., 2012).

Star formation in galaxies occurs in areas with higher densities of molecular gas, known as Giant Molecular Clouds (GMCs). Rather than being smooth, self-gravitating structures, GMCs are observed to have clumps and filaments of higher density (e.g., reviews by Williams et al., 2000; McKee and Ostriker, 2007; Heyer and Dame, 2015). These higher density regions, often referred to as "cores", are the locations of GMCs where individual stars and clusters are thought to form from the collapse of molecular gas (e.g., Girichidis et al., 2020). With enough material, the pressure from this collapse can cause the temperature and density to become high enough for hydrogen fusion to occur and a star to be formed. These stars emit high amounts of UV light which ionize neutral gas in the vicinity, forming an H II region. The more stars in the cluster and the more massive they are the higher the number of ionizing photons produced and the larger the H II region. The ionization of this gas is dominated by the most massive O and B-type stars which have the shortest lifetimes, meaning that observations of the ionized gas in H II regions trace the most recent burst of star formation over the last few million years.

H II regions start out spatially compact and expand over time before dissipating. Energy from the massive stars powering the H II region can interact with the surrounding gas in the molecular cloud and the Interstellar Medium (ISM) through feedback. These processes are thought to be critical for the regulation of star formation and setting the low observed star formation efficiency (e.g., Harper-Clark and Murray, 2009; Hopkins et al., 2014). Without disruption of the surrounding gas, star formation would proceed unhindered until all available gas was converted to stars. However, observations put the actual observed efficiency of star formation closer to $\sim 1\%$ (e.g., Krumholz, 2014), indicating that something like feedback must be disrupting and preventing further star formation. There are a variety of forms that this feedback can take. Radiation pressure occurs when photons produced in the star cluster interact with surrounding dust grains and transfer both energy and momentum. The ionizing photons also heat the surrounding gas to $\sim 10^4\,\mathrm{K}$, significantly higher than the $\sim 10\,\mathrm{K}$ temperature of the surrounding molecular cloud. Shocks from

stellar winds can generate bubbles of hot gas. And lastly, supernovae explosions provide significant amounts of energy in short bursts — though these events don't occur for a few million years by which point the molecular gas may have already been disrupted (e.g., Grudić et al., 2022). These mechanisms all result in outward pressures which can cause expansion or expulsion of gas from the star forming region and the surrounding molecular cloud. How effective each of these modes of feedback are in different environments is still somewhat uncertain and is the subject of both theoretical and observational investigations.

1.1 Observations of Star Forming Regions

There is a clear interplay between the sites of star formation and the evolution of galaxies. It is therefore critical to observe a wide range of star forming regions across diverse environments from Milky Way H II regions to high redshift star forming "clumps". Studies of the star formation history of the universe show that star formation activity peaked between redshifts $z \sim 1-3$ ($\sim 8-11$ Gyr in the past, e.g., Madau and Dickinson, 2014). If we want to understand galaxy evolution and the impact of star formation then this is a crucial epoch in which to study the conditions and properties of star forming regions. Early imaging studies of high-redshift galaxies with the *Hubble Space Telescope* revealed highly irregular morphologies with areas of concentrated star formation (e.g. Elmegreen et al., 2004b). Complimentary spectroscopic surveys from ground-based observatories allowed astronomers to compile the global properties of these galaxies (e.g., Shapley et al., 2003). With the advent of Integral Field Spectrographs (IFS) paired with Adaptive Optics (AO) at 8- & 10-m class ground-based telescopes, the resolved properties and kinematics of these high-redshift galaxies and their star forming regions were able to be studied for the first time (see review by Glazebrook, 2013).

A 10-m telescope paired with AO can achieve spatial resolutions of ~ 800 pc at z ~ 1. Combining this with IFS operating in the near-infrared allows for detailed studies of the ionization states and kinematics of the ionized gas that traces the most recent star formation activity while resolving the large, kiloparsec-scale clumps that have been observed at these redshifts (e.g., Genzel

et al., 2011). These studies have shown that galaxies in this epoch of "cosmic noon" (Grogin et al., 2011) have turbulent disk structures exhibiting high velocity dispersions which are thought to lead to areas of gravitational instability, triggering clump formation (Bournaud et al., 2007). These clumps tend to be $1-3\,\mathrm{kpc}$ across and are found to be present in the majority of high-z galaxies (Guo et al., 2015b). Even with the help of magnification from gravitational lensing to improve spatial resolution at high-z, these large observed clump sizes remain (e.g., Livermore et al., 2012; Swinbank et al., 2009; Walth et al., 2019). However, there are only a few in each galaxy compared to the hundreds of H II regions which are 10's - 100's parsec in size found in local galaxies. It is thought that these massive clumps at high-z may migrate to the center of the host galaxy over time, leading to the bulge and disc structure observed in spiral galaxies in the local universe (Mandelker et al., 2014).

1.1.1 Scaling Relationships

One way in which to investigate the likely formation mechanism of these structures is to study the scaling relationships between the measured clump properties; typically the clump sizes, luminosities (a tracer of star formation rate; SFR), and velocity dispersion (e.g., Livermore et al., 2012; Wisnioski et al., 2012). Obtaining resolved measurements of all three of these important properties at high-z currently requires the use of AO aided IFS. Local H II regions are often used as a comparison sample when fitting and interpreting the scaling relationships, but there has been some variability of the results depending on the local and high-z samples used; particularly in regards to whether there is evolution in the relationship between size and luminosity with increasing redshift. In Chapter 2, this question of what the relationships between star forming region properties are — particularly the size-luminosity relationship — is explored with a robust set of data gathered from the literature for both local H II regions and high-z clumps. We developed a Markov Chain Monte Carlo (MCMC) fitting method to investigate the relationship between these properties in a robust way, better incorporating measurement uncertainties and intrinsic scatter, and allowing the division of the data into subsets for the exploration of potential redshift evolution and/or selection biases.

We use this MCMC code to fit a power-law relationship between the star forming region size and Hα luminosity, as well as multi-parameter fits adding in the region's velocity dispersion or the host galaxy gas fraction. As will be shown, we found no clear indication that the size-luminosity relationship evolves with redshift, but instead that there is a break between regions with high- and low- star formation rate surface density ($\Sigma_{\rm SFR}$). For high $\Sigma_{\rm SFR}$ regions we found a slope of $L \sim r^2$, while for low $\Sigma_{\rm SFR}$ region we found $L \sim r^3$. These slopes can be interpreted as either due to a difference in the mode of collapse of the star forming region during its formation or a difference in region geometry relative to the disk of the host galaxy. Regardless of the redshift, these high and low $\Sigma_{\rm SFR}$ regions exhibit differences in the best fitting slope between the region size and luminosity. The investigation of these scaling relationships and the interpretation of these two slopes will be presented further in Chapter 2.

One limitation of this scaling relationship investigation, however, was a limited number of resolved observations of very small, low mass star forming regions — and none which were observed with IFS. In a practical sense, these small regions constrain the intercept of the scaling relationships and are therefore critical to any interpretation of variations in the fitted slope. More importantly, without these observations we cannot compare the scaling relationships (and therefore the insight into formation mechanism and physical conditions they provide) for star forming regions in low and high mass clumps. In order to fill in this missing parameter space, observations in the local universe are required in order to achieve high enough spatial resolution to separate compact structures. A prime candidate for such observations was the local starburst dwarf galaxy IC 10.

IC 10 is our nearest starburst at a distance of only ~ 700 kpc (Kim et al., 2009), making $1''$ on the sky equivalent to only ~ 3.5 pc. Further, there have been nearly 150 H II regions identified within IC 10 (Hodge and Lee, 1990), meaning that a large sample of the required H II regions can be built up in a single study. Chapter 3 details observations carried out with the Keck Cosmic Web Imager IFS (KCWI; Morrissey et al., 2018) of the central region of IC 10 in order to identify and measure the properties of H II regions in this crucial parameter space of compact, low mass regions.

1.1.2 Resolved Kinematics and Energetics

These observations of IC 10 have many uses other than simply constraining the intercept of the scaling relationships. IC 10 is also a fascinating environment in which to study the impact of ongoing star formation on the ISM, and KCWI allows the spatial and spectral resolution to do this at the smallest scales.

High resolution optical IFS like KCWI have only recently been developed. Previous IFS instruments that operated at the wavelengths necessary to study ionized gas in the local universe could only achieve kiloparsec resolution. While these could not resolve the smallest star forming regions, they were still extremely useful for mapping gas properties and kinematics throughout entire galaxies. In particular, these instruments have been used for highly productive surveys of large samples of local galaxies to perform statistically significant studies of galaxy properties and trends. The Cero Alto Legacy Integral Field Area survey (CALIFA, Sánchez et al., 2012a), for example, observed $\sim$600 nearby star forming galaxies using a moderate resolution, R$\sim$850-1650, fiber fed spectrograph. A multitude of scientific results has come from the CALIFA survey (e.g., Marino et al., 2013; Pérez et al., 2013; Sánchez et al., 2013; González Delgado et al., 2015). Interesting results include correlating emission line ratios with stellar population age and metallicity (Sánchez et al., 2015) showing that H II regions are affected by the underlying stellar population. The CALIFA survey also characterized the Diffuse Ionized Gas (DIG) and it's impact on measured H II region properties (Espinosa-Ponce et al., 2020). The Mapping Nearby Galaxies at APO survey (MaNGA, Bundy et al., 2015) as part of the larger Sloan Digital Sky Survey (SDSS) provides similar $\sim$kpc scale IFS observations as CALIFA in a sample of $>$4,500 galaxies. This publicly available data has resulted in studies of galaxy metallicity gradients (Belfiore et al., 2017), measurement of a "resolved" star forming main sequence (Ellison et al., 2018), and characterizations of ionized gas outflows (Rodríguez del Pino et al., 2019) among many other interesting results.

High resolution optical IFSs at 8- to 10-m class telescopes such as Keck/KCWI and the Multi-Unit Spectroscopic Explorer (MUSE; Bacon et al., 2010) at the Very Large Telescope (VLT) have allowed much more detailed observations of local H II regions. These powerful instruments

have been used to map the ionized gas in local H II regions to study their ionization state (e.g., Castro et al., 2018), the impact of different feedback mechanisms (e.g., McLeod et al., 2019, 2021), and the resolved kinematic state of the gas around star clusters (Bresolin et al., 2020).

The local starburst galaxy IC 10 provides a prime target to study with these recent high resolution optical IFSs. Observational evidence suggests that the starburst in IC 10 is quite recent. First, there is the previously mentioned high density of H II regions in IC 10 (Hodge and Lee, 1990), as well as a large number of Wolf-Rayet (WR) stars (e.g., Massey and Holmes, 2002; Tehrani et al., 2017). In fact, the WR stars found in IC 10 result in an unusually high ratio of WC/WN stars which may be reproduced by synchronized bursts of star formation in the last few Myr (Hunter, 2001). Polles et al. (2019) find similar properties in their photoionization models of multiple regions in the IC 10 starburst which they suggest indicates a common origin of the recent star formation, potentially triggered by feedback from a previous generation (ie., "positive" feedback). Further, observations of the CO gas content in IC 10 indicate that the irregular galaxy is still in the process of actively forming, with evidence of ongoing accretion from the intergalactic medium (Wilcots and Miller, 1998; Ashley et al., 2014). These characteristics make IC 10 a unique and fascinating environment in which to study the current state of the star forming regions and their surroundings and to investigate the various feedback processes occurring within them.

In Chapter 3 we will make use of high resolution kinematic and ionization state measurements throughout the H II regions and ISM of IC 10 to investigate the impact of energy from star formation. We will show that the identified H II regions are likely young and undergoing active expansion into their surroundings. The observations will be used to estimate the contribution of key mechanisms of feedback and to show that the pressure from heating the H II region gas is likely to be the dominant mechanism even in this environment of low mass ionizing clusters. H II regions with potential local outflows will also be identified and the possible sources of support for the resulting turbulent volumes investigated.

1.2 Novel Instrumentation

Chapters 4 and 5 will focus on the development of a new sequential imager and IFS for the W.M. Keck Observatory called Liger. Advances in observations naturally rely on improvements in instrumentation over time to continuously provide better sensitivity, resolution, fields of view, and wavelength coverage. Two out of the last three Nobel Prizes in Physics have been awarded for discoveries in astrophysics made possible by new generations of instruments operating on ground-based telescopes at optical and near-IR wavelengths. In 2019, the prize was awarded for the discovery of the first exoplanet around a main sequence star, which would not have been possible without improvements in spectral resolution. This allowed the detection of the stars Doppler shift caused by the pull of an orbiting planet (Mayor and Queloz, 1995). Then, in 2020, the prize was awarded for the discovery of the supermassive black hole at the center of our own Milky Way galaxy. This was made possible with extensive observations tracking the orbits of stars at the Galactic Center with state of the art instruments on large ground based telescopes using adaptive optics (e.g., Ghez et al., 1998, 2008; Genzel et al., 2010). Just as these ground breaking studies relied on the development of new tools like Doppler spectroscopy and AO, the work in this thesis would not be possible without the development and improvement of Integral Field Spectrographs.

The two most common types of observations are imaging and spectroscopy. Imaging cameras focus the light at a detector to generate an image of the object, though with no information on the wavelength of each detected photon aside from filters used to narrow the wavelength range of the image to focus on a desired feature. Spectroscopy makes use of a dispersive element such as a grating or prism to spread out the incoming light such that photons of different wavelengths land at different locations on the detector. The result is a spectrum showing the amount of light observed as a function of wavelength, but without the spatial information obtained with an image. IFS's combine these two techniques to generate a three-dimensional data cube with a spectrum at each pixel in the field of view with a single exposure. The first IFS was a prototype which used a bundle of flexible optical fibers to reformat a two-dimensional image into a straight line of fibers

from which the light is then dispersed in wavelength (Vanderriest, 1980).

Current IFS instruments typically make use of one of three methods to divide the two-dimensional field of view into distinct elements before dispersing the light in wavelength. The first is the use of flexible optical fibers to capture the light from discrete areas of an image and rearrange it into the desired format before dispersing the output of each fiber into a unique spectrum (e.g., Vanderriest, 1980). Since these fibers are flexible, they can be rearranged such that the configuration at the exit of the fiber is the most convenient for dispersing each spectrum on the detector in an efficient manner. However, one disadvantage is that there will be gaps in the coverage on sky due to the cylindrical nature of the fibers as well as some non-zero thickness of the fiber housings. The second technique is the use of a lenslet array to divide the incoming light into distinct beams which are each dispersed into individual spectra (e.g., Bacon et al., 1995). The lenslet method has an advantage over the fibers in that the lenslets can be packed tightly together to eliminate gaps in spatial coverage, but the packing of spectra on the detector is not as efficient, resulting in the need for either lower spectral resolution or a smaller wavelength range. Using fibers after the lenslet array can improve the efficiency of both spatial and spectral coverage, but this increases the cost and complexity of the instrument. The third technique is the image slicing method in which a segmented mirror is used to divide and reformat the field of view before dispersing the light (e.g., Weitzel et al., 1996). This method can arrange the slices similarly to using fibers without the loss of field coverage, but the spatial sampling is coarser than can be achieved with the lenslet method. These three methods are illustrated in Figure 1.1.

IFSs have had an incredible impact on observational astronomy. The combination of IFS operating in the near-IR with AO on powerful 8- & 10-m class ground based telescopes opened the door to a multitude of new observations. Not only are these instruments regularly used in the observations of the Galactic Center to constrain the black hole mass, but these instruments are also what allowed surveys like the Spectroscopic Imaging survey in the Near-infrared with SINFONI (SINS, Förster Schreiber et al., 2009) to resolve the morphology and kinematics of galaxies at $z \sim 1-3$, which showed the large clumps of star-formation within turbulent disks discussed in the

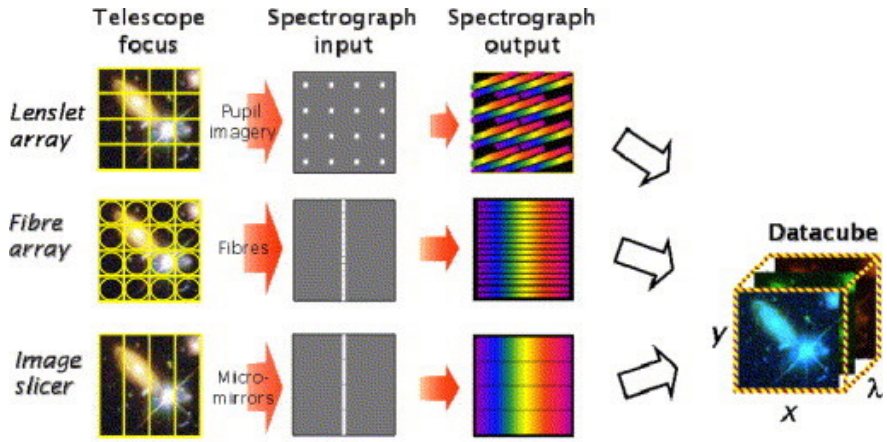

Figure 1.1: A cartoon illustration of the three main methods of constructing Integral Field Spectrographs discussed here. The leftmost column demonstrates how the two-dimensional field of view is divided into discrete segments. Next, the arrangement of these segments is shown at the input to the spectrograph. The right column shows the dispersed spectra and their orientation for each segment as the light leaves the spectrograph and goes to the detector. Each of these methods results in observations which are organized in a data cube as illustrated on the right, with an image (x and y) at each wavelength (λ). Image modified from Allington-Smith (2006); reproduced with permission from Elsevier.

preceding sections.

At optical wavelengths, fiber-fed IFS operating on $\sim$3-m telescopes also allowed the previously discussed surveys like CALIFA (Sánchez et al., 2012a) and MaNGA (Bundy et al., 2015) to map the gas properties, including kinematics, in thousands of local galaxies at kpc scales. More recently, wide field optical IFSs like VLT/MUSE and Keck/KCWI have been developed and commissioned. Without these instruments, and the simultaneous high spectral and spatial resolution they provide, the observations of local H II regions in Chapter 3 would not have been possible. We simply would not be able to map the ionized gas conditions and kinematics in local star forming regions in an efficient enough manner to build up a sufficient sample to study trends in their properties and compare them to massive clumps at high-z.

The new Liger instrument will provide even greater improvements over existing IFSs which will allow for more detailed studies of the kinematic conditions and chemical properties of local and high-z galaxies and their star forming regions. Liger, with first light planned for 2027, will consist of a sequential imager and IFS that will provide improvements in both spatial and spectral

resolving power, larger fields of view, and extend to shorter wavelengths than current AO fed instruments (Wright et al., 2019). There are two separate IFS channels built into Liger, a lenslet mode to provide high spatial resolution, and a slicer mode which provides a larger field of view. Chapters 4 and 5 discuss the development of three key components of the imager shown in Figure 1.2, which are therefore also used by the IFS modes. Chapter 4 discusses the design of the filter wheels which select the desired wavelength range of the observations as well as the selectable cold pupil stop which will mask the thermal background. Chapter 5 details the design of a finely adjustable mounting stage for the imager detector as well as the pick-off mirrors which feed the light to both the slicer and lenslet IFS modes.

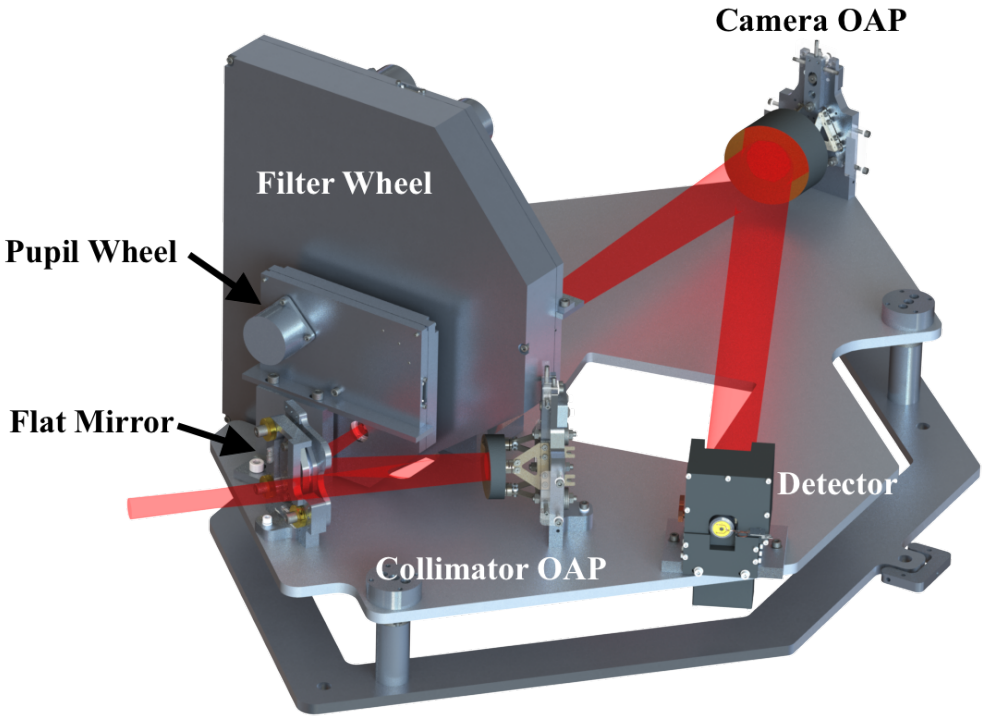

Figure 1.2: Rendering of the Liger imager with the beam path highlighted in red. Light from the telescope enters the instrument on the left side, after the AO system. The light then reflects off the collimator off-axis parabolic mirror (OAP) and is redirected by a flat mirror before passing through the pupil and filter wheels before reaching the camera OAP. Finally, the focused light reaches the CCD detector as well as the pick-off mirrors which will send a portion of the beam upward to feed the IFS. Chapter 4 discusses the design of the filter and pupil wheels while Chapter 5 focuses on the design of the detector stage which also holds the pick-off mirrors for the two IFS modes not shown here.

The remaining chapters of this thesis are divided between two main topics: Chapters 2 &

3 address the observational study of local and distant star forming regions, while Chapters 4 & 5 describe design work for key components of the Liger instrument. Chapter 2 focuses on studying the scaling relationships between measured properties of star forming regions locally and at high-z in order to better understand the mode of formation and evolution of these regions. Chapter 3 describes an observational study of the H II regions in the local starburst galaxy, IC 10, with the goals of both better constraining the scaling relationships with high resolution measurements of small star forming region properties, as well as addressing the detailed ionized gas conditions and effectiveness of feedback in these H II regions. Chapter 4 shifts to the development of new instrumentation, with a description of the design and analysis of the filter and pupil wheels for the planned Liger imager and IFS. Similarly, Chapter 5 details the design of a mounting and alignment stage for the Liger imager detector and the IFS pick-off mirrors. Finally, Chapter 6 provides a summary of these studies as well as a brief discussion of how the next generation of observatories and instruments will be able to build on this work and improve our understanding of star forming regions and their impact on galaxy evolution.

Acknowledgements

Figure 1.1 is reproduced from Allington-Smith (2006) with permission from Elsevier.

Chapter 2

Size-luminosity scaling relations of local and distant star forming regions

Abstract

We investigate star forming scaling relations using Bayesian inference on a comprehensive data sample of low- (z<0.1) and high-redshift (1<z<5) star forming regions. This full data set spans a wide range of host galaxy stellar mass ($M_* \sim 10^6 - 10^{11}$ $M_\odot$) and clump star formation rates (SFR $\sim 10^{-5} - 10^2$ $M_\odot$ yr^{-1}). We fit the power-law relationship between the size ($r_{H\alpha}$) and luminosity ($L_{H\alpha}$) of the star forming clumps using the Bayesian statistical modeling tool Stan that makes use of Markov Chain Monte Carlo (MCMC) sampling techniques. Trends in the scaling relationship are explored for the full sample and subsets based on redshift and selection effects between samples. In our investigation we find no evidence of redshift evolution of the size-luminosity scaling relationship, nor a difference in slope between lensed and unlensed data. There is evidence of a break in the scaling relationship between high and low star formation rate surface density (Σ_{SFR}) clumps. The size-luminosity power law fit results are $L_{H\alpha} \sim {r_{H\alpha}}^{2.8}$ and $L_{H\alpha} \sim {r_{H\alpha}}^{1.7}$ for low and high Σ_{SFR} clumps, respectively. We present a model where star forming clumps form at locations of gravitational instability and produce an ionized region represented by the Strömgren radius. A radius smaller than the scale height of the disk results in a scaling relationship of $L \propto r^3$ (low Σ_{SFR} clumps), and a scaling of $L \propto r^2$ (high Σ_{SFR} clumps) if the radius is larger than the disk scale height.

2.1 Introduction

Understanding the star formation properties in high-redshift galaxies is crucial for understanding galactic formation and evolution. Star formation rates at high-redshift (z$\sim$2) are an order of magnitude higher than at z$\sim$0 (Hopkins, 2004; Hopkins and Beacom, 2006; Madau and Dickinson, 2014), indicating that the majority of stellar mass and galactic substructure are established at early times. Rest frame UV *Hubble Space Telescope* (*HST*) imaging surveys implied star formation occurred in irregular morphologies (e.g., Elmegreen et al., 2004b,a; Law et al., 2007b), while ground-based spectroscopic surveys confirmed the large global star formation properties of high-redshift galaxies (Shapley et al., 2003; Law et al., 2007b). Yet these early surveys were unable to resolve individual star forming regions ("clumps") to study their internal kinematics and sizes. Studying the properities of individual high-redshift star forming clumps is imperative for comparing their properties to that of local H II regions and starburst regions, and for understanding their star formation mechanisms.

Integral field spectrographs (IFS) have been revolutionary for studying the resolved morphologies and kinematics of high redshift galaxies (Glazebrook, 2013). Using an IFS in combination with Adaptive Optics (AO) yields superb spatial resolutions, down to $\sim$ 800 pc at $z \sim 1$. This has allowed for detailed ionized gas kinematic studies of high-redshift galaxies and their individual clumps (Förster Schreiber et al., 2006, 2009, 2011; Genzel et al., 2006, 2008, 2011; Law et al., 2007a, 2009; Wright et al., 2007, 2009; Shapiro et al., 2008; Epinat et al., 2009, 2012; Swinbank et al., 2009, 2012a,b; Jones et al., 2010; Mancini et al., 2011; Livermore et al., 2015; Wisnioski et al., 2012, 2015; Newman et al., 2013; Buitrago et al., 2014; Stott et al., 2014, 2016; Leethochawalit et al., 2016; Mieda et al., 2016; Molina et al., 2017). The kinematics of these galaxies have shown large turbulent disks that have high velocity dispersions ($>>$10 km s^{-1}). These high-redshift disks have had their Toomre parameter, Q, measured to be less than 1 (Toomre, 1964), and therefore gravitational instability (Elmegreen et al., 2008; Genzel et al., 2011) may cause disk fragmentation and clump formation (e.g. Bournaud et al., 2007; Elmegreen et al., 2008; Mandelker et al., 2014).

In a large HST imaging-survey, Guo et al. (2015a) finds that the majority of high-redshift galaxies contain one or more off-center clumps, where the number of clumps per galaxy is decreasing with redshift to $z \approx 0.5$. These clumps are larger than local Giant Molecular Clouds (GMCs) and H II regions with size scales on the order of $\sim 1-3$ kpc, and only a small number of clumps in each galaxy as opposed to hundreds of GMCs and H II regions in local galaxies. One interpretation is that these massive clumps coalesce to form or grow the bulge of their host galaxy, spiraling towards the center due to the effects of dynamical friction (Bournaud et al., 2007; Elmegreen et al., 2008). The migration of massive clumps towards the center of the host galaxy is thought to occur on timescales of $\sim 2-3$ orbital times (Dekel et al., 2009; Ceverino et al., 2012; Bournaud et al., 2014; Mandelker et al., 2014, 2017). This process would then lead to the exponential disk structure we typically see in local spiral galaxies (Bournaud et al., 2007).

The ability to measure resolved clump properties provides insight into the physical processes driving high-redshift clump formation, and how these systems evolve into local galaxies. To explore the driving formation mechanisms, star formation scaling relations of high-redshift clumps are often compared to local analogs like H II regions. The relationships between clump size, luminosity (usually in Hα; $L_{H\alpha}$), and velocity dispersion have been investigated in various studies with differing results (Genzel et al., 2011; Wisnioski et al., 2012; Livermore et al., 2012, 2015; Mieda et al., 2016). In comparison to local H II regions, Livermore et al. (2012, 2015) (the latter including data from Jones et al. (2010)) find there is an offset to higher luminosities in their lensed, high-redshift clumps. However, both Wisnioski et al. (2012) and Mieda et al. (2016) find that the power-law relating clump size and luminosity for unlensed high-redshift samples extend well to local H II regions, with Wisnioski et al. (2012) finding the relationship $L_{H\alpha} \propto r^{2.72\pm0.04}$ when including local H II and giant H II regions. In order to determine whether these scaling relationship differences are due to redshift evolution, selection biases between studies, and/or intrinsic scatter requires additional local and high-redshift investigations.

An important consideration for studying high-redshift scaling relations is which local analogs to use as a comparison sample. Often H II regions like those found in the SINGS survey (Kennicutt

et al., 2003) are used as these comparative local analogs. However, high-redshift star forming clumps are sometimes found to be orders of magnitude more luminous than local H II regions (Swinbank et al., 2009), and may in fact be scaled up versions of more extreme giant H II regions such as 30 Doradus (Swinbank et al., 2009; Jones et al., 2010; Wisnioski et al., 2012). The DYNAMO survey (Fisher et al., 2017) provides another set of local clump analogs in turbulent galaxies that have similar properties to high-redshift clumps. Within the Milky Way there are distinctions between star forming regions based on size-scale, where GMCs are 1 to 2 orders of magnitude smaller than Molecular Cloud Complexes (MCCs). Nguyen-Luong et al. (2016) investigate a power-law break in varying star formation laws based on the differences between GMCs and MCCs that indicate MCCs may provide another analog to the high-redshift clumps.

We gathered a comprehensive data set from the literature to form a robust comparative sample in Section 2.2 to investigate possible causes of variation in the scaling relations between different samples. In Section 2.3 we discuss the Markov Chain Monte Carlo (MCMC) method developed to fit a power-law to clump sizes and luminosities. In Section 2.4, we present the results of this fitting method for a range of data subsets to investigate the clump size-luminosity scaling relationship. We apply a broken power-law fit to this relationship based on the star formation rate surface density, as presented in Section 2.4.1. The possible effects of beam smearing on the measured clump properties and scaling relations are explored in Section 2.4.2. We divide the data into various sub-samples to investigate potential redshift evolution in Section 2.4.3; and dependence on clump velocity dispersion and host galaxy gas fraction in Section 2.4.4. Lastly, in Section 3.4 we discuss two potential theoretical models that may explain the size-luminosity relationships measured. We present a new model that re-scales the Strömgren sphere in context to the galaxy disk size with large star forming clumps. We further discuss any observed biases and selection effects that could influence the fitting to the star forming clump scaling relationship. In Section 3.5 we summarize our results. Throughout this paper we use the concordance cosmology with $H_0 = 67.8 \mathrm{km\ s^{-1}\ Mpc^{-1}}$, $\Omega_M = 0.306$, and $\Omega_\Lambda = 0.692$ (Planck Collaboration et al., 2014).

2.2 Data Sample

Data of star forming clumps from both high and low redshift ($z \sim 0.6-5; z \sim 0-0.1$) galaxies measured and detected in different ways were gathered from the literature to form a comprehensive sample of the known data (Swinbank et al., 2009; Jones et al., 2010; Livermore et al., 2012, 2015; Walth et al., 2019; Genzel et al., 2011; Wisnioski et al., 2012; Freundlich et al., 2013; Mieda et al., 2016; Kennicutt et al., 2003; Gallagher and Hunter, 1983; Arsenault and Roy, 1988; Bastian et al., 2006; Rozas et al., 2006; Monreal-Ibero et al., 2007; Fisher et al., 2017; Nguyen-Luong et al., 2016). This sample is detailed in Table 2.1 and includes lensed (Swinbank et al., 2009; Jones et al., 2010; Livermore et al., 2012, 2015; Walth et al., 2019) and unlensed (Genzel et al., 2011; Wisnioski et al., 2012; Freundlich et al., 2013; Mieda et al., 2016) high-redshift galaxies, as well as a wide range of sizes and star formation rate densities in the local analogs (Kennicutt et al., 2003; Gallagher and Hunter, 1983; Arsenault and Roy, 1988; Bastian et al., 2006; Rozas et al., 2006; Monreal-Ibero et al., 2007; Fisher et al., 2017; Nguyen-Luong et al., 2016). Figure 2.1 illustrates the differences in the morphologies of these galaxy populations via a comparison of HST images of representative objects.

The majority of high-redshift samples make use of IFS systems for investigating the morphological and kinematic properties of the star forming clumps. This allows for detailed study of the kinematics of the galaxy at improved spatial resolution when coupled with AO. The range of properties spanned by the full sample is shown in the histograms of Figure 2.2. The set of high-redshift unlensed galaxies ($z \sim 1-2$) have an average stellar mass of $\sim 10^{11}$ $M_{\odot}$ and an average spatial resolution of 2000 pc (~ 0.6"). The high-redshift lensed galaxies ($z \sim 0.6-5$) tend to have a lower overall stellar mass ($\sim 10^{8}$ $M_{\odot}$), but better spatial resolution (avg ~ 300 pc; ~ 0.05") than the unlensed galaxies. The difference in the sampling of the lensed and unlensed surveys leads to the bimodal appearance of the histogram of host galaxy stellar mass (Figure 2.2b). The various local analogs span a wide range of total stellar masses ($\sim 10^{6}-10^{12}$ $M_{\odot}$) with spatial resolution similar to or slightly better than the high-redshift lensed sample. This wide range of local

analogs provides a robust comparison to the varied high-redshift clumps observed.

Table 2.1: Data Samples: Observational Properties of High and Low Redshift Star Forming Clumps

Study(ies) #, References	Redshift (z)	Instrument	Spatial Resolution (arcsec)	Spatial Resolution (pc)	Lensed/Unlensed	Galaxy M_* Range ($M_\odot$)	Galaxies (#)
1, Swinbank et al. (2009)	4.9	Gemini/NIFS	$0.06''$	320	lensed	$7 \pm 2 \times 10^8$	1
2, Jones et al. (2010)	∼1.7-3.1	Keck/OSIRIS	$0.01''^a$	~ 100	lensed	$10^{9.7-10.3}$ (dynamical)	6
3, Livermore et al. (2015)	∼1-4	VLT/SINFONI, Keck/OSIRIS, Gemini/NIFS	$\sim 0.04'' - 0.08''^a$	40-700	lensed	$4 \times 10^8 - 6 \times 10^8$	10 1 1
4, Livermore et al. (2012)	∼1-1.5	WFC3	$0.05''$	$\sim 70 - 600$	lensed	⋯	8
5, Walth et al. (2019)	0.61	HST/ACS[b] & WFC3[b,c] Magellan/LDSS-3[e] & MMIRS[e]	$0.01''/0.03''^a$	90/240	lensed	2.6×10^{10}	1
6, Genzel et al. (2011)	∼2	VLT/SINFONI	$\sim 0.2''$	$\sim 1700^a$	unlensed	$\sim 10^{10.6}$	5
7, Wisnioski et al. (2012)	∼1.3	Keck/OSIRIS	$\sim 0.1''$	$\sim 520 - 840$	unlensed	$\sim 10^{11}$	3
8, Freundlich et al. (2013)	∼1.2	IRAM & Keck/DEEP2	$0.6'' - 1.9''^f$	~ 8000	unlensed	$\sim 10^{11}$	4
9, Mieda et al. (2016)	∼1	Keck/OSIRIS	$\sim 0.1''$	800	unlensed	$10^{9.6-11.2}$	7
Kennicutt et al. (2003)[d]		KPNO & CTIO	$1''$-$3''$	40-325[a]		⋯	7
Gallagher and Hunter (1983)[e]		Kitt Peak video camera system	⋯	200[g]		⋯	10
10, Arsenault and Roy (1988)[e]		various	$>4''$	$>100^a$		⋯	20
Bastian et al. (2006)[e]	∼0	VLT-VIMOS	$0.66''$	$\sim 50^a$	unlensed	⋯	2
Rozas et al. (2006)[e]		OAN-SPM & William Herschel Telescope	$1.5''$-$1.6''$	$\sim 50 - 160^a$			10
Monreal-Ibero et al. (2007)[e]		INTEGRAL/WYFFOS & WFPC2	⋯	⋯		$\sim 2 \times 10^6 - 7 \times 10^8$	5
11, Fisher et al. (2017)	∼0.1	HST/WFC	$\sim 0.05''$	~ 100	unlensed	$1 - 9 \times 10^{10}$	10
12, Nguyen-Luong et al. (2016)[h]	Milky Way	CfA Suvey	8.8'	~ 15	unlensed	$\sim 10^{10}$	1

Note. — [a]: when resolution was only given in either pc or arcsec it was converted to the other units based on the cosmology used here. [b]: used for measurement of region size. [c]: used for measurement of flux. [d]: normal H II regions; re-analyzed by Wisnioski et al. (2012). [e]: Giant H II regions; corrections applied by Wisnioski et al. (2012). [f]: clump sizes for the Freundlich et al. (2013) sample are derived from IRAM CO luminosity with FWHM ranges given here; SFRs are derived from DEEP2 spectra using a 1" slit. [g]: Hα flux measured within a fixed aperture diameter of 200pc (Gallagher and Hunter, 1983). [h]: Molecular Cloud Complexes (MCC's).

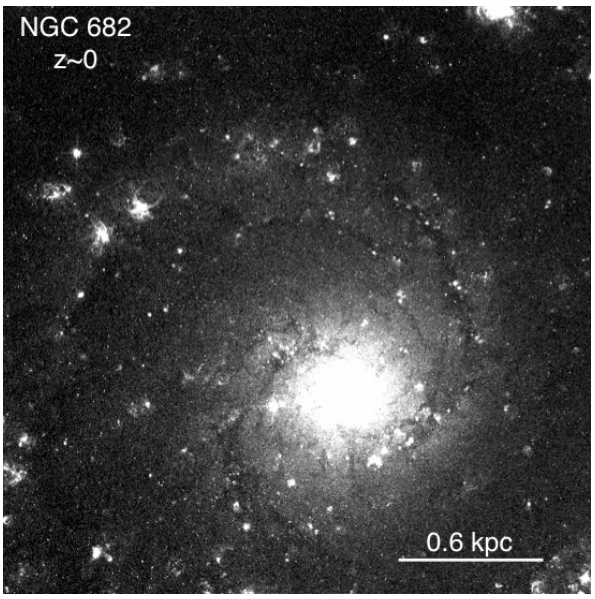

(a): local, low $\Sigma_{\rm SFR}$

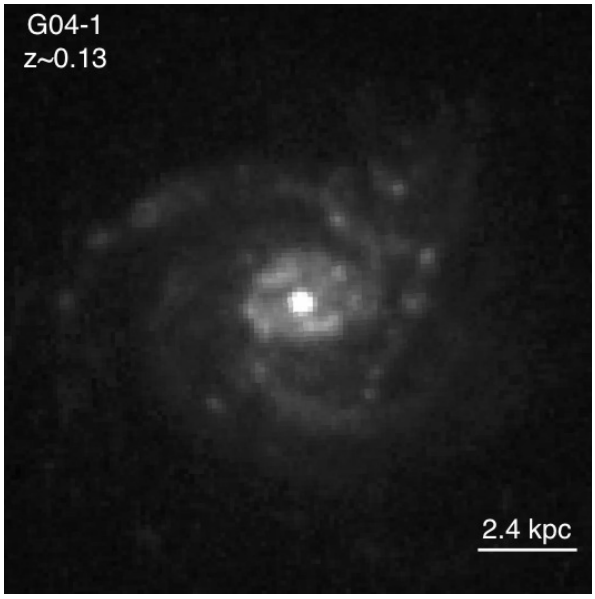

(b): local, high $\Sigma_{\rm SFR}$

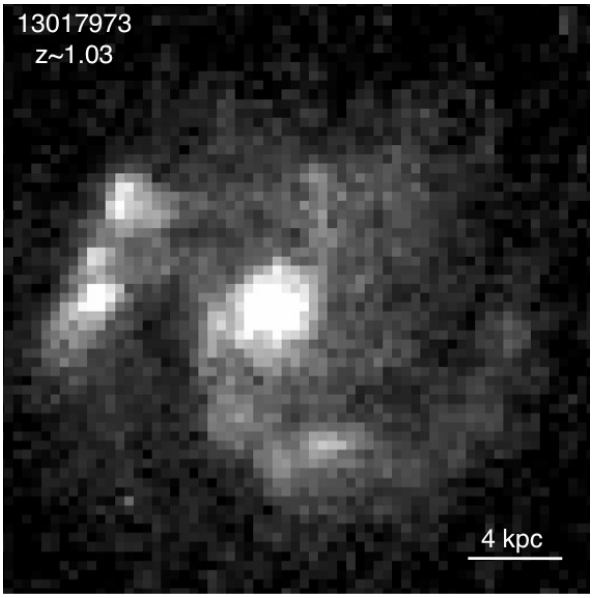

(c): high-redshift, unlensed

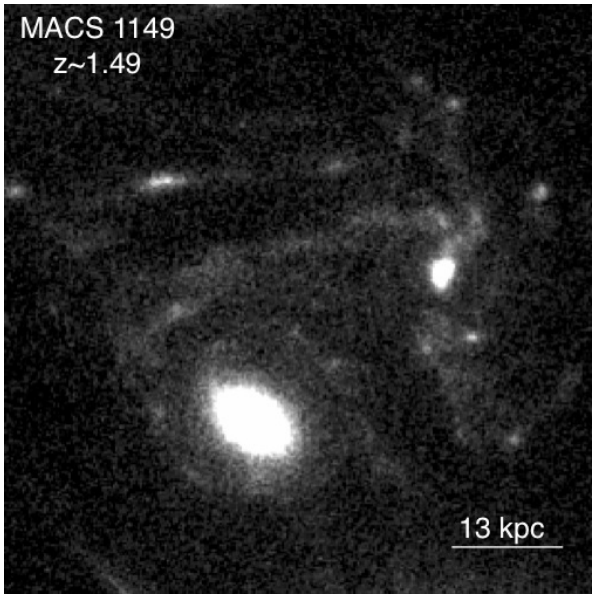

(d): high-redshift, lensed

Figure 2.1: HST images from archival ACS data of galaxies representative of the variation in morphology within the full sample investigated here. (a): local SINGS galaxy NGC 628 included in the sample of $z \approx 0$ H II regions (Kennicutt et al., 2003, data set #10 in Table 2.1) taken with ACS F658W filter. (b): turbulent local galaxy from the DYNAMO sample (Fisher et al., 2017, data set #11) taken in the ACS/WFC1-IRAMP FR716N filter. (c): $z \sim 1$ unlensed galaxy from the IROCKS sample (Mieda et al., 2016, data set #9) imaged in the F814W filter with ACS. (d): $z \sim 1.5$ lensed galaxy MACS 1149 (Livermore et al., 2015, data set #3) taken with the ACS F814W filter. Scale is at the redshift of MACS 1149 without taking into account the lensing effects which cause the spatial resolution to vary across the galaxy.

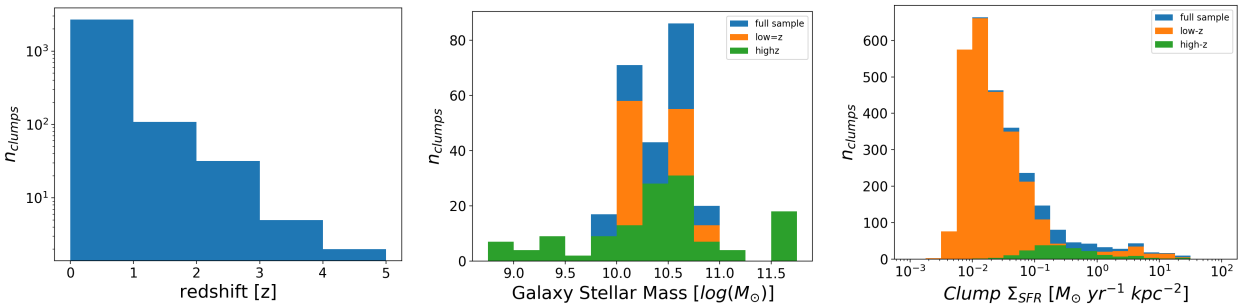

(a) (b) (c)

Figure 2.2: Histograms showing the distribution of clump properties for the full sample. (a): redshift of each clump. The abundance of local samples and difficulty of observing higher redshift galaxies leads to the bias towards low redshift seen here. (b): Stellar mass of the host galaxy for each clump used. Values of host galaxy stellar mass were not reported for data set numbers 4, 5, & 10 as designated in Table 2.1. (c): $\Sigma_{\rm SFR}$ of each clump. The bias towards lower $\Sigma_{\rm SFR}$ comes from the high numbers of local H II regions with lower $\Sigma_{\rm SFR}$.

2.3 Analysis: Bayesian Inference

Previous investigations of high-redshift clumps have employed least-squares fitting to determine clump scaling relations (i.e. Wisnioski et al. (2012); Mieda et al. (2016)). However, standard weighted least-squares relies on many assumptions about the inputs; to truly be reliable there are strict constraints that are often not really the case for the data (Hogg et al., 2010). These constraints are that one dimension has negligible uncertainties and the uncertainties in the other dimension are Gaussian with a known variance.

Most often there will be non-negligible uncertainties in both dimensions, and these uncertainties are not always Gaussian. An approximation to meeting the constraints above would be to propagate the uncertainties of both dimensions to an overall uncertainty for each data point, but this is only an approximation and therefore not as reliable as including the uncertainties on their respective dimension. This approximated uncertainty also may not be Gaussian, violating the second constraint.

Another possible method for determining the scaling relations is to employ Bayesian inference along with Markov Chain Monte Carlo (MCMC) sampling. Bayesian analysis maps the

posterior distribution, but the models can be complex and it is extremely difficult to work with this distribution directly. MCMC methods provide a way to sample the distribution and produce well defined statistical estimates of model parameters (Tierney, 1994).

Bayes' Theorem in its most basic form is stated as follows:

$$\mathscr{P}(A|B) = \frac{\mathscr{P}(B|A)\mathscr{P}(A)}{\mathscr{P}(B)} \tag{2.1}$$

$\mathscr{P}(A|B)$ is the likelihood of event A given that B is true (conditional probability); $\mathscr{P}(B|A)$ is the likelihood of event B given A is true; and $\mathscr{P}(A)$ and $\mathscr{P}(B)$ are the likelihood of observing A and B independently (marginal probability). In Bayesian inference $\mathscr{P}(A)$ is known as the "prior" and $\mathscr{P}(A|B)$ as the "posterior". For a set of data points or events, $\mathscr{P}(B) = \sum_{j=0}^{N} \mathscr{P}(B|A_j)\mathscr{P}(A_j)$ and Bayes Theorem becomes:

$$\mathscr{P}(A_i|B) = \frac{\mathscr{P}(B|A_i)\mathscr{P}(A_i)}{\sum_{j=0}^{N} \mathscr{P}(B|A_j)\mathscr{P}(A_j)} \tag{2.2}$$

By using Bayesian inference we are able to easily account for intrinsic scatter in the relationship as well as measured uncertainties in **both** dimensions without approximating to an overall uncertainty. We are also able to include previously known information about the data and relationship through the priors (Berger, 1985). Priors essentially define the domain of the parameters we are trying to determine in the fitting. How we choose these priors is informed both theoretically and empirically by previous data and fitting. Additionally, we can not only determine an estimate for a model parameter, but also an uncertainty for that estimate, meaning that we can determine the best fit and have a well defined uncertainty for that model. This comes from the fact that Bayesian analysis produces a distribution for the unknown model parameters, the posteriors (Berger, 1985).

Given the advantages of Bayesian inference as well as the shortcomings of a traditional least squares fit it seems prudent to employ Bayesian inference to investigate the clump scaling relations.

2.3.1 Fitting Data Using PyStan

Data from star forming clumps in local and high-redshift galaxies were fit using PyStan, the Python interface to Stan, a tool for Bayesian statistical modeling using MCMC sampling techniques (Stan Development Team, 2017). This MCMC script was run including measurement uncertainty on both clump luminosity and size. One difficulty in this fitting process is determining how best to incorporate uncertainties since each study being included determines their uncertainties differently. Some studies have very large uncertainties while others are very small or not calculated at all. Even within similar studies (i.e. lensed vs unlensed or similar instrument and redshift) the size of the uncertainties is not consistent. For example, in the unlensed sample, Wisnioski et al. (2012) has uncertainties on clump radius and luminosity, Mieda et al. (2016) only has uncertainty for luminosity[1], Genzel et al. (2011) have small uncertainties for both, and uncertainties were not listed for Freundlich et al. (2013).

In order to make the weighting of each point reasonable (and to include what we believe to be more accurate estimates of the uncertainty), some adjustments were made to the data set. First, the uncertainties on Mieda et al. (2016) clump radius were scaled to be proportional to the average uncertainty of the Wisnioski et al. (2012) radii measurements since both use Keck/OSIRIS at similar redshift. Second, 10% error[2] was added to both the clump radius and luminosity of the $z \approx 0$ H II regions as well as the data from Genzel et al. (2011) and Freundlich et al. (2013) to make the weighting of these data points consistent with surveys of similar objects in the PyStan fit. Lastly, the Nguyen-Luong et al. (2016) SFRs were measured using 21 cm continuum emission and CO 1-0 data with an assumed typical uncertainty of 50% (with variation from 30% to 100%) on the full sample of GMCs, MCCs, and galaxies used in their study. Since we are only using the nearby MCCs observed by Nguyen-Luong et al. (2016) we apply an uncertainty of 40% error for these clump radius and luminosity measurements. It should be noted that the measured uncertainties

[1]Mieda et al. (2016) determined that the definition used for a clump had a larger impact on the uncertainty of the radius than the measurement error itself.

[2]The average uncertainty for the unlensed data is $\sim 15\%$. 10% was used for these measurements so as to not underweight data points which may have lower uncertainties than the average based on methods or redshift.

do not account for differences in methods of detecting clumps and defining their sizes. This is a significant source of additional uncertainty discussed in detail in Livermore et al. (2012); Wisnioski et al. (2012)[3].

After these adjustments to the reported uncertainties were made the PyStan fitting was performed using a simple linear model:

$$ln(L_{H\alpha}) = \alpha\, ln(r_{clump}) + \beta \tag{2.3}$$

where α and β are the variables determined in the fit. Using this linear model required taking the natural logarithm of the data to produce a power-law fit of the form:

$$L_{H\alpha} = \exp(\beta) r_{clump}^{\alpha} \tag{2.4}$$

The Stan multinormal function was used to fit this model with uncertainties on both $L_{H\alpha}$ and r_{clump}, as well as allowing for intrinsic scatter in both dimensions. The multinormal function is a Hamiltonian Monte Carlo (HMC) method–a type of MCMC method which samples the derivatives of the probability density function (Stan Development Team, 2017). The geometry of the HMC is described further in Betancourt and Stein (2011).

The likelihood function used for a single data point in this model is:

$$\mathscr{P}(\vec{x_i}|\mathscr{M}) = \int d(x_{th,i}) \mathscr{N}(\vec{x_{th,i}}, \Sigma + V|\vec{x_i}) \tag{2.5}$$

With $\vec{x_i} = \{x_i, y_i\}, and\ \vec{x_{th}} = \{x_{th}, y_{th}\}$, where $\vec{x_{th}}$ is the theoretical true positions of x and y ($x = r_{clump},\ y = L_{H\alpha}$). $\mathscr{M}$ is the set of model parameters (slope, α; intercept, β; and intrinsic scatter, $\sigma_x,\ \sigma_y$; prior values listed in Table 2.2), Σ corresponds to the covariance matrix with uncertainties on clump size and luminosity, and V is a 2×2 matrix incorporating intrinsic scatter[4] ($V_{xx} = \sigma_x^2$,

[3]Wisnioski et al. (2012) estimates an additional 30% uncertainty on clump sizes due to the method of measuring the clump size as well as resolution and systematic effects. We do not include this in our fitting as it would be the same additional weighting for all points and therefore not impact the overall fitting.

[4]Note that the intrinsic scatter priors, σ_x and σ_y are squared in the matrix and therefore the resulting scatter values

$V_{xy} = V_{yx} = \sigma_x \sigma_y$, $V_{yy} = \sigma_y^2$). $\mathscr{N}(\vec{x_{th}}, \Sigma + V|\vec{x_i})$ is defined to be:

$$\mathscr{N}(\vec{x_{th}}, \Sigma + V|\vec{x_i}) \equiv \tag{2.6}$$
$$\frac{1}{\sqrt{2\pi|\Sigma+V|}} \exp\left[-\frac{1}{2}(\vec{x_i} - \vec{x_{th}}) \cdot (\Sigma + V)^{-1} \cdot (\vec{x_i} - \vec{x_{th}})\right]$$

The full likelihood function is found by summing Equation 2.5 over all data points:

$$\mathscr{P}(\vec{x}|\mathscr{M}) = \prod_{i=0}^{N-1} \mathscr{P}(\vec{x_i}|\mathscr{M}) \tag{2.7}$$

This model was also extended to three dimensions to investigate the dependence of the scaling relations on additional measured properties of the clumps. This gives a multi-parameter power-law fit of the form:

$$L_{H\alpha} = \exp(\beta) r_{clump}^{\alpha} \delta^{\gamma} \tag{2.8}$$

with α, β, and γ being determined in the PyStan fitting and δ being an additional property of the clump such as velocity dispersion (σ) or host galaxy gas fraction (f_{gas}). This is fit with the Stan multinormal function with uncertainties provided and intrinsic scatter allowed in all three dimensions.

Note that the luminosity of the clumps in Hα ($L_{H\alpha}$) is used to investigate the star forming relations of the clumps since it is proportional to the star-formation rate (SFR) (Kennicutt, 1998b) and avoids differences in choice of initial mass function (IMF) between studies. Both $L_{H\alpha}$ and SFR are used to investigate clump scaling relations throughout the literature. When Σ_{SFR} is used in our analysis a Chabrier IMF (Chabrier, 2003) is applied to convert from $L_{H\alpha}$ for all data.

It should also be noted that the data set from Mieda et al. (2016) consists of both resolved and unresolved[5] clumps. These will be denoted with different symbols in all plots but will be treated the same in the fitting. All $z \approx 0$ H II regions used in this paper (Kennicutt et al., 2003;

are absolute values and the distribution should be thought of as mirrored about zero.

[5]The unresolved clumps in Mieda et al. (2016) give an upper limit on the size of these regions. These clumps have a 30% uncertainty on their size included for weighting the data points and make up less than 2% of the total sample. Therefore we do not expect an overestimate on the size of the clumps to have a significant impact on the resulting fits.

Table 2.2: Priors used in PyStan Fitting

Model Parameter	Minimum	Maximum
slope, α	0	5
intercept, β	0	100
scatter(r), σ_x	0	100
scatter(L), σ_y	0	100
*second slope, γ	0	5
*scatter(δ), σ_z	0	100

Note. — All priors used covered a significantly wider range than the values settled on after the warm-up phase of the fitting (those used in determination of model results), except for the scatter parameters which settle around a value of zero. However, these should be thought of as an absolute value mirrored about zero.
*: parameters used in extension of model to 3-D fits only.

Gallagher and Hunter, 1983; Arsenault and Roy, 1988; Bastian et al., 2006; Rozas et al., 2006; Monreal-Ibero et al., 2007) will be grouped together for the purposes of fitting and figures since they are all unlensed galaxies at $z \sim 0$ and have had corrections applied by Wisnioski et al. (2012). The other local analogs (Fisher et al., 2017; Nguyen-Luong et al., 2016) are grouped individually due to typically larger clump sizes and higher star formation rate densities (Σ_{SFR}) than the group of local H II regions.

2.4 Results: Clump Size and Star Formation Scaling Relations

All data described in Section 2.2 and Table 2.1 were combined and divided into various subsets for fitting and investigating the clump size-luminosity relationship. This allows for the investigation of whether there is a dependence on redshift, study selection effects, velocity dispersion (σ) of the ionized gas in the clumps, star formation rate surface density (Σ_{SFR}), or gas fraction (f_{gas})

of the host galaxy. The results for each data subset are shown in Tables 3.3.8 - 2.5. These include the determined intercept, slope(s) and intrinsic scatter in each dimension as well as uncertainites on each of those values. The results of each fit discussed in the text as well as fits to additional data subsets (described in column 1) are included in these tables.

Table 2.3: Size - Luminosity Relation Fit Parameters: ($L_{H\alpha} = e^{\beta} r_{clump}^{\alpha}$)

Data Set	Reference #'s*	Figure	α	β	Scatter (r)	Scatter (L)	# of Clumps
all data	1-12	2.3	$3.029^{+0.027}_{-0.027}$	$74.384^{+0.122}_{-0.126}$	$0.186^{+0.124}_{-0.128}$	$0.194^{+0.125}_{-0.127}$	2848
no $z \approx 0$ H II regions	1-9, 11-12	⋯	$1.959^{+0.040}_{-0.037}$	$82.644^{+0.257}_{-0.255}$	$1.115^{+0.877}_{-0.822}$	$1.246^{+0.778}_{-0.912}$	356
high Σ_{SFR} (all z)	1-12	2.6	$1.741^{+0.060}_{-0.067}$	$85.159^{+0.377}_{-0.321}$	$0.476^{+0.355}_{-0.333}$	$0.484^{+0.354}_{-0.324}$	152
low Σ_{SFR} (all z)	1-12	2.6	$2.767^{+0.021}_{-0.023}$	$75.356^{+0.100}_{-0.104}$	$0.121^{+0.086}_{-0.073}$	$0.136^{+0.076}_{-0.086}$	2696
high Σ_{SFR} (z∼0)	10-12	⋯	$1.479^{+0.094}_{-0.052}$	$86.416^{+0.260}_{-0.504}$	$0.940^{+0.769}_{-0.629}$	$1.021^{+0.916}_{-0.666}$	114
low Σ_{SFR} (z∼0)	10-12	⋯	$2.656^{+0.034}_{-0.034}$	$75.798^{+0.149}_{-0.153}$	$0.138^{+0.097}_{-0.095}$	$0.143^{+0.091}_{-0.097}$	2527
corrected high Σ_{SFR}	1-12	2.9	$1.725^{+0.067}_{-0.059}$	$85.334^{+0.327}_{-0.364}$	$0.502^{+0.453}_{-0.344}$	$0.607^{+0.359}_{-0.411}$	200
corrected low Σ_{SFR}	1-12	2.9	$2.862^{+0.034}_{-0.037}$	$74.953^{+0.165}_{-0.156}$	$0.122^{+0.080}_{-0.081}$	$0.121^{+0.081}_{-0.080}$	2648
corrected; no $z \approx 0$ H II regions	1-9, 11-12	⋯	$2.296^{+0.070}_{-0.077}$	$81.230^{+0.386}_{-0.396}$	$0.639^{+0.488}_{-0.406}$	$0.636^{+0.460}_{-0.440}$	356
$z \approx 0$ H II regions only	10	2.10	$2.448^{+0.036}_{-0.034}$	$76.681^{+0.157}_{-0.160}$	$0.198^{+0.123}_{-0.131}$	$0.179^{+0.134}_{-0.123}$	2492
all $z \sim 0$	10-12	2.10	$3.057^{+0.038}_{-0.035}$	$74.229^{+0.148}_{-0.165}$	$0.176^{+0.119}_{-0.121}$	$0.174^{+0.120}_{-0.120}$	2641
$0.6 \leq z < 1.5$	3-5, 7-9	2.10	$2.099^{+0.078}_{-0.068}$	$80.498^{+0.457}_{-0.519}$	$0.318^{+0.221}_{-0.203}$	$0.328^{+0.227}_{-0.217}$	160
$z \geq 1.5$	1-4, 6	2.10	$1.828^{+0.180}_{-0.080}$	$84.175^{+0.626}_{-1.281}$	$1.959^{+1.828}_{-1.334}$	$2.020^{+1.852}_{-1.452}$	47
lensed high-z	1-5	2A.1	$2.099^{+0.199}_{-0.147}$	$81.188^{+0.859}_{-1.230}$	$0.790^{+0.750}_{-0.566}$	$0.804^{+0.706}_{-0.548}$	108
unlensed high-z	6-9	2A.1	$2.266^{+0.115}_{-0.086}$	$79.465^{+0.756}_{-0.867}$	$0.414^{+0.397}_{-0.285}$	$0.488^{+0.324}_{-0.326}$	209

Note. — *: Reference numbers correspond to data from studies as defined in Table 2.1.

Table 2.4: 3D Fit Parameters: σ ($L_{H\alpha} = e^{\beta} r_{clump}^{\alpha} \sigma_{clump}^{\gamma}$)

Data Set (Reference #'s)	α	γ	β	Scatter (r)	Scatter (σ)	Scatter (L)	# of Clumps
2,3,6,7,9,10*,11	$1.026^{+0.089}_{-0.086}$	$2.211^{+0.141}_{-0.138}$	$79.038^{+0.377}_{-0.492}$	$0.091^{+0.094}_{-0.062}$	$0.091^{+0.094}_{-0.062}$	$0.098^{+0.095}_{-0.067}$	346
2,3,6,7,9,10*,11 (2D)	$2.049^{+0.044}_{-0.036}$	⋯	$81.531^{+0.240}_{-0.302}$	$1.539^{+0.936}_{-0.992}$	⋯	$1.246^{+1.033}_{-0.918}$	346

Note. — *:Only Gallagher and Hunter (1983); Arsenault and Roy (1988); Bastian et al. (2006); Rozas et al. (2006); Monreal-Ibero et al. (2007) from this set number. Not all data sets in the full sample included measurements of σ_{clump}, leading to slightly higher uncertainties on the fit. The results of fitting this sample with the 3D model above are in the first row and the 2D fit excluding σ are in the second row for comparison of the change in slope, uncertainty, and scatter when including this third dimension in the fit.

The overall combined data set shown in Figures 2.3 and 2.4 results in a scaling relationship of $L_{H\alpha} \propto r^{3.029}$. This sample includes a wider range of data than has previously been used in this

Table 2.5: 3D Fit Parameters: $f_{gas}(L_{H\alpha} = e^{\beta} r_{clump}^{\alpha} f_{gas}^{\gamma})$

Data Set (Reference #'s)	α	γ	β	Scatter (r)	Scatter (f_{gas})	Scatter (L)	# of Clumps
5,8,9,11*	$1.345^{+0.087}_{-0.092}$	$0.471^{+0.064}_{-0.064}$	$86.716^{+0.666}_{-0.629}$	$0.412^{+0.455}_{-0.298}$	$0.412^{+0.455}_{-0.298}$	$0.370^{+0.477}_{-0.277}$	157
5,8,9,11* (2D)	$1.611^{+0.030}_{-0.030}$	$\cdots$	$84.942^{+0.289}_{-0.269}$	$2.223^{+1.555}_{-1.505}$	$\cdots$	$2.299^{+1.469}_{-1.502}$	157

Note. — *: Measurements of f_{gas} from White et al. (2017), size and luminosity from Fisher et al. (2017). Not all data sets included measurements of f_{gas}, leading to slightly higher uncertainties on the fit. The results of fitting this sample with the 3D model above are in the first row and the 2D fit excluding f_{gas} are in the second row for comparison of the change in slope, uncertainty, and scatter when including this third dimension in the fit.

type of comparison with these figures illustrating some key features of the data set. The large scatter shown in the size-luminosity plot of Figure 2.3 and highlighted in Figure 2.4 causes one of the main problems with determining a reliable size-luminosity relationship. Different relationships will be derived depending on what data is used for the comparison, which could account for some of the variation seen in previous studies. The large scatter ($\sim$3dex) at fixed radius illustrated in Figure 2.4 indicates dependence of the luminosity on a second parameter in addition to the radius of the clump. In order to investigate the reasons for this scatter and what drives the relationship we have divided the data into the subsets shown in Table 3.3.8 and described in the following pages.

The absence of data in the lower right of Figures 2.4 & 2.3 (corresponding to large, low surface brightness clumps) is likely due to a sensitivity limit in what clumps can be observed with current instruments. This is discussed further in Section 2.5.5 and may be partially responsible for the steeper slope here than determined in previous studies. In contrast to this, the lack of observed data with large, high surface brightness clumps cannot be due to a sensitivity limit. This corresponds to the shaded region in the upper right of Figure 2.4 referred to as the "Null Detection Region". This may be due to a physical absence of clumps at this regime which could be the result of feedback mechanisms (discussed further in Section 3.3.5).

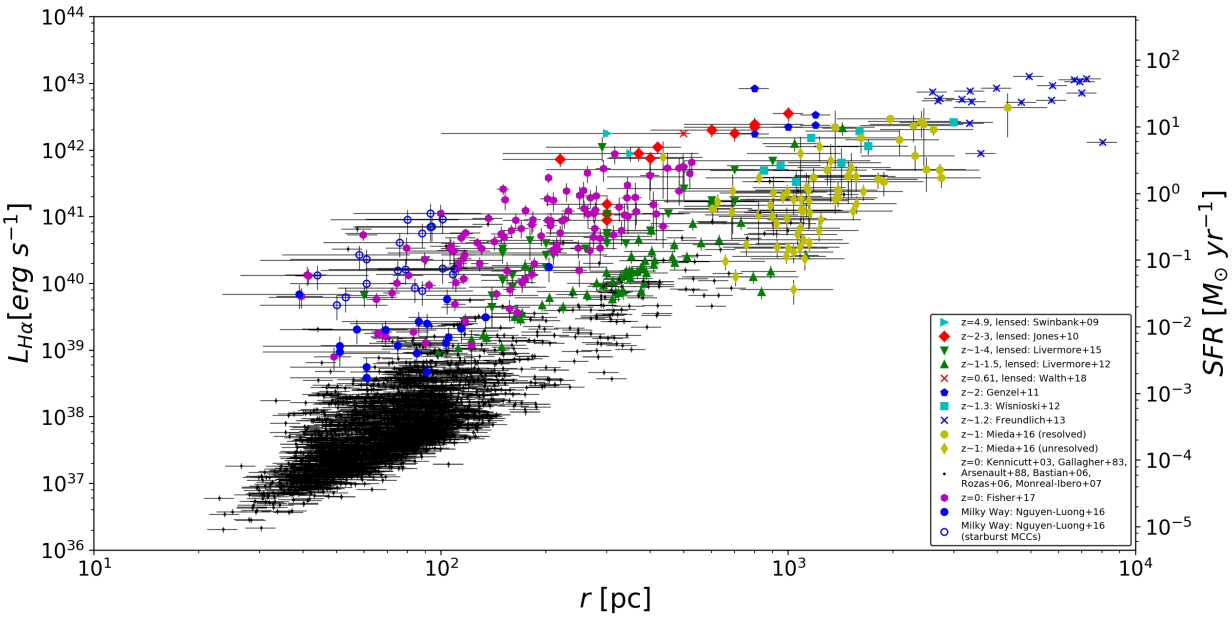

Figure 2.3: Clump size and luminosity for all the data used throughout this paper. In the case that the star formation rate (SFR) only is reported, this is converted back to the equivalent Hα luminosity following Kennicutt (1998b) and the initial mass function from Chabrier (2003). This was the case for the Livermore et al. (2012), Swinbank et al. (2009), Walth et al. (2019) and Freundlich et al. (2013) data. NOTE: The SFR reported in Swinbank et al. (2009); Freundlich et al. (2013) is derived from [[OII]] emissions, not $H\alpha$, which may introduce up to a factor of $\sim$2 difference from Hα derived SFR (Kewley et al., 2004). The size reported for Freundlich et al. (2013) clumps is derived from IRAM CO measurements and is sometimes less than the 1" slit used for [[OII]] luminosity measurements. Nguyen-Luong et al. (2016) use CO 1-0 and 21 cm continuum emission to estimate SFR which can contribute to the scatter between these measurements and those from ionized gas emission. However, the 40% uncertainty for these data points significantly reduces their weight in the fit.

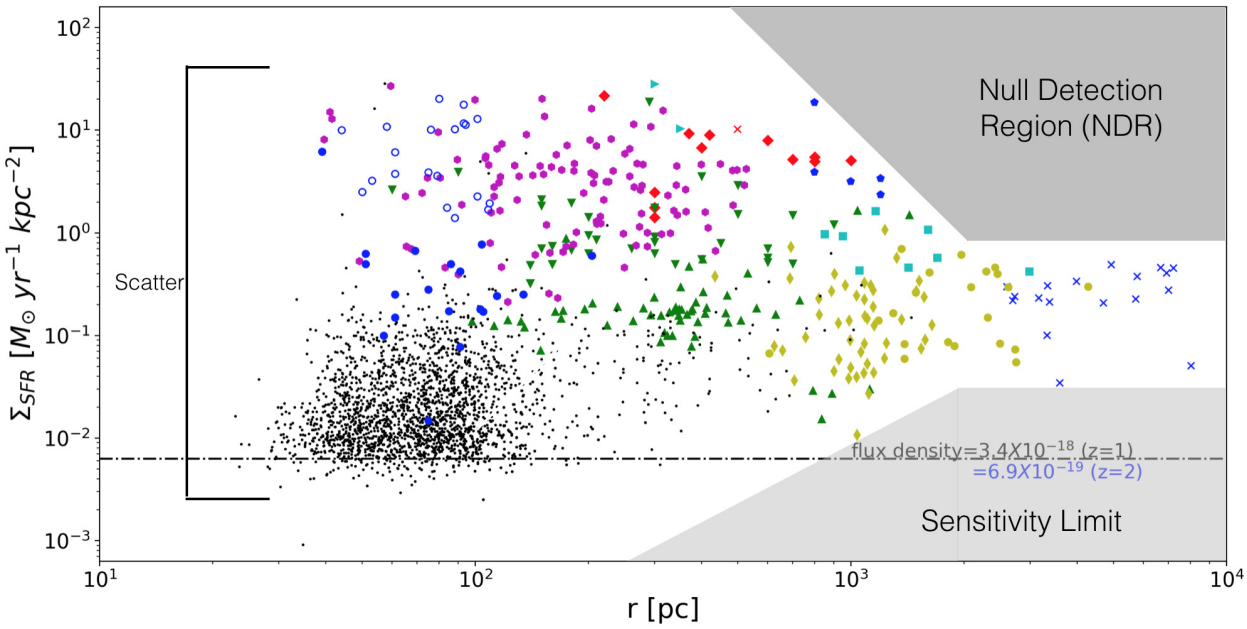

Figure 2.4: Clump size plotted against the star formation surface density (Σ_{SFR}) to illustrate the large variation in the various data sets (see Figure 2.3 for legend). The scatter is outlined to the left; this is prevalent for both the Milky Way up to high-redshift. This indicates that the clump size is not the only factor influencing the SFR. The shaded region in the lower right illustrates the lack of data seen at this regime of large, low surface brightness clumps which is likely due to a sensitivity limit of the instruments being used. The dashed black line shows what the observed flux density would be at this $\Sigma_{\rm SFR}$ for $z = 1$ (black text) and $z = 2$ (blue text). This exact limit will depend on the individual study and vary within studies in the case of gravitationally lensed galaxies (see Figure 2C.1 for more detailed sensitivity levels). The shaded region in the upper right labelled "Null Detection Region (NDR)" corresponds to a lack of observations of large clumps with *high* surface brightness. This would not be due to a sensitivity limit and likely corresponds to a physical absence of clumps in this regime.

2.4.1 Star Formation Surface Density (Σ_{SFR}) Break

Nguyen-Luong et al. (2016) determine that there is a break in the slope of the scaling relations and star formation laws locally in their sample of MCCs between normal star-forming objects and what they refer to as mini-starbursts (gravitationally unbound MCC's with $\Sigma_{SFR} > 1$ M$_\odot$ yr^{-1} kpc^{-2}). Johnson et al. (2017) find that H II regions in the SINGS sample (Kennicutt et al., 2003) have significantly lower Σ_{SFR} than the z$\sim$2 lensed samples they are comparing them to and that the higher Σ_{SFR} of the DYNAMO galaxies (Fisher et al., 2017) provide a better analog to the massive star forming clumps seen at high redshift. This indicates that there may be two different process occurring in different types of clumps with different scaling relations that skew the results of fitting the data as a whole.

In order to test this data were divided into two groups, high Σ_{SFR} and low Σ_{SFR} defined by varying Σ_{SFR} cut-offs. We investigate the location of the break by incrementally varying the cut-off Σ_{SFR} value and comparing the slope for the high and low Σ_{SFR} subsets to a baseline result with the break defined at $\Sigma_{SFR} = 1$ M$_\odot$ yr^{-1} kpc^{-2} as illustrated in Figure 2.5. We vary the Σ_{SFR} break in increments of 0.25 between $\Sigma_{SFR} = 0.25 - 2.5$ M$_\odot$ yr^{-1} kpc^{-2}, and then adjust the step size due to the logarithmic nature of the distribution[6]. Changes in slope > 0.12 (3$\times$ the average uncertainty in the baseline slope) are considered significant, but do not result from breaks between $\Sigma_{SFR} = 0.25$ M$_\odot$ yr^{-1} kpc^{-2} and $\Sigma_{SFR} = 1.25$ M$_\odot$ yr^{-1} kpc^{-2}. With Σ_{SFR} breaks located outside of this range the resulting slopes deviate more rapidly and by more than 0.12 from the baseline, supporting the break location in this Σ_{SFR} phase space. Further data at large clump sizes will help to constrain this break in the future. For simplicity we discuss the fitting results only with the break at $\Sigma_{SFR} = 1$ M$_\odot$ yr^{-1} kpc^{-2}. While this is only an approximate value for the cut-off, the resulting scaling relations for the high and low Σ_{SFR} bins are consistent with other cut-offs in this region. Dividing the full data set into high and low Σ_{SFR} clumps results in different slopes, which may imply two unique clump populations with different physical processes occurring:

[6]For example one step below $\Sigma_{SFR} = 0.25$ M$_\odot$ yr^{-1} kpc^{-2} would shift to including the full sample in the fitting, adding a significant number of data points and scatter. To ensure any change in slope is due to a real change in location of the power law break and not the increase in data points we decrease the step size below $\Sigma_{SFR} = 0.25$ M$_\odot$ yr^{-1} kpc^{-2}.

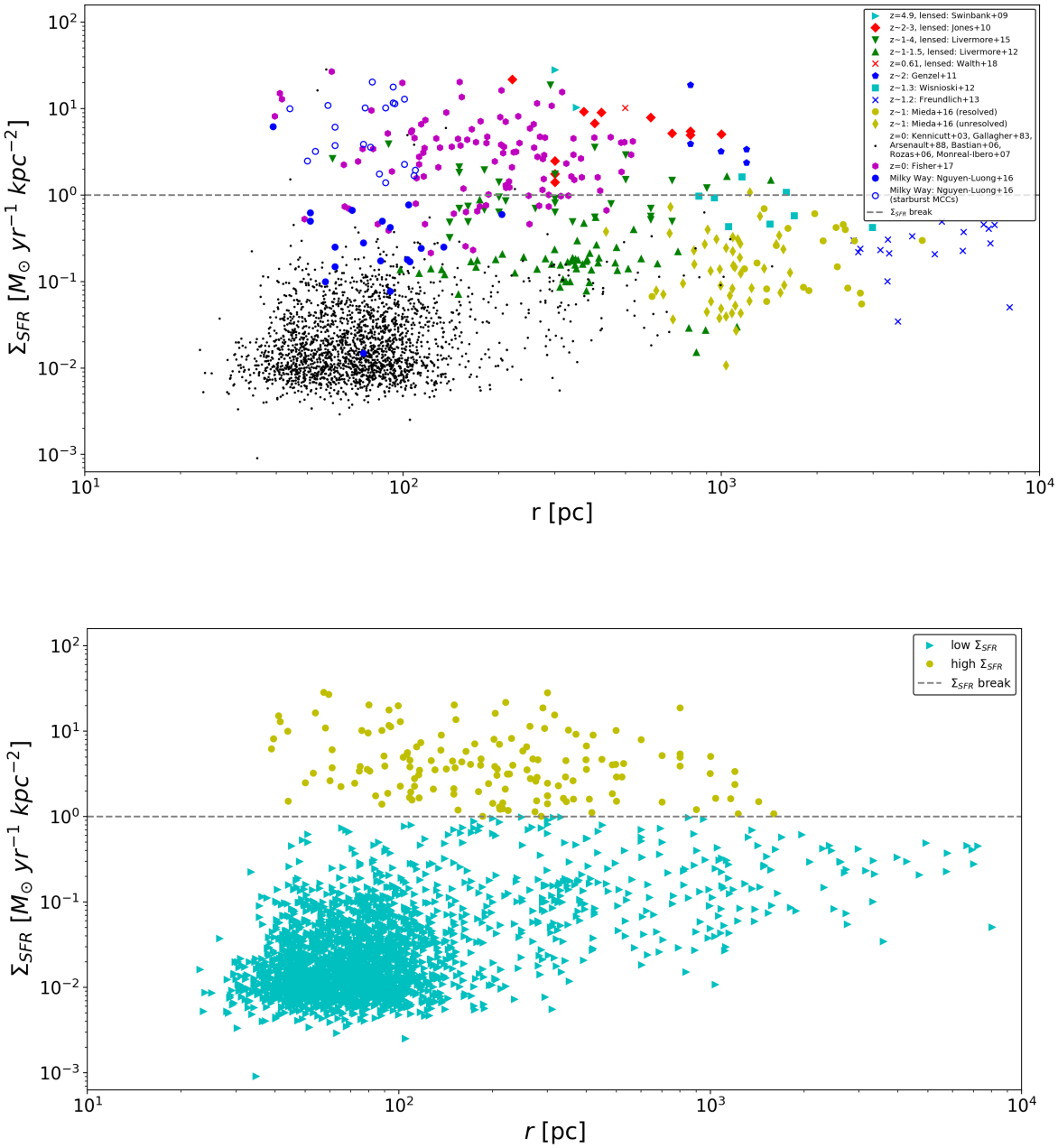

Figure 2.5: Clump size plotted against $\Sigma_{\rm SFR}$ illustrating the power-law break at $\Sigma_{\rm SFR} = 1\,{\rm M}_\odot\ {\rm yr}^{-1}\ {\rm kpc}^{-2}$ (grey dashed line). The top figure shows the data separated by study, while the bottom figure is divided into low and high $\Sigma_{\rm SFR}$.

$$\Sigma_{SFR} > 1\ \mathrm{M_\odot\ yr^{-1}\ kpc^{-2}} : \mathrm{L_{H\alpha}} \propto \mathrm{r_{clump}^{1.7}}$$
$$\Sigma_{SFR} \leq 1\ \mathrm{M_\odot\ yr^{-1}\ kpc^{-2}} : \mathrm{L_{H\alpha}} \propto \mathrm{r_{clump}^{2.8}}$$

The difference in these relationships and approximately where the cut-off lies on the size-luminosity plot are shown in Figure 2.6. Interestingly, the higher Σ_{SFR} data scales with $r^{1.7}$ which is near to what has been suggested for clump formation driven by Toomre instability ($L \propto r^2$ by extending the equations given in Genzel et al., 2011), while the lower Σ_{SFR} data scales like $r^{2.8}$, closer to the expected relation if the clumps are represented by Strömgren spheres ($L \propto r^3$) (Wisnioski et al., 2012). However, the true slope may be shallower than what we find here if lower surface brightness clumps are not being detected due to sensitivity limits. As is shown in the bottom portion of Figure 2.6 the division of the data into high and low Σ_{SFR} sets results in two separate regions on the size-luminosity plot with very little overlap due to scatter. This further supports the idea of multiple processes occurring in these two clump populations even with the possible sensitivity limit.

The scaling found when fitting the full data set with this power-law break is nearly the same as is found when applying the same break to only the $z \approx 0$ data at the smaller size end of the sample (maximum clump size of 1.4 kpc vs. 8 kpc for the full sample) (Kennicutt et al., 2003; Gallagher and Hunter, 1983; Arsenault and Roy, 1988; Bastian et al., 2006; Rozas et al., 2006; Monreal-Ibero et al., 2007; Fisher et al., 2017; Nguyen-Luong et al., 2016). With only this local data, a scaling relationship of $L_{H\alpha} \propto r^{2.7}$ is found for the low Σ_{SFR} star forming regions and $L_{H\alpha} \propto r^{1.5}$ for the high Σ_{SFR} star forming regions. The uncertainty and scatter on these fits is shown in Table 3.3.8 while the posterior probability distribution for the fit to the high and low Σ_{SFR} subsets of the full sample is displayed in Figure 2.7.

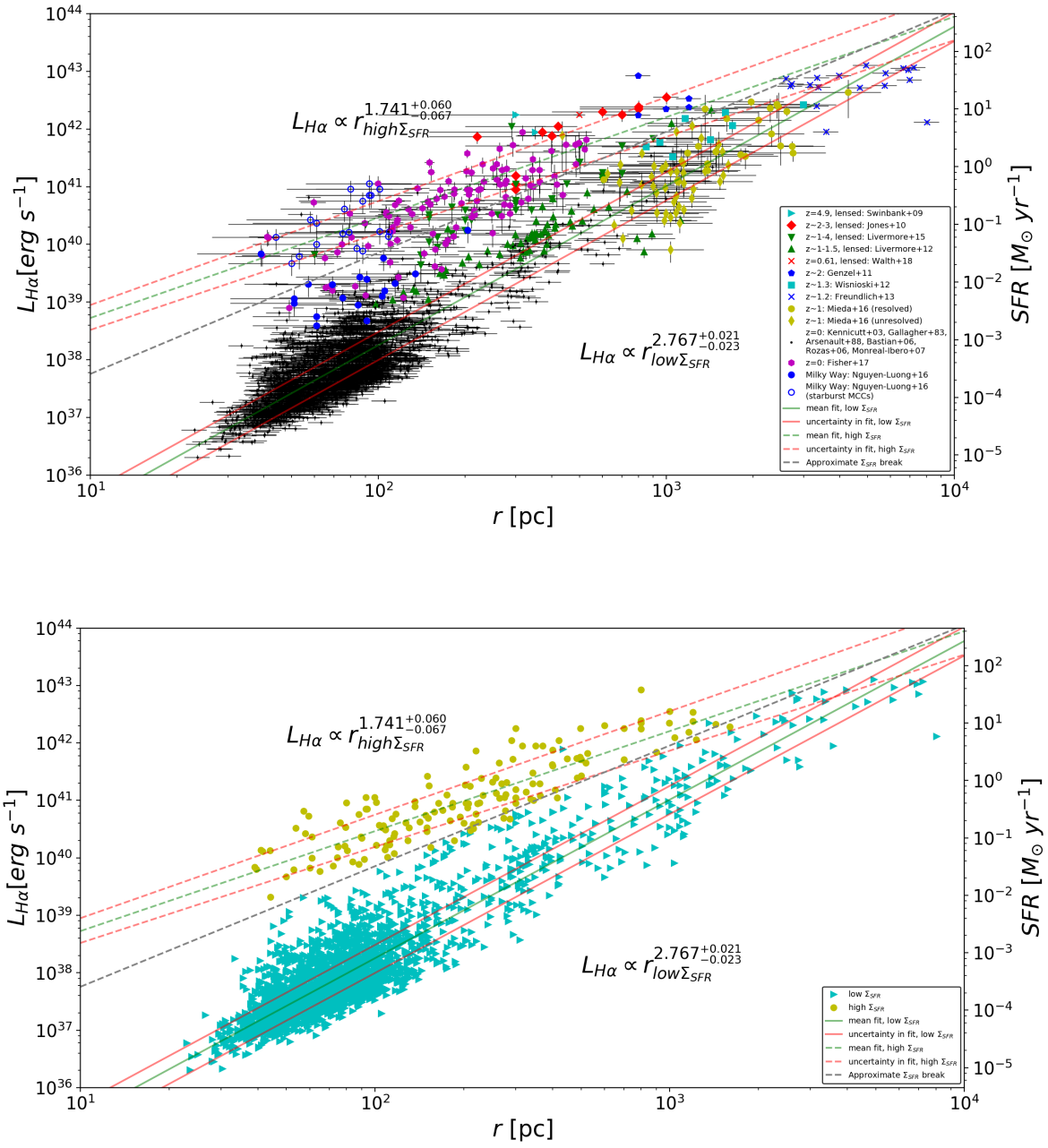

Figure 2.6: Clump size and luminosity relation for the high and low $\Sigma_{\rm SFR}$ bins. The dashed red and green lines show the best fit to the high $\Sigma_{\rm SFR}$ data, while the solid red and green lines show the best fit of the low $\Sigma_{\rm SFR}$ data. The grey dashed line is approximately where the $\Sigma_{\rm SFR} = 1\ {\rm M}_\odot\ {\rm yr}^{-1}\ {\rm kpc}^{-2}$ cut-off lies when converted to luminosity. The top figure shows the data separated by study, while the bottom figure is divided into low and high $\Sigma_{\rm SFR}$.

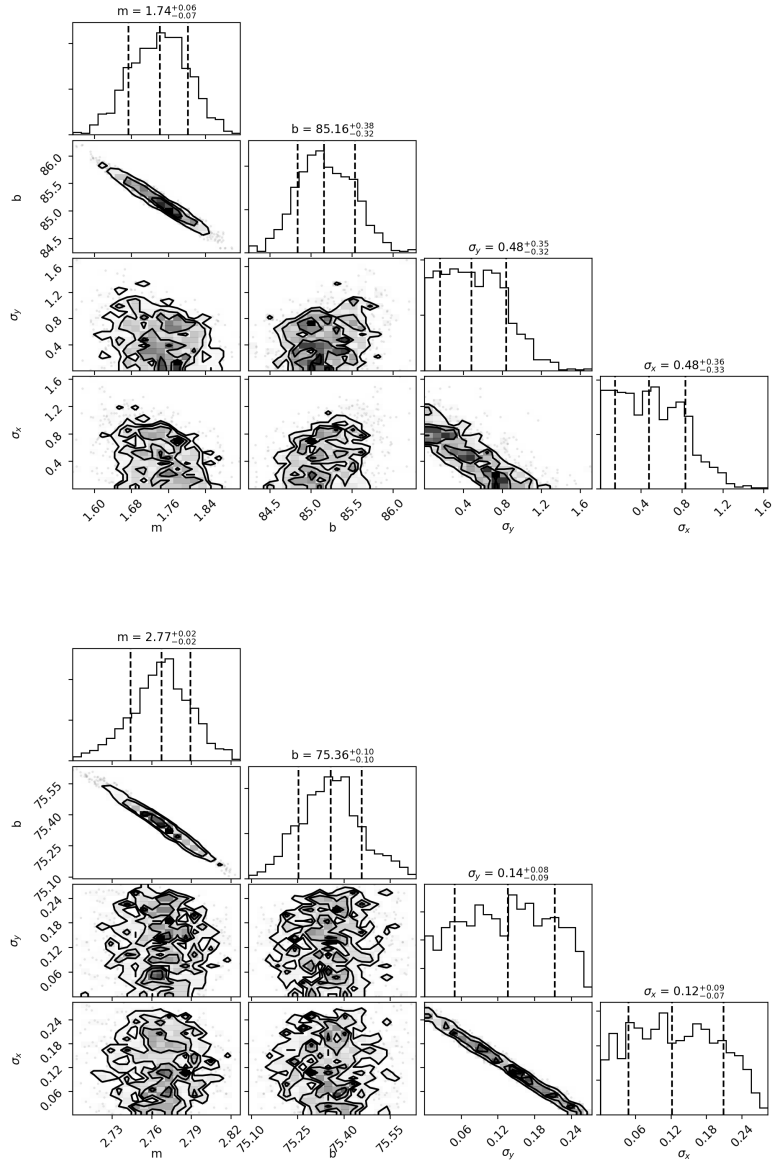

Figure 2.7: Posterior probability distribution for the fits shown in Figure 2.6 with a power-law break based on $\Sigma_{\rm SFR}$. The top figure shows the distribution for the fit to the data with $\Sigma_{\rm SFR} > 1\,{\rm M}_{\odot}$ yr^{-1} kpc^{-2} while the bottom figure corresponds to the fit to the data with $\Sigma_{\rm SFR} < 1\,{\rm M}_{\odot}$ yr^{-1} kpc^{-2}. σ_x and σ_y are intrinsic scatter parameters corresponding to $r_{H\alpha}$ and $L_{H\alpha}$ respectively. Both the slope and intercept of these fits are well constrained from a much broader range of priors (Table 2.2). The values for intrinsic scatter, σ_x and σ_y, are not limited on the high end, but do tend towards zero. As scatter is an absolute value negative values are not possible and the distribution can be thought of as mirrored about zero. These small values of intrinsic scatter indicate that the scatter seen in the data is not intrinsic scatter but may be due to uncertainties. This posterior probability distribution is representative of what is produced for all the fits performed in this analysis.

2.4.2 Corrections for Beam Smearing

It has been suggested that the lower spatial resolution (see Table 2.1) of unlensed high-redshift samples could lead to incorrectly measured clump sizes and an effect of observing "clumps within clumps" where what is actually a group of smaller clumps is observed as one large clump due to beam smearing (Fisher et al., 2017; Cava et al., 2018). To investigate what affect this may have on the measured clump properties, Fisher et al. (2017) degrade the images of their local galaxies to match the resolution of $z \sim 1-2$ observations (from $\sim$ 100 pc to $\sim$ 800 pc spatial resolution). They find that this typically leads to about a factor of 5 increase in the observed SFR (proportional to $L_{H\alpha}$) and a $\sim 6\times$ decrease in the observed $\Sigma_{\rm SFR}$ (translating to a $\sim 5.5\times$ increase in clump sizes). This effect of resolution has also recently been investigated by Cava et al. (2018) in multiple gravitationally lensed images of the same galaxy. The images divide into two distinct sets: the "cosmic snake" which consists of four elongated images of the galaxy, and what is referred to as the counterimage. Cava et al. (2018) report a resolution limit of $\sim$ 300 pc in the counterimage, but can get down to a scale of $\sim$ 30 pc in the cosmic snake. They find that the clumps observed in the counterimage are typically a factor of 2-3 larger than those observed in the cosmic snake.

In order to determine if these effects were occurring and could be currently observed in unlensed galaxies we chose one of the brightest galaxies in the IROCKS sample (Mieda et al., 2016) to re-observe at a smaller plate scale. The original observations made use of the 0.1" plate scale on the OSIRIS instrument at Keck in order to maximize the surface brightness sensitivity (hence, the choice of a high surface brightness galaxy).

Object 42042481 was observed on 2017 August 12 with Keck/OSIRIS at a plate scale of 0.05" per spaxel and the narrowband J filter. Seven 900s exposures (giving 1.75h total integration time; as opposed to 2.5h total integration time at 0.1") of 42042481 were taken along with a pure sky frame. The data was reduced using the OSIRIS data reduction pipeline (DRP) version 4.1 producing a combined cube of all seven frames. This cube was also binned down to the spatial resolution of the 0.1" plate scale for an additional comparison along with the initial observations. These cubes were spatially smoothed in the manner described in Mieda et al. (2016) and to an

equivalent FWHM before the same custom IDL scripts were used to determine the locations and sizes of Hα clumps (this process was also repeated by MC on the previous observation of 42042481 to ensure a consistent comparison). The resulting Hα maps for the original 0.1" observations, the 0.05" observations, and the binned data are shown in Figure 2.8 with marked clump locations and size of the point spread function (PSF). The properties of these clumps are reported in Table 2.6.

The shift from the original 0.1" to 0.05" plate scale resulted in an improved spatial resolution limit from $\sim$ 800 pc to $\sim$ 400 pc causing the largest clump to split into two clumps each roughly half the size originally measured. The new observations also resulted in the detection of two clumps not seen in the original observations (designated H* and I* in Table 2.6 and Figure 2.8). In addition to a change in plate scale for the observations, a new detector on OSIRIS could introduce differences in what clumps were measured.

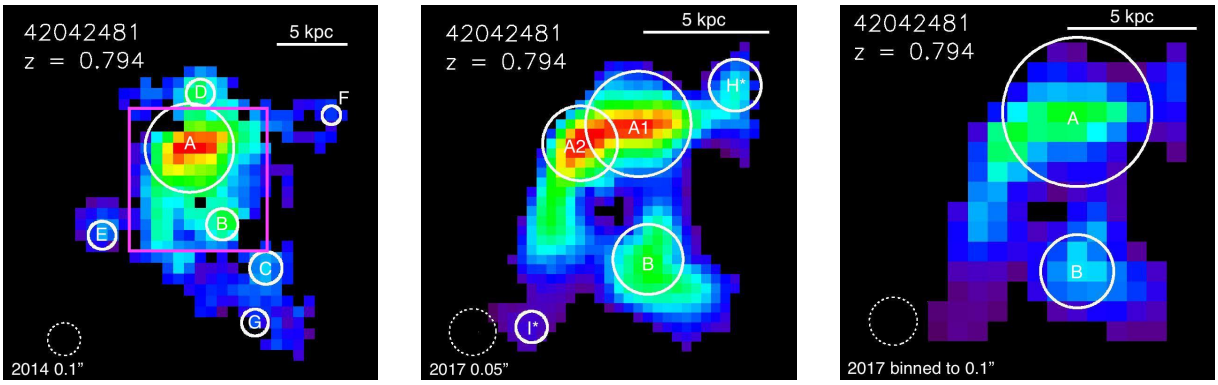

(a): 2014 0.1" observations

(b): 2017 0.05" observations

(c): 2017 0.05" observations binned to 0.1"

Figure 2.8: Clump locations and sizes identified from Hα flux. Following the definition of Mieda et al. (2016), clumps are located via a local Hα peak separated by at least two pixels from a neighboring peak. Clumps A and B are at the same location in all panels; clumps H* and I* in panel (b) are new clumps not found in the initial 0.1" observations. Clump A in the 0.1" plate scale observations appears to break up into two clumps at higher resolution. Sizes of all clumps are listed in Table 2.6. A scale bar is located at the top right of each figure; note that the pixel scale is different for the 0.1" and 0.05" observations. The pink box in panel (a) shows the region covered by the 2017 0.05" plate scale observations. The dashed circle in the lower left of each panel shows the PSF size for that night of observations.

In order to determine the reason for the detection of these additional clumps we compare the flux and Σ_{SFR} of all clumps detected in the new 0.05" observations to those found in the old

Table 2.6: Clump Sizes

Clump	Radius (mas)	Radius (kpc)	Luminosity (10^{40} erg s^{-1})	Σ_{SFR} (10^{-2} M$_\odot$ yr^{-1} kpc^{-2})
2014, 0.1" observations				
A	407	3.14	39.1	5.7
B	143	1.10	3.54	4.1
C	149	1.15	2.92	3.2
D	129	0.99	2.67	3.8
E	128	0.99	2.04	3.0
F	85	0.65	1.37	4.5
G	123	0.95	1.61	2.6
2017, 0.05" observations				
A1	272	2.10	30.2	9.8
A2	193.5	1.49	19.3	12.4
B	181	1.39	13.3	9.8
H*	134	1.03	4.07	5.4
I*	81.5	0.63	1.61	5.9
2017, 0.05" observations binned to 0.1"				
A	375	2.89	52.8	9.0
B	184	1.42	12.3	8.8

Note. — clump properties for observations of object 42042481 compared in Figure 2.8

0.1" observations as well as the results of binning the 0.05" observations to match the resolution of the 0.1" plate scale. These comparisons are shown in Figure 2B.1 (Appendix 2B). Since both the flux and Σ_{SFR} of clumps H* and I* are higher in the 0.05" observations than some of the small clumps in the original observations this cannot be the reason for the detection. Another possible cause for varying detections is the quality of the seeing on each night of observations. In order to investigate this we compare the PSF of the tip-tilt star used for the observations of object 42042481 as well as the seeing measurements from the MASS/DIMM instruments on Mauna Kea. The seeing measurements are reported in Table 2B.1 and the tip-tilt star comparison is shown in Figure 2B.2 with widths in kpc denoted by dashed lines in Figure 2B.1. The PSF and seeing across these two nights is very similar and indicates that this also is not the primary cause of detecting new clumps.

It is probable then that these detection differences stem from how we define and find clumps in our analysis. A clump is defined to be a local peak in Hα flux which is separated from the next local peak by more than 2 pixels in the Hα map (Mieda et al., 2016). All clumps in the 0.05"

observations are separated by a distance of more than 4 pixels (2 pixels at the 0.1" scale) from their nearest detected neighbor but are still not detected in the version of the cube binned to match the resolution of the 0.1" observations. These Hα peaks are then likely being spread out over more pixels leading to less defined peaks and/or smaller separations between them. The introduction of a new detector between these observations could also reduce the noise in the data leading to an increased SNR (even with the lower $\Sigma_{\rm SFR}$ of new clumps H* and I*) and definition between Hα peaks, however the difference between the new 0.05" observations before and after being binned to 0.1" plate scale resolution indicates that plate scale is the main driver of the detection differences.

The difference in resolution for these observations results in a similar change in the size of clump A ($\sim 1.7\times$ smaller) to that seen by Cava et al. (2018), but less than that seen by Fisher et al. (2017) with their degraded images. This difference is likely due to the differences in resolution: Fisher et al. (2017) have a factor of 8 difference in resolution between their local and degraded images, while we have only a factor of 2 difference. It should be noted that our results are only for one galaxy in the sample and while this is an interesting test case it may not be representative of the galaxy population as a whole.

To investigate the possible effect of resolution on the scaling relations determined for a large sample of data we apply the corrections determined by Fisher et al. (2017) to the unlensed, high-redshift data sets. We use these corrections since they are determined for a larger sample of local galaxies. The "true" correction in fact varies for each study and even each clump based on the resolution achieved. However, exactly what the true correction should be is not yet clear; the three cases discussed here all have different ratios for the change in resolution to the change in clump size. As this ratio is highest for the study by Fisher et al. (2017) we use this correction as the most dramatic change we may expect to see for these samples. This translates to increasing the calculated $\Sigma_{\rm SFR}$ by a factor of 6, reducing the measured $L_{H\alpha}$ by a factor of 5, and reducing the measured clump radius by a factor of $\sqrt{30}$. This results in a reduced scatter of $\Sigma_{\rm SFR}$ at fixed radius (from $\sim$3dex to $\sim$2dex) with the exception of the $z \approx 0$ H II region group (Kennicutt et al., 2003; Gallagher and Hunter, 1983; Arsenault and Roy, 1988; Bastian et al., 2006; Rozas et al., 2006;

Monreal-Ibero et al., 2007).

The same $\Sigma_{\rm SFR}$ break as section 2.4.1 was applied to this corrected data and the two subsets were fit individually. This resulted in the size-luminosity relation:

$$\Sigma_{SFR} > 1\ {\rm M}_\odot\ {\rm yr}^{-1}\ {\rm kpc}^{-2} : {\rm L}_{\rm H\alpha} \propto {\rm r}_{\rm clump}^{1.7}\ \text{(corrected)}$$
$$\Sigma_{SFR} \leq 1\ {\rm M}_\odot\ {\rm yr}^{-1}\ {\rm kpc}^{-2} : {\rm L}_{\rm H\alpha} \propto {\rm r}_{\rm clump}^{2.9}\ \text{(corrected)}$$

Figure 2.9 shows the effect of the beam smearing corrections on the high-redshift unlensed data (a), the application of the $\Sigma_{\rm SFR}$ break to the corrected data (b), and the fit to the two sets of data resulting from this break (c). Figure 2.9b also illustrates the reduction in the influence of the "Null Detection Region" and sensitivity limit.

Even after applying these corrections to individual clumps, the overall scaling relations of these high and low $\Sigma_{\rm SFR}$ bins does not change significantly. Individual clumps do change bins, but this does not change the overall slope. However, the break at $\Sigma_{\rm SFR} = 1\ {\rm M}_\odot\ {\rm yr}^{-1}\ {\rm kpc}^{-2}$ is more clearly evident for large clumps after this correction is applied (Figure 2.9b compared to Figure 2.5).

One caution with this correction is that of the large clumps observed in surveys with lower spatial resolution, it may be that only some of them are actually made up of multiple smaller clumps. There are clumps of similar size observed in lensed surveys (Jones et al., 2010; Livermore et al., 2012; Walth et al., 2019) that have much lower spatial resolution limits, so these large clumps do exist. How much of the population consist of large clumps versus groups of smaller clumps is not yet known, and the effect could be less significant than what is determined here. Due to the uncertain nature of this correction we use uncorrected values for the remainder of this paper.

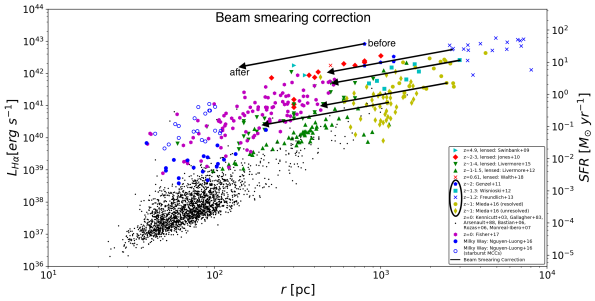

(a): Influence of beam smearing

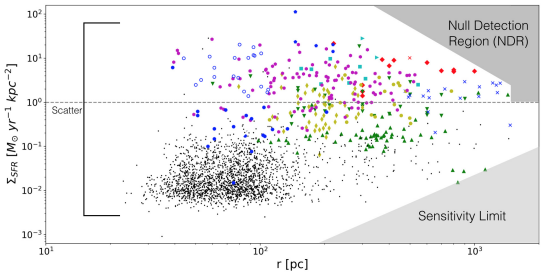

(b):$\Sigma_{\rm SFR}$ and size after corrections

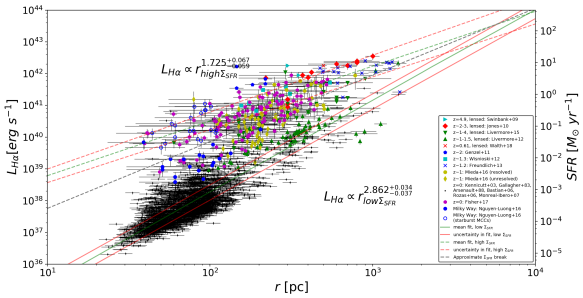

(c): Clump size-luminosity relation after correction

Figure 2.9: (a): Illustration of the beam smearing correction applied to the high-redshift unlensed samples. The correction (from Fisher et al., 2017) results in reducing the measured $L_{H\alpha}$ by a factor of 5 and the measured clump radius by a factor of $\sqrt{30}$. This in turn increases $\Sigma_{\rm SFR}$ by a factor of 6 (moving points down and to the left). Studies which required corrections ($z \gtrsim 1$, unlensed) are circled in the legend. (b): Clump size plotted against $\Sigma_{\rm SFR}$ with corrections for beam smearing applied. The grey dashed line shows the break at $\Sigma_{\rm SFR} = 1\ {\rm M}_\odot\ {\rm yr}^{-1}\ {\rm kpc}^{-2}$ used in dividing the data into high and low $\Sigma_{\rm SFR}$ subsets. The shaded region to the lower right shows the regime of data now missing due to instrumental sensitivity limits, while the shaded region in the upper right shows the new "Null Detection Region" which is not due to a sensitivity limit. (c): Clump size and luminosity relation for the high and low $\Sigma_{\rm SFR}$ bins after corrections for beam smearing. The dashed red and green lines show the best fit to the high $\Sigma_{\rm SFR}$ data, while the solid red and green lines show the best fit of the low $\Sigma_{\rm SFR}$ data. The scaling relations for these two subsets are consistent with those determined before beam smearing corrections indicating that while this moves individual clumps into a different subset, it does not have an impact on the scaling relations within these groups of data.

2.4.3 Redshift Evolution

Data from all of the studies were grouped by redshift into four bins to investigate whether there is a redshift evolution for the relationship between clump size and luminosity. Livermore et al. (2012, 2015) suggest that the intercept of this relationship does evolve with redshift, but Wisnioski et al. (2012) and Mieda et al. (2016) find that their high-redshift samples follow similar scaling relations when including local H II regions. The bins used here are (i) $z \approx 0$ H II regions (data set #10 only, as designated in Table 2.1), (ii) all $z \sim 0$ (data set #10-12 in Table 2.1), (iii) $0.6 \leq z < 1.5$, and (iv) $z \geq 1.5$. The inclusion of two different $z \sim 0$ bins is due to the differing nature of the star forming regions of these samples. The data in bin (i) is from various studies of local star forming H II regions (Kennicutt et al., 2003; Gallagher and Hunter, 1983; Arsenault and Roy, 1988; Bastian et al., 2006; Rozas et al., 2006; Monreal-Ibero et al., 2007), while the second bin includes this data as well as the clumps in Fisher et al. (2017) from low redshift galaxies with turbulent disks and the Milky Way MCCs from Nguyen-Luong et al. (2016). $\Sigma_{\rm SFR}$ is higher in these additional clumps and therefore they provide a local analog to the high-redshift galaxies like those in the lensed samples with higher $\Sigma_{\rm SFR}$; hence the use of two separate low-redshift bins.

Each bin was fit separately using PyStan configured as discussed in Section 2.3.1, and are presented in Figure 2.10. In bin (i) $L_{H\alpha} \sim r^{2.45^{+0.04}_{-0.03}}$, in bin (ii) $L_{H\alpha} \sim r^{3.06^{+0.04}_{-0.04}}$, in bin (iii) $L_{H\alpha} \sim r^{2.10^{+0.08}_{-0.07}}$, and in bin (iv) $L_{H\alpha} \sim r^{1.83^{+0.18}_{-0.08}}$. This shows that the slope does vary somewhat in each redshift bin, however, this is partly due to the smaller size of the data sets once binned; particularly for the highest redshift bin which only consists of 47 clumps. As can be seen here and in Table 3.3.8, the uncertainty on the slope of bin (iv) is an order of magnitude greater than the other bins which have more data points. This also leads to a less constrained intercept for bin (iv) which would affect the slope value determined. Therefore, it is difficult to say for sure whether there is a redshift evolution to the clump size-luminosity scaling relation.

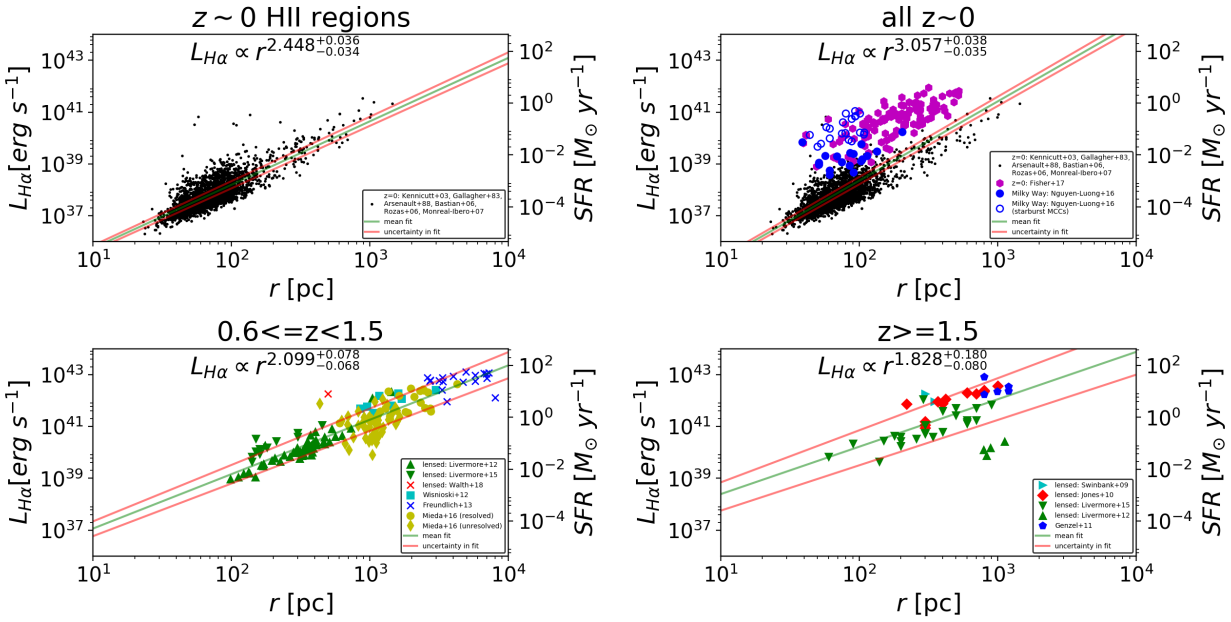

Figure 2.10: PyStan fit to data from each redshift bin. Upper left: bin (i). Upper right: bin (ii); Lower right: bin (iii); Lower left: bin (iv). The uncertainty on the fit determined is larger for the smaller bins (an order of magnitude for bin(iv)) as there is less data to constrain the fit. The variation seen in the slopes between bins is in part due to variation in the intercept which is not as well constrained with the smaller data sets after binning. However, the posterior probability distribution still appears normal for at least bins (i)-(iii). This leads to a caution on how the data sets are binned and fitted to avoid a case of a well constrained fit that is not physically reasonable or reliable.

2.4.4 Star Formation Dependencies: Gas Fraction and Velocity Dispersion

As has been shown in the previous sections, the star forming relations of clumps likely do not simply scale with size. There are other properties of the clumps that could influence this relationship and partly account for the large scatter in the data. So far we have used a third parameter, Σ_{SFR}, to determine a break in the power-law, but the dependence on a third parameter may not be a Heaviside step function, it may be a continuous dependence which needs to be incorporated as an additional dimension to the fit.

The velocity dispersion of the gas in the clumps gives an indication of the turbulence which likely influences the star formation rate. Here we use this to fit the relationship in Equation 2.8 with δ being replaced by σ. The fit converges to a consistent solution of $L_{H\alpha} \propto r^{1.03} \times \sigma^{2.21}$ with a reasonable posterior probability distribution, indicating that there may be a continuous dependence

of the star forming relationships on the velocity dispersion of the clumps. Only some of the clumps used in previous sections have measurements of σ, reducing the sample size of this fit to 346 of the total 2848 clumps. Fitting these 346 clumps with σ included as a third parameter reduces the overall scatter by $\sim 92\%$ compared to fitting clump size and luminosity only. The full fit parameters and their uncertainties are shown in Table 2.4.

It has also been suggested that the variations in the size-luminosity relationship determined for different data sets is due to differences in the gas fraction (f_{gas}) of the star forming regions which may evolve with redshift (Livermore et al., 2012, 2015). In order to test this we again fit a relationship of the same form as Equation 2.8, replacing δ with f_{gas} of the host galaxy. Ideally f_{gas} of the individual clumps would be used, but this is currently only known for the host galaxies as a whole and only for 157 of the total 2848 clumps. Further, two of the four samples used here (Mieda et al., 2016; Walth et al., 2019) rely on indirect estimates of f_{gas} rather than CO measurements. This data is also from a relatively small subset of the overall sample, but it agrees well with a theoretical dependence of the clump luminosity on both the clump size and the gas fraction. The fit to this data results in a scaling relationship of $L_{H\alpha} \propto r^{1.35} \times f_{gas}^{0.47}$. Interestingly, the scaling for f_{gas} is close to the relationship predicted by Toomre instability ($L_{H\alpha} \propto r^2 \times f_{gas}{}^{0.5}$). Adding f_{gas} as a third parameter also reduces the overall scatter by $\sim 78\%$ compared to the 2D size-luminosity fit of these 157 clumps. The full parameters determined in the fit are reported in Table 2.5.

Like the two-dimensional fit to the clump scaling relations, these multi-parameter fits also give a good fit to the data while spanning the parameter space well. However, these relationships suffer from smaller data sets and we caution against over interpretation of these early results (particularly when it comes to the reduction in scatter). More measurements of f_{gas} and σ would aid in further constraining these fits and investigating the relationship for subsets of the overall sample.

2.5 Discussion

What power-law relationship is determined for the clump size and $L_{H\alpha}$ has important implications for the physical processes occurring in the clumps and driving their formation. It is

thought that clumps form at regions of gravitational instability in the disk, corresponding with a Toomre parameter $Q < 1$ (Toomre, 1964; Genzel et al., 2011; Wisnioski et al., 2012). If the clump or H II region is represented by a Strömgren sphere then there is a well-defined boundary between the ionized and neutral gas. This type of region would have an expected scaling relation of $L_{H\alpha} \propto r^3$. However, if the geometry of this region is non-spherical then a luminosity scaling relation of $L_{H\alpha} \propto r^2$ would be expected. This scaling also results for clumps which are described by the Toomre mass and scale (Genzel et al., 2011). In the following sections we explore both the Strömgren sphere and Toomre instability scenarios, in particular how each of these approximations may delineate between the separation of high and low $\Sigma_{\rm SFR}$ data sets.

2.5.1 Toomre Instability

A common physical explanation for the scaling relationships seen in the high $\Sigma_{\rm SFR}$ data comes from investigating the Toomre mass and scale which are representative of a region that forms under the fastest growing mode of Jeans instability (Elmegreen, 2009; Murray et al., 2010; Genzel et al., 2011). The Toomre mass and scale (M_T, R_T) given in Genzel et al. (2011) are

$$M_T \propto Q^{-2} a^{-4} (\frac{\sigma_0}{v_c})^2 M_d \tag{2.9}$$

$$R_T \propto Q^{-1} a^{-2} \frac{\sigma_0}{v_c} R_d \tag{2.10}$$

where R_d and M_d are the radius and mass of the disk respectively, σ_0 is the local velocity dispersion of the gas, v_c is the circular velocity, and a is a constant describing the disk rotation curve. By solving for Q in Equation 2.9 and substituting into Equation 2.10, we arrive at the relationship

$$M_T \sim R_T^2 R_d^{-2} M_d \; or \; M_T \propto R_T^2 \tag{2.11}$$

In order to put this in terms of the clump luminosity we turn to an empirical linear relationship locally between the dense gas mass of molecular clouds and their star formation rates (Gao and Solomon, 2004; Wu et al., 2005; Lada et al., 2010); which also has a theoretical basis in the

radiation pressure on H II regions from star formation. From Equation 13 in Murray et al. (2010) describing the force due to this radiation pressure, $M_\star \propto L$ in the optically thin limit (optically thin to far-infrared emission while optically thick to ultraviolet). If we are observing clumps that are optically thin to Hα emission and assume the Toomre mass traces the dense gas in star forming regions and Toomre scale represents their size, then we expect a clump size-luminosity relationship of $L_{H\alpha} \propto r^2$. This approximates the observed $L_{H\alpha} \propto r^{1.7}$ we find fitting the high $\Sigma_{\rm SFR}$ clumps.

We suspect many clumps (or substructures within) may in fact be optically thick to Hα, making the assumption that $M_\star \propto L_{H\alpha}$ tenuous. As a check of this assumption we calculate the estimated virial mass of the clumps which have measurements of velocity dispersion:

$$M_{vir} = \frac{\pi^2 \sigma^2 r}{3G} \tag{2.12}$$

using the measured velocity dispersion, σ, and radius, r, of the clumps. Comparing this to the observed Hα luminosity we find a nearly linear relationship ($L_{H\alpha} \propto M_{vir}^{1.07}$). Thus we assume that the mass of the clumps and the dense gas mass are approximately proportional, leading to the $L_{H\alpha} \propto r^2$ relationship.

When the $\Sigma_{\rm SFR}$ power-law break is applied at $\Sigma_{\rm SFR} = 1$ M$_\odot$ yr^{-1} kpc^{-2}, the high $\Sigma_{\rm SFR}$ data follow a scaling relationship close to this r^2 value for the full sample ($L \propto r^{1.7}$) and the local analogs alone ($L \propto r^{1.5}$). This indicates that these high $\Sigma_{\rm SFR}$ clumps could be forming under the fastest mode of Jean's instability. This Toomre mass and scale argument can not however explain the $L \propto r^{2.8}$ scaling found for the low $\Sigma_{\rm SFR}$ clumps.

2.5.2 Strömgren Spheres

Another suggested explanation for the observed scaling relations is that star forming regions at high-redshift form under Jeans collapse at locations of disk instability and are well represented by Strömgren spheres (Wisnioski et al., 2012). One of the relationships expected from this model of clumps is a size-luminosity scaling of $L \propto r^3$ which comes from equating the recombination rate (left hand side; Equation 2.14) and ionization rate, Q, (right hand side) of the hydrogen gas in a

spherical region:

$$\frac{4\pi}{3}R_{ström}^3\alpha_B n_H^2 x^2 = Q = \frac{L_{H\alpha}\lambda_{H\alpha}}{hc} \tag{2.13}$$

where $R_{ström}$ is the Strömgren radius, α_B is the Case-B recombination coefficient (Osterbrock, 1989), and n_H is the number density of hydrogen atoms. x is the ratio of free electrons to hydrogen atoms ($x = \frac{n_e}{n_H}$) and is approximately equal to 1 for a fully ionized region. This results in the final size-luminosity relationship of:

$$L_{H\alpha} = \frac{4\pi hc\alpha_B n_H^2}{3\lambda_{H\alpha}}R_{ström}^3 \tag{2.14}$$

With the clump radii being representative of the Strömgren radius, this results in the $L \sim r^3$ scaling for the Hα luminosity of the clumps we find when fitting the data set as a whole, but this fit is likely skewed by the large scatter in the overall data set. However, when the power-law break is applied at $\Sigma_{\rm SFR} = 1$ M$_\odot$ yr^{-1} kpc^{-2}, the scaling determined for the low $\Sigma_{\rm SFR}$ subset is very close to this theoretical relationship at $L \propto r^{2.8}$ for the full data set and $L \propto r^{2.7}$ for just the local analogs. Wisnioski et al. (2012) find a relationship of $L \propto r^{2.72\pm0.04}$ for their full data set, and they suggest the shallower slope may be due to the clumps being density bound rather than being idealized Strömgren spheres. This would mean that the hydrogen atoms in the star-forming region can recombine faster than they are being ionized. This idea of having density bound clumps is discussed in more detail in Wisnioski et al. (2012) and Beckman et al. (2000).

This does not however explain the $L \propto r^{1.7}$ and $L \propto r^{1.5}$ scaling we see in the high $\Sigma_{\rm SFR}$ data for both the full sample and local analogs. A possible explanation for this is that the clump "radius" is set by the optical depth unity surface, but if the rate of production of ionizing photons Q is large enough then that the surface may not approximate a sphere, i.e.,

$$R_{ström}(Q) > H, \tag{2.15}$$

$$with\ Q = \tfrac{L_{H\alpha}\lambda_{H\alpha}}{hc} f_{rec} \tag{2.16}$$

$$and \quad f_{rec} \approx \left(\tfrac{H}{R_{\rm S}(Q)}\right)\tfrac{3}{2}\left[1 - \tfrac{1}{3}\left(\tfrac{H}{R_{\rm S}(Q)}\right)^2\right] \tag{2.17}$$

where H is the scale height of the disk and $f_{rec} = 1$ for an ideal Strömgren sphere (giving the scaling in Equation 2.14).

Plugging Equation 2.16 into Equation 2.14 we get the Strömgren radius as a function of Q:

$$R_{ström}(Q) = \left[\frac{3Q}{4\pi\alpha_B n_H^2}\right]^{1/3} \tag{2.18}$$

Combining this with Equations 2.17 and 2.16 (to get back to $L_{H\alpha}$) we find that for a clump with radius greater than the disk scale height,

$$L_{H\alpha} = 2\pi\alpha_B \frac{hc}{\lambda_{H\alpha}} R_{ström}^2 H \left[1 - \frac{1}{3}\left(\frac{H}{R_{ström}(Q)}\right)^2\right] \tag{2.19}$$

When $R_{ström}(Q) > H$ the term in brackets on the right is approximately 1, giving the scaling:

$$L_{H\alpha} \sim R_{ström}^2 H \tag{2.20}$$

Since we only plot the Hα luminosity against clump size, this gives us the nearly $L \sim r^2$ scaling seen in the high $\Sigma_{\rm SFR}$ data sets and could explain the reason for a power-law break. Note that this would give $L_{H\alpha} \propto r^3$ for cases where $R_{ström} \approx H$.

As a check of the power-law break we use, we can calculate the critical Hα luminosity, $L_{H\alpha,crit}$ above which we would expect to see $L_{H\alpha} \propto R_{ström}^2$. This critical point would be where $R_{ström}(Q) \approx H$, with H:

$$H = \frac{\sigma}{v_c} R_g \tag{2.21}$$

where R_g is the galactocentric radius, σ is the velocity dispersion of gas in the disk (which for the largest clumps in the Milky Way is similar to the velocity dispersion of the clump) , and v_c is the circular velocity of the disk.

Combining this with Equation 2.18 we arrive at an expression for the critical luminosity at

which the scaling would switch from r^3 to r^2:

$$L_{H\alpha,crit} \approx \frac{4\pi hc\alpha_B n_H^2}{3\lambda_{H\alpha}} \left(\frac{\sigma}{v_c}\right)^3 R_g^3 \tag{2.22}$$

If we take an average clump with a velocity dispersion, $\sigma = 50$ kms^{-1}, density, $n_H = 10$ cm^{-3}, disk circular velocity, $v_c = 250$ kms^{-1}, and galactocentric radius, $R_g = 1$ kpc, we arrive at a value of $L_{H\alpha} \approx 2 \times 10^{40}$erg s^{-1} and a scale height $H = 0.2$ kpc. Comparing with the size luminosity plot in Figure 2.6, this is approximately where the $\Sigma_{\rm SFR}$ cut-off lies for a clump radius of 0.2 kpc.

Figure 2.11 illustrates the physical difference and differences in the size-luminosity scaling relationship expected for clumps in these three size regimes relative to the scale height of the disk: $R_{ström} < H$, $R_{ström} = H$, and $R_{ström} > H$.

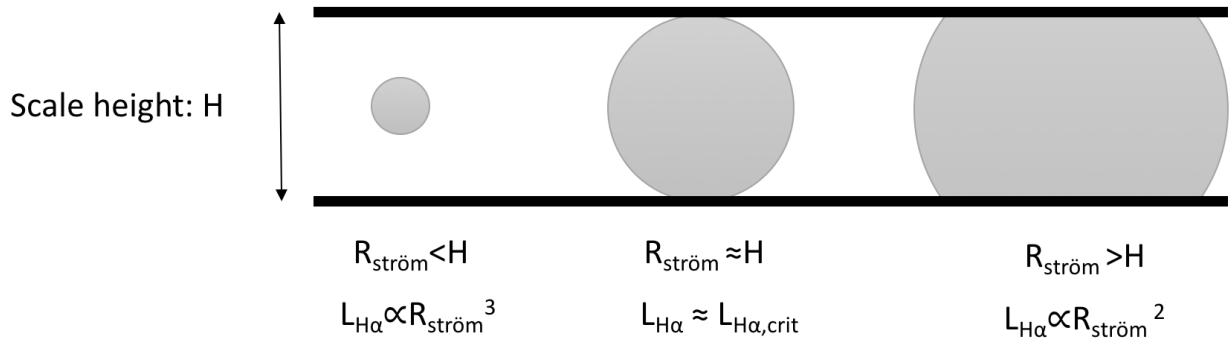

Figure 2.11: Illustration of the three regimes of clump size relative to the scale height of the host galaxy disk. The set of clumps smaller than their host galaxy scale height ($R_{ström} < H$) would give an expected size-luminosity scaling of $L_{H\alpha} \propto r^3$. Those with radii equal to the host galaxy scale height would fall along the critical luminosity and clumps with radii larger than the disk scale height would have an expected $L_{H\alpha} \propto r^2$ scaling.

2.5.3 Bound vs. Unbound Clumps

When investigating local star forming GMCs and MCCs, Nguyen-Luong et al. (2016) introduce a virial parameter based on the velocity dispersion (σ) which divides between gravitationally bound and unbound star forming regions. The velocity dispersion is a measure of the turbulance in the clumps and is used here as an indication of whether or not the clumps are gravitationally bound; a property that may cause a variation in the star formation scaling relations.

To investigate this we would like to introduce a "break" in the power-law that is dependent on σ of the ionized gas in the clumps. However, the velocity dispersion was only measured for a smaller number of data sets resulting in a large scatter. Fitting these small samples results in a poorly constrained fit and uncertainties which are on the same order as the nominal value (an order of magnitude greater than the uncertainties on larger samples). Without a larger data set to base these fits on it is difficult to say whether there is a break in the scaling relations based on the velocity dispersion cut-off. The influence of the clump velocity dispersion was still able to be investigated in Section 2.4.4 as a third fitting parameter since the sample size did not suffer from being divided into two subsets. We believe it is important for studies to include the velocity dispersion of the individual clumps in future investigations.

2.5.4 Feedback

In addition to providing evidence for two different clump populations, Figure 2.5 also provides valuable information about these populations from what we *do not* observe. There is a lack of star forming regions with both large size and high $\Sigma_{\rm SFR}$: the region with $\Sigma_{\rm SFR} > 1 M_{\odot}\ yr^{-1}\ kpc^{-2}$ and $r > 10^3$ pc. Due to this corresponding to clumps which would be both large and have high surface brightness, the lack of observations in this region cannot be due to a sensitivity limit. Instead, it is probable that these clumps just do not exist on a timescale which would make them likely to be observed, indicating some type of feedback mechanism regulating these star forming regions.

There are numerous possible feedback mechanisms put forward for disrupting star forming regions including supernovae explosions, jets due to star formation, thermal pressure from ionized gas, and radiation pressure due to dust absorbing and scattering photons (e.g. Murray et al., 2010; Fall et al., 2010). Murray et al. (2010) investigate these factors in detail and how they influence a wide range of star forming regions including GMCs in the Milky Way and clumps seen in a $z \sim 2$ galaxy. They find that in all cases the earliest supernovae would occur after the star forming region was already being disrupted and therefore could not be the main factor. The jets are also shown to only be a main factor early in the disruption of the star forming region while the thermal pressure

is important in the Milky Way GMCs but not in the more luminous star forming regions like the $z \sim 2$ clumps. The radiation pressure is found to be the dominant feedback mechanism contributing to the disruption of star forming regions (also found by Fall et al., 2010). However, more recent simulations by Krumholz and Thompson (2012, 2013) show that radiation trapping is negligible in giant clumps since it destabalizes the outflow winds. Dekel and Krumholz (2013) argue that this means that steady winds from radiation pressure would not disrupt the clumps before they migrate to the disk center.

Mandelker et al. (2017) discuss the two main scenarios seen in simulations for the lifetimes of clumps at high-redshift. For simulations which only include supernova feedback the clumps are not disrupted and migrate to the center of the disk to form and grow the bulge on an orbital timescale (250-500 Myr). However, in simulations that include radiation pressure feedback clumps tend to be disrupted on a dynamical timescale (50-100 Myr). In an investigation of a massive galaxy between $z \sim 2.2 - 1$ using the FIRE simulations (including radiation pressure and other forms of stellar feedback) the average lifetime of clumps above $10^8\,M_\odot$ is found to be comparatively short at $\sim$22 Myr (Oklopčić et al., 2017). For the clumps included in this study which have measurements of velocity dispersion we find an average dynamical time of 3.5 Myr. While the mechanisms of feedback in high-redshift clumps may not be fully understood it is possible that disruption of local and high-redshift clumps are leading to the lack of large, high Σ_{SFR} clumps observed.

2.5.5 Possible Sources of Bias

By combining different data sets (i.e. lensed and unlensed, high-redshift and low-redshift) there are various selection biases from each survey, which may have an impact on our results, especially when we split the data into smaller subsets. The unlensed surveys typically probe more massive galaxies than the lensed surveys which could introduce differences in the clumps present, however, we do not find significant differences in the scaling relationships of data from these two types of surveys. These selection effects still do weight the overall data set at high-redshift more heavily towards massive galaxies which are easier to observe (Figure 2.2). The unlensed surveys at

$z > 1$ tend to have higher limits to the spatial resolution which introduces the possibility of some of the observed clumps actually being complexes of smaller clumps whose properties are more similar to those observed in the lensed surveys, which still results in much the same scaling relations albeit with different scatter. However, it is unknown at this point what percentage of the clump population observed in these unlensed high-redshift surveys may actually be clump complexes since clumps of similar radius are also observed in lensed surveys with lower resolution limits (Jones et al., 2010; Livermore et al., 2012; Walth et al., 2019). While gravitational lensing provides the opportunity for better spatial resolution it should be noted that there are larger uncertainties involved (particularly in spatial measurements) due to the lensing model. In order to test the influence of these selection effects we fit the lensed and unlensed high-redshift samples individually (with no local analogs; Appendix 2A). The slopes between these two fits are consistent within the uncertainties at around $L \propto r^2$ indicating that these two sample types follow the same scaling relationship.

The results of fitting the overall data set is largely influenced by the group of $z \approx 0$ H II regions since this provides many more data points than the high-redshift samples. This is fine if the physical process and scaling relations are the same for these samples, but as discussed in Section 2.4.1 there is evidence that these H II regions are not the best local analog due to the lower $\Sigma_{\rm SFR}$ than the high-redshift star forming regions (part of this difference is of course due to a sensitivity limit at high-redshift) and the inclusion in the full data set creates a large scatter. This scatter results in very different scaling relations when fitting with and without these $z \approx 0$ objects ($\sim r^3$ and $\sim r^2$ respectively), so resolving this issue would be highly beneficial in determining the processes occurring in clump formation at high-redshift. Better spatial resolution and surface brightness sensitivity of the more massive galaxies typical of the unlensed sample may help resolve this since these are currently the galaxies that tend to have similar measured $\Sigma_{\rm SFR}$ as the local H II regions. However, if the beam smearing effects discussed in Section 2.4.2 and Fisher et al. (2017) are important then these galaxies will typically also have much higher intrinsic $\Sigma_{\rm SFR}$ than what we are currently measuring causing them to be offset from the $z \approx 0$ H II regions. If, on the other hand, there is a sensitivity limit causing us to currently miss clumps with lower SFR and $L_{H\alpha}$ there may

be lower luminosity clumps at the same size scales as our high-redshift unlensed samples.

The absence of large clumps characteristic of the high-reshift samples which also have very low $\Sigma_{\rm SFR}$ (lower right region of Figure 2.5) similar to the $z \sim 0$ H II regions indicates that such a sensitivity limit is likely affecting our observations and fitting. In particular this may be forcing the slope of the low $\Sigma_{\rm SFR}$ subset to a higher value, closer to $L \propto r^3$. To investigate this we calculated the observed flux density which corresponds to clumps with these lower values of $\Sigma_{\rm SFR}$ at $z \sim 1$ and $z \sim 2$ (illustrated in Figure 2C.1 in Appendix 2C). The actual sensitivity limit for each instrument will be dependent on the configuration and will vary with the performance of the AO system (if one was used). The lack of large, low $\Sigma_{\rm SFR}$ clumps in Figure 2.5 indicates that such a limit is impacting the clump population being observed.

Differences in how extinction was accounted for between samples can introduce an additional source of bias in our investigation. Not accounting for the effects of extinction in the determination of $L_{H\alpha}$ may cause some clumps to be artificially shifted down on the size-luminosity plots. There are some studies used here that do not take this into account for their measurements. Among the lensed samples, Swinbank et al. (2009); Jones et al. (2010) do not account for extinction effects, while Livermore et al. (2012, 2015); Walth et al. (2019) correct for the average extinction in each galaxy. Among the unlensed samples, Genzel et al. (2011); Freundlich et al. (2013); Mieda et al. (2016); Fisher et al. (2017) correct for the average extinction while Wisnioski et al. (2012) do not apply a correction. Among the H II regions Kennicutt et al. (2003); Bastian et al. (2006); Monreal-Ibero et al. (2007) correct for the extinction of individual star forming regions, Arsenault and Roy (1988) contains some objects corrected for average host galaxy extinction and others uncorrected, and Gallagher and Hunter (1983); Rozas et al. (2006) do not apply a correction. In Mieda et al. (2016) (z$\sim$1, unlensed) correcting for extinction resulted in an average increase in $L_{H\alpha}$ by a factor of ~ 2. Figure 2C.2 in Appendix 2C illustrates the effect of adding this average correction to studies which had not accounted for it. Due to where the data from these studies fall on the size luminosity plot this results in an increase in scatter at large clump sizes and the same decrease at small sizes (0.8 dex for a conservative $A_v = 2$mag correction). This is a relatively small

effect and likely does not significantly change the scaling relations we determine.

H II regions measured in the SMC & LMC (Kennicutt and Hodge, 1986), IC 10 (Hodge and Lee, 1990), and NGC 6822 (Hodge et al., 1989) were not included in this analysis, but were plotted with the data and scaling relationships determined here to check that the fits are physically realistic at lower size scales. These star forming regions have similar $\Sigma_{\rm SFR}$ to the H II regions used throughout this paper but still appear to follow the $\sim r^2$ scaling of the fit without the $z \approx 0$ H II regions just with the intercept shifted down.

It should be noted that some of the values measured at lower size scales could be affected by stochastic sampling of the stellar initial mass function (IMF) of the clump regions. In simulations performed by Calzetti et al. (2012) a lower limit on size of 200 pc is used to avoid these effects by keeping the SFR above $1.3 \times 10^{-3} M_{\odot}$ yr^{-1}. Below this limit they report that stochastic sampling of the IMF would have an impact on measurements of SFR indicators like $L_{H\alpha}$. This SFR limit corresponds to $L_{H\alpha} \sim 3 \times 10^{38}$ergs s^{-1} with a Chabrier IMF (Chabrier, 2003), a value which some of the data used in this study does fall below–particularly among the $z \approx 0$ H II regions. This may add to the uncertainty in the measurements of lower luminosity star forming clumps, but is not likely to have a significant effect on the results using the high-redshift data of this study.

2.6 Summary/Conclusion

We compiled a comprehensive set of data on the sizes and luminosities of both local and distant resolved star forming regions from the literature. These data sets were carefully binned based on differences in surveys and clump properties to exhaustively explore potential size-luminosity scaling relationships using MCMC fitting with PyStan. We find the following trends and conclusions from this analysis:

1. There is a large scatter of order 4 dex in luminosity for a given clump or H II region size. This scatter may significantly impact the inferred size-luminosity scaling relationship, depending on the choice of sample used in the fit. For example, if the local star forming data from Fisher et al. (2017) and Nguyen-Luong et al. (2016) are used then the scaling relation determined is

$L \propto r^2$. If the set of $z \approx 0$ H II regions are also included then the scaling relationship becomes $L \propto r^3$.

2. We observe a break in the size-luminosity scaling relation based on the measured clump $\Sigma_{\rm SFR}$ at 1 $M_\odot$ yr^{-1} kpc^{-2}. Clumps with lower $\Sigma_{\rm SFR}$ tend to have luminosities that scale closer to $\sim r^3$, while clumps with higher $\Sigma_{\rm SFR}$ tend to have luminosities that scale with $\sim r^2$. This is true for both the low-redshift sample and the entire collated data set.

3. We find that the $L \propto r^3$ scaling can be explained by clumps that are well represented by Strömgren spheres which are smaller than the scale height of the disk. We find that if the Strömgren radius is larger than the scale height of the disk and some ionizing photons are escaping, then the non-spherical geometry may result in a $L \propto r^2$ scaling. Alternatively, star formation regions driven by Toomre instability may result in a $\sim r^2$ scaling of the high $\Sigma_{\rm SFR}$ clumps, but is unable to be extended the low $\Sigma_{\rm SFR}$ clumps to yield a $\sim r^3$ scaling.

4. If there exists a power-law break in the size-luminosity scaling relationship of star forming regions, this may indicate a secondary dependence on additional clump properties. We investigated the dependence of the size-luminosity relationship with respect to the host galaxy gas fraction ($f_{\rm gas}$) and clump velocity dispersion (σ), but further data on these parameters are still needed to do a thorough investigation. Additional IFS studies would provide kinematics for galaxies and clumps, while ALMA observations of molecular gas would provide accurate gas fractions for host galaxies and individual clumps.

5. Spatial resolution effects observed for high-redshift (unlensed) galaxies may alter the measured properties ($r_{H\alpha}$, $L_{H\alpha}$, Σ_{SFR}) of the clumps. If such beam smearing effects are widespread then this could result in an increased artificial scatter, but does not influence the scaling relation results from the applied power-law break at $\Sigma_{\rm SFR} = 1 M_\odot$ yr^{-1} kpc^{-2}.

6. We find no evidence for redshift evolution of the clump size-luminosity relation, but more data at higher-redshift bins are still needed. The differences in slopes between redshift bins can

not be separated from the potential effects of the small sample sizes and larger uncertainties at high-redshift.

7. We find a scaling relation $L \propto r^2$ for both high-redshift lensed and unlensed clump data sets that are consistent within the uncertainties. Yet we point out that these are still small data sets that should be expanded for further investigation, in particular the high-resolution lensed sample.

Acknowledgements

The authors wish to thank Randy Campbell and Jim Lyke for their assistance at the telescope to acquire the Keck OSIRIS data sets. We appreciate the valuable discussions with Dusan Keres and Karin Sandstrom. The data presented herein were obtained at the W.M. Keck Observatory, which is operated as a scientific partnership among the California Institute of Technology, the University of California and the National Aeronautics and Space Administration. The Observatory was made possible by the generous financial support of the W.M. Keck Foundation. The authors wish to recognize and acknowledge the very significant cultural role and reverence that the summit of Maunakea has always had within the indigenous Hawaiian community. We are most fortunate to have the opportunity to conduct observations from this precious mountain. This research has made use of the NASA/IPAC Extragalactic Database (NED) which is operated by the Jet Propulsion Laboratory, California Institute of Technology, under contract with the National Aeronautics and Space Administration.

Facility: Keck:I (OSIRIS)

Software: PyStan (Stan Development Team, 2017), OSIRIS Data Reduction Pipeline (Lyke et al., 2017), Matplotlib (Hunter, 2007)

Appendix

2A Lensed vs. Unlensed Observations

We have binned the data sets into gravitationally lensed and unlensed high-redshift observations. This was done to test for any influences of selection biases in the data that is typically gathered from lensed versus unlensed surveys at higher redshift. Lensed surveys provide enhanced spatial resolution and can allow us to extend our analysis to lower luminosity galaxies due to the magnification effects (Livermore et al., 2015), which results in the tendency towards lower mass galaxies than can be probed by unlensed surveys. However, the lensing model does introduce larger uncertainties on the measured values, particularly when it comes to the size of clumps.

As is shown in Figure 2A.1 there is a very slight difference between the nominal slope values of the lensed ($L_{H\alpha} \sim r^{2.10}$) and unlensed ($L_{H\alpha} \sim r^{2.27}$) fits, however these values are consistent within the uncertainties. This indicates that regardless of the selection differences between the two types of studies, the scaling relations determined from each are consistent. The small offset seen in the intercept between these two bins could then be caused by the effect of beam smearing on the measurements of clump size and luminosity.

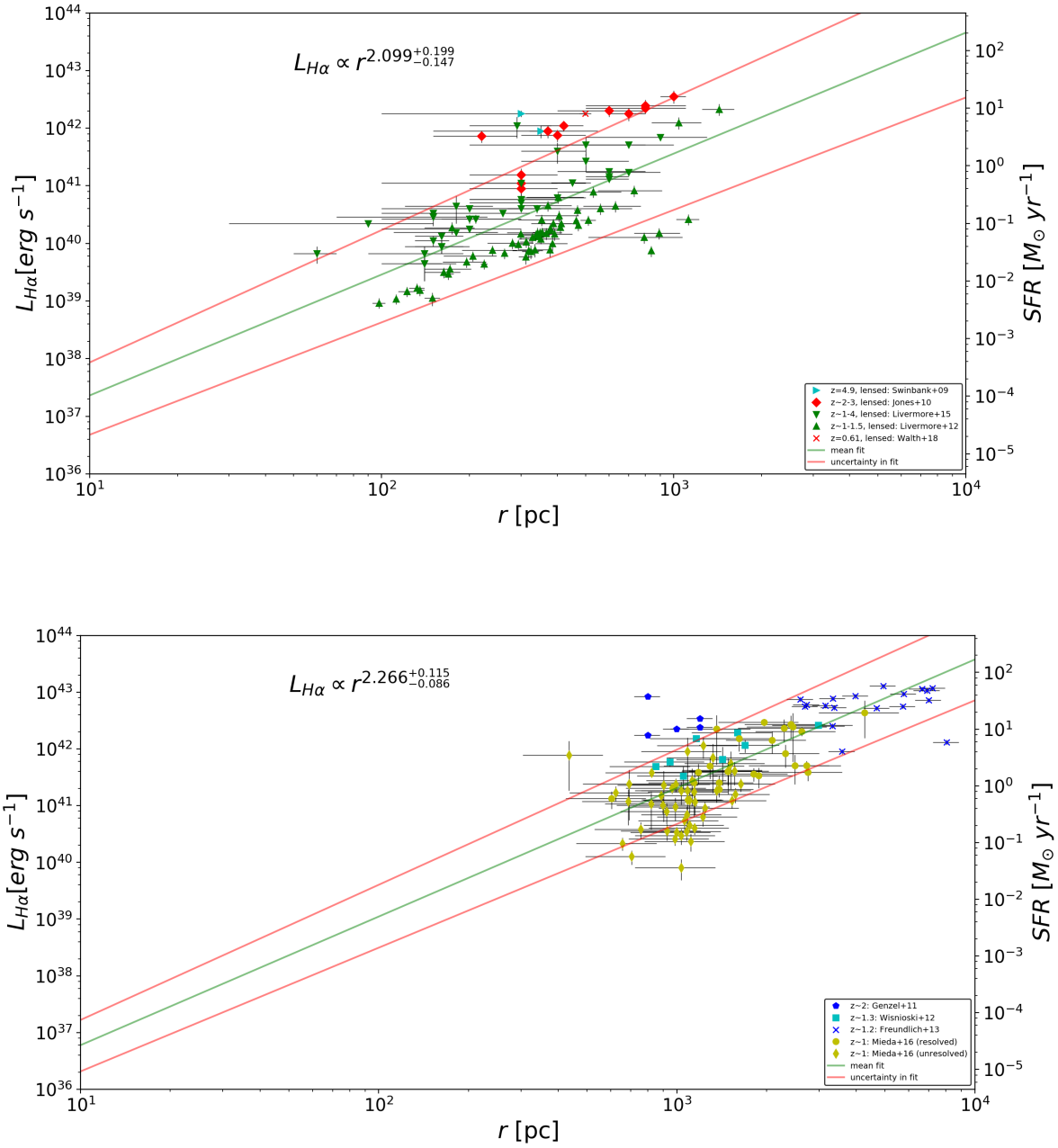

Figure 2A.1: Clump size and luminosity relation for high-redshift lensed data sets (top) and unlensed data sets (bottom). Error bars are shown to illustrate the large variations in each data set. NOTE: The $z \approx 0$ H II regions and other local analogs are excluded here since the large number of data points has an overwhelming influence on the fitting.

2B Beam Smearing Investigation with Object 42042481

In the investigation of beam smearing effects on measured clump properties we re-observed one of the brightest galaxies of the IROCKS sample (unlensed, $z \sim 1$ galaxy 42042481, Mieda et al., 2016) at a plate scale of 0.05" in order to increase the resolution over the initial 0.1" plate scale. This resulted in a factor of 2 improvement in spatial resolution (from $\sim$800 pc to $\sim$400 pc) and the largest clump breaking into two clumps nearly half the size originally measured (Table 2.6). In addition to this clump breaking into smaller components, two new clumps (H* and I*) were also detected in the 0.05" observations. In order to determine the cause of these additional clump detections we compare the flux and Σ_{SFR} of the clumps detected in the new 0.05" observation (binned to 0.1" resolution and un-binned) with the clumps found in the previous 0.1" observations. This is shown in Figure 2B.1 with clumps H* and I* having higher flux and Σ_{SFR} than some previously detected clumps. This therefore is not the driver of the new detections. The quality of seeing on each night of observations could also lead to differences in clump detection. Therefore both seeing measurements from the MASS/DIMM instruments on Mauna Kea (Table 2B.1) and the PSF of the tip-tilt star used for each observation (Figure 2B.2) are compared. Both the PSF and seeing measurements across the two nights is similar, suggesting this is not the cause of the new detections either and it is likely in our definition of Hα clumps.

Table 2B.1: MASS/DIMM Seeing Measurements

Instrument	Mean Seeing (arcsec)	Min Seeing (arcsec)	Max Seeing (arcsec)	Standard Deviation (arcsec)
2014 November 8-9; 0.1" observations				
DIMM	0.46	0.27	0.93	0.11
MASS	0.20	0.06	0.62	0.11
2017 August 11-12; 0.05" observations				
DIMM	0.58	0.30	1.59	0.18
MASS	0.23	0.06	0.52	0.09

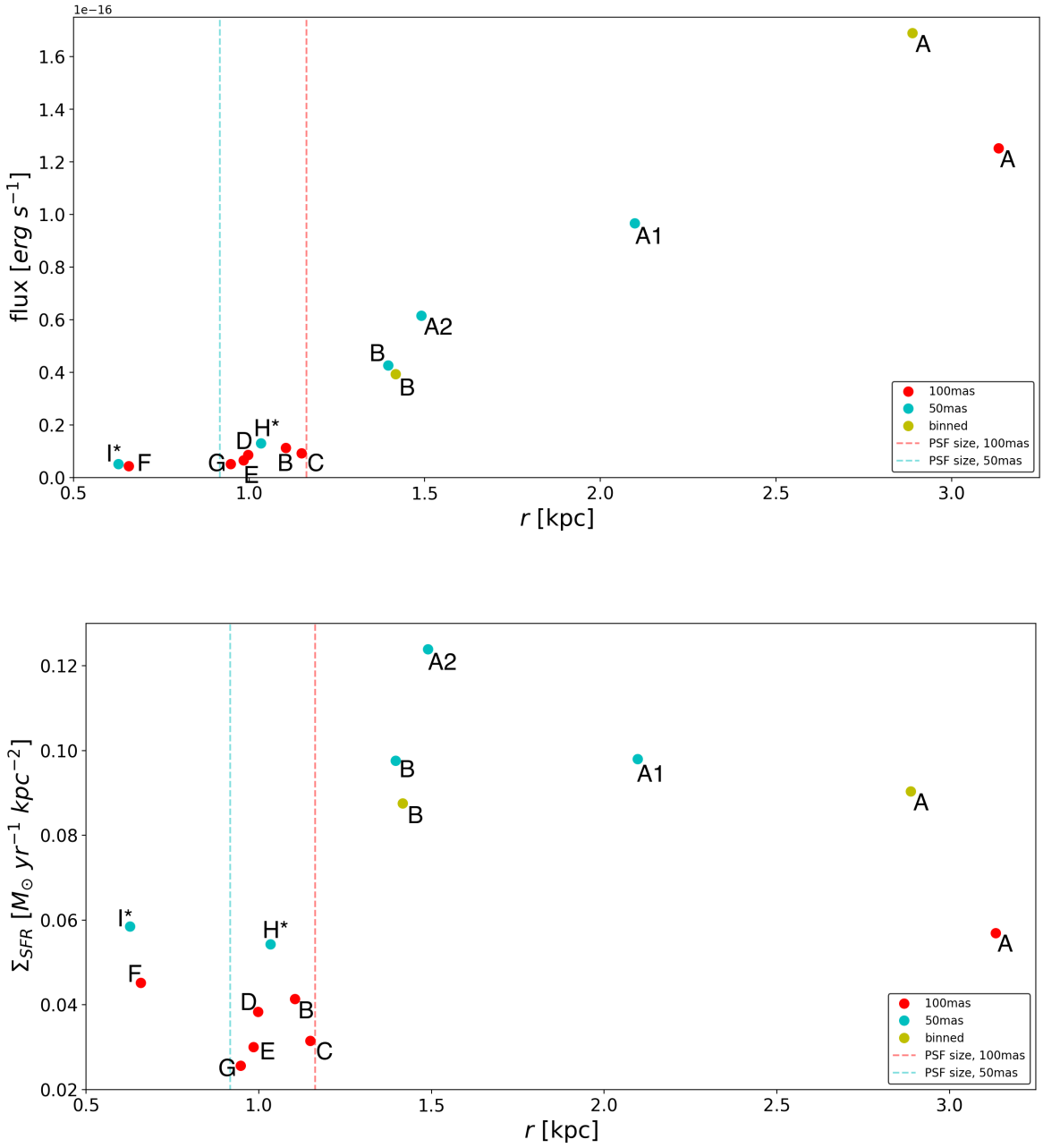

Figure 2B.1: Comparison of the flux (top) and Σ_{SFR} of each clump detected in the 2014 0.1" observations, 2017 0.05" observations, and the 2017 0.05" observations binned down to 0.1" resolution. The dashed lines show the scale of the PSF for each night and plate scale of observations. The clumps which fall to the left of these lines would be considered unresolved.

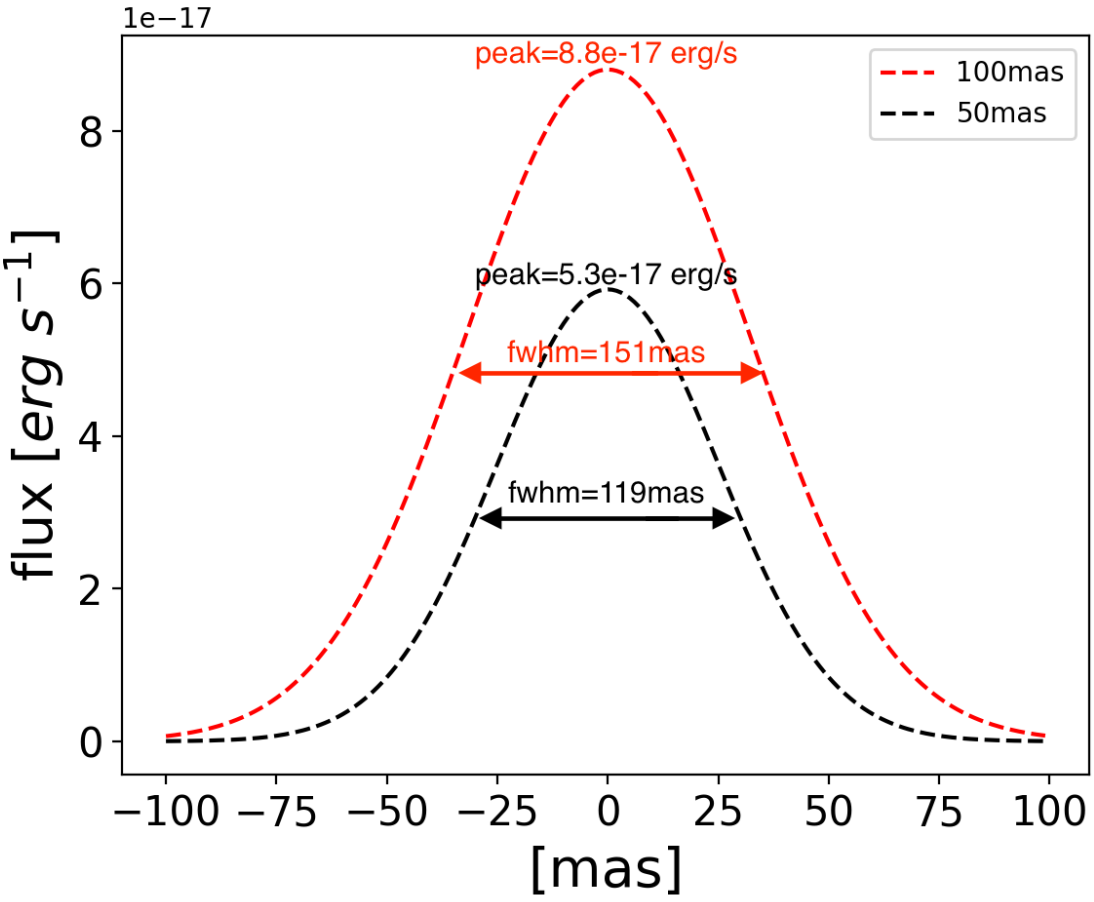

Figure 2B.2: Comparison of the tip-tilt star PSF for the 2014 and 2017 observations at a plate scale of 0.1" and 0.05" respectively. The smaller width of the 0.05" PSF could be a consequence of the lower peak flux as the width is smaller by a factor of ~ 0.8 and the peak flux is lower by a factor of ~ 0.6.

2C Additional Figures

The illustration in Figure 2C.1 shows where sensitivity limits may lie on the size-$\Sigma_{\rm SFR}$ plot at different redshifts in this data set. The actual sensitivity limit of each study will vary widely based on the telescope/instrument used and will even vary within studies based on lensing effects. To simplify this we only show the observed flux needed to detect a clump at different levels of $\Sigma_{\rm SFR}$ at $z = 1$ and $z = 2$.

Figure 2C.2 illustrates the estimated influence of adding extinction corrections to the luminosities measured in studies which did not already include these corrections. For these studies an average $2\times$ increase in $L_{H\alpha}$ would be expected.

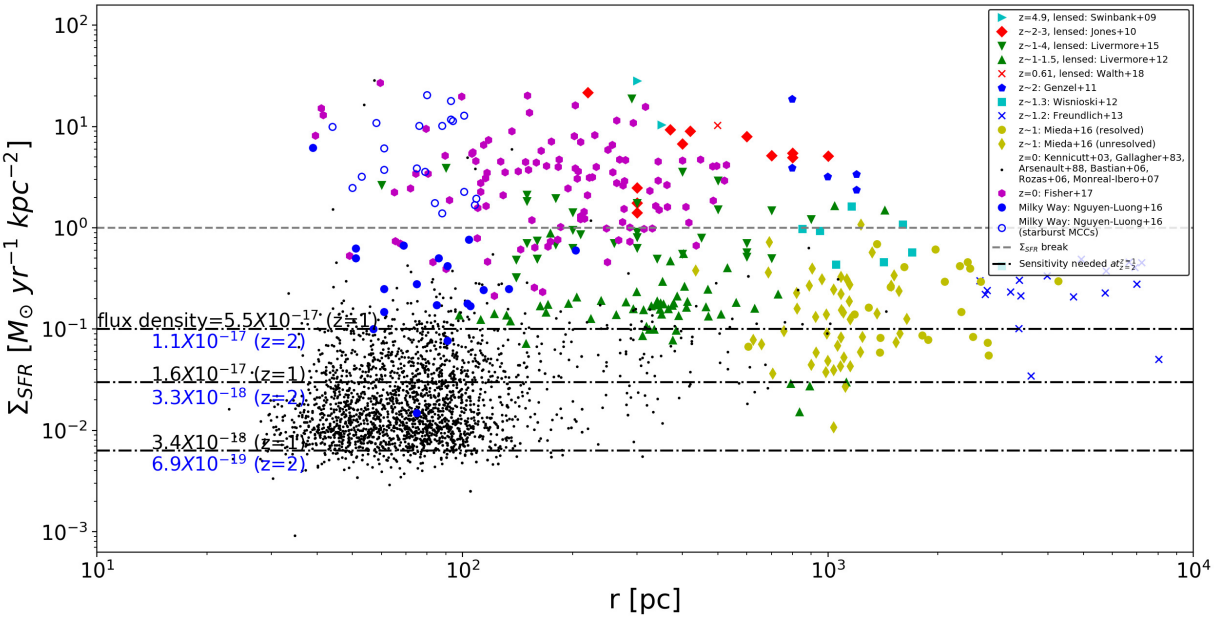

Figure 2C.1: Figure 2.5 comparing clump size and $\Sigma_{\rm SFR}$ with additional curves related to the potential sensitivity limit. The dashed black lines show the observed flux density at that $\Sigma_{\rm SFR}$ for a $z = 1$ (black text) and $z = 2$ (blue text) source. All flux densities are in units of erg s^{-1} cm^{-2} arcsec^{-2}.

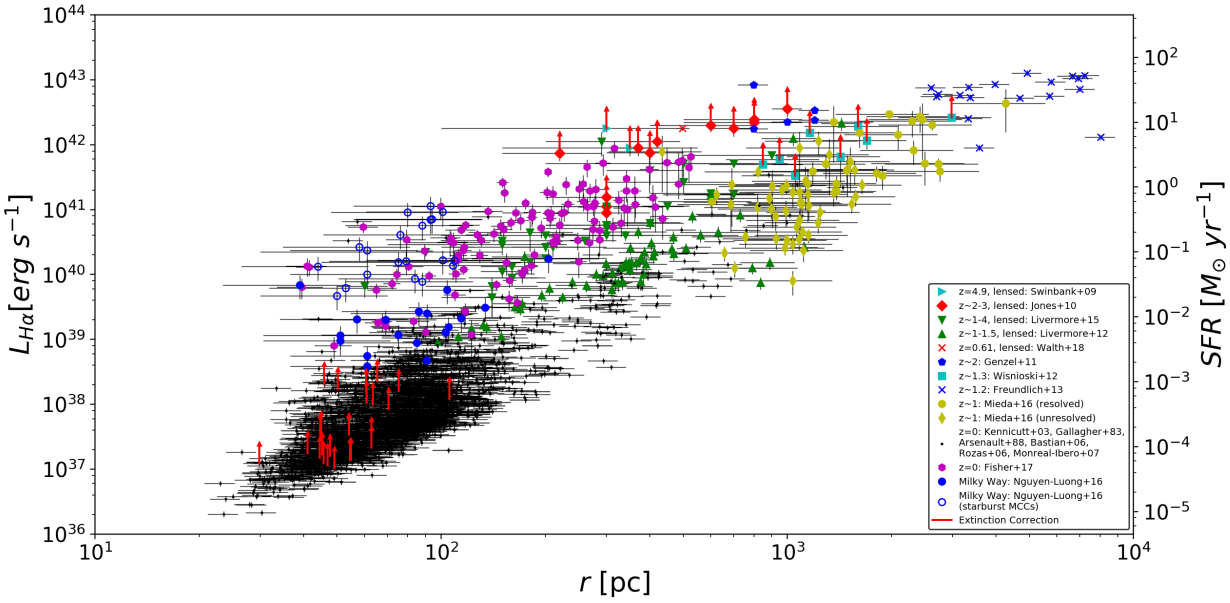

Figure 2C.2: Clump size and luminosity for all the data used throughout this paper with illustration of the estimated influence of adding extinction correction to those samples which do not already do this (data set #'s 1,2,7,10,12 from Table 2.1). The correction used is the average of the affect observed in Mieda et al. (2016) of increasing $L_{H\alpha}$ by a factor of ~ 2. The correction is only shown for a few of the $z \approx 0$ H II regions (data set 10) but would apply to all.

2D Dynamical Mass of Clumps

The dynamical mass (M_{dyn}) was estimated for all data which included a measurement of the clump velocity dispersion (σ). This was calculated from Equation 2.23 in order to estimate the dynamical time (τ_{dyn}) of the clumps (Equation 2.24).

$$M_{dyn} = 5\frac{\sigma^2 r_{clump}}{G} \tag{2.23}$$

$$\tau_{dyn} = \sqrt{\frac{3\pi}{32G\rho}}, \;\; \rho = \frac{M_{dyn}}{\frac{4}{3}\pi r_{clump}^3} \tag{2.24}$$

The average M_{dyn} of all clumps with measured velocity dispersion is 2.7×10^9 $M_\odot$ with an average dynamical time of 3.5 Myr. The results of these calculations are listed in Table 2D.1 for the IROCKS (Mieda et al., 2016) clumps as a sample.

Table 2D.1: Dynamical Mass and Time Estimates for IROCKS sources

Object (Galaxy-Clump)	M_{dyn} (10^9 $M_\odot$)	τ_{dyn} (10^6 yrs)
Resolved		
32016379-1	0.52	8.11
32016379-2	6.79	7.8
32036760-0	8.79	16.48
33009979-0	6.95	9.69
33009979-1	2.75	11.0
42042481-4	11.8	16.3
DEEP11026194-1	11.36	12.97
DEEP12008898-0	9.45	14.01
DEEP12008898-1	10.55	14.33
DEEP12008898-2	5.03	10.03
DEEP12019627-0	3.97	16.07
DEEP12019627-2	2.86	9.45
DEEP13017973-3	3.73	24.67
DEEP13017973-6	41.19	3.07
TKRS11169-2	21.39	7.4
TKRS11169-3	39.45	8.39
TKRS7187-4	24.59	11.44

Continued on next page

Table 2D.1 – *Continued from previous page*

Object (Galaxy-Clump)	M_{dyn} (10^9 $M_\odot$)	τ_{dyn} (10^6 yrs)
TKRS7615-01-1	6.67	7.86
TKRS7615-01-2	13.26	8.31
TKRS9727-4	39.91	17.36
UDS11655-0	5.58	15.84
	Unresolved	
32016379-0	4.23	6.6
32040603-0	2.64	5.7
33009979-2	4.09	7.11
42042481-0	5.15	3.24
42042481-1	3.49	8.18
42042481-2	1.21	11.01
42042481-3	2.44	9.23
42042481-5	13.27	1.82
42042481-6	2.9	7.26
DEEP11026194-0	10.61	7.46
DEEP12019627-1	3.17	6.19
DEEP12019627-3	5.4	8.49
DEEP12019627-4	0.81	15.58
DEEP12019627-5	6.77	5.9
DEEP13017973-0	1.98	9.98
DEEP13017973-1	1.84	2.62
DEEP13017973-2	5.9	7.77
DEEP13017973-4	6.15	4.3
DEEP13017973-5	11.09	2.14
DEEP13017973-7	2.61	8.08
DEEP13043023-0	2.74	4.27
DEEP13043023-1	6.38	6.03
DEEP13043023-2	18.88	5.19
DEEP13043023-3	4.96	6.82
J033249.73-0	6.97	9.28
J033249.73-1	7.66	2.95
J033249.73-2	4.32	2.95
J033249.73-3	5.19	7.39
TKRS11169-0	5.16	4.57
TKRS11169-1	4.97	5.27
TKRS11169-4	5.22	6.14
TKRS7187-0	4.02	6.95
TKRS7187-2	6.99	5.52
TKRS7187-3	0.72	15.37
TKRS7187-5	10.34	3.29
TKRS7187-6	5.52	4.71

Continued on next page

Table 2D.1 – *Continued from previous page*

Object (Galaxy-Clump)	M_{dyn} (10^9 $M_\odot$)	τ_{dyn} (10^6 yrs)
TKRS7615-01-0	5.16	7.57
TKRS7615-01-3	12.09	7.51
TKRS7615-01-4	4.24	5.97
TKRS7615-01-5	8.93	7.89
TKRS9727-0	2.08	9.77
TKRS9727-1	13.22	6.38
TKRS9727-3	2.01	6.51
TKRS9727-5	2.69	9.05
UDS10633-0	4.68	7.81
UDS11655-1	5.28	5.32

Note— Not all data sets included measurements of σ_{clump}.

Chapter 2, in full, is a reprint of the material as it appears in The Astrophysical Journal 2018. Cosens, M., Wright, S. A., Mieda, E., Murray, N., Armus, L., Do, T., Larkin, J. E., Larson, K., Martinez, G., Walth, G., and Vayner, A, *The Astrophysical Journal*, 869, 11, 2018. The dissertation author was the primary investigator and author of this paper.

Chapter 3

Kinematics and Feedback in H II regions in the Dwarf Starburst Galaxy IC 10

Abstract

We present a survey of the central region of the nearest starburst galaxy, IC 10, using the W. M. Keck Observatory Keck Cosmic Web Imager (KCWI) at high spectral and spatial resolution. We map the central starburst of IC 10 to sample the kinematic and ionization properties of the individual star-forming regions. Using the low spectral resolution mode of KCWI we map the oxygen abundance and with the high spectral resolution mode we identify 46 individual H II regions. These H II regions have an average radius of 4.0 pc, star formation rate $\sim 1.3 \times 10^{-4}$ $M_{\odot}$ yr^{-1}, and velocity dispersion $\sim$16 km s^{-1}. None of the H II regions appear to be virialized ($\alpha_{vir} >> 1$), and, on average, they show evidence of ongoing expansion. IC 10's H II regions are offset from the star forming region size-luminosity scaling relationships, as well as Larson's Law that relates size and velocity dispersion. We investigate the balance of inward and outward pressure, P_{in} and P_{out}, finding $P_{out} > P_{in}$ in 89% of H II regions, indicating feedback driven expansion even in these low mass H II regions. We find warm gas pressure (P_{gas}) provides the dominant contribution to the outward pressure (P_{out}). This counteracts the inward pressure which is dominated by turbulence in the surrounding gas rather than self-gravity. Five H II regions show evidence of outflows which are most likely supported by either stellar winds (2 regions) or champagne flows (3 regions). These observations provide new insights into the state of the star-forming regions in IC 10 and negative

feedback from low mass clusters.

3.1 Introduction

H II regions are formed when UV photons from young stars and clusters ionize the surrounding gas cloud. The ionization within these regions is typically dominated by the most massive and luminous stars. This can be due to just a single O or B star (e.g., Armentrout et al., 2021) or a cluster of massive stars. H II regions are observed to have typical lifetimes $\lesssim$ 10Myr, starting out spatially compact (<pc) and expanding as they age (e.g., Spitzer, 1978; Zamora-Avilés et al., 2019) before the H II region dissipates. As the H II regions expand they interact with and influence the surrounding gas. As the sites of recent massive star formation, H II regions are intrinsically linked to the efficiency of star formation in the larger molecular cloud, the properties of the Interstellar Medium (ISM), and the evolution of galaxies. The photometric and kinematic properties of H II regions are therefore of great interest for studying and understanding the progression of star formation.

There are a number of surveys studying ionized and diffuse gas in and around the H II regions of nearby galaxies. Some of the first studies of extragalactic H II regions used Hα imaging with photographic plates and CCD's to map the ionized gas in the Small Magellanic Cloud (SMC) and Large Magellanic Cloud (LMC) (e.g., Davies et al., 1976; Kennicutt and Hodge, 1986) as well as other nearby galaxies (e.g. NGC 6822, Hodge et al., 1989). With Hα imaging they were able to measure the size and flux of star forming regions and explore their size distributions and luminosity functions. As instrumentation improved, Fabry-Perot mapping added measurements of the ionized gas kinematics both within the H II regions and in the diffuse gas component, finding $\sim 4\times$ higher velocity dispersions (σ) in the diffuse gas (e.g., Valdez-Gutiérrez et al., 2002). With the advent of integral field spectrographs (IFS), surveys could map the resolved gas properties and kinematics at $\sim$kpc scale. Large surveys such as CALIFA (Sánchez et al., 2012a), SAMI (Croom et al., 2012), and MaNGA (Bundy et al., 2015), studied hundreds to thousands of star forming galaxies and their resolved properties. These surveys have resulted in numerous publications including studies of

galaxy dynamical scaling relations (Cortese et al., 2014), measurement of a "resolved" star forming main sequence (Ellison et al., 2018), and the fundamental metallicity relation (Cresci et al., 2019). The CALIFA survey also made the important characterization of the Diffuse Ionized Gas (DIG) showing a trend in the Hα equivalent width with both the position on the BPT diagram as well as galaxy morphological type for this large sample of galaxies (Espinosa-Ponce et al., 2020). Using the MaNGA survey, Rodríguez del Pino et al. (2019) identify ionized gas outflows in 7% of the studied Hα emitting galaxies, finding evidence of shocks in most of the outflows with larger velocities associated with more massive galaxies.

State of the art IFS's operating at visible wavelengths such as the Multi-Unit Spectroscopic Explorer (MUSE, Bacon et al., 2010), and the Keck Cosmic Web Imager (KCWI, Morrissey et al., 2018), have begun to allow incredibly high spatial and spectral resolution mapping of nearby H II regions. For example, Castro et al. (2018) used MUSE to map the giant H II region 30 Doradus, generating resolved maps of the ionization state and revealing bi-modal gas velocities surrounding the star cluster R136. In another study, McLeod et al. (2019) use MUSE to map two LMC H II region complexes and characterize the role of stellar feedback mechanisms, finding stellar winds and thermal gas pressure to be dominant. Studying two giant H II regions in M101 with KCWI, Bresolin et al. (2020) find evidence of expanding shells and an underlying broad emission component potentially attributable to stellar winds interacting with cold gas.

The process of energy from star formation being injected into and influencing the surrounding gas through feedback can be caused by a variety of mechanisms. These mechanisms and their impact are typically discussed in the context of the larger molecular clouds surrounding the compact H II regions where the pressure originates. An important form of feedback is radiation pressure which occurs when stellar photons interact with dust grains in the surrounding molecular cloud thereby transferring both energy and momentum. The energy imparted to the molecular gas may be radiated away, but the momentum cannot and therefore may be able to more effectively cause expansion of the gas (Krumholz et al., 2014).

The ionizing photons produced in a star cluster also act to heat the surrounding H II region

gas to typical temperatures of $\sim 10^4$K. This warm gas generates an important source of outward pressure that may cause the expansion and eventual disruption of the region and surrounding gas. An additional source of thermal pressure comes from hot gas heated by shocks from stellar winds. The bubbles of hot gas produced can be observed via emitted X-rays. However, this hot gas is less effective in disrupting the region since it is limited by leakage through low density regions and turbulent mixing occurring with the neighboring cold gas resulting in enhanced thermal emission (Krumholz et al., 2019). Supernovae explosions also produce shocked winds in a short burst that can disrupt star-forming regions, but these don't occur until a few million years after the formation of the first massive stars by which point the molecular gas may be significantly disrupted or cleared already.

Which of these feedback mechanisms is dominant in different star forming environments is still a matter of some debate. Observational studies seek to determine the relative impact of each of these forms of pressure by estimating the energy input to the ISM or the pressure produced by each component. For instance, the giant H II region, 30 Doradus, has been one target of such pressure studies investigating the physical processes leading to the complex structure in this single region (Lopez et al., 2011; Pellegrini et al., 2011). These types of studies are often limited to just a few H II regions or a single giant H II region, making it difficult to form conclusions about the general population of star forming regions. IC 10 provides a unique laboratory to study the effectiveness of many of these forms of feedback in a statistically significant sample. Thanks to the $>$100 previously identified H II regions, a large sample of compact regions can be studied simultaneously, and the recent nature of the starburst allows the effectiveness of pre-SNe feedback to be investigated.

IC 10 is the nearest starburst galaxy at a distance of 715kpc (Kim et al., 2009), and the only one in the Local Group. It is also a dwarf galaxy with low metallicity; approximately 0.25$\times$ solar (Magrini and Gonçalves, 2009; Skillman et al., 1989). IC 10 has a higher density of Wolf-Rayet stars than both the SMC and LMC (e.g. Tehrani et al., 2017), indicating that the current observed burst of star formation is relatively recent. These unique characteristics as well as it's close proximity have made IC 10 the subject of numerous studies.

Studies of the gas in IC 10 have shown an expansive H I component stretching $\sim$7$\times$ larger than the optical component of the galaxy (e.g., Huchtmeier, 1979; Namumba et al., 2019). The central region of the H I gas has been observed to have a regularly rotating disk structure with an extended counter-rotating component beyond that (e.g., Shostak and Skillman, 1989; Wilcots and Miller, 1998; Ashley et al., 2014). These studies also find kinematically distinct "spurs" and "plumes" that do not follow the main H I disk. The origin of these features is currently not well known but possible explanations presented include an as of yet undetected companion galaxy or a late stage merger (e.g., Ashley et al., 2014), ongoing accretion of primordial gas onto the main body of IC 10 (e.g., Wilcots and Miller, 1998), past interaction with a body such as another dwarf galaxy (e.g., Nidever et al., 2013), or some combination of these mechanisms.

Narrow-band Hα imaging by Hodge and Lee (1990) was used to identify 144 individual H II regions and complexes throughout IC 10 and measure their characteristic properties such as size and SFR. The majority of the identified star-forming regions lie in the central $2.5' \times 2.5'$ of the irregular galaxy. Thurow and Wilcots (2005) studied the ionized gas kinematics in a portion of this field with a fiber-fed IFS utilizing $3''$ fibers and achieving a maximum resolution of 23 km s^{-1}. Interestingly, they find larger line widths in the diffuse gas than in the compact H II regions which they attribute to a superposition of components with different velocities. They find that stellar winds are likely to have shaped much of the ionized and neutral gas in this region. Polles et al. (2019) model fine structure cooling lines observed in IC 10 with the photoionization code Cloudy (Ferland et al., 2017) finding relatively uniform properties between the five regions studied, which match the characteristics of matter-bounded regions allowing photons to escape and ionize the diffuse gas. These unique characteristics of IC 10 make it an ideal target to study a large sample of young, evolving star-forming regions.

In order to better understand the conditions of star formation and its impact on galaxy properties it is important to study not only local H II regions, but also the sites of star formation throughout cosmic time. The H II regions of IC 10 provide an important tool for comparison with the $\sim$kpc scale star-forming "clumps" found at z $\gtrsim$ 1 (e.g., Livermore et al., 2012; Mieda et al., 2016).

These clumps are found to have high velocity dispersions ($\sigma \gtrsim 50\mathrm{km\,s^{-1}}$, e.g., Genzel et al., 2011; Mieda et al., 2016) indicating strong energetics and significant amounts of turbulence present. In an effort to understand these massive star-forming regions and compare them to their more compact local counterparts, the scaling relationships between clump properties such as size, luminosity, and velocity dispersion are explored in order to provide insight into the process driving clump formation. However, these studies have yielded some conflicting results, in particular regarding whether high-z clumps are offset to higher luminosities than local H II regions for a given size (e.g., Wisnioski et al., 2012; Livermore et al., 2015). This was initially proposed as a possible redshift evolution in the size-luminosity scaling relationship (Livermore et al., 2012, 2015), but later studies by Wisnioski et al. (2012) and Mieda et al. (2016) did not find evidence of such an evolution. In order to investigate this discrepancy, our team compiled a comprehensive sample of high-z and local star-forming regions and developed a Bayesian Markov Chain Monte Carlo (MCMC) fitting framework to investigate these scaling relations in detail (Cosens et al., 2018). We did not find any clear evidence of redshift evolution with this expansive sample, nor a definite selection affect between lensed and field galaxies at high-z. Instead, we found evidence that there may be a break in the size-luminosity relationship based on the star formation rate (SFR) surface density, Σ_{SFR}.

A key area of parameter space missing in these scaling relationship investigations are compact ($\lesssim$50pc), low-luminosity (10^{34-36}erg s^{-1}) star-forming regions studied with the same methodology as at high-z. These compact regions set the constraint on the intercept of the relationship; a critical component in interpreting changes in slope or offsets between samples. Observing the H II regions of IC 10 with the KCWI IFS provides an ideal target to study a large sample of H II regions at unprecedented angular resolution, probing this missing parameter space and allowing for an improved comparison of local and high-z star-forming regions.

Despite the extensive study of IC 10, the exact distance to the dwarf galaxy remains rather uncertain since it lies close to the plane of the Milky Way. Measured distances have ranged between 500kpc (Sakai et al., 1999) and >2Mpc (Bottinelli et al., 1984), with distances $\sim$700kpc being used more recently (e.g., Ashley et al., 2014; Polles et al., 2019). Throughout this paper we will use the

distance of 715±60 kpc measured by Kim et al. (2009) but we will also report the angular size of all measured structures. For the systemic velocity of IC 10 we will use the value of $-348 \pm 10 \mathrm{km\,s^{-1}}$ determined from the 21 cm line (Tifft and Cocke, 1988).

In Section 3.2 we describe the observations carried out on the central starburst of IC 10 with KCWI and the method of reduction. Then we identify H II regions in our observations (Section 3.3.1), extract H II region spectra (Section 3.3.2), and determine SFRs (Section 3.3.3) and masses (Section 3.3.4). In Section 3.3.5 we investigate the kinematics of the field and H II regions, virialization and energetics. We estimate the metallicity throughout the field (Section 3.3.6), investigate the Diffuse Ionized Gas (Section 3.3.7), and study the star formation scaling relations (Section 3.3.8). In Section 3.4 we discuss how these results inform a picture of young H II regions still evolving. Lastly, in Section 3.5 we summarize our results.

3.2 Observations & Data Reduction

3.2.1 KCWI Observations

We used KCWI (Morrissey et al., 2018) at the W.M. Keck Observatory to observe the star forming H II regions of IC 10. These observations tile a combined ∼1.25 sq. deg. field of view (FoV) in the central region of the galaxy with the highest concentration of H II regions. We use a low resolution mode making use of KCWI's large slicer and BL grating which we will refer to as the "large slicer, R∼900" mode, as well as a high resolution mode which uses the small slicer and BH3 grating which we will refer to as the "small slicer, R∼18,000" mode. Observations in these two modes cover approximately the same FoV in order to combine the exceptional spatial sampling (0.35″/pixel) and spectral resolution (0.125Å/channel) of the small slicer, with the wavelength coverage afforded with the low resolution grating (3500-5500Å). We determine our achieved resolution by measuring the point-spread-function of the observed standard stars giving an average FWHM∼ 1" across the observing nights in both modes. In this paper we will limit our discussion primarily to the high resolution "small slicer, R∼18,000" observations with the "large slicer, R∼900" mode providing the extinction correction and metallicity diagnostics in Section 3.3.6.

In the high resolution mode we obtain a wavelength range of 4700-5200Å and a FoV of 8.4″ × 20.4″ for each exposure, providing coverage of Hβ, [OIII]4959Å, and [OIII]5007Å. A typical pointing consists of three 120s exposures with a dither pattern of 0, -1.5, +2 slices[1] perpendicular to the slices to improve sampling and avoid saturation of the bright [OIII]5007Å line. In the large slicer, R∼900 mode we obtain wider FoV and spectral coverage in each exposure (3500-5500Å and 33″ × 20.4″) with lower spatial resolution of 1.35″/pixel. We limit these exposure times to 6s to avoid saturation at [OIII]5007Å and complete 5 exposures per pointing with a dither pattern of 0, -0.5, -1.5, -2.5, -0.5, 0 slices. Due to the nature of the extended diffuse emission in the FoV of our science observations we took standalone sky frames approximately once every hour for each mode at an exposure time of 120s in the small slicer mode and 6s in the larger slicer mode. With each exposure we saved the associated guide camera image to be used in correcting WCS errors. The observation details are summarized in Table 3.1 with the total FoV of each observing mode illustrated in Figure 3.1.

Table 3.1: KCWI Observational Summary

Date (mm-dd-yyyy)	Time (UT)	Airmass	Pointings	Exposures/Pointing	Exposure Time (s)	Standard Star
small slicer, R∼18,000						
11-22-2017	4:30 - 5:40	1.41-1.36	1	3	900	L870-2
11-23-2017	4:17-5:50	1.43-1.31	3	3	300	Feige 24
08-16-2018	11:06 - 13:23	1.41-1.30	8	3	120	NGC 7293/Feige 24
09-03-2018	11:20 - 14:23[a]	1.3-1.5	5	3	120	NGC 7293
08-16-2020	10:57 - 14:22	1.30-1.41	11	3	120-360	NGC 7293/Feige 24
large slicer, R∼900						
08-16-2018	14:00 - 14:37	1.32-1.37	5	5	6	Feige 24
08-16-2020	14:41 - 15:20	1.38-1.46	7	5	6	Feige 24

Note. — Summary of Keck/KCWI observations of IC 10's H II regions. Approximately the same fields are observed in both modes for complimentary observations. There is some overlap in pointings between nights to increase SNR in fainter areas of IC 10 so the total number of pointings is not the sum of each night. Approximately 1/2 of the small slicer R∼900 pointings are still in progress with more exposure time needed to achieve sufficient SNR at [OII]3727Å to determine metallicities, but the SNR is sufficient throughout the field for determining an extinction correction at the H II regions.
[a]:There was an observational gap from 12:31-13:51 UT due to inclement weather.

[1](-): left; (+): right

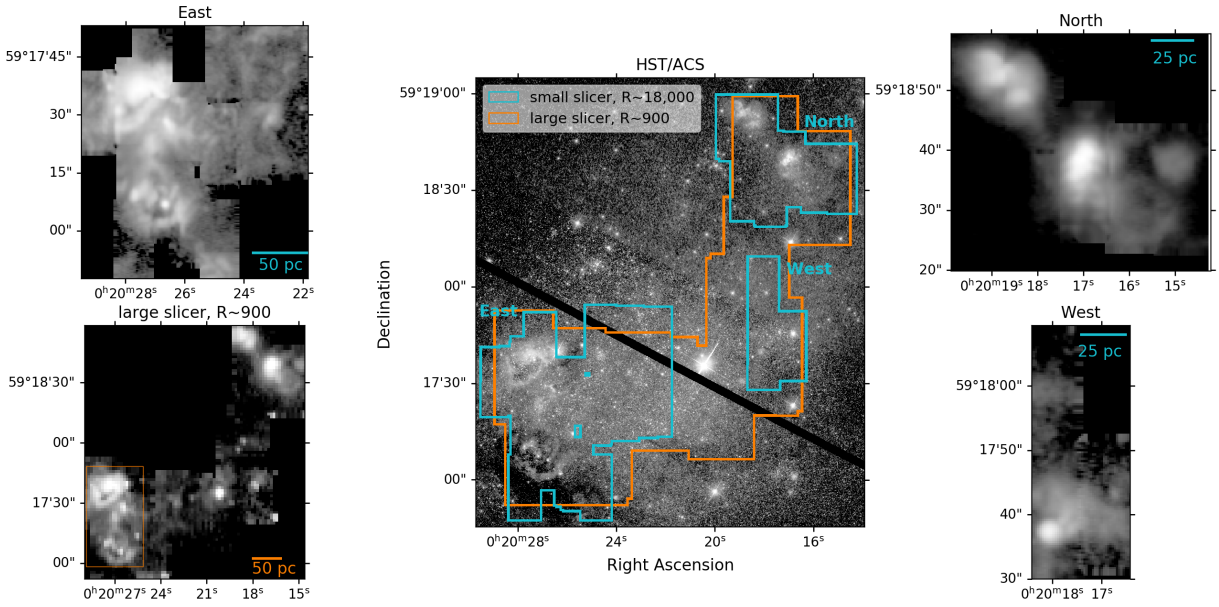

Figure 3.1: (Middle): HST/ACS image of IC 10's central 2′x2′ showing outlined field coverage of our completed and in progress KCWI observations in two modes: the high resolution small slicer, R∼18,000 mode (blue), and the coarse resolution large slicer, R∼900 mode (orange). (Top Left): Integrated [OIII]5007Å flux map from the East region of our small slicer, R∼18,000 observations. (Bottom Left): Large slicer, R∼900 observations. The extinction correction (Section 3.3.2) is determined from this full field, but the metallicity analysis of Section 3.3.6 is limited to the field inside the orange outline due to low SNR outside of the H II regions in the remainder of the field. (Top Right): North region of the small slicer, R∼18,000 observations. (Bottom Right): West region of the small slicer, R∼18,000 observations.

3.2.2 Data Reduction

Raw data were reduced using the IDL version of the public KCWI Data Reduction Pipeline (DRP) version 1.1.0 (Don et al., 2018) with modifications for our data set described here.

The first stage of the DRP consists of bias subtraction, gain correction, and cosmic ray removal procedures. In the default pipeline, the overscan region is used to perform a secondary bias subtraction after removal of the master bias to account for variation in the read noise between the calibration and science frames. We take this a step further to modify the bias subtraction used in our reduction to include a *scaled* bias subtraction. Before the bias subtraction occurs we take the ratio of the overscan regions in the science and master bias frame for each row of the detector and multiply the master bias row by this ratio before subtracting it. This gives us a better match to

the readnoise throughout the night and between the two distinct chips of the detector (with distinct amplifiers and readnoise).

Stages 2-4 of the DRP perform scattered light subtraction, determine transformations to 3D data cubes (used later), and flat field correction, respectively. We skip stage 5 of the DRP which performs sky subtraction in favor of using our own scaled sky subtraction routine on the reduced data cubes. Before this subtraction is performed, we run DRP stage 6 generating data cubes with the geometric solutions of stage 3, stage 7 to perform a correction for differential atmospheric refraction, and stage 8 which uses observations of standard stars to flux calibrate the cubes. The final data products from this pipeline are flux calibrated data cubes for both sky and science observations with associated variance cubes.

After completion of the standard pipeline steps we run a custom scaled sky subtraction on the data. This routine takes an average spectrum over the entire cube for the science frame and associated sky observation. The ratio of these two spectra are computed away from any known emission lines. This ratio is then used to scale the average sky spectrum, which is then subtracted from every spaxel of the science data cube. Errors are propagated in this step using the associated object and sky variance cubes along with the computed scale factor.

WCS offsets between individual frames in the "small slicer, R$\sim$18,000" mode were corrected by matching stars in the guide camera images to HST/ACS imaging of IC 10. The average offset of the measured and expected coordinates of stars in the field was used to shift the associated KCWI frame. On average, a $0.7''$ offset in declination and a $1.2''$ offset in right ascension were found for the "small slicer, R$\sim$18,000" frames. We did not find WCS offsets in the "large slicer, R$\sim$900 observations, and thus do not apply this step for that mode. All observations from each of the two observing modes were mosaicked with the rectangular KCWI pixels binned to square using the Python package `reproject` (Robitaille et al., 2020) before analysis.

Since the observations were spread over a multi-year period, we compared the calibration frames to ensure consistency in these steps. The master bias frames produced in DRP stage 1 for each night show a standard deviation in median flux of $< 0.5\%$ in the small slicer, R$\sim$18,000 mode

and $< 0.2\%$ in the large slicer, R$\sim$900 mode. Similarly, the master flats produced in DRP stage 4 show only a standard deviation of $< 1\%$ in the small slicer, R$\sim$18,000 mode and $< 0.1\%$ in the large slicer, R$\sim$900 mode.

3.3 Analysis

3.3.1 Identifying star-forming regions

Preliminary flux maps are generated for each emission line by summing over 15 channels (1.875Å) centered at the systemic velocity of IC 10 (-348km s^{-1}, Tifft and Cocke, 1988). More robust flux maps are generated later from spectral fitting, but these preliminary maps are used so as not to introduce boundary effects from low SNR regions in the H II region identification routine. We use the python package, `astrodendro` (Thomas et al., 2013), to find the locations and extent of star forming H II regions in our [OIII] and Hβ flux maps. `Astrodendro` finds hierarchical structure in data sets by starting at the pixels with the highest flux and progressing to lower flux pixels surrounding those. If a local maximum is found `astrodendro` creates a new structure with that as the peak when the local maximum is above a user defined threshold. As the algorithm progresses to lower flux values a system of leaves, branches, and trunks are defined relating these local maxima (see Rosolowsky et al., 2008, for an illustration of this method). In this system the leaves are the most compact structures, the individual H II regions in this study, while the branches connect the larger H II region complexes. The trunks are the bottom level of the hierarchical structure identified by `astrodendro` and show the extent of the ionized gas emission in our KCWI observations. If these observations covered the full optical extent of IC 10, we would expect the trunks to identify distinct areas of star-formation in the galaxy. However, since these observations are focused only on areas of high star formation activity the trunks fill the majority of the field and are therefore not physically significant in this study.

In order for a local flux maximum to be considered a real structure we have set a series of constraints to be applied by `astrodendro` - some of which are standard parameters in the package and some that are required routines unique to our data set. Standard parameters that we constrain

with `astrodendro` are the minimum peak value for a structure, the minimum flux a pixel can contain in order to be added to any structure, and the minimum step size between independent structures (leaves) derived from the variance cubes resulting from the KCWI DRP. We have also written custom routines to set the minimum radius and minor axis length required for a real structure defined by the point spread function (PSF) of standard star observations. The values provided for these constraints are given in Table 3.2 for the [OIII]5007Å flux maps; the analysis with the Hβ maps uses the values obtained with the same σ requirements.

Table 3.2: Clump Identification Constraints

Type	Value
Minimum radius (HWHM)	1.4px ~ 0.5"
Minimum peak flux [erg s^{-1} cm^{-2} Å^{-1}]	3.7×10^{-17} (5σ)
Minimum peak delta [erg s^{-1} cm^{-2} Å^{-1}]	7.3×10^{-18} (1σ)
Minimum flux [erg s^{-1} cm^{-2} Å^{-1}]	2.2×10^{-17} (3σ)

Note. — Parameters used to constrain the `astrodendro` clump fitting procedure after correcting the KCWI small slicer, R$\sim$18,000 flux maps for the background DIG. The values listed for each constraint are for the [OIII]5007Å flux maps, but the same constraint method (e.g., 5σ minimum peak flux) is used for all emission lines.

To accurately identify H II regions and determine SFRs, we first remove the background of Diffuse Ionized Gas (DIG). It is not possible to do this spectrally on individual spaxels since some locations have too low of SNR to determine the velocity shift (particularly in locations of greater DIG contribution). We identified three regions where there are no known H II regions in

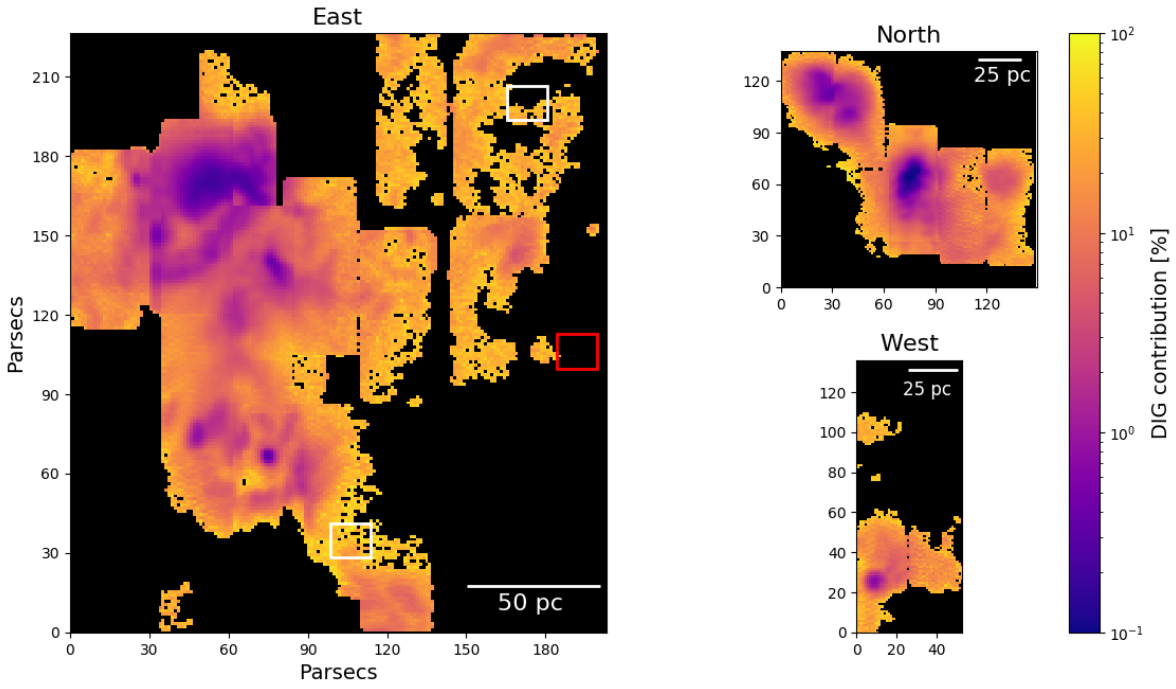

Figure 3.2: Map of the Diffuse Ionized Gas (DIG) contribution to the total [OIII]5007Å flux before subtraction. The locations of HII regions are identified after this DIG contribution is removed from the flux maps. Spaxels with SNR<2 are masked in this figure. The DIG flux per pixel was evaluated in the three outlined boxes, with the region outlined in red chosen for the DIG subtraction as it contained the minimum flux per pixel.

our observed field (identified by the white and red boxes in Figure 3.2). We find the mean flux per pixel in each of these regions, and take the minimum value to be our DIG contribution so as not to over-subtract flux at this stage (the red box). The average DIG contribution in all three cases is on the order of a percent in pixels associated with H II regions, so the DIG region chosen should not make a significant difference in the subsequent analysis. Maps of the DIG contribution to the integrated [OIII]5007Å flux are shown in Figure 3.2. Finally, we subtract the mean DIG flux/pixel from every location in our flux maps. For the small slicer, R$\sim$18,000 observations, this removes on average 21% of the [OIII]5007Å flux per spaxel, with significantly lower contribution at the H II regions. We repeat this subtraction on integrated flux maps for each emission line using the same DIG region throughout. We also extract a mean DIG spectrum over this same region for use in correcting H II region spectra to be discussed in Section 3.3.2.

The `astrodendro` package has the option to compute dendrograms on either 2D (position-

position) or 3D (position-position-velocity) data. We chose to use our flux maps for H II region identification due to the need to subtract the DIG contribution to identify fainter regions. To test whether any major differences in identified H II regions were produced by the choice of using flux maps, the dendrograms constructed from un-subtracted flux maps and data cubes were compared. For the latter, a defined range of spectral channels is used to limit the analysis to a single emission line and a requirement is added that the spectral extent of each structure exceeds 0.38Å, the average width of arc lines determined from Gaussian fits to lines in the calibration frames separated every 100Å. There was not a significant deviation in either the size or number of H II regions identified with these two methods and therefore we proceed in the analysis of regions identified from the DIG subtracted flux maps.

Running `astrodendro` on the 2D [OIII]5007Å flux map and manually removing narrow filaments or regions truncated by the edge of the mosaic results in the identification of 46 H II regions. The average radius is 4.0 pc with a Σ_{SFR} of 0.20 $M_\odot$ yr^{-1} kpc^{-2}. Each of these identified regions are listed in Table 3.3 with the contours shown in the [OIII]5007Å and Hβ flux maps of Figure 3.3. Using the 2D Hβ flux map produces the same H II region locations in areas of high SNR, but the lower SNR of the Hβ line means that faint regions cannot be identified in this map that can in [OIII]5007Å. Since the results are consistent in areas where the SNR is high for both lines, we proceed with the region identification from the [OIII]5007Å flux map.

It should be noted that there are more compact structures within the identified H II regions which can be seen visually (Figure 3.3) but do not result in unique structures detected by `astrodendro`. In some cases these structures do not meet the resolution requirements, but in others it is a result of using the same identification criteria across the entire field. A larger number of H II regions can be identified using location dependent criteria, but that introduces an extra element of uncertainty in requiring manual tuning of the parameters. It is more prudent to maintain consistent requirements for H II region identification across the study even if it does not result in perfect separation of compact structures.

Table 3.3: H II Region Catalogue (small slicer, R∼18,000)

Region ID	Complex	HL90 ID	RA (J2000)	Dec (J2000)	Radius (pc)	Radius (arcseconds)
G16	···	125	00h20m29.14s	+59d17m32.37s	2.60 ± 0.22	0.75 ± 0.06
G17	···	···	00h20m28.81s	+59d17m21.76s	2.11 ± 0.18	0.61 ± 0.05
H16a	c_H16	111c/111e	00h20m27.35s	+59d17m36.49s	10.32 ± 0.87	2.98 ± 0.25
H16b	c_H16	111d	00h20m28.23s	+59d17m31.24s	2.95 ± 0.25	0.85 ± 0.07
H17a	c_H17	111a	00h20m26.57s	+59d17m27.05s	5.08 ± 0.43	1.47 ± 0.12
H17b	c_H17	111b	00h20m27.12s	+59d17m22.66s	4.14 ± 0.35	1.20 ± 0.10
H17c	c_H16	111e	00h20m28.06s	+59d17m26.90s	3.54 ± 0.30	1.02 ± 0.09
H18a	c_I18	106a	00h20m26.61s	+59d17m07.72s	4.74 ± 0.40	1.37 ± 0.12
H18b	c_H18	106b	00h20m27.53s	+59d17m09.82s	4.08 ± 0.34	1.18 ± 0.10
H18c	c_H18	106	00h20m27.08s	+59d17m08.61s	2.19 ± 0.18	0.63 ± 0.05
H18d	···	106	00h20m27.33s	+59d17m02.74s	3.38 ± 0.28	0.98 ± 0.08
H18e	···	115	00h20m28.05s	+59d17m11.42s	2.72 ± 0.23	0.79 ± 0.07
I16a	···	···	00h20m24.82s	+59d17m35.54s	2.60 ± 0.22	0.75 ± 0.06
I16b	···	···	00h20m24.66s	+59d17m42.49s	2.31 ± 0.19	0.67 ± 0.05
I17a	···	100	00h20m25.33s	+59d17m24.36s	2.56 ± 0.21	0.74 ± 0.06
I17b	···	···	00h20m24.82s	+59d17m26.99s	3.02 ± 0.25	0.87 ± 0.07
I17c	···	···	00h20m24.72s	+59d17m17.36s	2.10 ± 0.18	0.61 ± 0.05
I18	c_I18	106	00h20m26.26s	+59d17m04.28s	7.02 ± 0.59	2.03 ± 0.17
I19a	c_I19	97	00h20m25.18s	+59d16m51.19s	3.51 ± 0.30	1.01 ± 0.09
I19b	c_I19	91	00h20m24.69s	+59d16m51.24s	3.30 ± 0.28	0.95 ± 0.08
J15	···	···	00h20m23.07s	+59d17m43.78s	2.71 ± 0.23	0.78 ± 0.07
J16a	···	86/87	00h20m23.91s	+59d17m42.08s	7.72 ± 0.65	2.23 ± 0.19
J16b	c_J16	73	00h20m23.06s	+59d17m29.61s	4.46 ± 0.37	1.29 ± 0.11
J16c	c_J16	77	00h20m23.38s	+59d17m31.51s	2.24 ± 0.19	0.65 ± 0.05
J16d	···	···	00h20m23.01s	+59d17m38.83s	3.74 ± 0.31	1.08 ± 0.09
J17a	···	74	00h20m23.37s	+59d17m17.83s	3.76 ± 0.32	1.09 ± 0.09
J17b	···	···	00h20m24.08s	+59d17m15.08s	3.50 ± 0.29	1.01 ± 0.08
J17c	···	85	00h20m23.99s	+59d17m27.41s	2.94 ± 0.25	0.85 ± 0.07
J17d	···	74a	00h20m22.83s	+59d17m18.09s	3.09 ± 0.26	0.89 ± 0.08
J17e	c_J17	83	00h20m23.92s	+59d17m19.54s	2.61 ± 0.22	0.75 ± 0.06
J17f	···	74	00h20m22.97s	+59d17m21.34s	3.18 ± 0.27	0.92 ± 0.08
J17g	c_J17	84	00h20m23.93s	+59d17m21.84s	2.91 ± 0.24	0.84 ± 0.07
K16	···	···	00h20m22.50s	+59d17m42.22s	5.10 ± 0.43	1.47 ± 0.12
L11	c_L11	50b/50c	00h20m18.85s	+59d18m53.14s	5.32 ± 0.45	1.54 ± 0.13
M11	c_L11	50a	00h20m18.38s	+59d18m49.17s	2.77 ± 0.23	0.80 ± 0.07
M12	c_M12	45	00h20m16.95s	+59d18m37.43s	9.24 ± 0.78	2.67 ± 0.23
M14	···	49	00h20m18.10s	+59d17m58.82s	6.74 ± 0.57	1.95 ± 0.16
M16a	c_M16	46a/46b	00h20m17.84s	+59d17m38.78s	8.45 ± 0.71	2.44 ± 0.21
M16b	c_M16	46c	00h20m18.32s	+59d17m43.01s	2.62 ± 0.22	0.76 ± 0.06
M16c	c_M16	44	00h20m16.76s	+59d17m39.25s	2.61 ± 0.22	0.75 ± 0.06
M16d	···	48	00h20m18.17s	+59d17m31.05s	3.33 ± 0.28	0.96 ± 0.08
N12a	···	36	00h20m15.03s	+59d18m37.82s	6.79 ± 0.57	1.96 ± 0.16
N12b	···	37	00h20m15.56s	+59d18m33.30s	1.98 ± 0.17	0.57 ± 0.05

Continued on next page

Table 3.3 – *Continued from previous page*

Region ID	Complex	HL90 ID	RA (J2000)	Dec (J2000)	Radius (pc)	Radius (arcseconds)
N13a	c_M12	41	00h20m16.02s	+59d18m25.67s	3.91 ± 0.33	1.13 ± 0.10
N13b	···	35	00h20m15.28s	+59d18m27.28s	3.26 ± 0.27	0.94 ± 0.08
N15	···	43	00h20m16.56s	+59d17m45.47s	2.85 ± 0.24	0.82 ± 0.07

Note— H II regions identified in small slicer, R$\sim$18,000 observations of IC 10 following the new region identification scheme laid out in Section 3.3.1 and the radius definition adopted in Section 3.3.1.

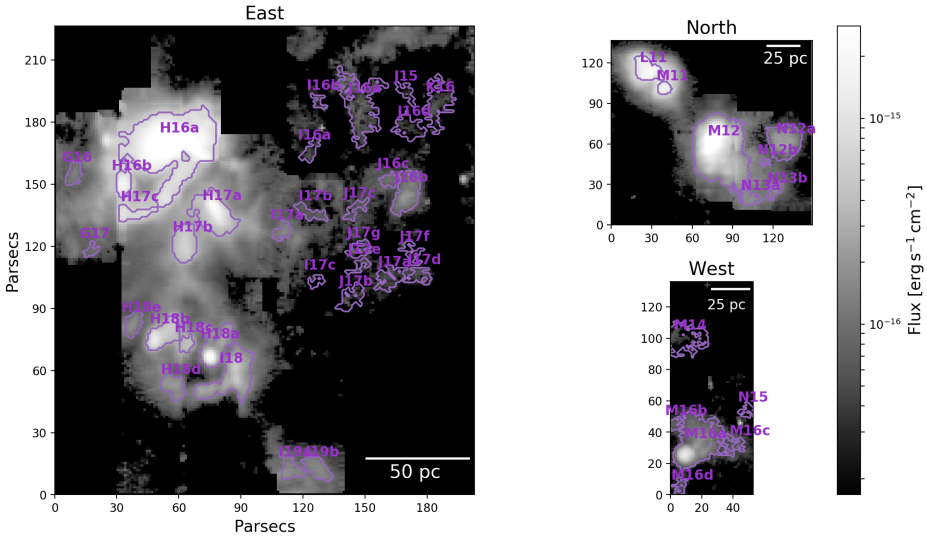

(a) [OIII]5007Å

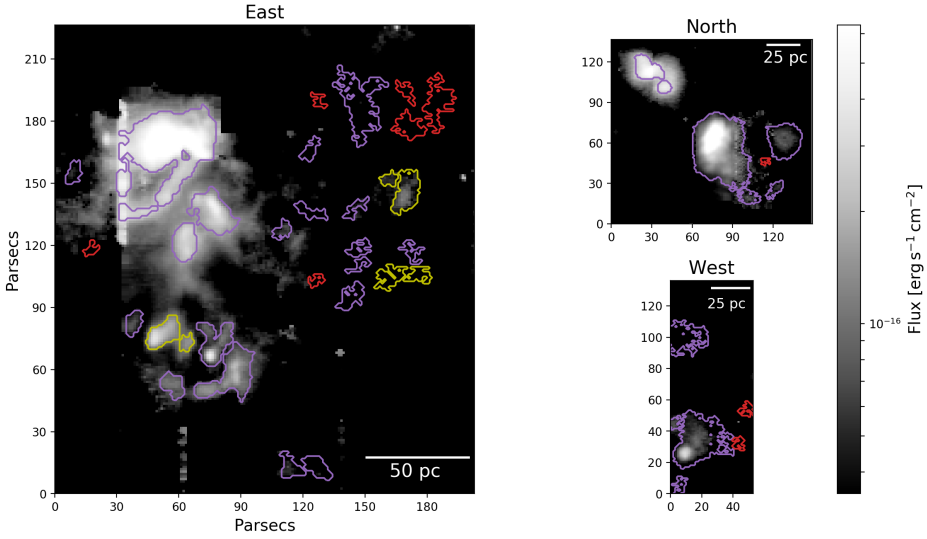

(b) Hβ

Figure 3.3: Maps of integrated flux of the ionized gas in IC 10 measured from Gaussian fits to the [OIII]5007Å (a) and Hβ (b) lines at each spaxel for the high resolution "small slicer, R$\sim$18,000" observing mode. Each map is divided into the "North" portion of the FoV in the upper right, the lower right shows the "West" field, and the "East" region of the observed field on the left. The purple contours mark the edges of the most compact H II region structures found by `astrodendro` in the [OIII]5007Å flux map. The H II regions outlined in red in the Hβ map were not found by `astrodendro` on this lower SNR map, and the H II regions outlined in yellow were blended into single regions. SNR $>$2 is required for these maps, with more spaxels falling below this cut in Hβ. It should be noted that the H II region contours are determined from integrated flux maps at [OIII]5007Å rather than these maps generated from Gaussian fits at each spaxel due to the regions with too low of SNR to perform DIG subtraction at the individual spaxel.

3.3.1.1 H II Region Naming

Throughout this paper the identified H II regions will be referred to with a naming convention based on a simple grid divided into $15'' \times 15''$ regions spanning the optical extent of IC 10. This grid based naming convention provides a simpler method of comparison between studies and extension to a larger FoV than the initial H II region naming developed in the study by Hodge and Lee (1990), as discussed in more detail in Appendix 3A. The grid rows are numbered from 0 - 24 with columns designated A - X as illustrated in Figure 3.4 and Appendix Figure 3A.1. H II regions will be assigned a name consisting of their column followed by their row (e.g., J16). In the case of multiple H II regions falling into the same square of this grid, they are assigned an additional letter, "a,b,c,etc.", in order of decreasing luminosity (e.g., J16a). Each knot belonging to a larger complex will be given its own designation based on the knot center with the parent complex listed in column 2 of Table 3.3 along with the designation from Hodge and Lee (1990) if there is a corresponding one in column 3.

3.3.1.2 Defining the Radius

There are a number of ways in which to define the size of star-forming regions, and the use of these methods is not always consistent between studies, particularly when comparing local and high-redshift samples with widely varying resolution. One method is to assume a spherically symmetric region (such as a Strömgren sphere) and fit the flux profile with a 2D elliptical Gaussian (e.g., Wisnioski et al., 2012). The half-width at half-maximum (HWHM) then gives an estimate of the half-light radius, $r_{1/2}$. A second method is to fit contours to the flux profile at a defined level above the noise and then sum the pixels contained within the contour to determine the area, A, of the region. This area can then be used to define the effective radius, $r_{\rm eff} = \sqrt{A/\pi}$ (e.g., Larson et al., 2020). This total area is produced by the `astrodendro` algorithm, from which we calculate $r_{\rm eff}$ of the H II regions in IC 10. A third method, also produced by `astrodendro`, takes an approach that compromises between the two previous methods. Rather than summing the pixels within the defined contour the second moment of the structure is determined along the direction of greatest elongation

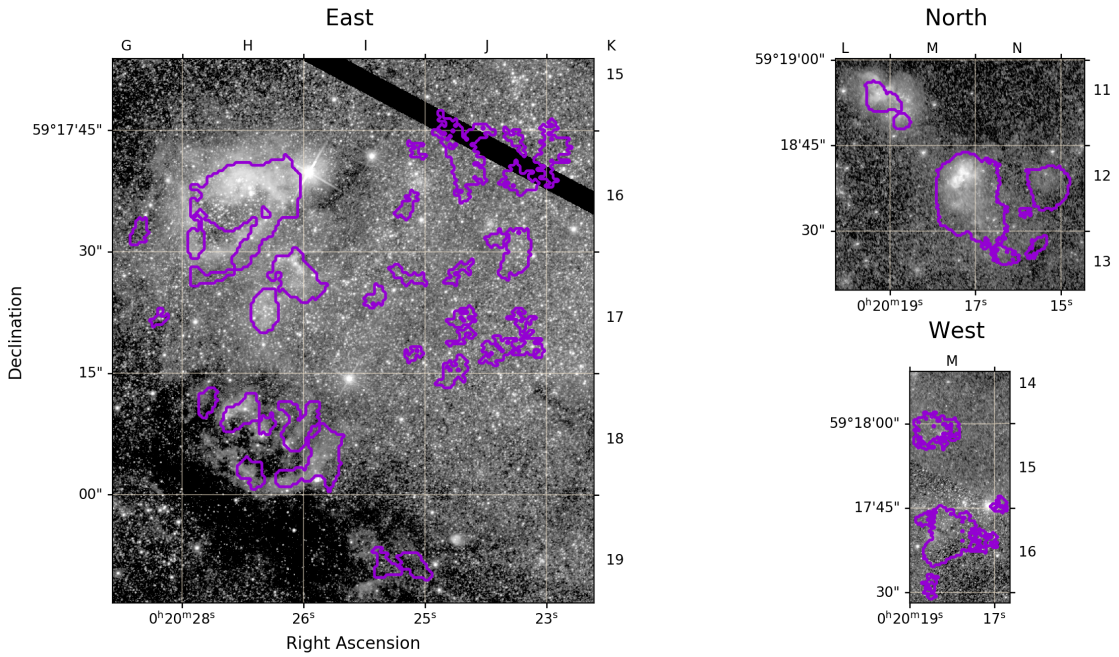

Figure 3.4: Coordinate grid for proposed H II region naming scheme overlaid on an HST/ACS image of the galaxy. The column letter is shown along the top of each image with the row number along the right hand side. H II regions are named based on the column and row corresponding to their center. The HST image is divided into the "East", "West", and "North" sections as in the presentation of the KCWI maps throughout this paper (e.g., Figure 3.3) with the identified H II regions outlined in purple.

and the direction perpendicular to that. The HWHM determined by these second moments is then used to define an ellipse centered at the region peak and calculate its area. We use this area to define a pseudo half-light radius, $r^*_{1/2} = \sqrt{A_{\rm ellipse}/\pi}$ which we will use as the characteristic size of the H II regions throughout this paper. We compare the result of using each of these three methods to define the extent of the H II regions in IC 10 in Appendix 3B along with a discussion of the definitions used in similar studies.

Our choice of determining region sizes from the second moments will be most directly comparable to high-redshift studies which use $r_{1/2}$, but we do not expect significant biases from including studies using $r_{\rm eff}$ in our investigation of the scaling relationships (Section 3.3.8) due to the larger impact of the PSF in high-redshift observations and the systematically larger uncertainties on measured sizes.

3.3.2 H II Region Spectra

Spectra are extracted for each identified H II region by integrating the flux over a circular aperture defined by the region center position and $r^*_{1/2}$ at each wavelength channel using the `aperture_photometry` function in the Python package `photutils`. With this we produce an integrated flux and error spectrum for each region. The use of a circular aperture will necessarily exclude the edges of asymmetric H II regions, but it will capture the core which provides the dominant contribution to the flux. The use of a circular aperture has also been found to include less bias from background emission (Wisnioski et al., 2012). Since the DIG subtraction prior to the construction of the dendrogram uses a lower limit on this emission source, the exact boundaries may be biased by this estimation while the circular aperture is less impacted. To ensure the choice of aperture does not bias the conclusions of this paper key analysis was carried out with both integration methods. While the size, luminosity, and dependent properties do increase slightly for integration over the exact area, the trends observed and conclusions reached in the following analysis do not change. Therefore we proceed with the analysis and results using the circular aperture with $r^*_{1/2}$. The integrated spectra are corrected for the underlying DIG contribution. To do this a Gaussian profile is fit to the [OIII]5007Å line in both the region and mean DIG spectrum. Any wavelength shift between these Gaussian centers is corrected and the DIG spectrum is subtracted from the integrated region spectrum with a scaling factor for the number of spaxels in the integrated region. For the remainder of our analysis we use this DIG subtracted spectrum.

We fit each spectrum with a continuum and a Gaussian profile at each emission line, weighted by the associated error spectrum. An example of these fits is shown in Figure 3.5 for region G16 with the full figure set of fits for the remainder of the H II regions available in Appendix 3C. The velocity shift of the region is determined from the mean of the Gaussian fit to [OIII]5007Å relative to the proper motion of IC 10 ($-348 \pm 1\,\mathrm{km\,s^{-1}}$; Tifft and Cocke, 1988). The velocity dispersion is determined from the standard deviation of the Gaussian fit with the instrumental width subtracted in quadrature. The total flux of the emission line is determined by integrating over the Gaussian profile and is converted to luminosity using a distance to IC 10 of $715 \pm 60\,\mathrm{kpc}$ (Kim et al., 2009). For

nearly all cases the emission is well represented by a single Gaussian, but one region, J16a, exhibits a double peaked [OIII]5007Å line. For this special case integrating over the single Gaussian profile underestimates the flux by ∼30% compared to a pure sum over the emission line. For this region we instead fit a double Gaussian, using the primary component to derive the velocity shift and dispersion, and integrating over both peaks to determine the flux.

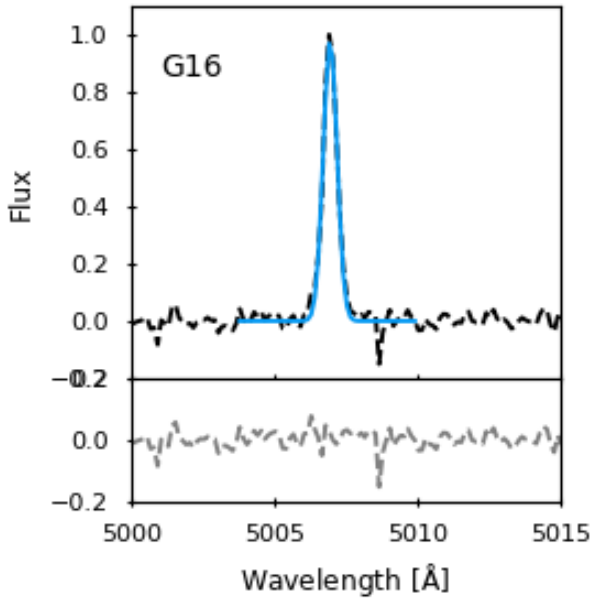

Figure 3.5: Thumbnail of region G16 integrated spectrum at [OIII]5007Å in the small slicer, R∼18,000 observing mode. The complete figure set including spectra from all identified H II regions (46 images) are available as thumbnails in Appendix 3C. The spectral lines are fit by a single Gaussian profile (except for J16a with a double Gaussian profile) shown in cyan with the residuals shown in grey below the associated spectrum. The spectra have been normalized to the peak of the [OIII]5007Å line.

Emission line luminosities are corrected for extinction determined from the ratio of the Hβ and Hγ Balmer lines in the large slicer, R∼900 H II region spectra. We use the ratio of the integrated flux of each of these lines along with the theoretical line ratio of 0.47 assuming Case B recombination (Osterbrock and Ferland, 2006) to determine the E(B − V) reddening in each of the identified H II regions following Momcheva et al. (2013)'s Equation A10:

$$E(B-V) = \frac{-2.5}{\kappa(H\beta) - \kappa(H\gamma)} \times log_{10}\left(\frac{0.47}{(H\gamma/H\beta))_{\rm obs}}\right) \tag{3.1}$$

where $\kappa(H\beta) = 4.6$ and $\kappa(H\gamma) = 5.12$.

For the H II regions identified, we determine an average total reddening value of $E(B-V) = 0.67 \pm 0.10$ with a higher nominal reddening $E(B-V) = 0.97 \pm 0.24$ in a stacked spectrum of spaxels outside the H II regions, though these values overlap when incorporating the measurement uncertainties. The reddening in the stacked spectrum outside the H II regions had to be determined using the peak flux of the Hβ and Hγ lines due to lower SNR at Hγ resulting in a poor fit. We expect this to be a reasonable approximation as the difference introduced by this method inside the H II regions is less than 1/3 of the uncertainty on the associated $E(B-V)$. The larger uncertainty on the estimated reddening outside the H II regions is likely to encompass the possible source of error introduced by the use of peak flux.

The reddening determined in our H II region spectra are lower than the values found by Kim et al. (2009) via NIR colors of RGB stars ($E(B-V) = 1.01 \pm 0.03$) and from UBV photometry of early type stars ($E(B-V) = 0.95 \pm 0.06$), but the estimated reddening for IC 10 varies widely throughout the literature. These estimates have ranged from $E(B-V) = 0.47$ (Lequeux et al., 1979) to upwards of 1.7 (Yang and Skillman, 1993) with a variety of methods used. These estimates are of the total reddening, including the foreground reddening from the Milky Way. IC 10 is at a low galactic latitude, so estimates of even the foreground reddening show large variation. The estimate from the commonly used survey by Schlegel et al. (1998) gives $E(B-V) \sim 1.6$, larger than many of the estimates for the total reddening in IC 10. Kim et al. (2009) notes the large uncertainties in the Schlegel et al. (1998) maps at low galactic latitude and finds a foreground extinction of $E(B-V) = 0.52$ towards IC 10. Given the wide variation in reddening determined for IC 10 we therefore proceed with the values determined from our spectra as this is likely to provide the most accurate measure of the extinction in our FoV.

For the remainder of the analysis all spectra will be extinction corrected according to the associated $E(B-V)$ determined from the appropriate stacked spectrum of spaxels either inside or outside of H II regions and a Cardelli et al. (1989) extinction law. These two different measurements of extinction are particularly important in accurately correcting the extinction of these two distinct

gas regions prior to estimates of the metallicity in Section 3.3.6 using the R_{23} parameter with emission lines covering a wide wavelength range (e.g., Kewley et al., 2019). Ideally each spaxel would be extinction corrected individually, but the SNR was not sufficient to reliably measure Hγ at each spaxel in order to determine the localized extinction. However, due to the high foreground extinction the uncertainty in using global average extinction corrections is reduced compared to environments with a high amount of internal extinction.

3.3.3 Star Formation Rate Indicators

Our high resolution observations cover the Hβ and [OIII]5007Å emission lines, both of which can be used as SFR tracers. Kennicutt (1992) and Moustakas et al. (2006) investigate the accuracy of these emission lines as SFR diagnostics and provide a detailed description of their advantages and disadvantages. Both determine the Hα luminosity to be the more reliable SFR indicator, but unfortunately this lies beyond the wavelength coverage of KCWI. We provide here a brief description of the method of calculating SFR from each of the observed emission lines.

3.3.3.1 Hβ

In order to determine the SFR from the extinction corrected Hβ flux we first convert to equivalent Hα luminosity based on the Balmer decrement and then use the calibration of Murphy et al. (2011):

$$SFR = 5.37 \times 10^{-42} L_{\mathrm{H}\alpha} \tag{3.2}$$

This calibration is based solar metallicity and a Kroupa (2001) IMF. It is updated from the calibration of Kennicutt (1998a); Moustakas et al. (2006) which make use of a Salpeter (1955) IMF.

3.3.3.2 [OIII]5007$\mathring{A}$

Moustakas et al. (2006) uses their sample of SDSS star-forming galaxy spectra to explore the uncertainties present when using [OIII]5007Å to calculate SFR. They find a significant amount of scatter when comparing the luminosity of [OIII] to the Hα derived SFR, resulting in a factor of 3-4 uncertainty which they attribute to variation in chemical abundance and excitation. However,

for a single galaxy like IC 10, and particularly for H II regions in the central starburst, we would not expect the same level of variation in these parameters as would be present in a sample of unique galaxies. Further, previous studies have used the [OIII]5007Å, flux to estimate SFR when Balmer line measurements were not present by assuming an [OIII]5007Å/Hα ratio of unity (Teplitz et al., 2000).

We investigate substituting the extinction corrected [OIII]5007Å luminosity for $L_{\mathrm{H}\alpha}$ in Equation 3.2 to estimate the SFR in the H II regions of IC 10, beginning with the same factor of $\mathrm{L}_{[\mathrm{OIII}]}/\mathrm{L}_{\mathrm{H}\alpha} = 1$ as Teplitz et al. (2000). This is compared to the Hβ derived SFR in Figure 3.6 to determine if the two SFR estimates are correlated and if the coefficient of 1 between $L_{[\mathrm{OIII}]}$ and $L_{\mathrm{H}\alpha}$ provides the best match. We find that there is good agreement between the two methods with an average $\mathrm{SFR}_{[\mathrm{OIII}]5007}/\mathrm{SFR}_{\mathrm{H}\beta} = 0.9$, though this ratio drops to $\mathrm{SFR}_{[\mathrm{OIII}]5007}/\mathrm{SFR}_{\mathrm{H}\beta} = 0.63$ in the faintest $1/3$ of the H II regions. Since these are well matched overall in this sample, the higher signal-to-noise ratio [OIII]5007Å line will be used in the remainder of the analysis allowing for the identification of fainter star-forming regions. We checked whether the apparent lower $\mathrm{SFR}_{[\mathrm{OIII}]}/\mathrm{SFR}_{\mathrm{H}\beta}$ ratio in the faintest regions would introduce a bias in the results of the following sections by underestimating $\mathrm{L}_{\mathrm{H}\alpha}$. This was not found to have a significant impact on the results and conclusions in the remainder of this paper with the potential differences being captured in the existing uncertainties. We therefore report only measurement uncertainties on quantities like SFR which rely on $\mathrm{L}_{[\mathrm{OIII}]}$ as a proxy for $\mathrm{L}_{\mathrm{H}\alpha}$ and proceed with $\mathrm{L}_{[\mathrm{OIII}]}/\mathrm{L}_{\mathrm{H}\alpha} = 1$ for the full sample of IC 10 H II regions for consistency with previous studies.

3.3.3.3 Low SFR H II Regions

As can be seen in Figure 3.6, many of the identified H II regions in IC 10 have very low SFR. The rate of production of ionizing photons for a single $18M_{\odot}$ O9 star is $\mathrm{Q} = 10^{47.90}\,\mathrm{s}^{-1}$ (Martins et al., 2005). Assuming Case B recombination this results in an expected $\mathrm{L}_{\mathrm{H}\alpha} \approx 10^{36}\,\mathrm{erg\,s}^{-1}$. In this sample of IC 10 H II regions, 23/46 of the identified regions have luminosities less than this, indicating that the primary ionization source is a less massive star or cluster. There are a limited number of extragalactic surveys which to compare to in this low luminosity regime as the spatial

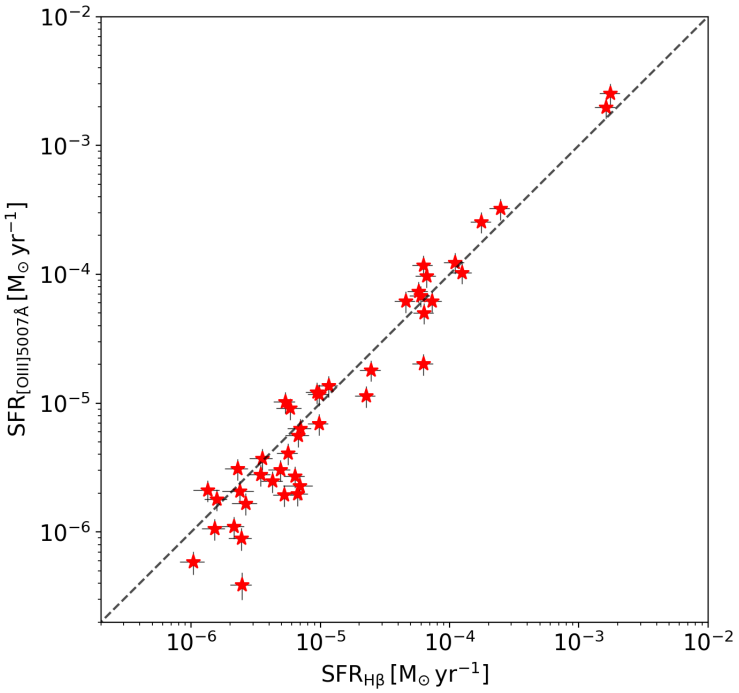

Figure 3.6: Comparison of the SFR determined from Hβ and [OIII]5007Å. The dashed black line denotes the one-to-one line. Given an average $\mathrm{SFR}_{[\mathrm{OIII}]5007}/\mathrm{SFR}_{\mathrm{H}\beta} = 0.9$, the $\mathrm{SFR}_{[\mathrm{OIII}]5007}$ does, on average, provide a good match to the more commonly used $\mathrm{SFR}_{\mathrm{H}\beta}$.

resolution needed to differentiate these compact sources necessitates nearby objects as well as the sensitivity to detect low luminosities. The identification of IC 10's many H II regions by Hodge and Lee (1990) in Hα imaging survey does get to this regime as well. They also find some regions in which they attribute the ionization to a single late B or early A type star. The same regime of single star ionization is reached by Hodge et al. (1989) in NGC6822 though they note that some of the regions with low surface brightness may instead be diffuse emission rather than the H II regions they are identified as.

Within the Milky Way a number of studies of compact and ultra-compact H II regions have been conducted which fall into this category of ionization by a single intermediate mass star at radio and infrared wavelengths. Lundquist et al. (2014) studied four intermediate mass star forming regions identified in the *Infrared Astronomical Satellite (IRAS)* Point Source Catalog and *Wide-field Infrared Survey Explorer (WISE)* images which they determined were powered by low mass clusters with mid-B stars as the most massive components and therefore the dominant source of ionizing

photons. Over 900 so-called "yellowball" regions, compact H II regions sometimes ionized by a single B type star were identified by citizen scientists as part of the Milky Way Project (Kerton et al., 2015). The yellowballs regions show spatially coincident 8 and 24μm fluxes,which the authors attribute to the early stages of the H II region evolution. As part of HRDS, Armentrout et al. (2021) identify single star H II regions with *WISE* and the Very Large Array (VLA). They find that these single star regions have similar morphologies as their more luminous counterparts and can be powered by a single B2 or earlier spectral type star.

To determine the likely stellar type for the ionizing star in IC 10's H II regions, we compare the observed luminosity to models of the number of Lyman continuum photons produced by a given stellar type. For consistent comparison with the Armentrout et al. (2021) Milky Way study we use the same stellar models for the number of ionizing photons produced by a single star, Martins et al. (2005) for O type stars and Smith et al. (2002) for B type stars. The minimum number of ionizing photons required to power a given H II region is given by:

$$Q_{\rm req} = 7.31 \times 10^{11} L_{\rm H\alpha} \tag{3.3}$$

under case B recombination (Osterbrock and Ferland, 2006). The lowest luminosity region identified in IC 10 can be produced by ionization from a B0.5 star, with 10 H II regions potentially being produced by ionization from a single B star. Forty-four of the identified H II regions have luminosities which can be produced by a single star, while the remaining two would require an ionizing photon production rate equivalent to at least six O3 stars. The number of IC 10 H II regions that could be produced by ionization from a single star of each spectral type is shown in Figure 3.7.

3.3.4 Mass

The mass for each H II region is estimated based on the assumption that the H II regions are approximately spherical making the gas mass simply a function of the volume and density:

$$M_{\rm HII} = \frac{4}{3}\pi r^3 n_{\rm h} m_{\rm h} \tag{3.4}$$

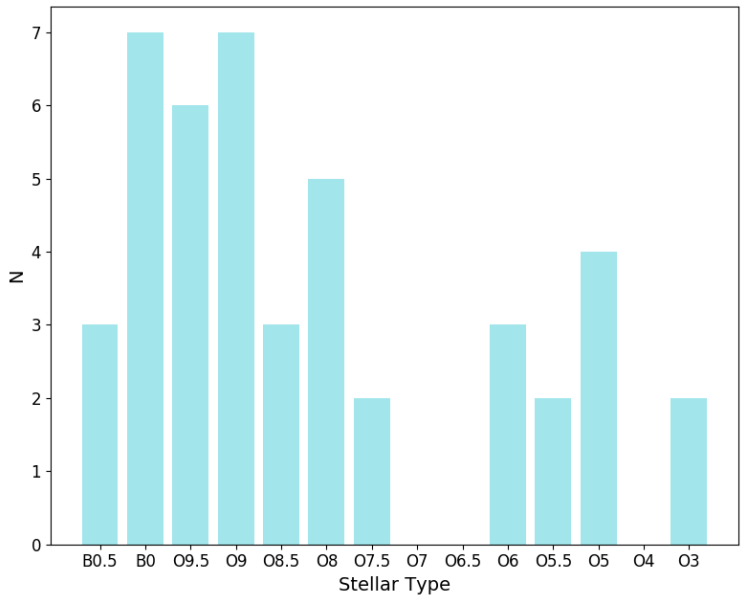

Figure 3.7: Distribution of the potential central ionizing source for each H II region. The stellar type identified here is determined by the minimum number of ionizing photons which can produce the observed luminosity. In the case of a single star providing the dominant source of ionization, each IC 10 H II region requires at least a B0.5 star.

where r is the H II region radius and m_h is the mass of a hydrogen atom. We cannot directly measure the number density of hydrogen, n_h, in our KCWI spectra, but we can estimate it via the Strömgren sphere approximation; the assumption that the gas is fully ionized and therefore the measured luminosity directly measures the amount of hydrogen gas present:

$$n_{\rm h} = \sqrt{\frac{3L_{\rm H\alpha}\lambda_{\rm H\alpha}}{4\pi hc\alpha_{\rm B}r^3}} \tag{3.5}$$

where $\lambda_{\rm H\alpha}$ is the wavelength of Hα, h is Planck's constant, c is the speed of light, and α_B is the Case B recombination coefficient.

Combining these two equations we can solve for the mass of ionized hydrogen gas in each H II region. The resulting masses are shown in the histogram of Figure 3.8 with a median region mass for the sample $\sim 56\,M_\odot$ and a total $M_{\rm H\,II} \sim 2\times10^4\,M_\odot$ residing in the identified H II regions. We will compare this to estimates of the mass based on the measured H II region kinematics in Section 3.3.5.

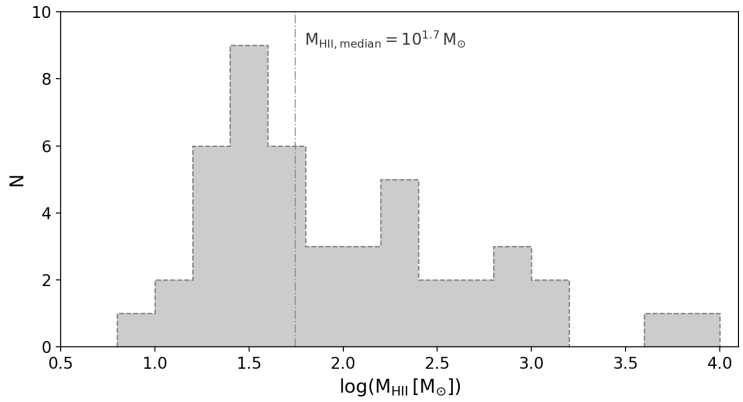

Figure 3.8: Histogram of the H II region ionized gas masses, M_{HII}, estimated from the Strömgren sphere approximation and the measured size and luminosity.

The stellar mass of each region is estimated by integrating the IMF over the full mass range from $0.1 M_\odot$ to $100 M_\odot$ following the method laid out in Relaño et al. (2005). We summarize the method here but refer the reader to Relaño et al. (2005) for a more detailed discussion.

The total stellar mass with the previously stated upper and lower bounds is defined as:

$$M_* = \int_{0.1M_\odot}^{100M_\odot} m\Phi(m)dm \tag{3.6}$$

where $\Phi(m) = Am^{-2.3}$ for a Kroupa (2001) IMF. In order to perform the integration, the normalization factor, A, needs to be determined. This is done by estimating the stellar mass over a smaller range of stellar types. A first order estimate of M_* is determined by calculating a required number of O5 stars needed to produce the measured H II region luminosity and multiplying by the mass of an O5 star ($49.53\,M_\odot$). This is then substituted into Equation 3.6 with the upper and lower limits of integration replaced by the masses of an O3 ($55.3\,M_\odot$) and O9 ($22.1\,M_\odot$) star, respectively. The normalization factor, A, can then be solved for and the IMF can be integrated over the full mass range to give a more accurate estimate of M_*. For the low mass H II regions of IC 10 where we find luminosities consistent with ionization by a single early B star, integrating over the full IMF is somewhat uncertain. To address this, we include an estimated 30% systematic uncertainty on M_* in addition to the propagated uncertainty from the measured luminosity.

For IC 10's H II regions we find a mean $M_* \sim 400\,M_\odot$ from this method with a significantly lower median $M_* \sim 18\,M_\odot$. The large difference in the mean and median masses is due in part to a number of very low M_* estimates for low luminosity regions in which the assumption of a fully sampled IMF is less reliable. The estimates of M_{HII} and M_* for each H II region are shown in Figure 3.9, with $M_* \sim 0.3 \times M_{HII}$ on average.

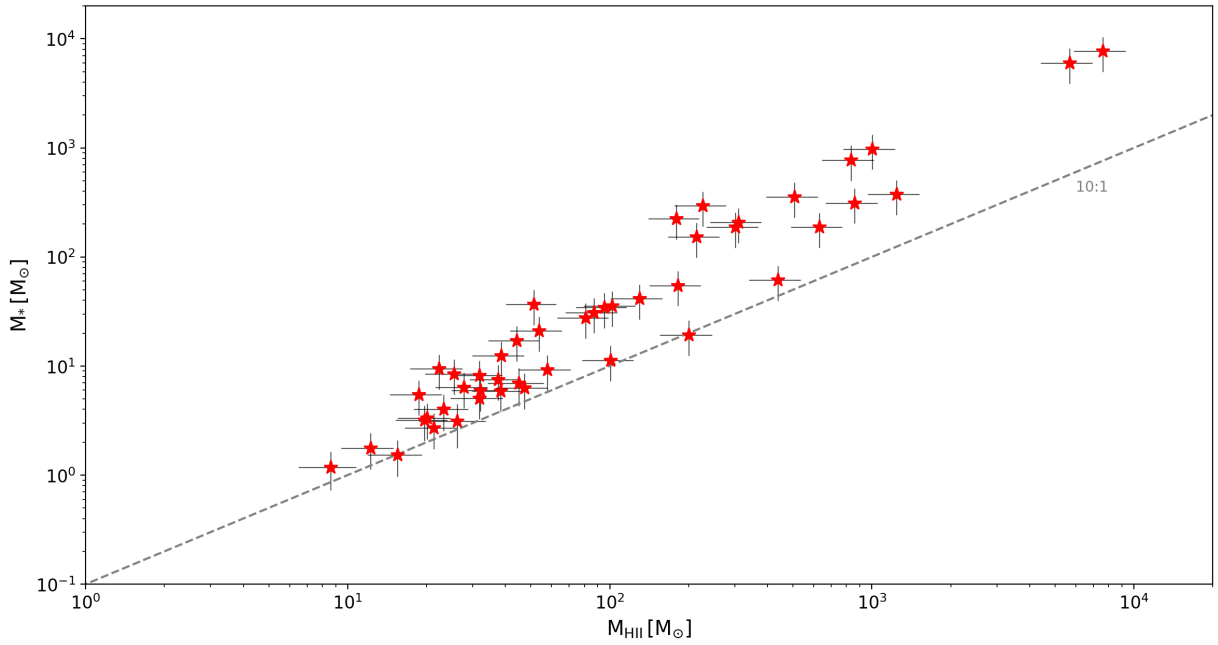

Figure 3.9: Comparison of the estimated M_{HII} and M_* for each IC 10 H II region identified in the KCWI data. On average $M_* \sim 30\% M_{HII}$.

3.3.5 Kinematics

As discussed in Section 3.3.2, we fit a Gaussian to each emission line in the integrated region spectra to determine the velocity shift and dispersion in each detected H II region. Due to the higher SNR of the [OIII]5007Å line, we will report the values from this fit here, though the trends are the same regardless of emission line used. Previous studies of ionized gas in giant H II regions find a systematic difference in linewidths measured from Hα or Hβ and [OIII], with [OIII] measurements giving a $\sim 2\mathrm{km\,s^{-1}}$ underestimate of the dispersion, σ (e.g., Bresolin et al., 2020). After correcting for thermal broadening of both lines, we do not observe such an offset in the spectra of IC 10's H II regions indicating that turbulence is likely the dominant source of the line broadening

(O'Dell et al., 2017). We will therefore proceed with the [OIII]5007Å measurements to trace the kinematics of the ionized gas. The fitted kinematic properties for [OIII]5007Å are shown in Table 3.4 with properties for [OIII]4959Å and Hβ included in Appendix 3E. The average velocity shift is -12$\pm$12 km s^{-1}relative to the systemic velocity of IC 10 with typical velocity dispersions of 16$\pm$8 km s^{-1}.

Each of the H II region DIG subtracted spectra are shifted to a common velocity based on the mean of the Gaussian fit to [OIII]5007Å, normalized to the [OIII]5007Å peak flux, and stacked to generate a composite spectrum as shown in Figure 3.10. Other than removal of the DIG, no other corrections are applied to the spectra before stacking. This reveals a lower luminosity broad component to the [OIII]5007Å line too faint to be detected in the individual H II region spectra or the lower SNR Hβ line. The broad component has a velocity dispersion $\sigma = 36.6$ km s^{-1}and shows only a 2.4km s^{-1} velocity shift relative to the narrow component. Its peak is only 21% of the narrow component peak, but contributes $\sim$37% of the integrated flux. The double Gaussian fit is shown in Figure 3.10 with the stacked spectrum.

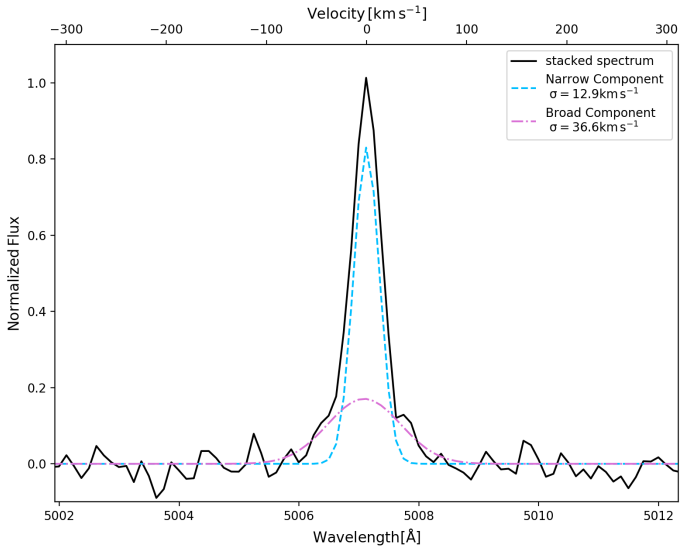

Figure 3.10: Stacked spectrum from each identified H II region (black). Each individual spectrum is normalized to the [OIII]5007Å flux before stacking to investigate the shape of the emission lines. This reveals a faint broad component at [OIII]5007Å that could not be detected in the individual regions. Fits to the broad and narrow components of the [OIII]5007Å line are shown in magenta and cyan, respectively.

Table 3.4: H II Region Properties (small slicer, R∼18,000)

Region	radius (pc)	$\Delta V_{[OIII]5007}$ ($km\,s^{-1}$)	$\sigma_{[OIII]5007}$ ($km\,s^{-1}$)	$L_{[OIII]5007}$ ($10^{35}\,erg\,s^{-1}$)	SFR ($10^{-6}\,M_\odot\,yr^{-1}$)	M_{HII} ($M_\odot$)	τ_{cr} (10^6 yrs)
G16	2.60 ± 0.22	-8.73 ± 1.77	14.52 ± 0.18	7.62 ± 1.43	4.09 ± 0.77	38.48 ± 8.59	0.18 ± 0.05
G17	2.11 ± 0.18	5.62 ± 1.57	14.52 ± 0.28	3.35 ± 0.63	1.80 ± 0.34	18.65 ± 4.19	0.14 ± 0.04
H16a*	10.32 ± 0.87	-11.98 ± 1.61	17.02 ± 0.00	4741.00 ± 889.10	2546.00 ± 477.40	7591.80 ± 1690.19	0.59 ± 0.17
H16b*	2.95 ± 0.25	-11.52 ± 1.50	15.15 ± 0.08	181.00 ± 33.95	97.20 ± 18.23	226.71 ± 50.65	0.19 ± 0.06
H17a*	5.08 ± 0.43	-4.43 ± 2.18	15.85 ± 0.01	476.90 ± 89.41	256.10 ± 48.01	831.57 ± 185.60	0.31 ± 0.09
H17b*	4.14 ± 0.35	-0.44 ± 1.98	11.83 ± 0.01	115.60 ± 21.68	62.08 ± 11.64	301.21 ± 67.18	0.34 ± 0.10
H17c*	3.54 ± 0.30	-3.46 ± 5.64	12.95 ± 0.03	93.73 ± 17.58	50.33 ± 9.44	214.45 ± 47.91	0.27 ± 0.08
H18a*	4.74 ± 0.40	-14.98 ± 1.52	16.84 ± 0.03	218.70 ± 41.01	117.40 ± 22.02	507.55 ± 113.07	0.28 ± 0.08
H18b	4.08 ± 0.34	-38.16 ± 1.67	11.83 ± 0.01	127.50 ± 23.90	68.47 ± 12.83	309.48 ± 68.38	0.34 ± 0.10
H18c	2.19 ± 0.18	-31.40 ± 1.72	11.75 ± 0.03	22.63 ± 4.24	12.15 ± 2.28	51.27 ± 11.23	0.18 ± 0.05
H18d	3.38 ± 0.28	-18.39 ± 1.50	13.70 ± 0.04	21.16 ± 3.97	11.36 ± 2.13	95.07 ± 20.93	0.24 ± 0.07
H18e	2.72 ± 0.23	-15.82 ± 1.50	11.93 ± 0.08	12.89 ± 2.42	6.92 ± 1.30	53.56 ± 11.95	0.22 ± 0.06
I16a	2.60 ± 0.22	-6.80 ± 1.51	12.18 ± 0.55	1.97 ± 0.38	1.06 ± 0.20	19.59 ± 4.40	0.21 ± 0.06
I16b	2.31 ± 0.19	-1.66 ± 1.51	16.64 ± 1.53	1.09 ± 0.22	0.59 ± 0.12	12.20 ± 2.76	0.14 ± 0.04
I17a*	2.56 ± 0.21	7.85 ± 1.68	17.05 ± 0.57	10.48 ± 1.99	5.63 ± 1.07	44.10 ± 9.69	0.15 ± 0.04
I17b	3.02 ± 0.25	-3.88 ± 1.50	15.08 ± 0.43	4.62 ± 0.87	2.48 ± 0.47	37.50 ± 8.28	0.20 ± 0.06
I17c*	2.10 ± 0.18	-2.29 ± 1.50	36.14 ± 6.23	0.73 ± 0.17	0.39 ± 0.09	8.63 ± 2.14	0.06 ± 0.02
I18*	7.02 ± 0.59	-63.67 ± 1.65	15.16 ± 0.06	192.30 ± 36.07	103.30 ± 19.37	857.80 ± 190.61	0.45 ± 0.13
I19a	3.51 ± 0.30	-22.49 ± 1.51	32.39 ± 0.23	21.85 ± 4.10	11.73 ± 2.20	102.23 ± 22.97	0.11 ± 0.03
I19b*	3.30 ± 0.28	-29.09 ± 1.64	19.26 ± 0.13	19.07 ± 3.58	10.24 ± 1.92	87.06 ± 19.47	0.17 ± 0.05
J15	2.71 ± 0.23	-1.79 ± 1.51	53.08 ± 6.37	2.46 ± 0.52	1.32 ± 0.28	23.27 ± 5.46	0.05 ± 0.02
J16a	7.72 ± 0.65	-6.02 ± 1.50	11.91 ± 0.47	37.66 ± 7.13	20.22 ± 3.83	437.78 ± 97.70	0.63 ± 0.19
J16b	4.46 ± 0.37	-9.92 ± 1.76	9.88 ± 0.17	33.71 ± 6.35	18.10 ± 3.41	181.87 ± 40.13	0.44 ± 0.13
J16c	2.24 ± 0.19	-20.49 ± 1.56	10.21 ± 0.16	5.21 ± 0.98	2.80 ± 0.53	25.45 ± 5.69	0.21 ± 0.06
J16d	3.74 ± 0.31	-15.46 ± 1.53	22.29 ± 1.51	3.87 ± 0.76	2.08 ± 0.41	47.33 ± 10.59	0.16 ± 0.05
J17a	3.76 ± 0.32	-12.90 ± 1.50	15.70 ± 0.47	5.67 ± 1.07	3.05 ± 0.58	57.76 ± 12.98	0.23 ± 0.07
J17b	3.50 ± 0.29	0.80 ± 1.50	21.47 ± 3.60	4.27 ± 1.00	2.29 ± 0.53	44.98 ± 10.84	0.16 ± 0.05
J17c	2.94 ± 0.25	1.89 ± 1.52	14.66 ± 0.92	3.68 ± 0.72	1.98 ± 0.39	32.16 ± 7.32	0.20 ± 0.06
J17d*	3.09 ± 0.26	-2.98 ± 1.50	13.66 ± 0.76	3.11 ± 0.60	1.67 ± 0.32	31.85 ± 7.18	0.22 ± 0.07
J17e	2.61 ± 0.22	4.98 ± 1.50	22.06 ± 1.57	2.05 ± 0.40	1.10 ± 0.22	20.06 ± 4.55	0.12 ± 0.03
J17f	3.18 ± 0.27	-16.69 ± 3.92	18.31 ± 5.39	1.92 ± 0.60	1.03 ± 0.32	26.13 ± 7.45	0.17 ± 0.07
J17g	2.91 ± 0.24	-33.59 ± 6.47	12.12 ± 0.91	1.66 ± 0.33	0.89 ± 0.18	21.28 ± 4.77	0.23 ± 0.07
K16	5.10 ± 0.43	-26.38 ± 1.55	12.79 ± 0.32	6.91 ± 1.31	3.71 ± 0.70	100.70 ± 22.48	0.39 ± 0.11
L11	5.32 ± 0.45	-14.92 ± 3.02	10.21 ± 0.01	601.40 ± 112.80	323.00 ± 60.57	1000.78 ± 223.30	0.51 ± 0.15
M11*	2.77 ± 0.23	-19.93 ± 1.51	11.42 ± 0.02	137.30 ± 25.75	73.73 ± 13.83	179.66 ± 39.61	0.24 ± 0.07
M12*	9.24 ± 0.78	-45.03 ± 1.57	14.88 ± 0.00	3693.00 ± 692.40	1983.00 ± 371.80	5676.59 ± 1264.79	0.61 ± 0.18
M14	6.74 ± 0.57	-17.98 ± 1.60	25.23 ± 0.95	11.84 ± 2.25	6.36 ± 1.21	200.24 ± 44.91	0.26 ± 0.08
M16a*	8.45 ± 0.71	-12.73 ± 1.66	10.06 ± 0.02	230.30 ± 43.19	123.70 ± 23.19	1239.72 ± 275.42	0.82 ± 0.24
M16b	2.62 ± 0.22	-9.04 ± 1.50	9.98 ± 0.15	5.06 ± 0.95	2.72 ± 0.51	31.73 ± 7.05	0.26 ± 0.07
M16c	2.61 ± 0.22	-13.06 ± 1.50	8.91 ± 0.21	3.92 ± 0.74	2.11 ± 0.40	27.78 ± 6.20	0.29 ± 0.08
M16d	3.33 ± 0.28	-3.86 ± 1.50	14.12 ± 0.38	3.61 ± 0.68	1.94 ± 0.37	38.39 ± 8.55	0.23 ± 0.07
N12a*	6.79 ± 0.57	-27.95 ± 1.53	12.18 ± 0.04	115.20 ± 21.61	61.86 ± 11.60	631.57 ± 140.24	0.55 ± 0.16
N12b*	1.98 ± 0.17	-24.54 ± 2.13	15.93 ± 0.30	5.78 ± 1.09	3.10 ± 0.58	22.28 ± 5.03	0.12 ± 0.04
N13a	3.91 ± 0.33	-21.74 ± 1.50	11.97 ± 0.08	25.42 ± 4.77	13.65 ± 2.56	129.64 ± 28.89	0.32 ± 0.09
N13b*	3.26 ± 0.27	-20.63 ± 1.65	12.80 ± 0.28	17.06 ± 3.22	9.16 ± 1.73	80.85 ± 17.84	0.25 ± 0.07
N15	2.85 ± 0.24	-6.88 ± 1.58	14.88 ± 1.77	0.94 ± 0.20	0.50 ± 0.11	15.52 ± 3.64	0.19 ± 0.06

Note— Properties of the [OIII]5007Å emission line for H II regions in the small slicer, R∼18,000 observing mode. Spectral properties are determined by fitting a single Gaussian model to the emissionline. Regions with elevated σ in the surrounding gas are identified with a *.

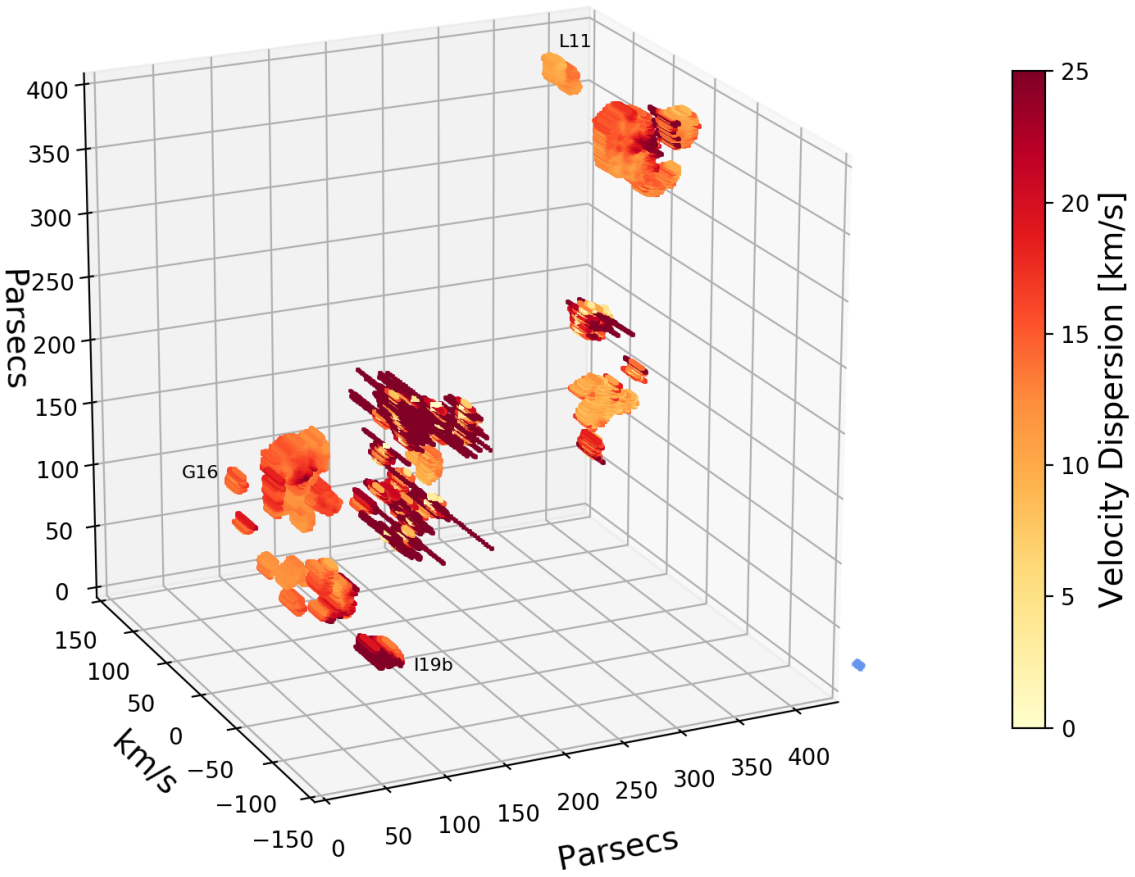

Figure 3.11: Three dimensional view of the 46 identified H II regions in the center of IC 10 based on Gaussian fits to [OIII]5007Å at each spaxel within the region contours. For each spaxel belonging to an identified H II region, the central velocity is set by the velocity shift relative to the systemic velocity of IC 10 and the depth by the velocity dispersion. The colormap also illustrates the measured velocity dispersion at each spaxel. The blue cylinder at the lower right represents a single spectral (depth) and spatial (width/height) resolution element.

3.3.5.1 Resolved Kinematics

In addition to spectra integrated over IC 10's H II regions, we investigate the resolved kinematic properties of the ionized gas at each spaxel. The velocity shift relative to the systemic velocity ($v_{sys} = -348 \mathrm{km\,s^{-1}}$), ΔV, and dispersion, σ, are measured from single Gaussian fits to [OIII]5007Å and Hβ emission lines. The properties determined from the [OIII]5007Å line in spaxels inside H II regions are used to illustrate the three dimensional structure of the identified H II regions in Figure 3.11. Additionally, maps of ΔV and σ at each spaxel in the FoV with SNR>2 for both the [OIII]5007Å and Hβ fits are shown in Figures 3.12 & 3.13. Thumbnail flux and kinematic maps for each H II region are included in Appendix 3D with an example for region G16 in Figure 3.14. These maps show interesting kinematic trends between gas inside and outside the H II regions. The velocity shift shows clear differences between gas residing in the population of H II regions (blue-shifted) and the diffuse gas not associated with a particular region (red-shifted). This is illustrated in both the map of Figure 3.12 and the distributions of Figure 3.15a which shows a much broader distribution of ΔV in spaxels outside the H II regions. This is not surprising as less structure would be expected in the kinematics of this gas than that which is associated with a coherent H II region.

Furthermore, it can be seen in the maps of Figure 3.14 and Appendix 3D that the velocity dispersion is highest at many of the H II region borders, particularly those that reside in larger complexes. In fact, 37% of the identified H II regions, identified with a * in Table 3.4, show elevated velocity dispersions at one or more of their edges which could be indicative of outflowing gas. The distributions of measured σ at each spaxel inside and outside of the H II region boundaries are shown in Figure 3.15b for further comparison. The mean σ for spaxels inside and outside H II regions is quite similar (13 and 14 km s^{-1}, respectively), but the width of the distribution is twice as large for spaxels outside the region boundaries. We investigate the possibility of shocked gas at the H II region boundaries by evaluating the [OIII]5007Å/Hβ ratio. An area with an elevated line ratio may indicate the presence of shocked gas. To ensure this ratio is evaluated over the same physical gas column, we define a fixed velocity shift and width for [OIII] and Hβ in each spaxel

determined from the Gaussian fit to the lower SNR Hβ line. Figure 3.16 shows the map of this line ratio along with contours of elevated velocity dispersion, and as can be seen, the spaxels which show the highest log $\left([\mathrm{OIII}]5007\text{Å}/\mathrm{H}\beta\right)$ also correspond to the areas of elevated velocity dispersion. This result indicates that the elevated velocity dispersion observed at the H II region borders is due to shocked gas.

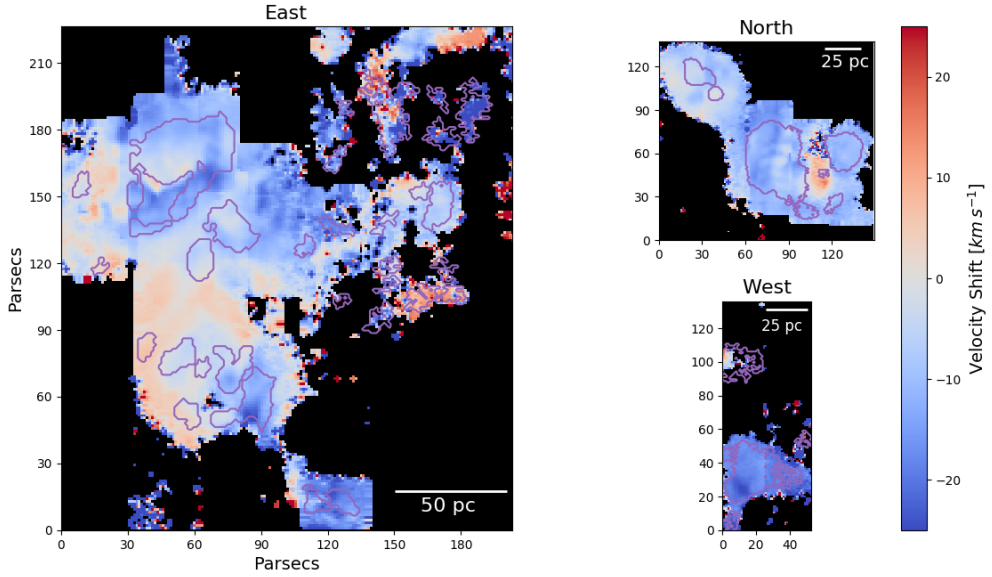

(a) [OIII]5007Å

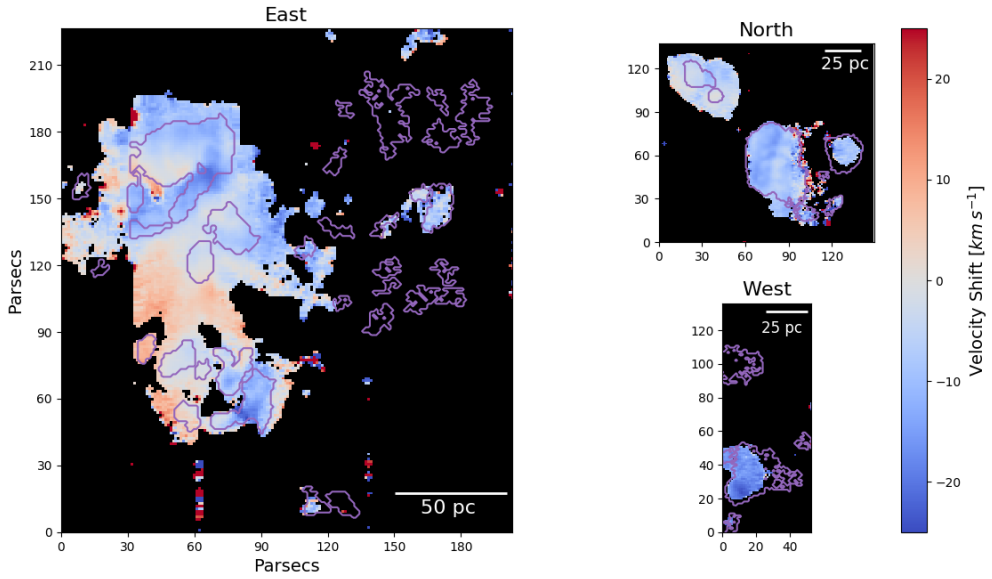

(b) Hβ

Figure 3.12: Maps of velocity shift of the ionized gas in IC 10 measured from Gaussian fits to the [OIII]5007Å (a) and Hβ (b) lines at each spaxel for the high resolution "small slicer, R$\sim$18,000" observing mode. Each map is divided into the "North" , "West", and "East" regions of the observed field. The purple contours mark the edges of the most compact H II region structures found by `astrodendro`. Interestingly, these H II regions predominantly show gas which is blue-shifted relative to the systemic velocity of IC 10 while the surrounding diffuse gas more often shows red-shifted components. SNR >2 is required for these maps, with more spaxels falling below this cut in Hβ, but with the velocity fields matching when measured from either emission line where the SNR is high enough for comparison.

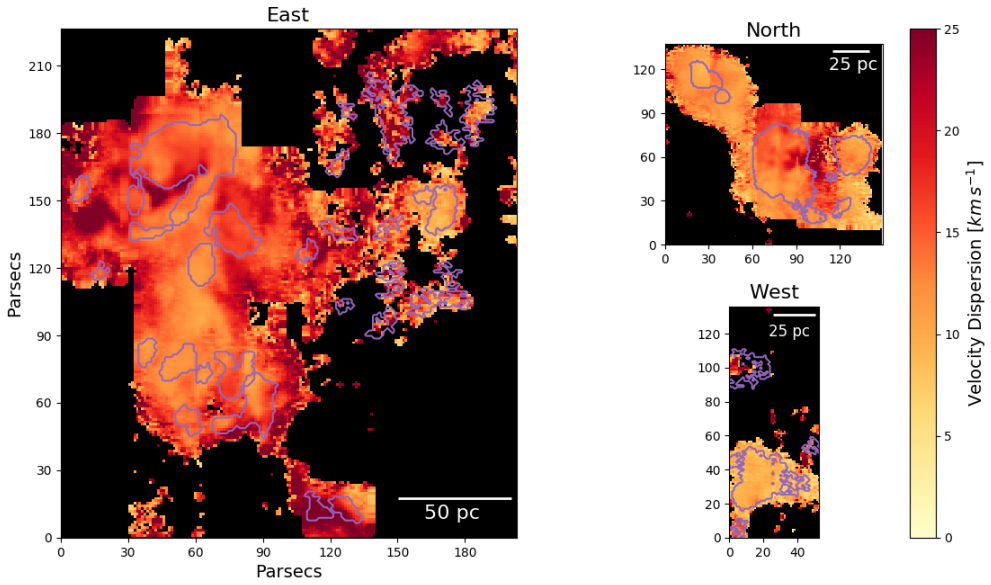

(a) [OIII]5007Å

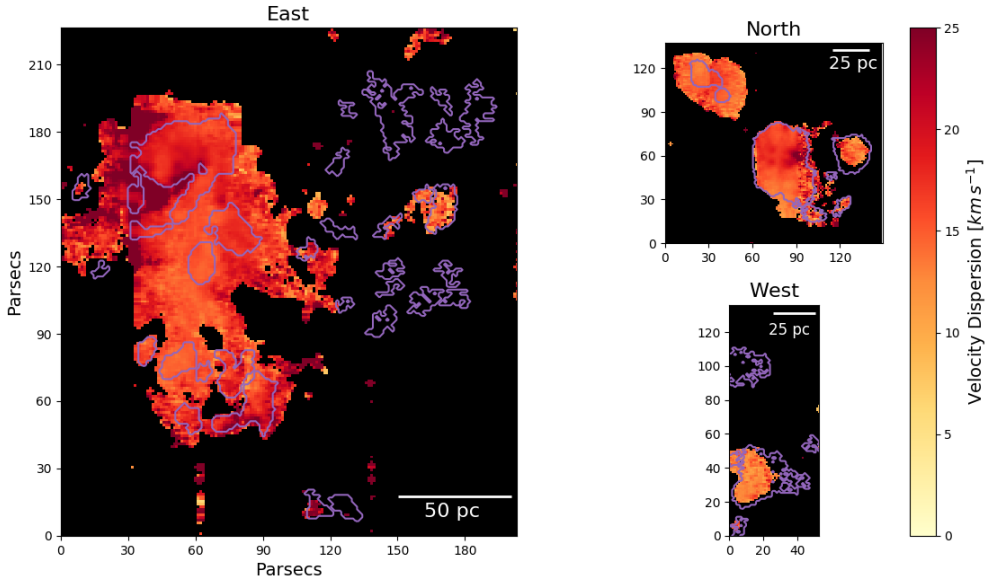

(b) Hβ

Figure 3.13: Maps of velocity dispersion of the ionized gas in IC 10 measured from Gaussian fits to the [OIII]5007Å (a) and Hβ (b) lines at each spaxel for the high resolution "small slicer, R$\sim$18,000" observing mode. Each map is divided into the "North" , "West", and "East" regions of the observed field. The purple contours mark the edges of the most compact H II region structures found by `astrodendro`. SNR $>$2 is required for these maps, with more spaxels falling below this cut in Hβ, but with the velocity fields matching when measured from either emission line where the SNR is high enough for comparison. In particular note the elevated dispersion along the outer edges of some H II regions.

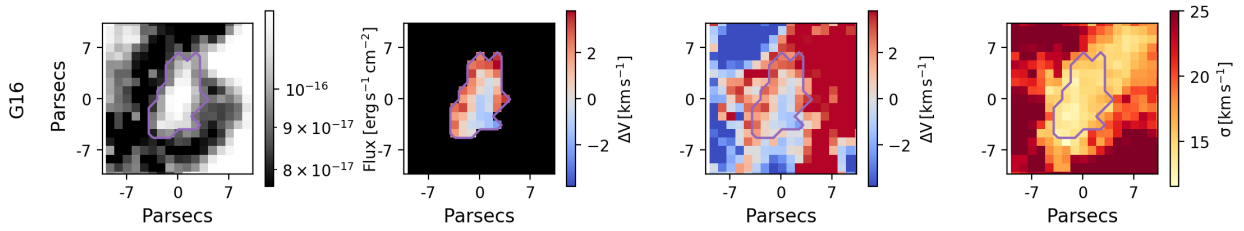

Figure 3.14: Thumbnail map of H II region G16 identified in our KCWI observations. The complete figure set (46 images) is available in Appendix 3D. (Left): Flux maps of the surrounding area. (Center Left): Velocity shift of spaxels within the H II region relative to the systemic velocity of the region. (Center Right): Velocity shift of the H II region and the surrounding gas. (Left): Velocity dispersion within the H II region and the surrounding gas. Regions of elevated velocity dispersion may be indicative of outflowing gas, particularly when correlated with a velocity shift relative to the surrounding gas.

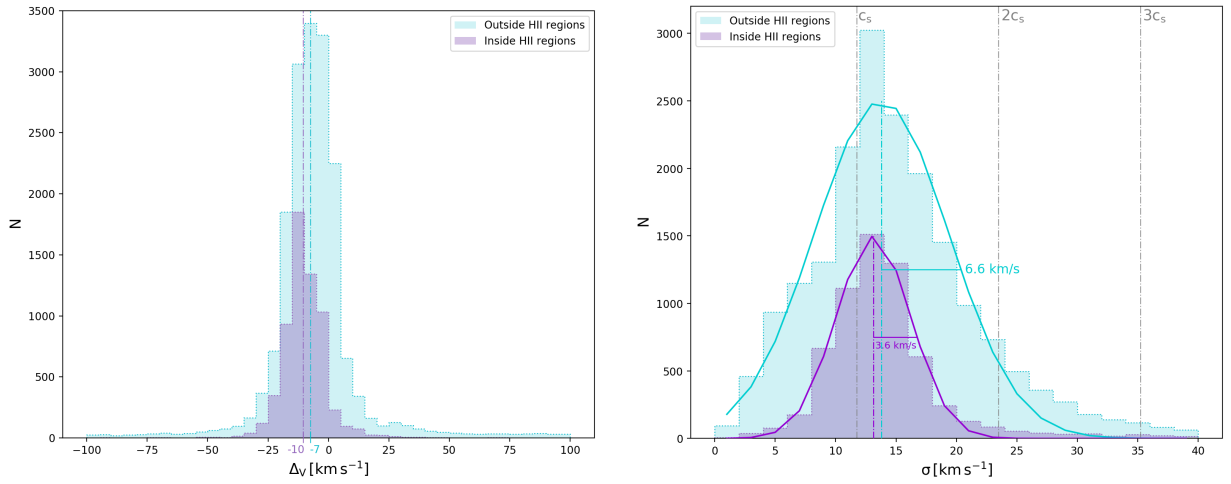

(a) (b)

Figure 3.15: Distributions of kinematic properties derived from Gaussian fits to the [OIII]5007Å line at each spaxel. These distributions are seperated into spaxels which lie outside the H II region boundaries (purple) and inside (cyan). (a): Distribution of ΔV determined from the Gaussian mean relative to the systemic velocity of IC 10 (-348km s^{-1}). The median of each distribution is denoted with a dashed line, but it should be noted that the distributions are quite broad at the base, in particular for those spaxels which are not associated with an H II region. (b): Distribution of σ, the Gaussian standard deviation after subtraction of instrumental width. These distributions are more regularly distributed about their peaks than their ΔV counterparts and are therefore fit with Gaussians (solid lines). The mean of the Gaussian fits to the distributions are marked with dashed lines and are quite similar (13km s^{-1} for spaxels inside H II regions and 14km s^{-1} outside), but the width of the distribution outside the H II regions is twice as large as can be seen in the annotated standard deviation of the fitted distribution.

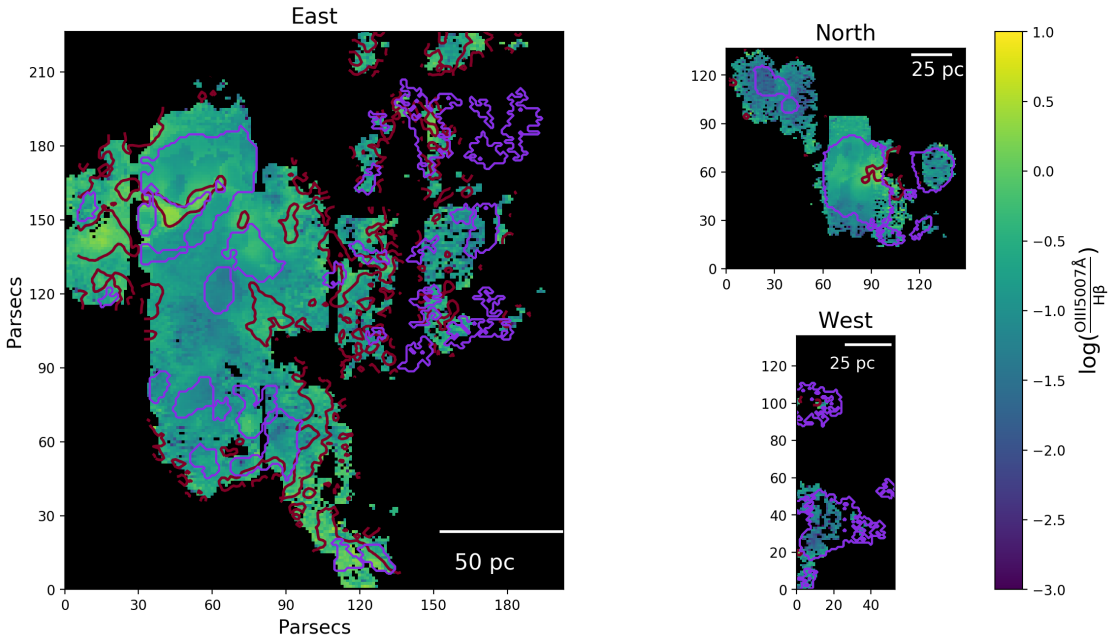

(a)

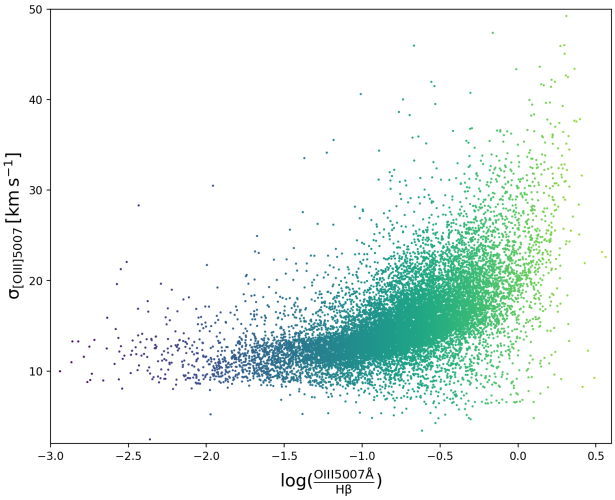

(b)

Figure 3.16: (a): Map of the [OIII]5007Å/Hβ ratio for spaxels with SNR>2 at the weaker Hβ line. As in Figure 3.3, the purple contours show the edges of the identified H II regions. The dark red contours show areas with velocity dispersion > 20 km s^{-1} as measured from the [OIII]5007Å line. (b): The [OIII]5007Å/Hβ ratio plotted against velocity dispersion for each spaxel with the same requirement that SNR$_{\mathrm{H}\beta} > 2$. There is a significant amount of scatter here, but the general trend is for increased velocity dispersion with higher [OIII]5007Å/Hβ, which largely coincides with the edges of the identified H II regions in (a).

3.3.5.2 Region Rotation

In order to classify the kinematic structure of the individual H II regions we generate ΔV maps centered on each region adjusted so the systemic shift of the H II region is 0 km s^{-1}(based on the mean of the Gaussian fit to the integrated region spectrum). For each region we designate whether it is rotating both visually and quantitatively. In order for a region to be considered rotating by eye it must have a bimodality of the velocity shift relative to the region's systemic velocity shift; meaning it must have one region of negative shift and one of positive shift. If for example, there is positively shifted gas surrounded by negatively shifted gas or vice-versa we do not consider that to be ordered rotation. With this method we find 35% of regions to be rotating, which is likely a conservative estimate due to the strict visual criteria.

To assign a quantitative rotation criteria we fit the velocity gradient across the region at different position angles. For each position angle we generate a "fit quality factor" based on the reduced χ^2 combined with the steepness of the slope. The maximum value of the fit quality factor is taken to be the most probable rotation direction and magnitude for that region. If the slope is greater than a threshold value of 0.57 km s^{-1}pc^{-1} then the region is considered rotating. This threshold was determined by assuming an electron density, $n_e = 100\,cm^{-3}$ and determining the mass contained within a region of radius 1pc. Assuming the gas is virialized we then determined the expected value of velocity dispersion and range of velocity shifts[2]. With this criteria we find 65% of H II regions to be rotating. More regions are classified as rotating using this method than the visual classification which in part is due to restricting our visual classification to regions which only have one transition between positive and negative velocity shifts rather than based only on the overall gradient. This restriction is then susceptible to bias from velocity shifts in a small number of pixels that may be outliers for the H II region, classifying regions as "not rotating" when they do in fact have underlying rotation. The quantitative method is also free from the inherent bias with all visual classification and is more easily extended to other samples and studies. Therefore we proceed with

[2]For an H II region with the average radius of this sample,r = 4 pc at $n_e = 100\,cm^{-3}$, the resulting mass $M_{H\,II}$ 500$M_\odot$. This is larger than the average mass estimated in the previous section for IC 10's H II regions, but that simply results in a conservative threshold for rotation.

the rotation classification of the quantitative method in further analysis.

3.3.5.3 Virialization

In addition to M_{HII}, we can also estimate the H II region masses based on the measured kinematics of the ionized gas by calculating the virial, M_{vir}, and enclosed, M_{encl}, masses. However, these rely on the assumption that the motion of the ionized gas is dominated by the self-gravity of the region.

For M_{vir} the region is assumed to be bound and we apply the virial theorem:

$$M_{\rm vir} = \frac{5\sigma^2 r}{G} \tag{3.7}$$

where the factor of 5 is a geometric factor representing the shape of the potential well for a spherical region. This results in a median $M_{vir} = 7.6 \times 10^5\,M_\odot$, orders of magnitude greater than M_{HII}.

As a second method of estimating the H II region masses kinematically we calculate the enclosed mass, M_{encl}, for regions that were determined to be rotating.

$$M_{\rm encl} = \frac{v_{\rm c}^2 r}{G} \tag{3.8}$$

where v_c is the circular velocity determined from the measured velocity shift, v, at a distance, r, from the H II region center corrected for the inclination, i:

$$v_{\rm c} = v\,sin(i) \tag{3.9}$$

Assuming a circular region and no preferred inclination relative to the direction of rotation, we take an average of $sin(i)$ between 0 and $\pi/2$, resulting in a factor of $\frac{\pi}{4}$. The median M_{encl} for rotating regions is $\sim 1.0 \times 10^4\,M_\odot$, more than an order of magnitude less than M_{vir}, but still significantly greater than M_{HII}.

The more than 3 orders of magnitude discrepancy between M_{HII} or M_{encl} and M_{vir} implies that, on average, the H II regions are not in fact virialized and the use of the velocity dispersion

is overestimating the gravitational potential. Furthermore, the measured rotational velocity is also overestimating the gravitational potential, indicating that rotation is not the dominant cause of the velocity gradient observed across the H II regions. To explore this further we first investigate the virial parameter, $\alpha_{\rm vir} = \frac{5\sigma^2 r}{GM_{\rm gas}}$, of the H II regions. We determine $\alpha_{\rm vir}$ using the H II region radius following the $r^*_{1/2}$ definition and the velocity dispersion, σ measured from the Gaussian fit to the integrated spectrum. For $M_{\rm gas}$, we use $M_{\rm HII}$, assuming that the gas in the vicinity of the identified H II region is fully ionized. The resulting values for $\alpha_{\rm vir}$ are shown plotted as a function of $L_{[OIII]5007}$ in Figure 3.17 with the resulting $\alpha_{\rm vir} >> 1$, falling in the regime of H II regions which are not virialized.

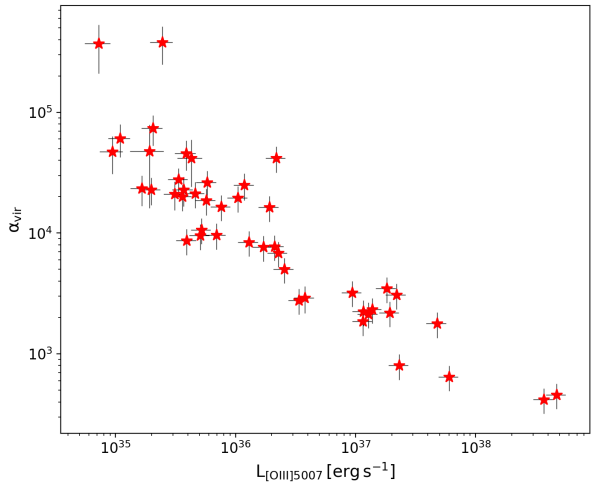

Figure 3.17: The virial parameter, $\alpha_{\rm vir} = \frac{5\sigma^2 r}{GM_{\rm gas}}$, plotted as a function of the integrated H II region luminosity. For all regions $\alpha_{\rm vir} >> 1$, indicating regions which are not virialized.

Studies of H II regions have often investigated the relationship between the luminosity and velocity dispersion, the $L - \sigma$ relation, to study the the region dynamics. Rather than finding a correlation between these two properties for all H II regions, studies typically fit the upper envelope of the relationship defining the area of the correlation where H II regions in virial equilibrium would lie (e.g., Arsenault et al., 1990). We compare the identified H II regions in IC 10 to the relationships measured for the upper $L - \sigma$ envelope in three such studies (Zaragoza-Cardiel et al., 2015; Relaño et al., 2005; Rozas et al., 1998) as another test of virialization. As can be seen from this comparison in Figure 3.18, IC 10's H II regions fall below the envelope fits further supporting the conclusion

that the H II regions are not virialized and the dynamics are dominated by sources of energy besides gravity.

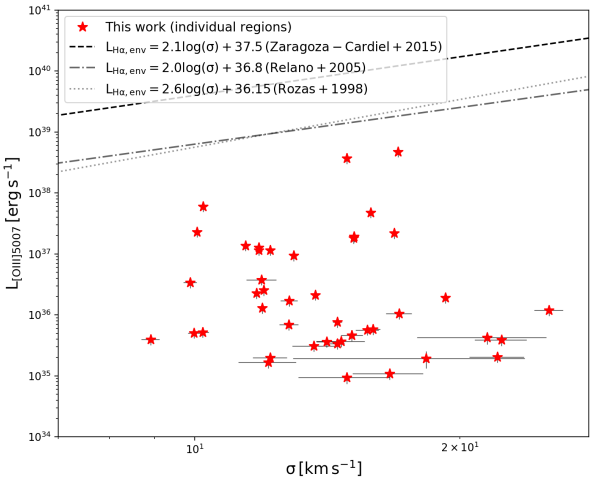

Figure 3.18: Measured $L_{[OIII]5007}$ plotted against σ from Gaussian fits to integrated H II region spectra. The lines show the fits to the upper envelope of this $L - \sigma$ relationship for other samples of H II regions. Regions that fall near the envelope are thought to be virialized while those below the curve are under-luminous for their velocity dispersion. This is the regime where the IC 10 regions fall, further supporting the interpretation that they are not virialized and show significant non-gravitational motion.

The free-fall time estimate is a useful quantity for regions which are forming stars under simple gravitational collapse. We have shown that the H II regions of IC 10 are not virialized, however, and thus the free-fall time may not be the best characterization in this case. The crossing time, based on the measured velocity dispersion may provide a more useful characterization of the timescale relevant for an expanding H II region. The crossing time is defined as:

$$\tau_{cr} = \frac{r}{\sigma} \tag{3.10}$$

The average $\tau_{cr} \sim 2 \times 10^5$ yrs for IC 10's H II regions.

3.3.5.4 Energetics

As outlined in the previous section, the H II regions identified in IC 10 are not virialized, and the velocity dispersions are therefore not a good estimate of the gravitational potential. To quantify

the amount of dispersion due to sources other than gravitational motion we generate model spectra with only rotational motion included for those regions classified as rotating. For this simple model we sum individual Gaussian profiles at each pixel along the direction of rotation with the center set by the measured ΔV, and the width set only by the instrumental width, $\sim$7.5km s^{-1}. The peak flux of each component of the sum is based on a simple Gaussian flux profile for the H II region. After each model pixel is summed the total flux is normalized by the measured [OIII]5007Å flux of the region for accurate comparison. These model spectra are then fit with a single Gaussian profile and the velocity dispersion compared to the measured value for the H II region. The non-rotational motion in the measured profile is defined as $\Delta\sigma = \sqrt{\sigma^2_{\rm meas} - \sigma^2_{\rm mod}}$, the difference between measured and modeled. The distribution of $\Delta\sigma$ is shown in Figure 3.19 along with a cartoon illustrating the Gaussian components of the model spectrum. The average value for $\Delta\sigma$ is $\sim$14km s^{-1}, similar to the sound speed expected in a typical H II region.

We checked the accuracy of this simple rotating H II region model using the software SHAPE (Steffen et al., 2011). SHAPE allows the user to generate a model with potentially complex geometry and kinematic structure. We use a spherical geometry with only rotational motion at the spatial and spectral resolution for each observation. We model this for 3 of our identified rotating H II regions (H18d, H18e, G16) and compare the velocity dispersion from the SHAPE model and simplified Gaussian sums. For region G16, we find that the SHAPE model produces a velocity dispersion 0.3 km s^{-1} greater than our model, in the other two the difference is less than 0.03 km s^{-1}. With measured spectra producing velocity dispersions $\sim$14km s^{-1} greater than either model, this discrepancy is negligible. We therefore use the simple model summing Gaussian components for the full sample of H II regions due to the ease of extending this to a larger sample.

The excess in velocity dispersion that is not attributable to rotational motion can not be explained by virialization and therefore may lead to expansion of the H II regions. We estimate the amount of inward, $P_{\rm in}$, and outward pressure, $P_{\rm out}$, in the H II region, with an imbalance indicating that the region is not in equilibrium with the ISM. As a first order approximation, we estimate the

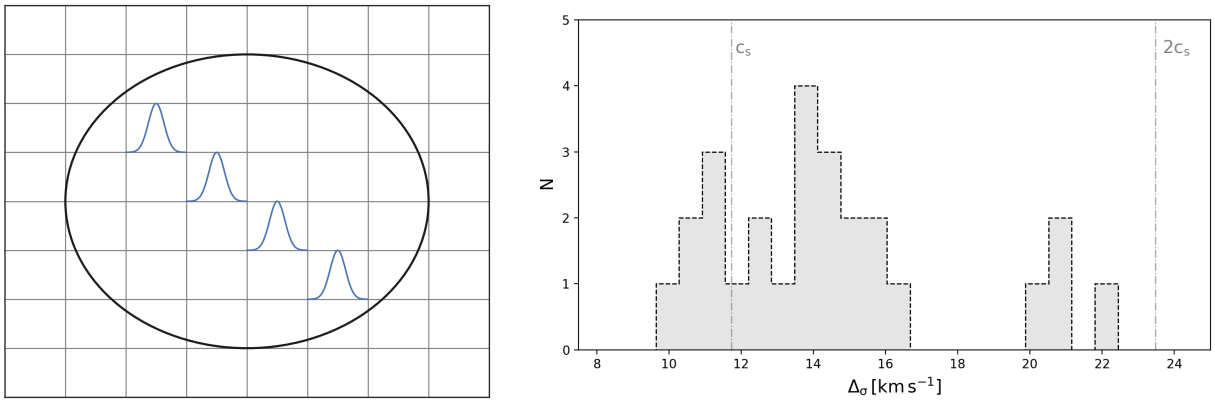

(a) (b)

Figure 3.19: (a): Illustration of the Gaussian components summed in the simple model of a rotating H II region. Components are added at each spaxel along the axis of rotation with the flux of the final profile normalized to the measured spectrum. The width of each spaxel Gaussian is set by the instrumental width with the centers set by the measured rotational velocity. (b): Histogram of the non-rotational component of velocity dispersion measured in each of the rotating H II regions where $\Delta\sigma = \sqrt{\sigma^2_{\rm meas} - \sigma^2_{\rm mod}}$, the difference between the measured and model velocity dispersion. The vertical dashed line shows the estimated sound speed in a typical H II region, c_s, treating the region as an ideal gas with temperature $T = 10^4$K.

outward sources of pressure to come predominantly from thermal gas pressure,

$$P_{\rm gas} = 2nkT, \tag{3.11}$$

internal turbulence in the region,

$$P_{\rm turb,int} = \frac{1}{2}\rho\sigma_{\rm t}^2, \tag{3.12}$$

and direct radiation pressure,

$$P_{\rm dir} = \frac{Qh\nu}{4\pi r^2 c}. \tag{3.13}$$

where Q is the ionizing photon production rate which we can estimate from the integrated [OIII] luminosity of the H II region:

$$Q = \frac{L_{\rm [OIII]}\lambda}{hc} = \frac{L_{\rm [OIII]}}{h\nu}. \tag{3.14}$$

Combining Equations 3.13 & 3.14 results in the formula for direct radiation pressure based on the

measured luminosity:

$$P_{\rm dir} = \frac{L_{\rm [OIII]}}{4\pi r^2 c}. \tag{3.15}$$

We use the definition of $r^*_{1/2}$ for the radius, r, k is the Boltzmann constant, and c is the speed of light. We are unable to directly measure the gas temperature, T, and number density, n, from our spectra so we use a constant temperature of $\mathrm{T} = 10^4\,\mathrm{K}$ and estimate n for each region from the Strömgren sphere approximation resulting in a median $\mathrm{n} \sim 20\,\mathrm{cm}^{-3}$. This is significantly lower than the $\sim 10^2\,\mathrm{cm}^{-3}$ density determined by Polles et al. (2019) from models of infrared cooling lines in five of the brightest H II region complexes which are also included in this study, suggesting that we may be underestimating the actual density in the assumption of a Strömgren sphere representation. To maintain internal consistency with other measured and estimated quantities we will proceed with density determined from our KCWI spectra with the caveat that this may result in an underestimate of $\mathrm{P_{gas}}$ and $\mathrm{P_{turb}}$. This estimated value of n is combined with the mass of the hydrogen atom to determine the value of ρ used in the calculation of $\mathrm{P_{turb,int}}$. The turbulent linewidth, $\sigma_{\rm t}$ is evaluated by removing the thermal sound speed from the measured velocity dispersion, $\sigma_{\rm t} = \sqrt{\sigma^2 - \mathrm{c_s^2}}$, with $\mathrm{c_s}$ is defined as:

$$c_{\rm s} = \sqrt{\frac{\gamma k T}{m_{\rm h}}} \tag{3.16}$$

where $\gamma = 5/3$ for an ideal gas.

The average values estimated for these pressure components are $\mathrm{P_{dir}} \sim 4 \times 10^{-14}\,\mathrm{dyne\,cm^{-2}}$, $\mathrm{P_{turb,int}} \sim 1 \times 10^{-11}\,\mathrm{dyne\,cm^{-2}}$, and $\mathrm{P_{gas}} \sim 5 \times 10^{-11}\,\mathrm{dyne\,cm^{-2}}$, making $P_{\rm gas}$ and $P_{\rm turb,int}$ the dominant factors in the outward pressure. One caveat is that the form of direct radiation pressure used here based on Q is specifically at the ionization front (McLeod et al., 2019). Another often used method to use the bolometric luminosity of all the stars in the region, which is estimated as $L_{\rm bol} \approx 138 L_{\rm H\alpha}$ (or $L_{\rm bol} \approx 138 L_{\rm [OIII]}$) (Lopez et al., 2014) in place of $L_{\rm [OIII]}$ in Equation 3.15. This would increase the impact of $\mathrm{P_{dir}}$, while still leaving it an order of magnitude less than $\mathrm{P_{gas}}$. However, there is some uncertainty in the correlation of $L_{\rm bol} \approx 138 L_{\rm H\alpha}$ based on the age and star formation history of a region. This could overestimate the bolometric luminosity for a young stellar

population like that of an H II region (Lopez et al., 2014). Further, there is some disagreement on whether this definition of radiation pressure traces the force that is actually exerted on the gas, as this may be lower than the pressure in an optically thin medium like the interior of an H II region (Pellegrini et al., 2011; Krumholz et al., 2014). Since both definitions produce a radiation pressure here that is sub-dominant compared to P_{gas} we will proceed with the definition based on $L_{[OIII]}$, but note that the uncertainty in the definition of P_{dir} may result in a less drastic difference in the sources of pressure.

An additional source of outward pressure that is not included here is the hot gas pressure observed in X-rays. A diffuse X-ray component is observed in this same region of IC 10 with an average temperature of $\sim 4 \times 10^6$ K (Wang et al., 2005). Determining the temperature and number density of the X-ray emitting gas at the resolution of individual H II regions needed to include in P_{out} at this scale is beyond the scope of this study, but it would likely provide a smaller contribution than P_{gas} as found in a sample of 32 LMC and SMC H II regions which show evidence of leakage of this hot gas (Lopez et al., 2014).

For the inward pressure we combine the contributions of pressure due to self-gravity,

$$P_{grav} = GM^2/4\pi r^4 \tag{3.17}$$

where $M = M_{HII}$, with external turbulent pressure, $P_{turb,ext}$, from the surrounding gas evaluated following Equation 3.12. We estimate this latter pressure source with $\sigma_{t,ext}$ evaluated in a 3.5 pc (3 pixel) border around each H II region with the sound speed removed in the same way as the internal turbulent linewidth. The density, ρ used in the external turbulent pressure is the same as its internal counterpart as we do not have a direct method of measuring the gas density. This should still provide a reasonable first order estimate that may even be conservative as Polles et al. (2019) find lower typical densities in modelled zones containing diffuse gas than the bright H II regions in IC 10. On average the difference ($P_{turb,ext}$-$P_{turb,int}$), or the resulting turbulent pressure, provides an inward pressure which is $\sim 500 \times P_{grav}$ due to the compact, low-mass nature of the

identified H II regions. As shown in Figure 3.20, 89% of the H II regions show $P_{out} > P_{in}$ with on average $P_{out} \sim 3P_{in}$. As these are all approximations it does not necessarily indicate that a given H II region exhibiting greater P_{out} will be expanding (and vice versa), but rather that it is likely that the majority of the H II regions in our sample are expanding into the ISM, especially since P_{out} can be considered a lower estimate with the exclusion of the hot gas pressure. This additional component would increase the inbalance towards greater P_{out} and increase the likelihood and/or strength of the H II region expansion.

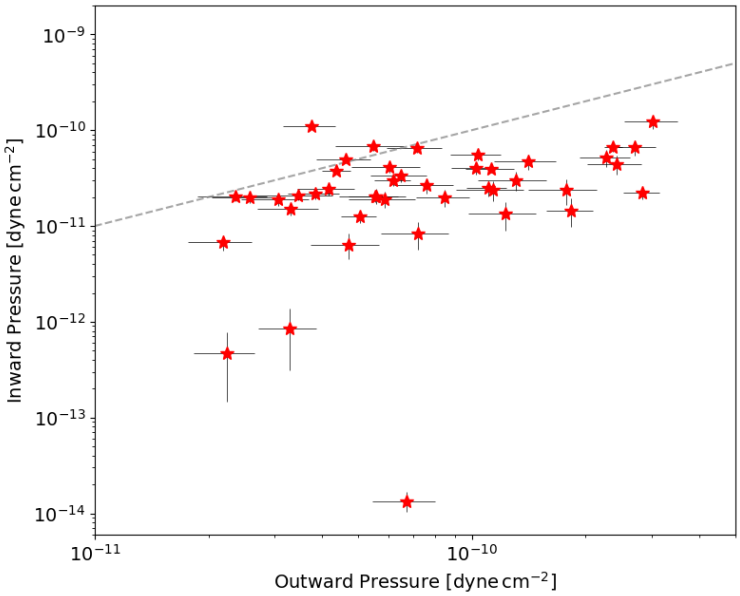

Figure 3.20: Comparison of inward and outward sources of pressure in the identified H II regions with the 1:1 line shown in gray. The inward pressure estimate is a sum of $P_{grav} + P_{turb,ext}$, while the outward estimate is a sum of $P_{gas} + P_{dir} + P_{turb,int}$. On average $P_{out} \sim 3P_{in}$, with 89% of the H II regions showing $P_{out} > P_{in}$.

Additionally, there are 6 H II regions where we find significantly elevated velocity dispersions at the region boundaries indicating the presence of outflows. These areas of elevated velocity dispersion are defined and identified using a similar method as identifying the H II regions described in Section 3.3.1. We use the `astrodendro` package along with the velocity dispersion map in Figure 3.13 to identify areas with a peak velocity dispersion $> 25 \mathrm{km\,s^{-1}}$ and a minimum of $21 \mathrm{km\,s^{-1}}$. These regions must also be resolved with a diameter greater than the FWHM measured from standard star observations. Of the regions identified with elevated velocity dispersion only

those located at the border of an H II region are considered as potential outflows. These outflows and the host H II regions are shown in Figure 3.21.

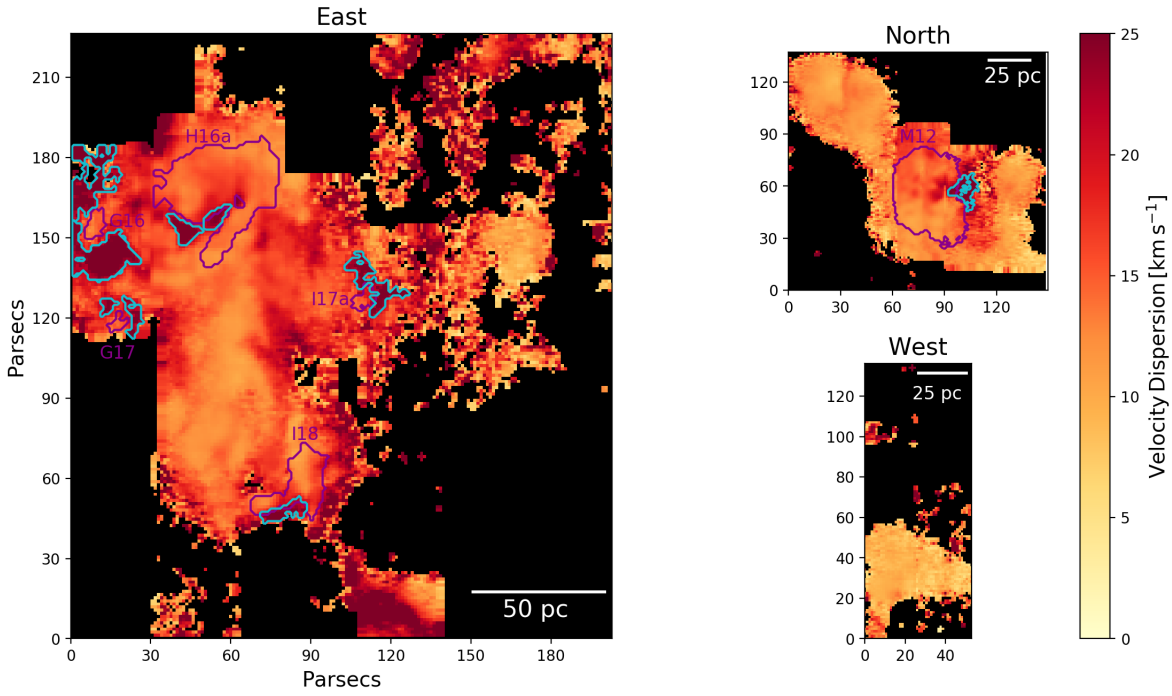

Figure 3.21: Maps of velocity dispersion of the ionized gas in IC 10 measured from Gaussian fits to the [OIII]5007Å line at each spaxel for the high resolution "small slicer, R∼18,000" observing mode. Each map is divided into the "North" portion of the FoV, the middle row shows the "West" field, and the bottom row shows the "East" region of the observed field. The purple contours mark the edges of the H II regions which are bordered by areas of elevated velocity dispersion which may be due to possible outflows, (outlined in cyan). These potential outflows must have a maximum velocity dispersion $\geq 25 \mathrm{km\,s^{-1}}$ and a minimum of $21 \mathrm{km\,s^{-1}}$. SNR >2 is required for these maps

We interpret the regions with elevated velocity dispersion as turbulent volumes. Turbulence is believed to decay on an eddy turnover time (roughly the crossing time of the turbulent region, l/σ), where l is the linear size of the turbulent region. Using the average properties measured from these turbulent regions of $l \approx 5.4\,\mathrm{pc}$ and $\sigma \approx 25.5\,\mathrm{km\,s^{-1}}$ the turbulence will decay over $2 \times 10^5\,\mathrm{yrs}$, much shorter than the lifetimes or ages of the H II regions. This raises the question of what powers the turbulence. We consider three possibilities: expansion of the H II regions causing outflows through lower density channels; photoionization heating of neutral gas; or stellar winds mixing with dense gas leading to turbulence.

In the simplest model we would expect all three of these mechanisms to act outward in a spherically symmetric zone around the central star cluster. However, H II regions do not typically exist in a medium of uniform density (e.g., Harper-Clark and Murray, 2009; Rogers and Pittard, 2013). There are holes and channels for outflowing gas to escape, which would produce isolated areas of increased turbulence rather than covering the entire perimeter, just as we see in these H II regions. This non-uniform density can clearly be seen from the irregular morphology of these 6 regions as well as the rest of IC 10's H II regions.

To first determine whether these regions of elevated velocity dispersion can be maintained by outflows generated from expansion of the observed H II regions, we compare the kinetic luminosity, $L_{\rm kin}$, inside the star-forming region with the turbulent luminosity, $L_{\rm turb}$ in the potential outflow.

The kinetic luminosity crossing the boundary of the H II region is

$$L_{\rm kin} \equiv \dot{E}_{\rm kin} = \frac{1}{2} M_{\rm H\,II} v_{\rm exp}^2 \frac{v_{\rm exp}}{r^*_{1/2}}, \tag{3.18}$$

where v_{exp} is the expansion velocity of the region defined as the half-width at zero intensity (HWZI)[3] of the emission line.

The turbulent luminosity in each elevated dispersion region is determined similarly from the rate of change of the kinetic energy attributable to turbulence, which we will refer to as $\dot{\rm E}_{\rm turb}$ to differentiate it from the internal H II region kinetic energy above. This is defined as follows:

$$L_{\rm turb} \equiv \dot{E}_{\rm turb} = \frac{1}{2} M_{\rm t} \sigma^2 \frac{\sigma}{l} \tag{3.19}$$

where $\rm M_t$ and σ are the ionized gas mass and velocity dispersion in the potential turbulent region, measured in the same way as their counterparts inside the H II regions and l is the average of the turbulent region major and minor axes. σ is measured from the Gaussian fit to [OIII]5007Å and $\rm M_t$ is calculated from the density determined via the Strömgren sphere approximation. This relies

[3]Note that the HWZI is proportional to the velocity dispersion, σ, but is a more physically intuitive way of denoting the expansion velocity as it captures the full range of velocities contributing to the Gaussian line profile.

on the assumption that most of the gas in the areas of elevated velocity dispersion is ionized, which may not be reliable outside of an H II region and particularly for the more extended areas of elevated dispersion. We may then be underestimating M_t and thus L_{turb}.

The second possible scenario for these turbulent regions at the edges of the identified H II regions are "champagne" or "blister" flows (e.g., Israel, 1978; Tenorio-Tagle, 1979) in which radiation from the central star cluster heats and ionizes neutral gas. This causes an area of overpressure, resulting in rapid expansion of the gas and could explain the observed elevated velocity dispersions. We estimate the amount of energy available for this mechanism from the type and number of ionizing stars in each H II region determined in Section 3.3.3. We take the effective temperature, $T_{\rm eff}$ for the stellar type from the models of Martins et al. (2005) for O stars and Smith et al. (2002) for B stars, combined with Wien's Law to estimate the wavelength at the peak of the black-body curve. We assume this represents the average energy of the emitted photons. We take the amount of energy above 13.6 eV as the energy imparted to the electron after ionizing a hydrogen atom. This is combined with the ionizing photon production rate for the determined stellar type and the number of stars required, $N_{\rm stars}$. This is 1 except for the case of H16a and M12 which require multiple O3 stars to produce the measured luminosity:

$$L_{\rm champagne} = \left(E_{\rm peak} - 13.6eV\right) Q N_{\rm stars} \tag{3.20}$$

where $E_{\rm peak}$ is the energy of a photon at the peak wavelength.

The third possible explanation for the observed velocity dispersions are winds from massive stars. This can result in turbulence at the interface of the hot wind and cold dense gas where mixing occurs and thermal energy is dissipated (Krumholz et al., 2019). The wind luminosity is described by the following equation

$$L_{\rm wind} = \frac{1}{2}\dot{M} V_{\rm wind}^2 N_{\rm stars} \tag{3.21}$$

where $\dot{M}$ is the mass loss rate in the stellar wind and $V_{\rm wind}$ is the wind speed. For the B0 star in H II region G17, $\dot{M}$ and $V_{\rm wind}$ are taken directly from the Smith et al. (2002) models. For the O stars in

the other 5 H II regions, these quantities are estimated from the stellar mass, M, luminosity, L, and radius, R, determined in the Martins et al. (2005) models. The wind velocity is then estimated as

$$V_{\rm wind} = 3\sqrt{2GM/R}, \tag{3.22}$$

with a maximum mass loss rate of

$$\dot{M} = \frac{L}{V_{\rm wind}c} \tag{3.23}$$

following Lamers and M. Levesque (2017).

The required $L_{\rm turb}$ as well as the luminosities available from each scenario to power the observed turbulence are reported in Table 3.5. It should be noted that each of these scenarios assumes a spherically symmetric deposition of energy and thus should be multiplied by the factor, Ω, the fraction of a sphere covered by the outflow as seen from the stars, determined from the ratio of the projected area of the outflow and H II region. If the luminosity available in the outflow mechanism multiplied by Ω is greater than $L_{\rm turb}$, it indicates that the mechanism could provide sufficient energy to support the energy dissipated in the turbulent region.

For the three largest regions with potential outflows, H16a, I18, and M12 $L_{\rm kin}\Omega > L_{\rm turb}$ with H16a $L_{\rm kin}\Omega \sim 1.5L_{\rm turb}$, M12 with $L_{\rm kin}\Omega \sim 3L_{\rm turb}$, and $L_{\rm kin}\Omega \sim L_{\rm turb}$ for I18. However, for these same three H II regions the early O stars needed to produce the measured $L_{\rm [OIII]}$ produce estimated $L_{\rm wind}$ and $L_{\rm champagne}$ that are greater than $L_{\rm kin}$. For region I18 which requires a single O5 star, $L_{\rm wind} \sim 2 \times L_{\rm kin}$ while $L_{\rm wind} \sim 10 \times L_{\rm kin}$ for H16a and M12 which require multiple O3 stars. In all three of these H II regions, $L_{\rm champagne}$ is estimated to be $\sim$2 orders of magnitude greater than $L_{\rm kin}$. This scenario of observing champagne flows in the turbulent regions around these 3 H II regions is therefore the most likely.

For the three smaller regions, G16, G17, and I17a, $L_{\rm kin}$ is not high enough to sustain the turbulence we see. This is unsurprising as the turbulent regions are comparable in size or larger than the H II region they border (see Figure 3.21). G16 and I17a both require a single O9 star to produce the required ionization, and the estimated winds from this type of star produce

$L_{\rm wind}\Omega \sim 100 - 1000 \times L_{\rm turb}$ indicating that stellar winds are a possibly sufficient source of energy to sustain the turbulent regions around G16 and I17a. For G17, none of three scenarios considered here produce a sufficient amount of energy to support the measured turbulence in the surrounding region. While these estimates are approximate, this along with the extended nature of the turbulence around G17 indicate an external source of energy.

Table 3.5: Outflow Properties

			Turbulent Region				H II Region				
ID	radius (pc)	stellar type	σ ($\mathrm{km\,s^{-1}}$)	$\tau_{\rm eddy}$ (10^6 yrs)	$L_{\rm turb}$ ($\mathrm{erg\,s^{-1}}$)	Ω	$v_{\rm exp}$ ($\mathrm{km\,s^{-1}}$)	$\tau_{\rm dyn}$ (10^6 yrs)	$L_{\rm kin}$ ($\mathrm{erg\,s^{-1}}$)	$L_{\rm champagne}$ ($\mathrm{erg\,s^{-1}}$)	$L_{\rm wind}$ ($\mathrm{erg\,s^{-1}}$)
G16	2.60	O9	27.12	0.35	1.94×10^{36}	0.30	44.06	0.07	4.08×10^{35}	5.99×10^{35}	6.31×10^{38}
G17	2.11	B0	22.92	0.11	1.59×10^{35}	0.19	44.05	0.05	2.44×10^{35}	-2.73×10^{35}	5.46×10^{34}
H16a	10.32	O3	25.98	0.11	7.02×10^{35}	0.03	51.65	0.22	3.27×10^{37}	3.06×10^{39}	1.40×10^{38}
I17a	2.56	O9	25.31	0.24	3.27×10^{35}	0.20	51.76	0.06	7.70×10^{35}	5.99×10^{35}	6.31×10^{38}
I18	7.02	O5	25.19	0.15	2.12×10^{35}	0.05	46.02	0.17	3.84×10^{36}	1.13×10^{38}	7.04×10^{36}
M12	9.24	O3	27.01	0.19	4.79×10^{35}	0.08	45.17	0.23	1.82×10^{37}	2.29×10^{39}	1.05×10^{38}

Note. — Measured properties and estimated energies in the turbulent regions and associated H II regions. *a:* The negative value of $L_{\rm champagne}$ for region G17 is due to the method of estimation (Equation 3.20). The peak photon energy for a B0 star used to estimate the average is < 13.6eV, giving a negative estimate of $L_{\rm champagne}$. This merely indicates that the turbulent region observed is unlikely to be due to a champagne flow.

3.3.6 Metallicity

The KCWI small slicer, R$\sim$18,000 mode observations used throughout this analysis provide a detailed look at the structure and kinematics of the ionized gas, but the wavelength coverage is extremely limited. Our supplementary observations in the large slicer, R$\sim$900 mode rectify this shortcoming with coverage from 3500-5500Å, at the expense of more limited spatial sampling and spectral resolution. This wavelength range allows us to estimate the gas-phase metallicity throughout IC 10. Ideally, the auroral [OIII]4363Å line would be used with [OIII]5007Å to infer the electron temperature and metallicity (e.g., Kewley et al., 2019), but this is a very weak emission line and is unfortunately not detected in our stacked or individual spaxel spectra. Instead, we use the empirical R_{23} strong line calibration. The commonly used R_{23} was proposed by Pagel et al. (1979) as a calibration with the oxygen abundance as it is less sensitive to geometric factors than

the [OIII]/Hβ ratio alone. It is defined as:

$$R_{23} = \frac{F([OII]3727,3729\text{Å}) + F([OIII]4959\text{Å}) + F([OIII]5007\text{Å})}{F(H\beta)} \tag{3.24}$$

One caveat with this diagnostic is that it is degenerate, providing two possible values of the metallicity for a given R_{23}. Another diagnostic ratio is therefore required to determine the correct solution. These nebular ratios often make use of the [NII]6584Å line (Nagao et al., 2006), but since this is not in the observed wavelength range we will instead use the line flux ratios utilizing [OIII]5007Å, [OIII]4959Å, and the [OII]3727,3729Å doublet; an indicator of the ionization parameter.

After applying the dereddening correction and DIG subtraction described in Section 3.3.2, we employ a similar fitting method as for the [OIII]5007Å/Hβ line ratio at each spaxel: fitting a Gaussian profile to the Hβ line and using the center to define the systemic velocity shift at that spaxel and the width to define the number of wavelength channels over which to integrate the emission line fluxes. These fluxes are determined by a direct sum of the flux at that wavelength channel in the spectrum rather than integrating over the fitted Gaussian so as not to skew the resulting flux of the [OII]3727,3729Å doublet by the fitting of a single Gaussian. Defining the same central velocity and line width ensures that each line flux is evaluated over the same gas column. Any spaxel with a SNR of the [OII]3727,3729Å doublet ($SNR_{[OII]} < 3$ is removed from the analysis. Due to this cut only the "East" (lower left) portion of the field covering the HL111 and HL106 complexes of Hodge and Lee (1990) is included here and shown in Figure 3.22, with the vast majority of this field showing $SNR_{[OII]} > 4$.

There are a number of calibrations in the literature utilizing the R_{23} parameter, but we will limit our discussion to just three: the theoretical calibration of Kobulnicky and Kewley (2004) (hereafter KK04), and empirical calibrations from Pilyugin and Thuan (2005) (PT05) and Nagao et al. (2006) (N06). Both the KK04 and PT05 calibrations rely on separate equations for what are referred to as the "upper" and "lower" branches of the diagnostic, while N06 uses a single continuous calibration. All three employ a diagnostic ratio involving one or more [OIII] lines and [OII]3727,3729Å in addition to R_{23}.

The KK04 equations for oxygen abundance on each branch are dependent on R_{23} as well as the ionization parameter, q, which is in turn dependent on the oxygen abundance and O_{32}, defined as:

$$O_{32} = \frac{F([OIII]4959\mathring{A}) + F([OIII]5007\mathring{A})}{F([OII]3727,3729\mathring{A})} \tag{3.25}$$

Since the equations for oxygen abundance and ionization parameter are dependent on each other this method requires an iterative solution, but the result converges after a few iterations. The transition between the two branches is noted to be at $12 + \log(\mathrm{O/H}) = 8.4$. This is slightly higher than the global metallicity typically measured for IC 10 at $12 + \log(\mathrm{O/H}) \sim 8.2$ (e.g., Skillman et al., 1989; Lebouteiller et al., 2012), making the lower branch likely a better match.

The PT05 calibration does not require iteration, with each branch simply being dependent on the value of R_{23} and the line ratio P:

$$P = \frac{F([OIII]4959\mathring{A}) + F([OIII]5007\mathring{A})}{F([OIII]4959\mathring{A}) + F([OIII]5007\mathring{A}) + F([OII]3727,3729\mathring{A})} \tag{3.26}$$

For this calibration there is a "transition zone" between $8.0 < 12 + \log(\mathrm{O/H}) < 8.5$ where the lower branch applies for values < 8.0 and the upper branch applies for values > 8.5. This transition zone does fall at the expected metallicity for IC 10, so the results from this method should be taken with caution.

The N06 calibration, by contrast does not have a separate equation for the upper and lower branches. The equation for the oxygen abundance is also only dependent on the value of R_{23}, however the solution is double valued, relying on the [OIII]5007Å/[OII]3727,3729Å (or other) line ratio to break this degeneracy. We evaluate the oxygen abundance in our IC 10 field using this method to determine the most likely solution for each spaxel independently and also by constraining the solution for the entire field to either the upper or lower portion of the curve, mimicking the two branches of the KK04 and PT05 methods.

The results for all three calibrations and the branches of each are summarized in Table 3.6 which includes the mean metallicity throughout the field, for spaxels inside detected H II regions, and for spaxels outside H II regions. The upper branch solutions seem to systematically

overestimate the oxygen abundance, a not unexpected result given the low global metallicity of IC 10. The continuous N06 calibration gives an unrealistic result when the degeneracy is broken at each spaxel based on the [OIII]/[OII] ratio, resulting in an abrupt jump from low to high solutions at the edges of H II regions rather than a smooth transition. Even when constrained to the lower solutions, the N06 calibration appears to give less realistic estimates with a ~ 0.9dex lower average metallicity than the previous estimates for IC 10.

Table 3.6: Metallicity Calibration Results

Method	Mean Inside Regions $12+\log(\mathrm{O/H})$	Mean Outside Regions $12+\log(\mathrm{O/H})$	Total Mean $12+\log(\mathrm{O/H})$
	Lower Branch		
KK04	8.14 ± 0.01	8.26 ± 0.02	8.22 ± 0.02
PT05	7.76 ± 0.01	7.89 ± 0.03	7.85 ± 0.03
N06[a]	7.50 ± 0.01	7.53 ± 0.01	7.52 ± 0.01
	Upper Branch		
KK04	8.85 ± 0.01	8.79 ± 0.01	8.81 ± 0.01
PT05	8.40 ± 0.01	8.22 ± 0.02	8.27 ± 0.02
N06[a]	8.61 ± 0.01	8.58 ± 0.01	8.59 ± 0.01
	Continuous Calibration		
N06	8.26 ± 0.03	8.10 ± 0.04	8.13 ± 0.04

Note. — Average oxygen abundance derived from the three different calibrations for the upper and lower branches. The means are derived inside and outside the contours of the identified H II regions as well as over all spaxels. The lower branches of the PT05 and KK04 branches provide the most reasonable solutions for the metallicity given the existing global measurements of IC 10 which are below the branch transitions. The results from these two methods likely bracket the true metallicity. [a]:The "upper" and "lower" branches of the N06 calibration are evaluated from the same equation with the root in the desired range taken as the solution rather than using the [OIII]5007Å/[OII]3727,3729Å line ratio to break the degeneracy.

The lower branches of the KK04 and PT05 calibrations give the most reasonable results for the metallicity throughout this field of view in IC 10 with average metallicities $12+\log(\mathrm{O/H})_{\mathrm{PT05,lower}} \approx 7.85 \pm 0.03$ and $12+\log(\mathrm{O/H})_{\mathrm{KK04,lower}} \approx 8.22 \pm 0.02$. There is a well stud-

ied offset between these two calibrations and it is thought that they span the range of potential "true" values (e.g., Moustakas et al., 2010; Kewley and Ellison, 2008), making this 0.4dex range a good indicator of the likely metallicity in this region of IC 10. While the values differ, the variation in metallicity across the field is consistent between both the KK04 and PT05 results. With both calibrations there is an average $\sim$0.1dex lower metallicity inside the H II regions than in the surrounding gas. On average this difference is within the uncertainties, with some areas of higher metallicity in the diffuse gas being more apparent in the maps of Figure 3.22. This trend is consistent with the study by McLeod et al. (2019) of two H II region complexes in the LMC in which they find lower oxygen abundance within the compact H II regions than elsewhere in the complex. The difference in metallicity in this study is larger than in IC 10, although the authors note that there is a dependence in their calibrations on ionization parameter (as the MUSE spectra do not cover [OII]3727Å needed for R_{23}) and the abundances may therefore be underestimated in the H II regions. An earlier study by Russell and Dopita (1990) also found slightly lower metallicity in individual H II regions in the SMC and LMC (0.1dex and 0.22dex respectively) than the global measurements. Deeper and wider field observations in IC 10 and other local galaxies are needed in order to form a clearer picture of the metallicities of H II regions relative to the surrounding gas.

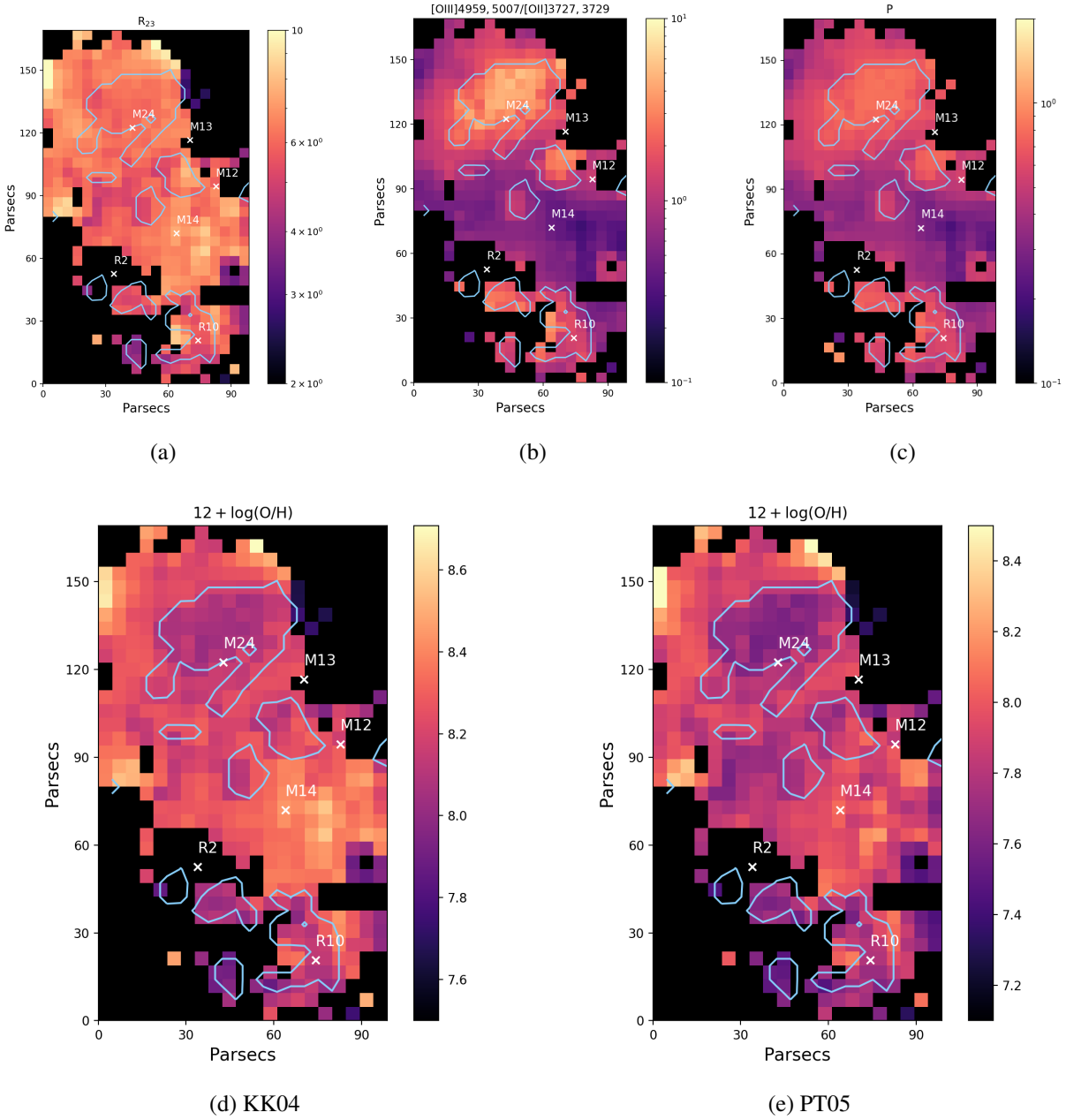

(a) (b) (c)

(d) KK04 (e) PT05

Figure 3.22: Diagnostic line ratio maps from the "large slicer, R∼900" mode observations. Due to the lower SNR of the [OII]3727Å line only the lower left portion of the field is shown, coinciding with the "East" field of the high resolution observations discussed in the majority of this study. (a): R_{23} metallicity diagnostic. (b): O_{32} line ratio (Equation 3.25) used in the KK04 metallicity calibration. (c) P line ratio (Equation 3.26) used in the PT05 calibration. (d) Metallicity as determined by the KK04 diagnostic. (e) Metallicity as determined by the PT05 diagnostic. The metallicities are systematically lower than in the KK04 map, but the locations of lower *relative* metallicity are consistent. The H II regions identified in the high resolution mode are shown with the light blue contours (binned to the resolution here) and the locations of known WR stars are marked with white X's.

3.3.7 Diffuse Ionized Gas

A significant fraction of the ionized gas emission in star forming galaxies has been observed outside of the H II regions in the DIG. Often studies will differentiate the DIG from the star formation based on the Hα surface brightness. For example, in a sample of 109 galaxies, Oey et al. (2007) attribute $\sim$60% of the Hα flux to the DIG with no correlation based on the galaxy Hubble type. Lacerda et al. (2018) on the other hand, propose a system of differentiating the DIG based on the equivalent width instead. They do find a correlation in the DIG fraction with Hubble type, with the highest contribution in ellipticals and lowest in late type galaxies, resulting in a similar average DIG fraction but with a wide distribution, $56\% \pm 38\%$. Part of the cause for the differing conclusions from these two large studies is likely due to the two methods of differentiating DIG from star forming regions.

Before the identification and spectral analysis of IC 10's H II regions we performed a conservative subtraction of the DIG contribution based on the choice of a low surface brightness region free of known H II regions. This resulted in an average DIG contribution of $\sim$21% of the [OIII]5007Å flux per spaxel across the FoV, with only $\sim$1% at the H II regions. Of the total [OIII]5007Å flux observed in our FoV, 78% is contained in the H II regions, 20% in the connecting complexes, and the remaining 2% from the DIG. This is significantly lower than what would be expected for the overall DIG contribution in IC 10, but our field of view intentionally selected an area dense with H II regions and complexes. To estimate the flux contribution of these three components throughout IC 10 as a whole the measured flux is scaled based on the ratio of the number of H II regions observed to total identified previously in IC 10 (Hodge and Lee, 1990) and the ratio of area observed to total area. This reduces the total estimated flux contribution from H II regions to only 26%, complexes to 7%, and increases the estimated DIG contribution to 57% throughout IC 10. This estimate for the galaxy as a whole is more in line with values seen in previous studies for the DIG contribution to galaxy flux (e.g., Oey et al., 2007), but highlights the irregular distribution of H II regions and DIG in irregular galaxies such as IC 10.

We differentiate the H II regions and DIG based on the ionized gas surface brightness, but

compare the equivalent width between these areas of emission. Interestingly we find no significant difference between the distribution of Hβ equivalent width between spaxels identified as belonging to an H II region and that belonging to DIG in IC 10. This may be a selection effect of our study. The high density of H II regions not only gives a small sample of diffuse gas, but also makes it likely to be more closely associated with the inter-dispersed H II regions than is typical of DIG studies. However, the DIG in IC 10 may be ionized by different sources than typically observed. (Hidalgo-Gámez, 2005) finds higher excitation in the IC 10 DIG than for spiral galaxies which they find can be produced by leakage from H II regions and the large number of WR stars. The gas throughout IC 10, and particularly in the KCWI FoV, may be more similar to what Lacerda et al. (2018) refers to as mDIG, or 'mixed' DIG in which the ionization source is due to a combination of processes such as emission from an older stellar population in addition to photon leakage from H II regions. This is consistent with the small difference in metallicity we see between the H II regions and surrounding gas in comparison with other studies, as well as Polles et al. (2019) Cloudy simulations showing matter-bounded regions in IC 10 which would result in escaping photons ionizing the DIG.

3.3.8 Scaling Relations

In Cosens et al. (2018) we developed a framework to use Bayesian inference via PyStan to fit the scaling relationships between the properties of local and high-redshift star-forming regions in the literature. In this study we focused primarily on the relationship between star forming region size and Hα luminosity ($L_{H\alpha}$), which takes on the form of a power law:

$$L_{\mathrm{H}\alpha} = exp(\beta) r_{\mathrm{clump}}^{\alpha} \tag{3.27}$$

with r_{clump} giving the radius of the star forming region and β giving the intercept of the fit. The key model parameter of interest is the slope, α. The value of this slope holds information about the driving formation mechanism of the star-forming regions. A slope of r^3 is often explained by a region which forms under Jeans collapse and is then well-represented by a Strömgren sphere. On

the other hand, a slope of r^2 is often explained by a region which forms under Toomre instability and undergoes the fastest mode of Jeans collapse resulting in a different form for the characteristic mass and size (e.g., Genzel et al., 2011). In Cosens et al. (2018) we found that this r^2 slope could also be explained by a Strömgren sphere argument where the ionizing photon production rate is large enough that the radius of the region is larger than the scale height of the galaxy disk. This would lead to a non-spherical geometry and an observed relationship of $L \sim r^2$.

Using Bayesian inference provides a number of advantages over standard least-squares fitting. First, uncertainties in every dimension can be incorporated in the fitting; there is no need to estimate a single overall uncertainty assigned to one dimension. Second, we can use our existing knowledge of the scaling relationships between parameters to inform our model through the use of Bayesian priors. Third, this method reproduces a distribution for each model parameter, allowing the determination of not only the best fit model, but robust determination of uncertainties for each model component as well. Using this framework allowed us to perform robust fits to the overall scaling relationships as well as investigate potential differences in smaller subsamples such as redshift bins and lensed versus field galaxies. Interestingly, we were able to identify a possible break in the size-luminosity scaling relationship based on the $\Sigma_{\rm SFR}$ of the star-forming region.

However, a key missing area of the parameter space in our previous investigation was small, low $L_{H\alpha}$ star-forming regions (< 50 pc, $< 10^{34-36}$ erg s^{-1}). This sets the limit on the low-mass end of the relationship and helps to constrain the intercept when performing fits. One challenge in interpreting fitting results for sub samples of the local and high-redshift clumps was that the best fit slope and intercept are not entirely independent parameters. Therefore, missing constraints on the low-mass intercept of the size-luminosity relationship makes it difficult to be certain whether a change in slope is really a change in that parameter or just in the lever arm of the fit. With the proximity of IC 10 and the sensitivity of KCWI we are able to target a large sample of H II regions at this crucial scale.

3.3.8.1 Size-Luminosity Relationship

While these small, low-mass star-forming regions are critical for constraining the intercept of the size-luminosity relationship, one must first check that the possibility of stochastic sampling is not biasing the measured properties. The lower mass limit to avoid stochastic effects is typically determined to be $M_* \sim 10^3 M_\odot$ (e.g., Hollyhead et al., 2015; Krumholz et al., 2015). Below these masses random sampling of the IMF can lead to deviations between the actual physical properties and those determined from photometric measurements. The average stellar mass distribution determined for the IC 10 H II regions from the measured [OIII]5007Å flux is $M_* \sim (4 \pm 14) \times 10^2\, M_\odot$, with 96% falling below the $10^3 M_\odot$ limit. Further, IC 10's H II regions are largely consistent with ionization predominantly from a single O or B type star which will be stochastic by nature. Hannon et al. (2019) found themselves faced with a similar dilemma studying a sample of ∼700 young star clusters with over 90% below the stochastic limit. They investigate a method of mitigating the impact of stochastic sampling by stacking the fluxes of individual clusters with similar properties. These composite clusters no longer fall into the regime of stochastic sampling, but Hannon et al. (2019) still find results consistent with the individual clusters. We apply a similar check to our sample, but rather than stacking the H II region spectra, we instead make use of the hierarchical structure determined from `astrodendro` which identifies the H II region complexes. Using the complexes results in a smaller sample than with individual regions, but one that lies above the stochastic limit with a mean $M_* \sim 2 \times 10^3 M_\odot$. We do not find any significant deviation in the trends determined for the complexes vs. the individual H II regions, finding proportional increases in the mass and luminosity to the increase in radius (e.g., Figure 3.23). The measured properties of individual regions may show an increase in scatter due to stochastic sampling, but the average sample properties and trends do not appear to be affected. Therefore we will proceed with the determination of the scaling relationships using the individual regions in the fitting, but we will include the complexes in all figures for comparison.

Fitting the size-luminosity relationship using our MCMC framework with just IC 10 H II regions yields a slope of $L_{H\alpha} \propto r_{clump}^{3.6}$. The complexes do shift to slightly larger radii than the

individual H II regions but with a proportional increase in luminosity, placing them along the same relationship. We also combine these regions with the full sample of H II regions and high-redshift clumps outlined in Cosens et al. (2018), now including additional published samples of star-forming regions in the SMC (Kennicutt and Hodge, 1986), LMC (Ambrocio-Cruz et al., 2016), NGC6822 (Hodge et al., 1989), and local LIRGs (Zaragoza-Cardiel et al., 2017; Larson et al., 2020). These LIRG studies also make use of `astrodendro` to identify star-forming regions and their properties[4]. Collating all low and high-redshift samples results in a significantly shallower slope of approximately $L_{H\alpha} \propto r^3$; matching the result of fitting the full sample in Cosens et al. (2018) and indicating the IC 10 H II regions may be an outlier. The IC 10 fit and entire sample fit are shown in Figure 3.23, where it can be can see that the IC 10 H II regions lie above the size-luminosity relation found for the full sample. This is also true of some other local samples, particularly in more extreme environments such as the LIRGs (e.g. Larson et al., 2020) and turbulent galaxies (Fisher et al., 2017). Whether the offset of the IC 10 H II regions is then due to improved resolution breaking the IC 10 regions down into more compact components, or due to a fundamental difference in the environments of star-forming regions driving scatter in the scaling relationships is not fully clear. It may be that active expansion of these regions as discussed in Section 3.3.5 leads to the offset we see here with the H II regions currently being under-sized for their luminosity.

The full results of these fits and those described in Section 3.3.8 are shown in Table 3.3.8 for the intercept, slope, and intrinsic scatter along with their uncertainties. Results of fitting additional data subsets (as detailed in column 1) are also included for completeness.

[4]The effective radii, r_{eff}, of Zaragoza-Cardiel et al. (2017) are adjusted to match our definition of $r^*_{1/2}$ for a consistent comparison.

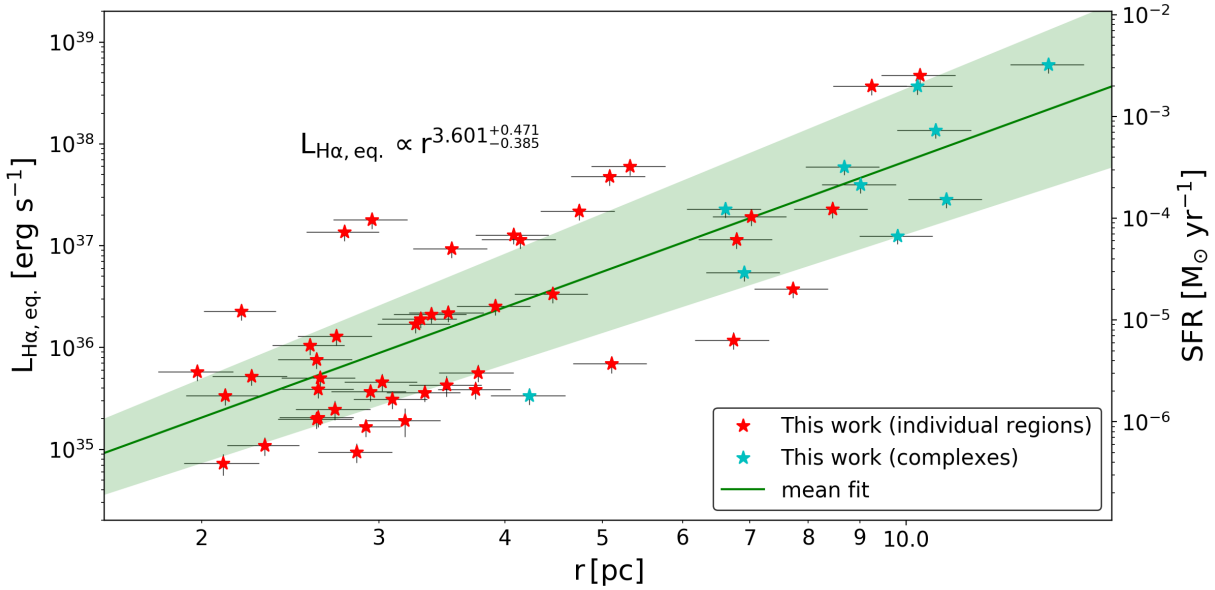

(a)

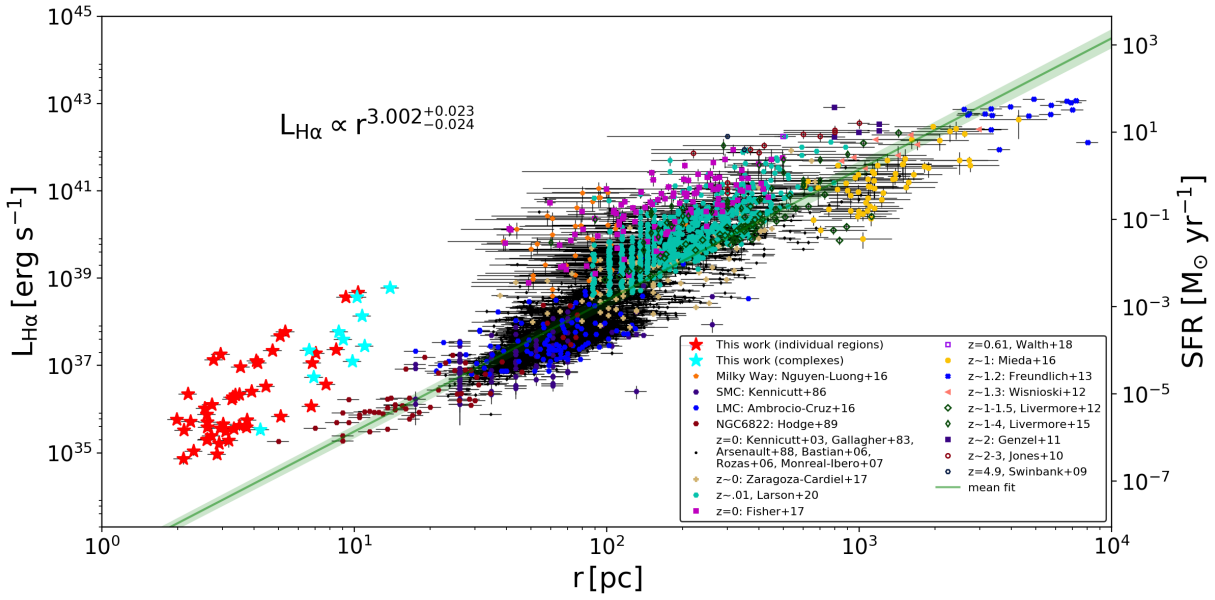

(b)

Figure 3.23: (a): Results of fitting the size-luminosity scaling relationship for IC 10 H II regions identified in our KCWI observations. (b): Results of fitting the size-luminosity scaling relationship for IC 10 H II regions (red stars) as well as the rest of the local and high-redshift sample. The IC 10 region complexes are shown for comparison (cyan stars) but are not included in the determination of the fit.

Table 3.7: Size - Luminosity Relation Fit Parameters: ($L_{H\alpha} = e^{\beta} r_{clump}^{\alpha}$)

Sample	Subset Criteria	Figure	α	β	Scatter (r)	Scatter (L)	# of Clumps
IC 10	···	3.23	$3.601^{+0.471}_{-0.385}$	$78.812^{+0.455}_{-0.652}$	$0.147^{+0.154}_{-0.103}$	$0.156^{+0.144}_{-0.103}$	46
all comparisons	···	···	$3.215^{+0.023}_{-0.030}$	$73.782^{+0.129}_{-0.119}$	$0.184^{+0.118}_{-0.112}$	$0.171^{+0.115}_{-0.114}$	3858
	high Σ_{SFR}	···	$1.788^{+0.063}_{-0.059}$	$84.617^{+0.314}_{-0.357}$	$0.461^{+0.317}_{-0.316}$	$0.470^{+0.320}_{-0.314}$	264
	low Σ_{SFR}	···	$2.967^{+0.024}_{-0.027}$	$74.670^{+0.123}_{-0.111}$	$0.142^{+0.092}_{-0.095}$	$0.136^{+0.092}_{-0.093}$	3573
IC 10 & all comparisons	···	3.23	$3.002^{+0.023}_{-0.024}$	$74.800^{+0.100}_{-0.115}$	$0.240^{+0.147}_{-0.154}$	$0.249^{+0.154}_{-0.151}$	3904
	high Σ_{SFR}	3.24	$1.841^{+0.070}_{-0.059}$	$84.310^{+0.335}_{-0.384}$	$0.426^{+0.279}_{-0.285}$	$0.360^{+0.323}_{-0.268}$	266
	low Σ_{SFR}	3.24	$2.775^{+0.021}_{-0.018}$	$75.577^{+0.086}_{-0.090}$	$0.194^{+0.136}_{-0.132}$	$0.194^{+0.132}_{-0.138}$	3617

Note. — Results of model parameters determined from MCMC fitting of IC 10 H II regions and the local and high-redshift comparison sample for all fits discussed in Section 3.3.8 as well as additional fits to only the comparison sample (rows 2-4).

3.3.8.2 Σ_{SFR} break

In Cosens et al. (2018), we found that there was a potential break in the size-luminosity relationship that divides star-forming regions into two samples: one with high Σ_{SFR} and one with low Σ_{SFR} with the break nominally located at a value of $\Sigma_{SFR} = 1\,M_{\odot}\ yr^{-1}\ kpc^{-2}$. Both locally and at high redshift we found that lower Σ_{SFR} star-forming regions followed a size-luminosity relationship of $L \sim r^3$, while the high Σ_{SFR} sub-sample followed a relationship closer to $L \sim r^2$.

In our observations of IC 10's H II regions, the average size of identified H II regions is $r_{avg} = 4.0\,pc$ with a $\Sigma_{SFR,avg} = 0.20\,M_{\odot}\ yr^{-1}\ kpc^{-2}$ with only 2 identified H II regions falling above the $\Sigma_{SFR} > 1\,M_{\odot}\ yr^{-1}\ kpc^{-2}$ limit. When combined with the full comparison sample this does still provide some improvements on constraining the size-luminosity relationship at low masses by reducing the uncertainties on the fitted parameters. The resulting slopes for the two populations remain consistent with the previous results, with nominal values differing by $< 2\sigma$.

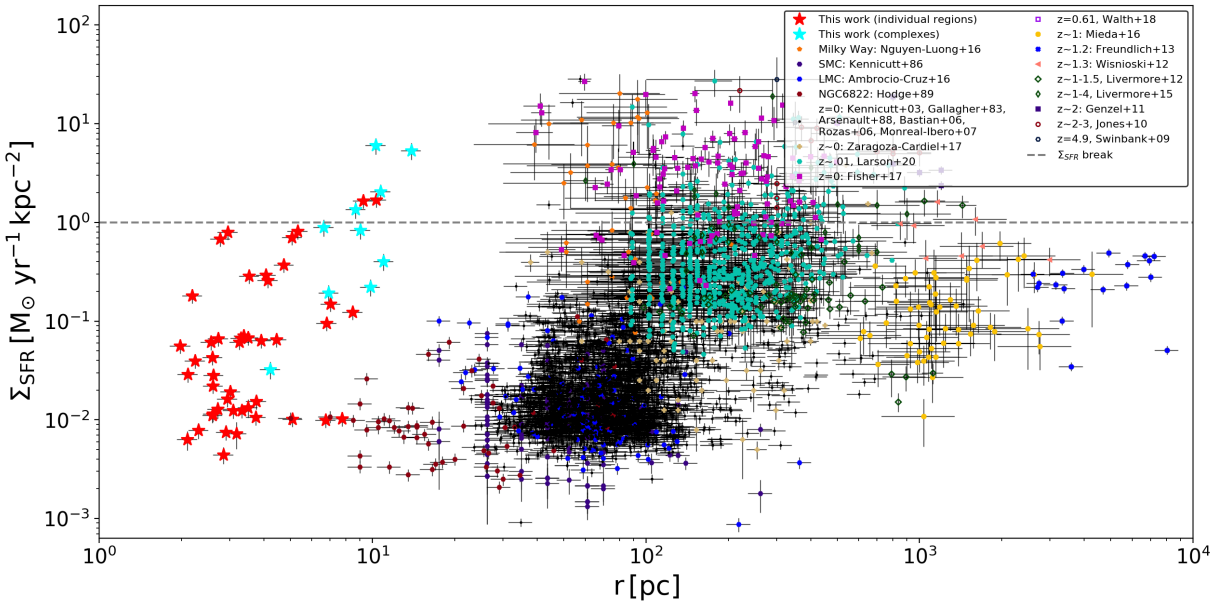

(a)

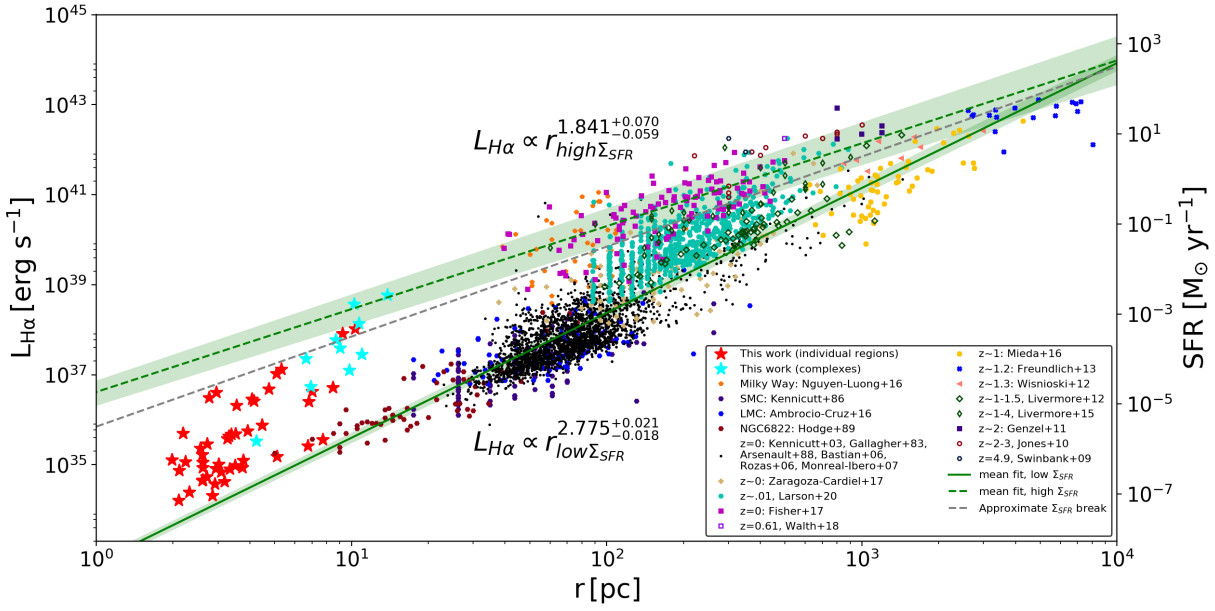

(b)

Figure 3.24: (a): Size vs. $\Sigma_{\rm SFR}$ for H II regions identified in our observations of IC 10 as well as each comparison sample. These data are divided into high and low $\Sigma_{\rm SFR}$ based on a break at $\Sigma_{\rm SFR} = 1\,{\rm M}_\odot\ {\rm yr}^{-1}\ {\rm kpc}^{-2}$(dashed line). (b): Results of fitting the size-luminosity scaling relationship for these two groups. The low $\Sigma_{\rm SFR}$ subset tends towards a slop of $L \sim r^3$, while the high $\Sigma_{\rm SFR}$ subset produces a slope closer to $L \sim r^2$. The IC 10 region complexes are shown for comparison (cyan stars) but are not included in the determination of the fit.

3.3.8.3 Size - Velocity Dispersion

Larson (1981) found an empirical relationship between the size of molecular clouds and their velocity dispersion that is tied to turbulence in the clouds and ISM. For resolved Milky Way GMCs in virial equilibrium, Larson (1981) found a relationship:

$$\sigma = 1.1 r^{0.38} \tag{3.28}$$

where r is the radius of the GMC in pc and σ is in $\mathrm{km\,s^{-1}}$. This has been refined and updated with expanded galactic (Solomon et al., 1987) and extra-galactic (Bolatto et al., 2008) data sets of molecular clouds, arriving at slight changes to the scaling but the same basic conclusion that the line width increases with cloud size approximately $\propto \mathrm{r}^{1/2}$. This scaling is typically interpreted as being due to turbulence in the molecular clouds (e.g., Larson, 1981; Bolatto et al., 2008).

While Larson's Law is usually discussed in relation to GMCs it may also apply to ionized gas in star-forming regions if they are in virial equilibrium and exhibit turbulent motions. Wisnioski et al. (2012) fit this relationship with a portion of the local and high-redshift data sets used in the present study and find a scaling of $\sigma \propto r^{0.42}$, but determine that their $\mathrm{z} \sim 1$ clumps are likely not virialized. We test this now with the addition of local and high-z star-forming regions measured with IFS observations since the study by Wisnioski et al. (2012). Unfortunately, not all data sets used to investigate the size-luminosity relationship have spectral information, but it is still a large enough sample (515 regions) to investigate the presence of a similar size-velocity dispersion relationship. In fact, we do see a clear trend where the velocity dispersion increases with larger size regions, except with IC 10, which is still a notable outlier. On their own, IC 10 H II regions do not show any evidence of this power law scaling, and instead when included significantly skew the resultant slope. Without IC 10 included we arrive at a relationship of $\sigma \propto r^{0.4}$ using the same MCMC framework as described in Section 3.3.8, in line with the results of Wisnioski et al. (2012) and similar to the GMC results. However, when the IC 10 H II regions are included, they clearly lie above the size - σ relationship found for the other samples as shown in Figure 3.25. Furthermore, including the IC 10

regions in the fitting reduces the slope to $\sigma \propto r^{0.2}$. This further supports the conclusion in Sections 3.3.4 & 3.3.5 that the H II regions identified in this study are not generally virialized. In fact, if we retain only the component of velocity dispersion due to rotational motion as identified in Section 3.3.5, then the identified H II regions in IC 10 follow the same relationship identified for the rest of the samples (see Figure 3.25b). There is a significant amount of scatter in the r $-$ σ relationship, but it suggests that rotational motion is a much more significant source of the measured line widths in the other star-forming regions than in IC 10's H II regions.

Table 3.8: Size - Velocity Dispersion Relation Fit Parameters: ($\sigma = \beta r_{clump}^{\alpha}$)

Sample	Figure	α	β	Scatter (r)	Scatter (σ)	# of Clumps
all comparisons	3.25b	$0.406^{+0.025}_{-0.025}$	$3.704^{+1.129}_{-1.154}$	$0.444^{+0.288}_{-0.276}$	$0.414^{+0.275}_{-0.294}$	469
IC 10 & all comparisons	3.25a	$0.216^{+0.013}_{-0.012}$	$10.442^{+1.072}_{-1.060}$	$0.262^{+0.165}_{-0.171}$	$0.257^{+0.176}_{-0.172}$	515

Note. — Results of model parameters determined from MCMC fitting of IC 10 H II regions and the local and high-redshift comparison sample for the size-velocity dispersion relationship discussed in Section 3.3.8.

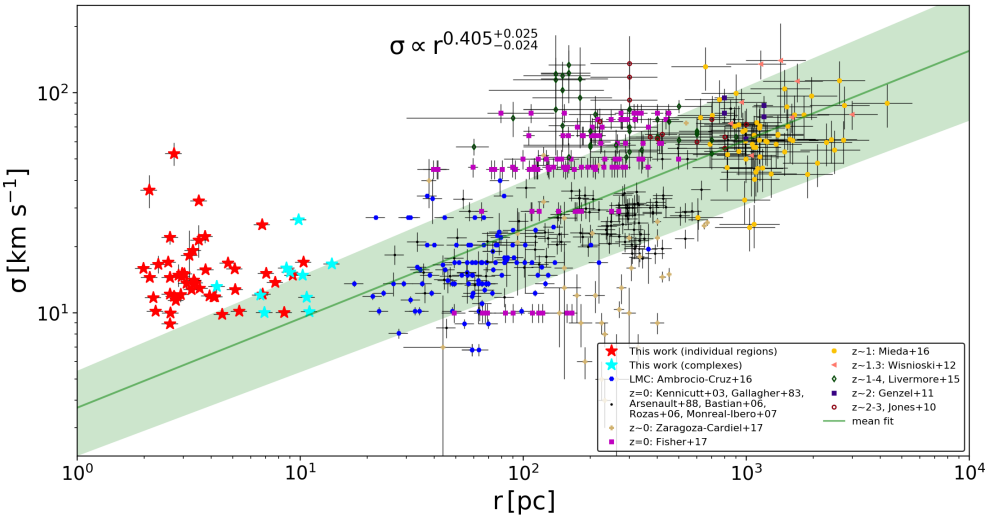

(a)

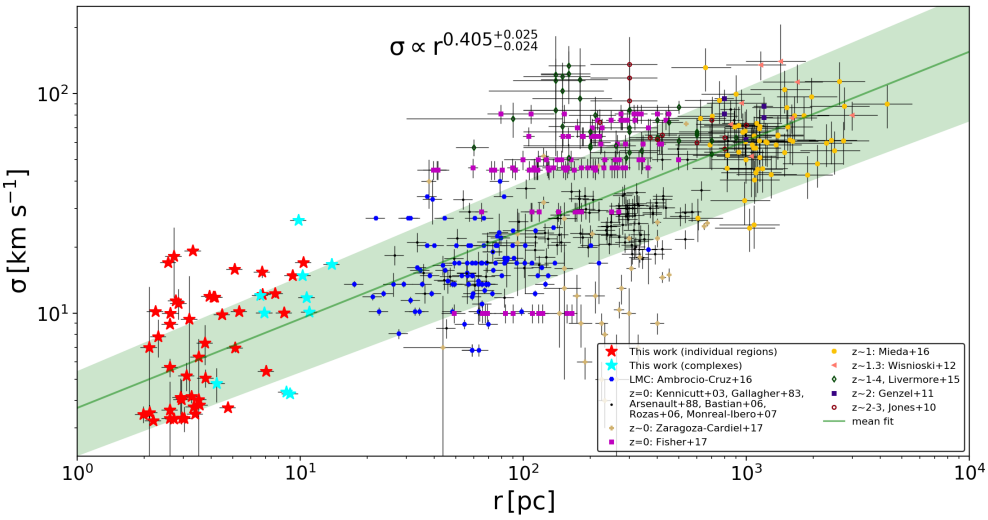

(b)

Figure 3.25: Size vs. σ relationship for the star-forming regions in each comparison sample containing spectral information. The fit is computed using our MCMC framework excluding the IC 10 H II regions (red stars) and complexes (cyan stars) from the analysis. The mean fit is shown with the green line while the uncertainty in the fit is denoted by the shaded green region. (a): Both the IC 10 H II regions and complexes fall above this mean fit, and in most cases above the uncertainty as well, indicating that these H II regions are not virialized. The complexes lie closer to the mean relationship while still tending towards higher σ for a given size, further supporting the conclusion that the individual regions are not virialized as the increase in size does not result in a proportional increase in measured line width. (b): The IC 10 H II regions and complexes lie along the mean size - σ *after* the excess velocity dispersion determined in Section 3.3.5 is removed. The excess dispersion was found to be in addition to that produced by rotational motion of the H II region gas and is therefore likely due to outflows or expansion of the ionized gas.

3.4 Discussion

Observational studies of the stars and H II regions in IC 10 suggest that the starburst occurred relatively recently, likely in the past $\lesssim$ 10Myr (e.g., Hodge and Lee, 1990; Hunter, 2001). Clustering of the young stellar population (Vacca et al., 2007) and similar properties across multiple regions of the starburst (Polles et al., 2019) indicate a potential common origin for the recent star formation.

In our KCWI observations of the H II regions in IC 10's central starbursting region, we find further evidence that these regions are young, with average crossing times $<$ Myr. Feedback plays an important role in the regulation of star forming environments and the dissipation of material. There are many forms this feedback can take and their contribution can be estimated from their energy or momentum input into the ISM. In our KCWI observations, we only observe the ionized gas and therefore cannot estimate the contribution of every form of potential feedback, but we do estimate the contribution of two important factors: direct radiation pressure, P_{dir}, and warm gas pressure, P_{gas}. Of these two we find the contribution of P_{gas} to be dominant over P_{dir} by $\sim$3 orders of magnitude. It should be noted that radiation pressure is sensitive to the effects of stochastic sampling of the initial mass function since the majority of the radiation is produced in the most massive stars. The impact of radiation pressure can therefore be somewhat uncertain in smaller clusters like those powering IC 10's H II regions where the stellar population of the ionizing cluster is not well represented by the assumed IMF. Though, since P_{gas} is $\sim$3 orders of magnitude greater than the estimated P_{dir} we do expect radiation pressure to be comparably negligible even if the estimate is impacted by stochasticity. The same trend with a minor contribution from P_{dir} is also found in the giant H II region 30 Doradus (Pellegrini et al., 2011; Lopez et al., 2011), a sample of 32 LMC and SMC H II regions (Lopez et al., 2014), and an additional sample 11 LMC H II regions (McLeod et al., 2019), although to a lesser extent.

The total P_{out} is on average 3$\times$ the inward pressure which is predominantly due to turbulence in the surrounding gas. The self-gravity of the H II regions is comparably weak in the compact H II regions found in IC 10. This is in contrast to results found in the molecular ISM of nearby

galaxies showing kpc and sub-kpc scale equilibrium between gravitational potential and outward pressure (e.g., Sun et al., 2020). However, our H II regions observations are on much smaller size scales, resulting in the average $P_{out} \sim 3 \times P_{in}$, and with 89% of the H II regions identified in IC 10 showing greater P_{out} indicating expansion. This is somewhat at odds with theoretical expectations of feedback effectiveness. For both direct radiation pressure and warm gas pressure, massive stars are expected to be the dominant source of the required ionizing photons, and thus these mechanisms are not expected to limit the star formation efficiency in populations with low stellar mass clusters ($\lesssim 400\,M_{\odot}$, Krumholz et al., 2019). This may vary by cluster due to stochasticity of the IMF, but given we find P_{gas} to be an effective counter to inward pressure in the majority of IC 10's H II regions this may require further exploration. We should note that discussions of limiting the star formation efficiency are usually explored in the context of the larger molecular cloud, while we are limited to studying these mechanisms within the H II regions and therefore cannot directly measure how much impact these mechanisms will have on clearing gas further from the ionizing cluster, but this still implies that P_{gas} may effectively limit star formation efficiency in a wider range of environments than previously expected. This is compounded by another potential source of expansion in the detection of diffuse X-ray emission by Wang et al. (2005) for which they note a morphological similarity with the Hα gas in the region of IC 10 that we observe with KCWI. They argue that this indicates the hot gas is still confined and may be driving expansion of the surrounding ionized gas structures. However, the effectiveness of this hot gas in driving feedback is dependent on leakage and mixing and likely sub-dominant compared to P_{gas} (Lopez et al., 2014).

The stacked spectrum of all the identified H II regions shows further evidence of expansion and/or outflowing gas, with an underlying broad component to the [OIII]5007Å emission line with $\sigma \sim 35\,\mathrm{km\,s^{-1}}$. Even the regions with evidence of rotation do not seem to have reached an equilibrium state with the surrounding gas as seen in the $\sim$14km s^{-1} higher measured velocity dispersions than what would be due to just rotation as well as virial parameters, $\alpha_{vir} >> 1$. The higher velocity dispersions and elevated $\log([\mathrm{OIII}]/\mathrm{H}\beta)$ at the edges of many of the H II regions indicate that there may be shocks present which could be due to expansion of the region, champagne

flows, or hot stellar winds mixing with cold gas. Over 35% of the regions show these pockets of elevated velocity dispersion at or near the edges of the H II region. The velocity dispersions are not high enough to be produced by shocks in the H II regions themselves as the elevated dispersions are $\sim$2$\times$ the sound speed, c_s. However, at the H II region boundaries the expanding gas may collide with cold molecular gas in the ISM which could induce a shock. With typical ISM temperatures of $\sim$100K, c_s would be on the order of 1km s^{-1} for an ideal gas; 20$\times$ less than the areas considered to have elevated velocity dispersion. A previous study of IC 10 ionized gas by Thurow and Wilcots (2005) also found systematically larger line widths outside of H II regions, but they attribute this to superposition of different filaments or shells. These IFU observations have similar spectral resolution to our small slicer, R$\sim$18,000 observations, but with KCWI we are able to achieve 3$\times$ greater spatial resolution, limiting the potential for superposition of structures with different velocities. Given that we observe areas of higher velocity dispersion at spaxels with the highest $\log\left([\mathrm{OIII}]5007\text{Å}/\mathrm{H}\beta\right)$ we find shocked gas to be a plausible alternative to the superposition of independent filaments, particularly with the significant improvement in spatial resolution of KCWI requiring these structures to be aligned along the line of sight on $\sim$few pc scales.

Resolved areas of significantly elevated velocity dispersion ($\sigma > 25\mathrm{km\,s^{-1}}$) were identified around 6 H II regions with average eddy turnover times $\tau_{\mathrm{eddy}} = l/\sigma \sim 0.2$Myr. The turbulent volumes around the three largest of these H II regions are most likely caused primarily by champagne flows, but stellar winds from early O stars could also provide sufficient energy to support the rate of turbulent dissipation (L_{turb}). Two of the smaller H II regions with resolved turbulent volumes at the border are ionized by lower mass stars with therefore lower rates of ionizing photon production. In this case we find that stellar winds are more likely to support the observed turbulence and are again sufficient to support L_{turb}. One of the six turbulent volumes has an estimated L_{turb} greater than what we estimate could be provided by the H II region and therefore is likely due to some external source of turbulence.

τ_{eddy} measured for these turbulent regions is at the low end of the range observed in galactic scale outflows driven by starbursts (0.1 - 10 Myr; Veilleux et al., 2005). However, the velocity

measured in these ionized gas outflows, FWHM $\sim 61 \mathrm{km\,s^{-1}}$, is significantly lower than that measured in galactic winds and outflows from individual star forming clumps in other studies. In a sample of 25 star-forming clumps located in LIRGs, Arribas et al. (2014) identify outflows in 83% of clumps with typical FWHM $\sim 200 \mathrm{km\,s^{-1}}$. Similarly, in the Rodríguez del Pino et al. (2019) study of ionized gas outflows in MaNGA galaxies, finding typical FWHM $\sim 350 \mathrm{km\,s^{-1}}$ in outflows originating from star-forming regions. Both of these studies find significantly higher velocities to the ionized gas outflows than the IC 10 H II regions which could be due to larger SFR (particularly in the case of the LIRGs), but they also have $\sim 100\times$ lower spatial resolution to what is achieved in IC 10 with KCWI. These measured outflows may then be due to aggregate measurements of multiple compact H II regions and outflows. Some of this variation may also be due to biases introduced by differences in outflow detection methods. Both Arribas et al. (2014) and Rodríguez del Pino et al. (2019) rely on separating a broad outflow component in the emission line of the integrated star-forming region spectra while the resolution of this study allows direct detection of the influence of outflows in the ionized gas surrounding the H II regions. This may then simply probe more localized, lower velocity outflows than has been possible in previous studies.

The velocity dispersions measured inside the identified H II regions are also elevated relative to what would be expected for a rotating region in equilibrium for all cases showing evidence of rotational motion. The H II regions we identify in IC 10 tend to be offset from the scaling relationships found between the region size & luminosity as well as from the Larson's Law between size & velocity dispersion. Krieger et al. (2020) find a similar offset to larger line widths for a given size when comparing molecular clouds in the starburst NGC 253 to clouds in the Milky Way's Galactic center, which they attribute to gas that is not gravitationally bound and rather lies in transient structures. Based on the discrepancies in mass estimates and the young ages of IC 10's H II regions, it seems likely that these H II regions are still young enough to be undergoing expansion. They may then evolve onto the typical size-luminosity and size-velocity dispersion sequences after reaching an equilibrium state with the surrounding ISM.

The evolutionary stage of the Wolf-Rayet stars in the field of view provide another clue that

the H II regions which host them are young. Wolf-Rayet stars are a later evolutionary stage of O stars which occurs before a type I SNe. In general, high mass O stars ($> 40 M_{\odot}$) evolve to a WN type WR, then a WC, and then a SNIc, whereas lower mass O stars are thought to not reach the WC stage and simply explode as a SNIb (Crowther, 2007). Of the eight WR stars in the field covered by our KCWI observations, four of these fall in an H II region. Two have been identified as WN spectral types (M24 and T5 in H II regions H16a and M12 respectively), one is identified as an early WC (R10 in region I18), and the last has not yet been spectroscopically confirmed. Of the four WR stars outside of IC 10 H II regions, one is a late WN type and the rest are identified as WC. These stars are located in areas where ionized gas is nearby, but more diffuse and filamentary in appearance. The locations of these WR stars and their spectral type are shown in Figure 3.26 with the observed [OIII]5007Å flux and H II region contours. Though this is a small sample, the trend implies that WR stars in the WN stage could be more likely to be found in current H II regions, whereas WC types might be more likely found in areas of diffuse gas where an H II region may have previously been present. This would imply that the star clusters the WN stars belong to are younger and the surrounding gas has not yet been disrupted.

3.5 Summary

We made use of the highest resolution mode of the Keck Cosmic Web Imager IFS $-$ $0.35''$ spatial sampling with $1''$ FWHM and R$\sim$18,000 $-$ to study the population of H II regions in our nearest starburst galaxy IC 10. These high quality IFS observations allowed us to study the spatial and kinematic properties of the H II regions in detail. We identified 46 individual H II regions in the central burst of the irregular galaxy with a total SFR$\sim 6 \times 10^{-3}$ $M_{\odot}$ yr^{-1}. The average H II region identified has a size of 4.0 pc, an SFR of 1.3×10^{-4} $M_{\odot}$ yr^{-1}, an ionized gas mass $M_{HII} \sim 56 M_{\odot}$, and a velocity dispersion of $\sim$16km s^{-1}.

Over 95% of the identified H II region luminosities are consistent with the ionizing photon production rate of a single O or B star. 10 of the H II regions ($\sim$22%) can be powered by a single B star, with the lowest luminosity region requiring at minimum a star of spectral type B0.5.

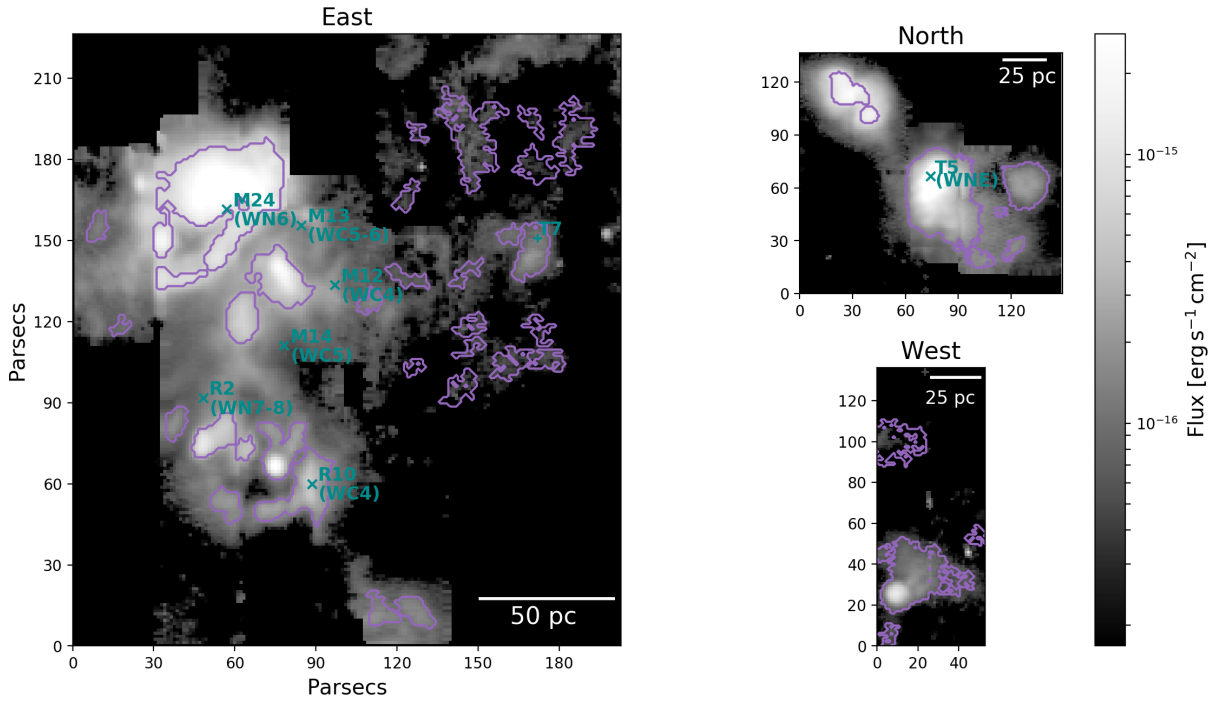

Figure 3.26: [OIII]5007Å integrated flux map with region contours reproduced from Figure 3.3 with marked locations of all known WR stars ('X') and WR candidates ('+'). The stars designation is included to the right of the location marker with the WR type in parentheses if it has been spectroscopically confirmed.

The H II regions appear to be blue-shifted relative to the systemic velocity of IC 10 ($\sim$12km s^{-1}) while the diffuse surrounding gas often shows a relative red-shift. Supplementary KCWI observations with lower resolution and wider wavelength coverage are used to estimate the oxygen abundance via the KK04 and PT05 metallicity calibrations, both of which make use of the R_{23} strong-line calibration. These estimates yield averages of $12+\log(\mathrm{O/H})_{\mathrm{PT05,lower}} \approx 7.85 \pm 0.03$ and $12+\log(\mathrm{O/H})_{\mathrm{KK04,lower}} \approx 8.22 \pm 0.02$ with the "true" metallicity expected to lie within this range.

IC 10's H II regions have very short crossing times ($\tau_{\mathrm{cr}} <$ Myr) and are not virialized ($\alpha_{\mathrm{vir}} >> 1$ and $\mathrm{M_{vir}} >> \mathrm{M_{HII}}$). The measured velocity dispersions in the H II regions are also too high to be due to rotational motion alone (by $\sim$11-12 km s^{-1}). We see evidence that these regions are generally still undergoing expansion. The IC 10 H II regions are offset from the scaling relationships found between the region size & luminosity as well as the size & velocity dispersion

relationship. As these regions expand they may evolve onto the scaling relationships determined for the other samples of H II regions and star-forming clumps.

We estimated the contribution of the thermal gas pressure, P_{gas}, and direct radiation pressure, P_{dir}, to the outward pressure in the H II regions. We find P_{gas} to be the dominant force of expansion in IC 10's H II regions, being $\sim$3 orders of magnitude greater than P_{dir} using the definition of P_{dir} based on ionizing photon production rate. We also find $P_{out} > P_{in}$ in 89% of the H II regions before accounting for additional expansion from hot gas pressure, a somewhat surprising result given the low stellar masses estimated for the ionizing stars. Five of the H II regions show evidence of outflows that may be supported by energy in the ionizing cluster either in the form of stellar winds or champagne flows. These pressure and energy estimates add further evidence that the H II regions in IC 10 are young and undergoing expansion into the ISM and suggest that thermal gas pressure may be a more effective form of feedback than previously expected from low mass clusters.

These high resolution and SNR observations were possible in just 1.5 nights of Keck observing time. From just this short time we were able to obtain detailed kinematic and flux maps of a significant number of H II regions. With additional observations the remainder of IC 10's H II regions can be observed in the same modes, with deeper observations of the diffuse gas and the supplementary low resolution mode. More expansive coverage of H II regions and the DIG in IC 10 will allow for detailed study of the kinematic and ionization state differences between these unique regions of ionized gas. KCWI observations at high spectral resolving power of the remainder of IC 10 would also double the number of H II regions in this unique starburst environment in which the impact of different modes of feedback and outflows can be investigated.

A relatively small investment of time with optical IFS's such as KCWI and VLT/MUSE can quickly yield a large sample of local star-forming regions in a wide range of environments. The large field of view and moderate spectral resolving power (R$\sim$2000-4000) of MUSE provides an efficient tool for mapping ionization states of H II regions and the ISM, while the R$\sim$18,000 mode of KCWI can be leveraged for a detailed look at the gas kinematics in compact regions. Utilizing these powerful IFU's across a wide sample of star forming galaxies will allow a detailed and statistically

significant study of how environmental conditions impact the effectiveness of feedback mechanisms and vice versa; and whether there are age and environmental dependencies when looking at the scaling relationships. Targeted IFU studies of this kind are already well underway and as a larger collective sample is built we will be able to better compare these results with theoretical predictions of feedback and inform new models.

The reduced data cubes used in this study are available by request to facilitate further study beyond the scope of this project.

We thank the anonymous referee for their comments which helped improve the quality of this paper. The data presented herein were obtained at the W. M. Keck Observatory, which is operated as a scientific partnership among the California Institute of Technology, the University of California and the National Aeronautics and Space Administration. The Observatory was made possible by the generous financial support of the W. M. Keck Foundation. The authors wish to recognize and acknowledge the very significant cultural role and reverence that the summit of Maunakea has always had within the indigenous Hawaiian community. We are most fortunate to have the opportunity to conduct observations from this mountain.

Facility: Keck:II(KCWI)

*Software:*astrodendro (Thomas et al., 2013), Astropy (Astropy Collaboration et al., 2013; Price-Whelan et al., 2018), IPython (Perez and Granger, 2007) Matplotlib (Hunter, 2007), NumPy (Harris et al., 2020), pandas (The Pandas Development Team, 2016; Wes McKinney, 2010), photutils (Bradley et al., 2019), PyStan (Stan Development Team, 2017), reproject (Robitaille et al., 2020) SHAPE (Steffen et al., 2011)

Appendix

3A H II Region Naming Convention

The previous naming of IC 10 H II regions was developed by Hodge and Lee (1990) where regions are assigned a number in order of increasing RA. If that region breaks up into smaller knots then a letter is added after the complex number (e.g., 111a). Throughout the literature this region identifier is typically preceded by either "HL90" or simply "HL" to indicate the origin of the identifier. This is a simple and clear way of tabulating the H II regions found in this early study but there are some significant shortcomings of this system now. One difficulty is in quickly identifying regions in the Hα maps as regions are only numbered based on their RA while there can be a large spread in Dec from one region to the next in the sequence. The other more problematic issue is that with better resolution and sensitivity one would expect to identify new H II regions and complexes breaking into more knots. When this occurs there is not a clear way in which to assign an identifier to these new regions. If the next number in the sequence is assigned to each new region there would no longer be a clear ordering based on RA, and reassigning numbers to each region with every new identification would make comparison between studies exceedingly difficult.

We have therefore proposed a new naming convention that we believe addresses these issues for our study and allows extension to future studies with even wider fields using the grid described in Section 3.3.1. This numbering scheme simplifies identification of nearby regions in both RA and Dec as well as extension to a larger FoV. This could be applied to the larger IC 10 H I envelope by increasing the numbering range in Dec. and extending the RA designation to double and/or negative lettering (e.g., AA or -A). Fainter H II regions may be identified in already occupied grid squares, but the next trailing letter in the sequence can be added as these should have lower luminosity than what is identified here.

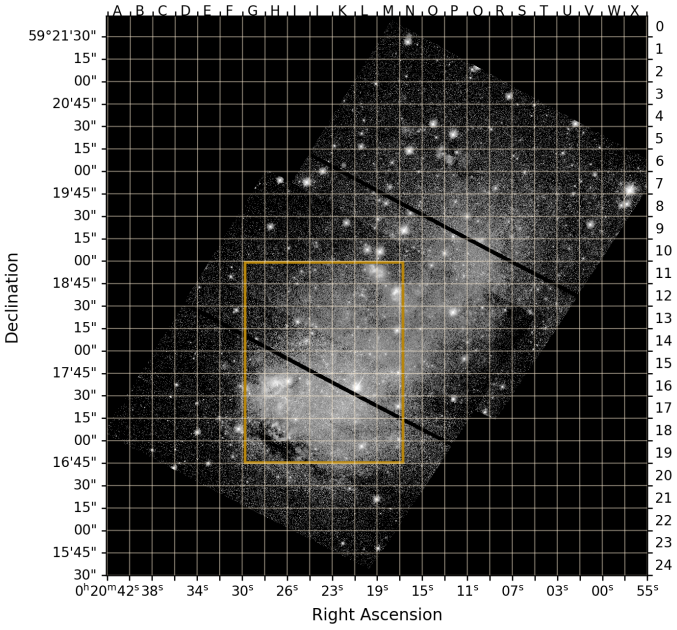

Figure 3A.1: Coordinate grid for proposed H II region naming scheme overlaid on an HST/ACS image showing the optical extent of the galaxy. H II regions are named based on the lettered column and numbered row corresponding to their center. This could be extended to the larger H I envelope of IC 10 by going to larger positive and negative numbers as well as double and/or negative lettering (e.g., AA or -A). The gold rectangle outlines the region of IC 10 which our KCWI observations fall in.

3B Impact of Radius Definition

The choice of how to define the radius of an H II region varies significantly between studies, and particularly between local and high-redshift studies.

In observational studies of local H II regions there is wide variation in the methods used to define the size of the region, with this often not being a critical aim of the study. For example, the Green Bank Telescope H II Region Discovery Survey (HRDS) measures the sizes of 441 H II regions in the Milky Way by taking the mean of the FWHM of Gaussians fit to the RA and Dec components of continuum observations (Anderson et al., 2011). In the extensive CALIFA survey of over 26,000 extragalactic H II regions, a custom procedure called `HIIEXPLORER` (Sánchez et al., 2012b) (and the Python version `PYHIIEXPLORER`; Espinosa-Ponce et al., 2020) is used to identify H II regions. This procedure is similar in methodology to `astrodendro` except that the maximum expected extent of H II regions is provided as an input constraint. The sizes of identified regions then tend towards a relatively uniform distribution (Sánchez et al., 2012b), and the authors note that extracting reliable sizes was not a main goal of their methodology partly due to the resolution of their observations.

Studies of local GMCs typically use the second moments of the cloud structure to determine its properties (Heyer and Dame, 2015). Often the geometric mean of the second moments of the cloud structure (in the direction of greatest elongation and perpendicular to that) is used to describe the RMS extent of a cloud, σ_r. An empirical factor is then used to determine the radius of a spherical cloud, $R = \eta \sigma_r$. This factor was first determined empirically in Solomon et al. (1987) to be $\eta = 1.91$ for converting their rectangular regions to spherical clouds and is used throughout the literature to convert the second moments of a variety of structures to a spherical radius. Rosolowsky and Leroy (2006) go through the derivation of this factor of η for a spherical cloud with a density profile of $\rho \propto r^{-1}$ and determine a theoretical value of $\sqrt{6} \approx 2.45$. They suggest that deviation may be due partly to the use of CO data to trace the GMC density which is shallower than the actual density profile due to saturation in dense regions and lack of detection in low density regions. This would

mean that the "true" value of η would lie somewhere between the empirical value of 1.91 from Solomon et al. (1987) and the value of 2.45 determined from their toy model of a GMC. However, they recommend continued use of the radius definition from Solomon et al. (1987) in order to remain consistent with this data set. Since our observations are of ionized rather than molecular gas we do not use this same factor of η, and instead assume a Gaussian profile in our determination of $r^*_{1/2}$ from the second moments.

Zaragoza-Cardiel et al. (2017) combine CO and Hα observations in local LIRGs with regions identified using `astrodenro`. They define the radius, r, using the second moments of the structures in both cases, with the factor of 1.91 from Solomon et al. (1987). They compare the ratio of this radius to that derived from the area of the full structure, $r_{\rm eff}$, and find an average $\frac{r}{r_{\rm eff}} = 0.86 \pm 0.14$. In another sample of local LIRGs with star-forming regions identified by `astrodendro`, Larson et al. (2020) use $r_{\rm eff}$ to define the size of regions. Larson et al. (2020) also performs a comparison of the `astrodendro` and `CLUMPFIND` identification routines finding similar average radii and SFR, but a narrower range of fluxes for a given radius of star-forming region due to a lack of local background subtraction.

In studies of high-redshift star-forming clumps, differences in the method used to determine region sizes are also present, although perhaps less significant due to the decrease in resolution. Wisnioski et al. (2012) compares the size determined from isophotes of constant flux and from fitting a Gaussian to the radial surface profile of H II regions. They find $r_{\rm eff}$ from the isophotal method to be systematically larger than $r_{1/2}$ determined via Gaussian fitting, but the luminosities to be consistent between the two methods. This comes from the emission being dominated by the higher intensity cores of the H II regions. They argue that $r_{1/2}$ from Gaussian fitting is a better defined observational parameter as it is less likely to be contaminated by diffuse emission that could be significant at high-redshift. Livermore et al. (2012) also compare clump sizes determined by $r_{\rm eff}$ of `CLUMPFIND` isophotal structures and from fitting a 2D elliptical Gaussian profile to emission peaks. They find that using `CLUMPFIND` for their sample gives 25% larger estimates of size than from the FWHM of the 2D elliptical Gaussian, but include error bars encompassing both measures.

They note a smaller deviation between their CLUMPFIND radii and the FWHM of fitted Gaussians than in Wisnioski et al. (2012) due in part to the use of multiple isophote levels in CLUMPFIND that does not need to be tuned in the same way as other single isophote methods.

Which of the many possible radius definitions is used has a significant impact on the typical size of star-forming regions and on the scaling relationships determined from those properties. To quantify just how much impact the choice of using the pseudo half-light radius ($r^*_{1/2}$) definition for the H II region radii has in this study we perform MCMC fitting with different choices of radius definition and identification constraint for our sample. We fit the relationship between region size and luminosity for (i) the IC 10 H II regions alone, for (ii) local samples only, and for (iii) the full sample of local and high-redshift H II regions and clumps. These results are shown in Table 3B.

Table 3B.1: Radius Definition Implications

astrodendro Constraint	Radius Definition	Filtering	$N_{regions}$	R_{avg} (pc)	Slopes IC 10	Slopes Local	Slopes All Data
2r > FWHM	$r^*_{1/2}$	···	46	4.0	$3.601^{+0.471}_{-0.385}$	$3.049^{+0.029}_{-0.025}$	$3.002^{+0.023}_{-0.024}$
	$r^*_{1/2}$	r>FWHM	20	5.6	$2.972^{+0.793}_{-0.483}$	$3.147^{+0.032}_{-0.035}$	$3.067^{+0.032}_{-0.021}$
	$r_{\rm eff}$	···	45	6.8	$2.979^{+0.426}_{-0.344}$	$3.045^{+0.025}_{-0.026}$	$2.987^{+0.020}_{-0.028}$
	$r_{\rm maj}$	···	46	5.1	$3.176^{+0.451}_{-0.351}$	$2.999^{+0.036}_{-0.026}$	$2.951^{+0.031}_{-0.025}$
r > FWHM	$r^*_{1/2}$	···	23	6.1	$2.888^{+0.558}_{-0.388}$	$3.161^{+0.026}_{-0.025}$	$3.043^{+0.025}_{-0.024}$

Note. — Results of model slope determined from MCMC fitting of the size-luminosity relationship for IC 10 H II regions and the local and high-redshift comparison sample based on different ways of defining and constraining the radius of IC 10 H II regions.
Col 1: constraint used in astrodendro to define an independent structure. The top section uses the more relaxed constraint that the diameter of the region must be larger than the FWHM determined from standard star observations (this always uses the definition of $r^*_{1/2}$ to match the Gaussian fit to the stars PSF). In the bottom row we require this diameter to be twice the standard star FWHM.
Col 2: radius definition used to determine H II region size; $r^*_{1/2}$, and $r_{\rm eff}$ used as described in Section 3.3.1, and $r_{\rm maj}$ is determined by converting the second moment in the direction of greatest elongation to the HWHM of a Gaussian.
Col 3: additional filtering applied to exclude regions from MCMC fits beyond the manual filtering of bad regions as described in Section 3.3.1
Col 4: Number of H II regions found in IC 10 based on these constraints and filtering.
Col 5: Average radius of IC 10 H II regions.
Col 6 - 8: slope and uncertainty determined from MCMC fitting of the size-luminosity relationship for IC 10 regions only (7), local regions only (8) and all local and high-redshift data (9).

Regardless of our chosen definition for region size, the slope of the local and full sample is

consistent within $< 5\%$. However, there is a larger difference in the slope of the IC 10 H II region sample alone. Using the most relaxed resolution constraint in `astrodendro` and $r^*_{1/2}$ produces a slope for which the nominal value deviates by 18% from either a stricter resolution constraint (bottom row) or the definitions of $r_{\rm eff}$ and $r_{\rm maj}$ for the region size. Fitting only the IC 10 H II regions, however, leads to significantly larger uncertainties so the nominal slopes for each radius constraint are still consistent within the 1σ uncertainties.

3C Spectra Thumbnails

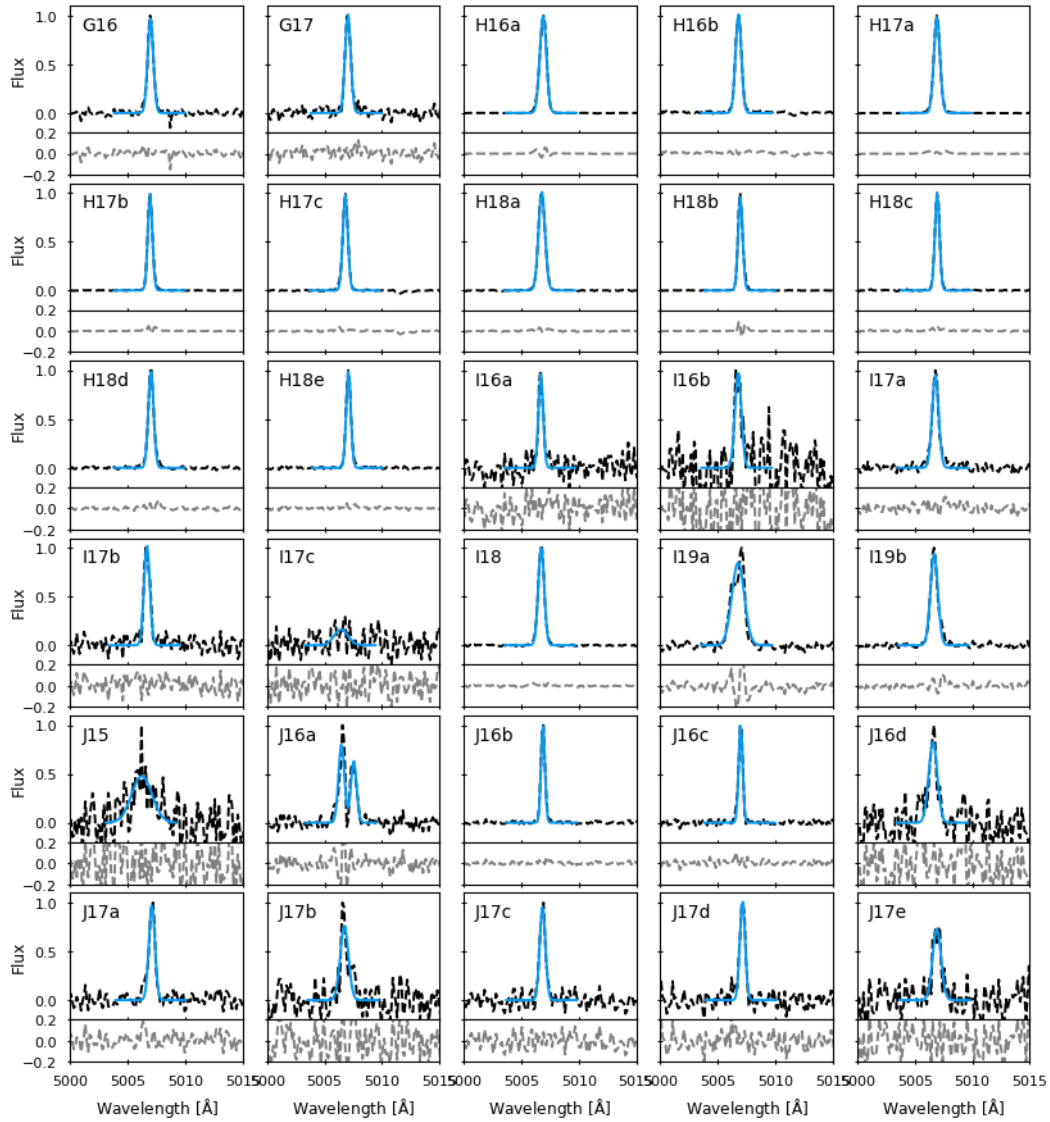

Figure 3C.1: Spectral thumbnails of [OIII]5007Å from all H II regions detected in the small slicer, R∼18,000 observing mode. These lines are fit by a single Gaussian profile (except for J16a with a double Gaussian profile) shown in cyan with the residuals shown in grey below the associated spectrum. The spectra have been normalized to the peak of the [OIII]5007Å line.

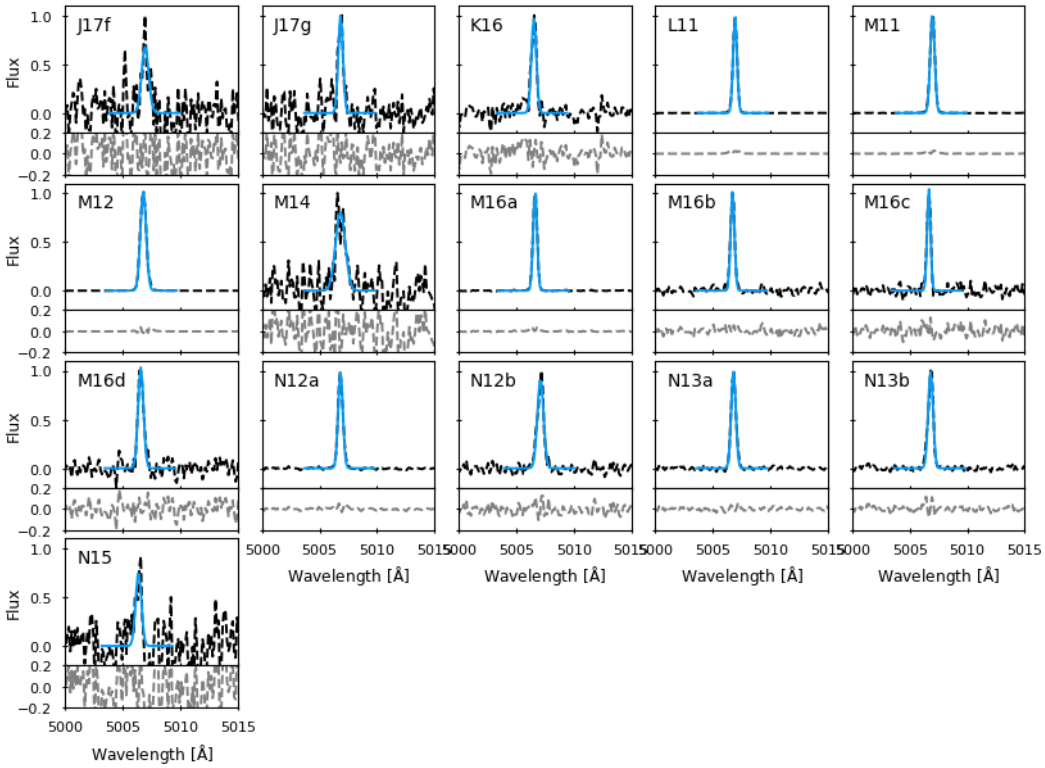

Figure 3C.2: Figure 3C.1 cont'd.

3D H II Region Maps

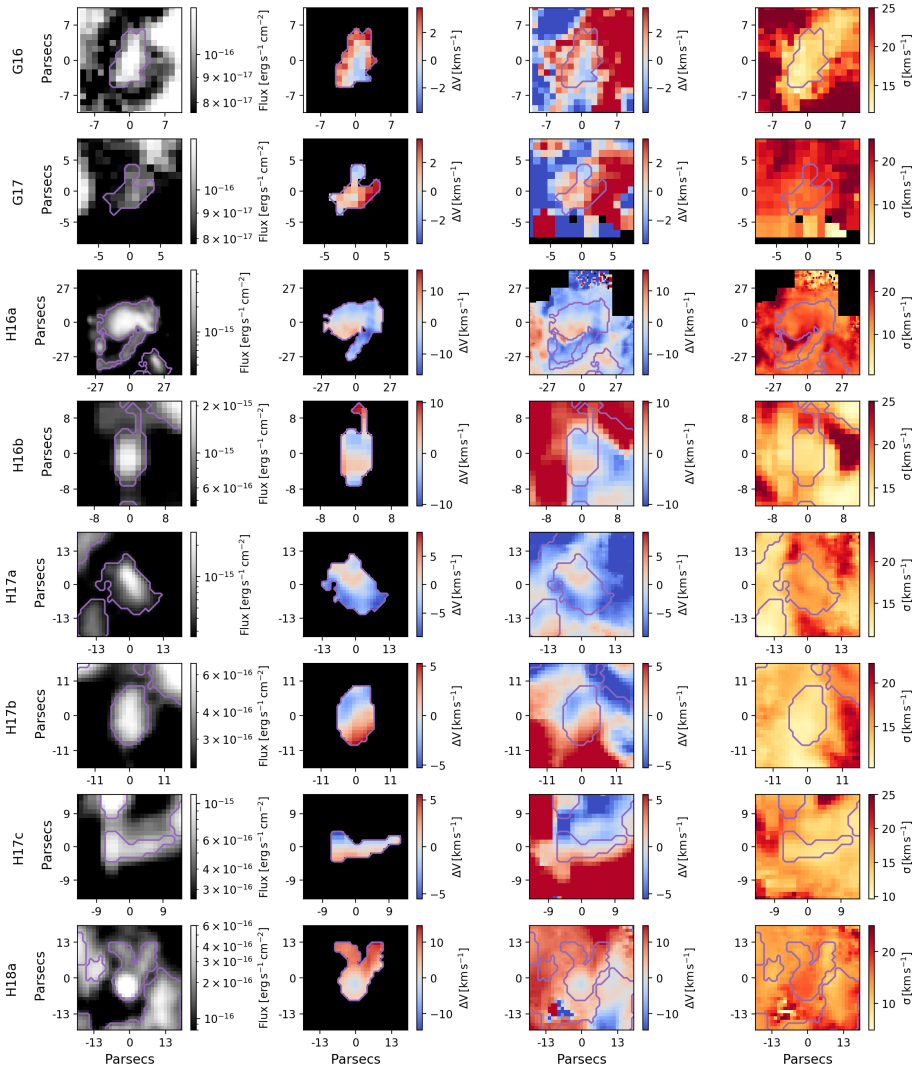

Figure 3D.1: Thumbnail maps of H II regions identified in our KCWI observations. (Left): Flux maps of the surrounding area. (Center Left): Velocity shift of spaxels within the H II region relative to the systemic velocity of the region. (Center Right): Velocity shift of the H II region and the surrounding gas. (Left): Velocity dispersion within the H II region and the surrounding gas. Regions of elevated velocity dispersion may be indicative of outflowing gas, particularly when correlated with a velocity shift relative to the surrounding gas.

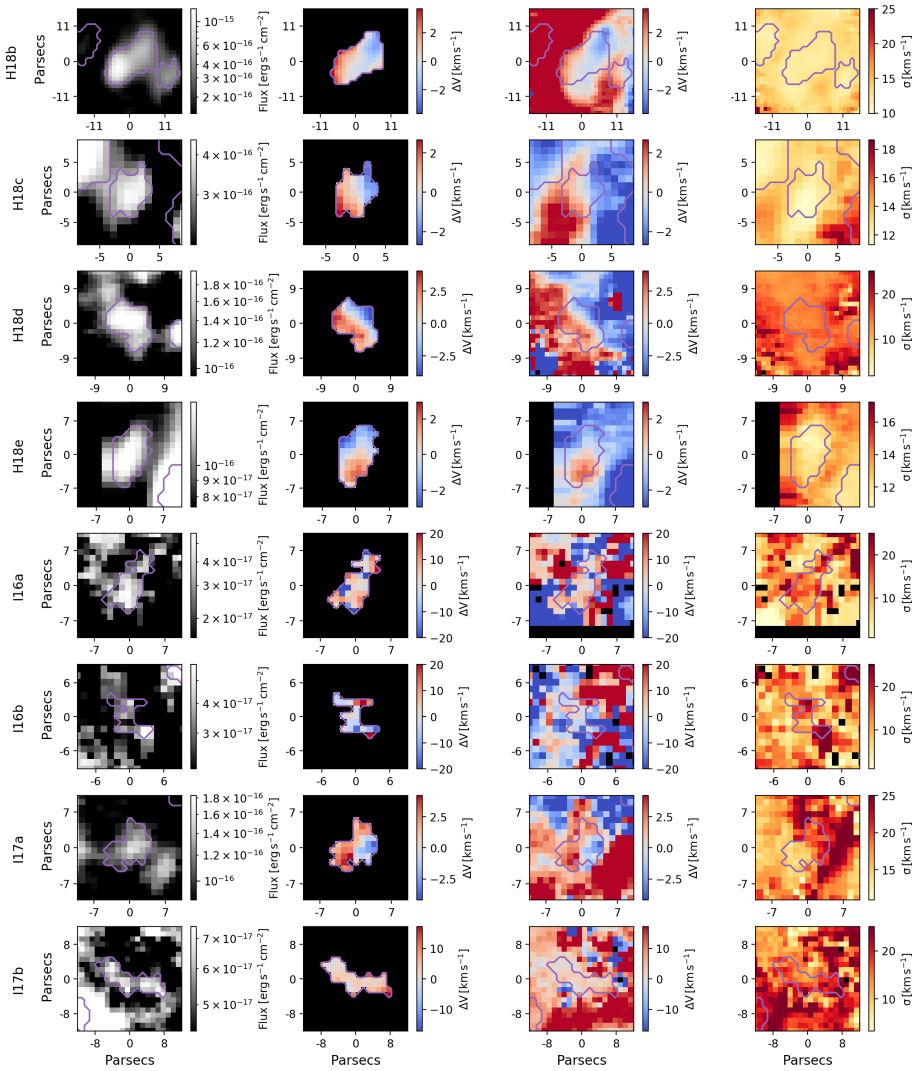

Figure 3D.2: Figure 3D.1 cont'd.

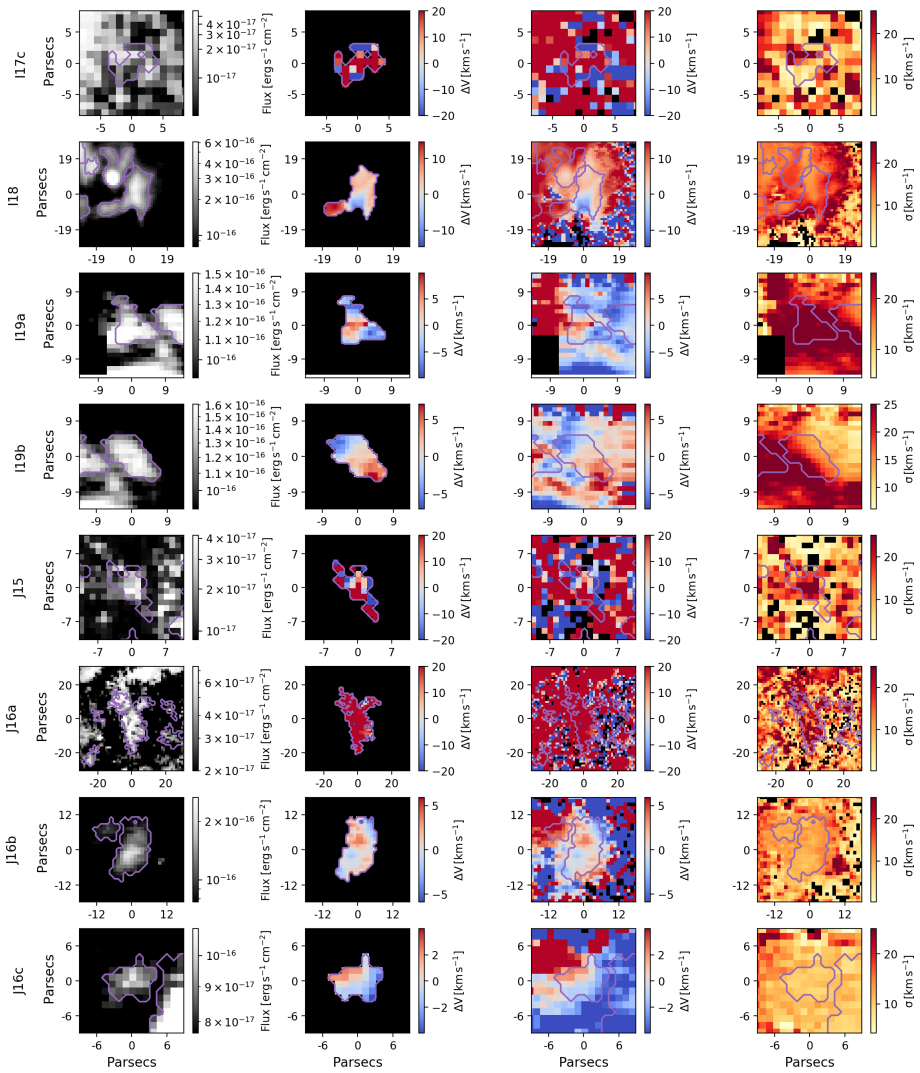

Figure 3D.3: Figure 3D.1 cont'd.

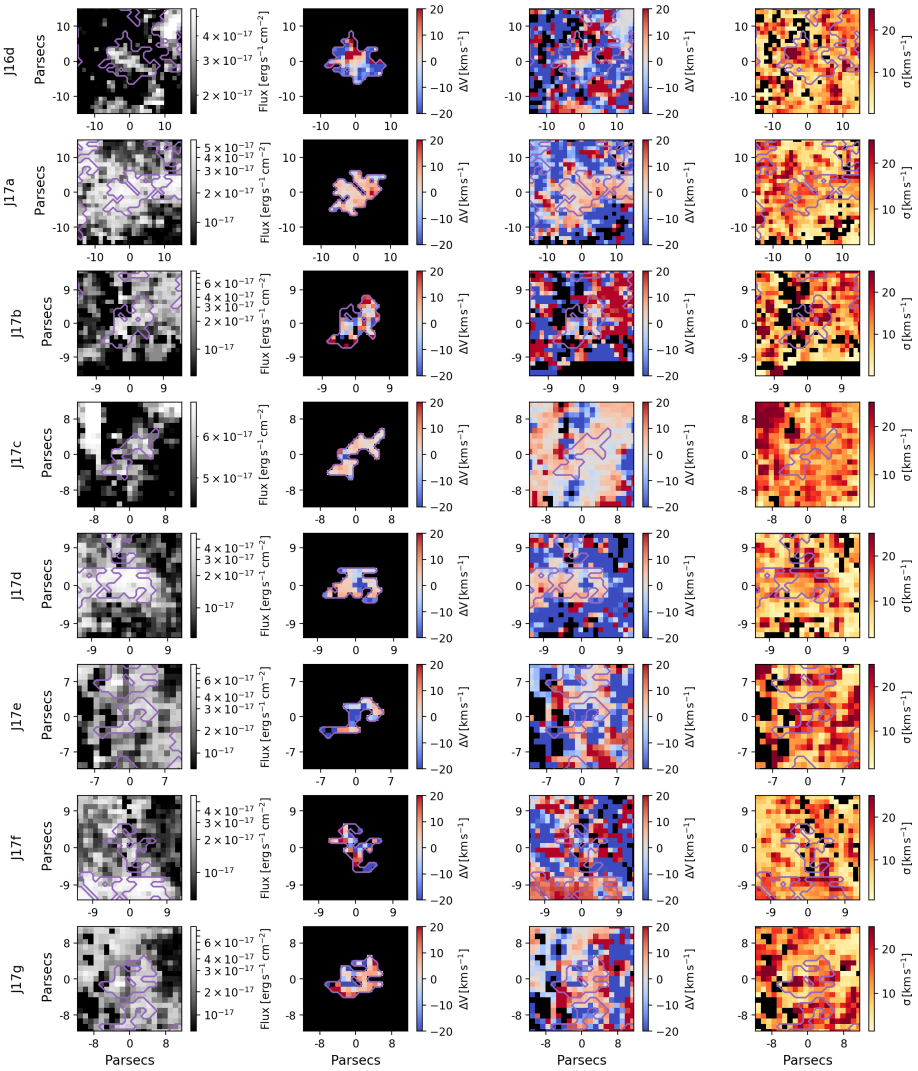

Figure 3D.4: Figure 3D.1 cont'd.

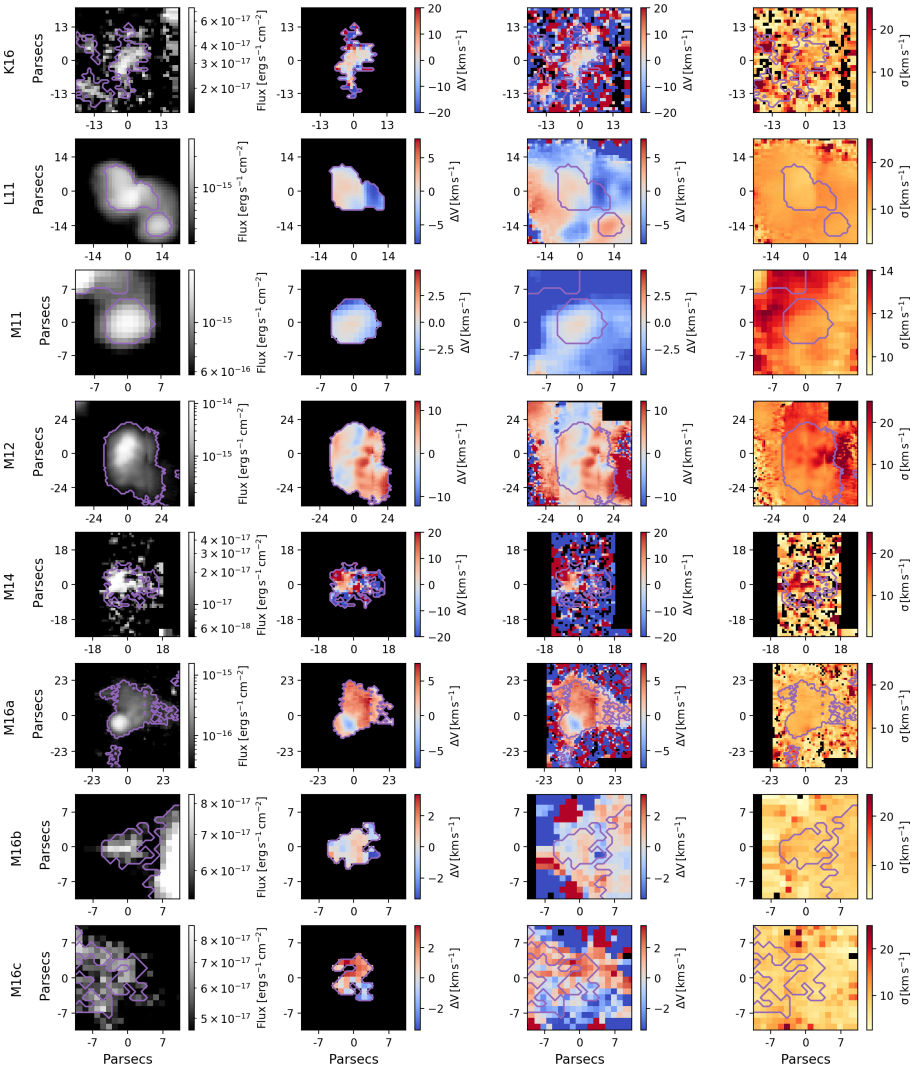

Figure 3D.5: Figure 3D.1 cont'd.

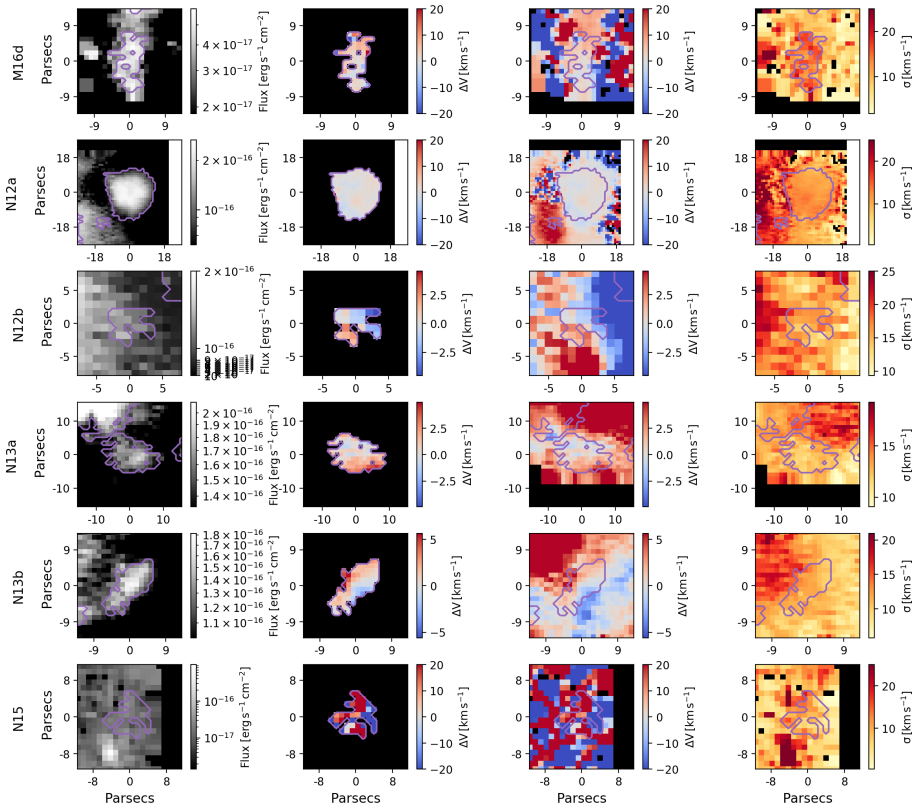

Figure 3D.6: Figure 3D.1 cont'd.

3E Additional Tables

Table 3E.1: H II Region Properties (small slicer, R∼18,000) — [OIII]4959Å

Region	$\Delta V_{[OIII]4959}$ ($km\,s^{-1}$)	$\sigma_{[OIII]4959}$ ($km\,s^{-1}$)	$L_{[OIII]4959}$ ($10^{35}\,erg\,s^{-1}$)
G16	-5.58 ± 3.31	16.62 ± 2.93	1.78 ± 0.43
G17	8.93 ± 2.00	16.06 ± 1.30	2.14 ± 0.42
H16a*	-9.93 ± 2.24	17.82 ± 1.64	3.83 ± 0.77
H16b*	-8.43 ± 1.51	13.90 ± 0.08	27.58 ± 5.10
H17a*	-13.03 ± 2.85	15.04 ± 2.41	0.64 ± 0.15
H17b*	-11.19 ± 2.82	11.25 ± 2.37	1.42 ± 0.37
H17c*	114.11 ± 7.08	6.29 ± 6.84	0.00 ± 0.00
H18a*	-11.98 ± 1.62	27.70 ± 0.57	6.86 ± 1.27
H18b	-139.53 ± 3.71	13.74 ± 3.40	0.12 ± 0.04
H18c	0.06 ± 8.43	40.66 ± 8.33	0.71 ± 0.18
H18d	-16.77 ± 1.56	19.40 ± 0.37	6.29 ± 1.17
H18e	-13.15 ± 1.52	15.40 ± 0.16	63.51 ± 11.76
I16a	-4.43 ± 1.58	10.02 ± 0.45	12.36 ± 2.34
I16b	1.11 ± 1.60	11.96 ± 0.51	1.83 ± 0.35
I17a*	10.58 ± 3.07	17.33 ± 2.64	1.64 ± 0.37
I17b	-0.75 ± 1.51	12.05 ± 0.03	33.67 ± 6.23
I17c*	0.62 ± 1.51	11.96 ± 0.08	7.59 ± 1.41
I18*	9.91 ± 2.77	16.96 ± 2.32	1.85 ± 0.41
I19a	-18.99 ± 1.59	23.72 ± 0.50	7.44 ± 1.38
I19b*	94.05 ± 3.17	10.23 ± 2.78	0.44 ± 0.13
J15	-0.23 ± 1.59	14.13 ± 0.47	2.32 ± 0.44
J16a	-2.57 ± 1.51	17.19 ± 0.01	1575.00 ± 291.40
J16b	-15.57 ± 3.22	13.99 ± 2.83	0.55 ± 0.15
J16c	-20.61 ± 1.82	13.70 ± 1.01	1.37 ± 0.27
J16d	-13.21 ± 1.78	14.29 ± 0.94	2.91 ± 0.56
J17a	-10.16 ± 1.51	17.10 ± 0.09	71.35 ± 13.20
J17b	3.42 ± 1.51	13.35 ± 0.10	7.21 ± 1.33
J17c	4.91 ± 1.69	14.73 ± 0.75	1.27 ± 0.24
J17d*	-0.09 ± 1.51	11.75 ± 0.03	36.51 ± 6.75
J17e	8.05 ± 1.52	12.34 ± 0.19	4.55 ± 0.84
J17f	7.52 ± 12.41	30.73 ± 12.27	2.29 ± 0.94
J17g	-17.71 ± 2.03	6.48 ± 1.36	0.00 ± 0.00
K16	-25.07 ± 1.86	17.76 ± 1.08	2.15 ± 0.41
L11	-2.98 ± 3.67	33.66 ± 3.36	2.22 ± 0.45
M11*	-17.36 ± 1.56	7.70 ± 0.40	1.87 ± 0.36
M12*	-45.03 ± 1.57	11.91 ± 0.47	38.69 ± 7.22

Continued on next page

Table 3E.1 – *Continued from previous page*

Region	$\Delta V_{[OIII]4959}$ ($km\,s^{-1}$)	$\sigma_{[OIII]4959}$ ($km\,s^{-1}$)	$L_{[OIII]4959}$ ($10^{35}\,erg\,s^{-1}$)
M14	-15.74 ± 1.99	14.06 ± 1.29	0.84 ± 0.17
M16a*	-18.22 ± 1.94	18.99 ± 1.20	5.37 ± 1.03
M16b	-5.80 ± 1.53	15.02 ± 0.22	15.42 ± 2.86
M16c	-9.71 ± 1.53	16.50 ± 0.23	63.82 ± 11.83
M16d	-0.74 ± 1.51	15.85 ± 0.02	152.90 ± 28.28
N12a*	-28.78 ± 1.74	13.44 ± 0.85	3.01 ± 0.58
N12b*	-18.42 ± 4.73	27.99 ± 4.51	2.01 ± 0.46
N13a	-18.81 ± 1.51	10.10 ± 0.05	79.24 ± 14.66
N13b*	-20.45 ± 2.46	18.18 ± 1.94	4.25 ± 0.88
N15	-5.27 ± 2.31	31.11 ± 1.75	4.18 ± 0.80

Note — Properties of the [OIII]4959Å emission line for H II regions in the small slicer, R∼18,000 observing mode. Spectral properties are determined by fitting a single Gaussian model to the emission line. Regions with elevated σ in the surrounding gas are identified with a *.

Table 3E.2: H II Region Properties (small slicer, R∼18,000) — Hβ

Region	$\Delta V_{H\beta}$ ($km\,s^{-1}$)	$\sigma_{H\beta}$ ($km\,s^{-1}$)	$L_{H\beta}$ ($10^{35}\,erg\,s^{-1}$)	$SFR_H\beta$ ($10^{-6}\,M_\odot\,yr^{-1}$)
G16	17.92 ± 2.19	15.97 ± 1.53	3.66 ± 0.67	5.62 ± 1.03
G17	29.23 ± 1.99	16.81 ± 1.24	1.03 ± 0.20	1.58 ± 0.31
H16a*	10.40 ± 2.95	20.68 ± 2.46	1144.00 ± 205.80	1757.00 ± 316.10
H16b*	14.96 ± 1.55	16.42 ± 0.11	43.12 ± 7.81	66.22 ± 11.99
H17a*	17.68 ± 1.91	11.24 ± 1.12	114.60 ± 20.61	176.00 ± 31.65
H17b*	27.19 ± 4.09	21.70 ± 3.78	47.68 ± 8.58	73.23 ± 13.17
H17c*	-9751.25 ± 0.00	0.00 ± 0.00	41.29 ± 7.43	63.41 ± 11.41
H18a*	12.89 ± 1.78	29.62 ± 0.88	40.64 ± 7.32	62.42 ± 11.25
H18b	-2.11 ± 1.72	3.70 ± 1.11	38.82 ± 6.98	59.62 ± 10.73
H18c	162.40 ± 2.09	4.12 ± 1.06	6.11 ± 1.10	9.39 ± 1.69
H18d	15.09 ± 1.96	23.50 ± 1.21	14.68 ± 2.64	22.55 ± 4.06
H18e	10.59 ± 1.56	18.70 ± 0.23	6.34 ± 1.15	9.73 ± 1.76
I16a	16.77 ± 1.73	14.57 ± 0.76	0.98 ± 0.20	1.51 ± 0.31
I16b	21.68 ± 1.67	14.42 ± 0.63	0.68 ± 0.15	1.04 ± 0.23
I17a*	37.91 ± 2.54	14.63 ± 2.01	4.37 ± 0.90	6.71 ± 1.38
I17b	23.04 ± 1.54	14.88 ± 0.04	2.78 ± 0.52	4.27 ± 0.81
I17c*	23.40 ± 1.55	15.23 ± 0.14	1.60 ± 0.31	2.46 ± 0.47
I18*	44.85 ± 1.90	3.56 ± 1.23	81.26 ± 14.64	124.80 ± 22.48
I19a	27.09 ± 1.99	21.20 ± 1.26	6.36 ± 1.16	9.77 ± 1.77

Continued on next page

Table 3E.2 – *Continued from previous page*

Region	$\Delta V_{H\beta}$ ($\mathrm{km\,s^{-1}}$)	$\sigma_{H\beta}$ ($\mathrm{km\,s^{-1}}$)	$L_{H\beta}$ ($10^{35}\,\mathrm{erg\,s^{-1}}$)	$\mathrm{SFR}_H\beta$ ($10^{-6}\,\mathrm{M_\odot\,yr^{-1}}$)
I19b*	185.28 ± nan	0.91 ± nan	3.48 ± 0.65	5.34 ± 0.99
J15	23.10 ± 1.71	17.59 ± 0.74	0.00 ± 0.00	0.00 ± 0.00
J16a	19.31 ± 1.54	19.47 ± 0.02	40.97 ± 7.44	62.92 ± 11.43
J16b	14.83 ± 1.90	11.49 ± 1.10	16.01 ± 2.97	24.59 ± 4.56
J16c	8.23 ± 1.89	16.91 ± 1.08	2.24 ± 0.41	3.44 ± 0.63
J16d	12.63 ± 1.69	14.14 ± 0.69	1.55 ± 0.42	2.38 ± 0.65
J17a	13.15 ± 1.56	18.80 ± 0.23	3.18 ± 0.61	4.89 ± 0.94
J17b	25.87 ± 1.55	18.16 ± 0.14	4.49 ± 1.15	6.90 ± 1.76
J17c	28.13 ± 1.92	13.38 ± 1.14	4.32 ± 0.86	6.63 ± 1.32
J17d*	22.76 ± 1.54	14.28 ± 0.04	1.72 ± 0.38	2.64 ± 0.58
J17e	32.93 ± 1.57	15.87 ± 0.30	1.39 ± 0.28	2.13 ± 0.42
J17f	14.11 ± 3.93	17.39 ± 3.59	0.00 ± 0.00	0.00 ± 0.00
J17g	19.14 ± 2.09	18.42 ± 1.40	1.59 ± 0.32	2.44 ± 0.49
K16	3.06 ± 1.77	17.26 ± 0.86	2.30 ± 0.47	3.54 ± 0.71
L11	120.89 ± nan	0.00 ± nan	160.50 ± 28.87	246.50 ± 44.34
M11*	-3.30 ± 2.52	12.71 ± 1.98	37.43 ± 6.74	57.49 ± 10.34
M12*	-45.03 ± 1.57	11.91 ± 0.47	1053.00 ± 189.40	1617.00 ± 290.90
M14	15.33 ± 1.98	12.16 ± 1.24	4.56 ± 0.93	7.00 ± 1.42
M16a*	16.24 ± 2.48	27.71 ± 1.94	71.69 ± 12.90	110.10 ± 19.81
M16b	16.99 ± 1.58	16.10 ± 0.33	4.14 ± 0.75	6.35 ± 1.15
M16c	13.23 ± 1.61	19.09 ± 0.45	0.87 ± 0.20	1.34 ± 0.30
M16d	20.07 ± 1.54	17.55 ± 0.03	3.42 ± 0.63	5.25 ± 0.97
N12a*	2.10 ± 2.05	12.41 ± 1.35	29.75 ± 5.36	45.69 ± 8.23
N12b*	2.73 ± 5.30	20.49 ± 5.07	1.48 ± 0.30	2.28 ± 0.46
N13a	4.87 ± 1.54	13.21 ± 0.09	7.51 ± 1.36	11.53 ± 2.09
N13b*	10.81 ± 2.10	19.56 ± 1.44	3.80 ± 0.84	5.83 ± 1.29
N15	15.79 ± 2.03	19.66 ± 1.30	0.00 ± 0.00	0.00 ± 0.00

Note— Properties of the Hβ emission line for H II regions in the small slicer, R$\sim$18,000 observing mode. Spectral properties are determined by fitting a single Gaussian model to the emission line. Regions with elevated σ in the surrounding gas are identified with a *.

Chapter 3, in full, is a reprint of the material as it appears in The Astrophysical Journal 2022. Cosens, M., Wright, S. A., Murray, N., Armus, L., Sandstrom, K., Do, T., Larson, K., Martinez, G., Sabhlok, S., Vayner, A, and Wiley, J., *The Astrophysical Journal*, 929, 74, 2022. The dissertation author was the primary investigator and author of this paper.

Chapter 4

Liger for Next Generation Keck AO: Filter Wheel and Pupil Design

Abstract

Liger is a next-generation near-infrared imager and integral field spectrograph (IFS) for the W.M. Keck Observatory designed to take advantage of the Keck All-Sky Precision Adaptive Optics (KAPA) upgrade. Liger will operate at spectral resolving powers between R$\sim$4,000 - 10,000 over a wavelength range of 0.8-2.4μm. Liger takes advantage of a sequential imager and spectrograph design that allows for simultaneous observations between the two channels using the same filter wheel and cold pupil stop. We present the design for the filter wheels and pupil mask and their location and tolerances in the optical design. The filter mechanism is a multi-wheel design drawing from the heritage of the current Keck/OSIRIS imager single wheel design. The Liger multi-wheel configuration is designed to allow future upgrades to the number and range of filters throughout the life of the instrument. The pupil mechanism is designed to be similarly upgradeable with the option to add multiple pupil mask options. A smaller wheel mechanism allows the user to select the desired pupil mask with open slots being designed in for future upgrade capabilities. An ideal pupil would match the shape of the image formed of the primary and would track its rotation. For different pupil shapes without tracking we model the additional exposure time needed to achieve the same signal to noise of an ideal pupil and determine that a set of fixed masks of different shapes provides a mechanically simpler system with little compromise in performance.

4.1 Introduction

Liger is a next generation adaptive optics-fed integral field spectrograph (IFS) and imager being designed to utilize the upcoming Keck All-Sky Precision Adaptive Optics (KAPA) upgrade. Liger will provide improvements over existing instruments, operating at spectral resolving powers up to R$\sim$4,000-10,000 over a wavelength range of 0.8-2.4μm. The Liger imager will provide a 10mas per pixel plate scale with a field of view of 20.4x20.4 arcseconds. The design of the Liger imager draws on the heritage of the existing OSIRIS imager (Larkin et al., 2006; Arriaga et al., 2018) at Keck while the spectrograph is adapted from the extensive design work done for the InfraRed Imaging Spectrograph (IRIS; Larkin et al., 2016), the first light instrument for the Thirty Meter Telescope (TMT). The Liger IFS will be a duplicate of IRIS and become a pathfinder instrument for it's development, while the imager is being custom designed for Liger. A more complete overview of the Liger instrument is provided in Wright et al. (2020).

Here we present the design of the Liger filter wheel and pupil stop. The imaging camera serves as the reimaging optical system for the spectrographs, so these elements (as well as the rest of the imager optics) will be simultaneously used by the spectrograph. This allows for improved AO correction in the imager as well as improvements in masking the thermal background for the IFS by making use of the larger pupil located in the imager. The key requirements for the design of the filter and pupil wheels are listed in Table 4.1 below.

4.2 Filter Wheel

The design of the filter wheel draws from the heritage of the OSIRIS imager upgrade (Arriaga et al., 2018), but is expanded to provide a significant increase in the number of available filter slots. In order to provide a sufficient number of filter slots and fit the volume of the Liger cryostat, we make use of three stacked filter wheels. Each wheel has it's own dedicated motor, switches, and detent, but follow the same design. A model of this three wheel design is shown in Figure 4.1.

Table 4.1: Filter and Pupil Wheel Requirements

Parameter	Value
Operating Temperature	77 K
Operating Pressure	10^{-5} Torr
Shock Load	4g (+ gravity)
Resonant Frequency to Avoid	$8-80$ Hz
Time for Configuration Change	30 seconds
Filter Wheel	
Minimum of Filters	42
Filter Diameter	1.5 in
Filter Tilt	3° parallel to bench
Clear Aperture	36 mm
Repeatability (radial)	1.5 mm
Pupil Wheel	
Positioning Tolerance (radial)	150 μm
Positioning Tolerance (along beam)	2 mm

Each wheel consists of 18 filter slots for a total of 51 available slots (1 slot per wheel will need to be a clear aperture). Each filter will be placed in a cylindrical housing sandwiched between 3.5 mm spacers assembled so as to give each filter a 3° tilt. This complete filter assembly is shown in Figure 4.2a and will be mounted to the filter wheels as a complete unit. The position of each wheel is determined by a set of six binary switches, with each filter position corresponding to a unique combination of open and closed switches. A corresponding "switch activator ring" is attached to each wheel with slots for the needed "open" positions. A detent with an independent arm for each wheel aids in holding the wheels in a stable position after they are moved to the desired slot and the stepper motors are turned off.

The front wheel will be located 50 mm behind the pupil plane at which point the beam will be 25.8 mm in diameter. The exit of the last filter wheel is ~ 43 mm behind this point. The beam diameter by this point will be 29.4 mm. We will be using 1.5 in (38.1 mm) filters mounted with a retainer of diameter 36 mm. The filters are held with a 3° tilt, making the projected clear aperture area 35.95 mm. This leaves 3.28 mm radially for tolerance in positioning (with greater tolerance at the first two wheels) before vignetting will occur. The stepper motors being used to position

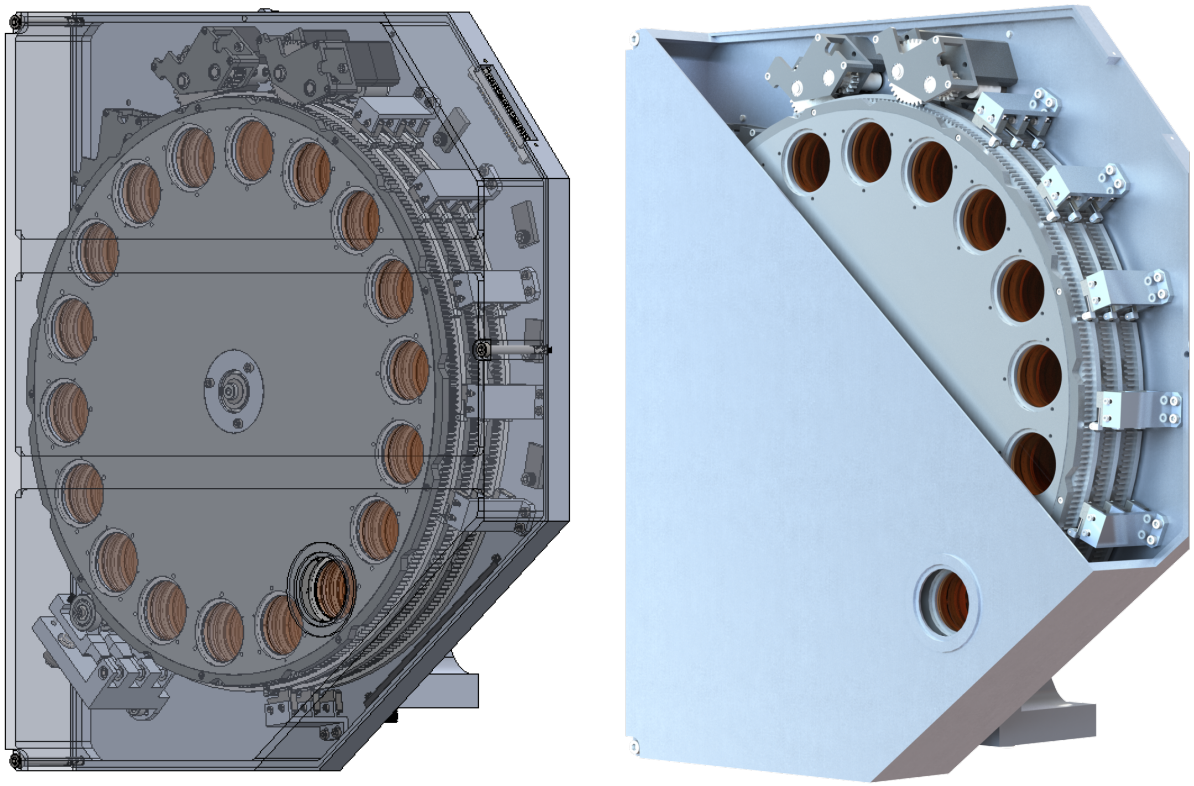

Figure 4.1: Model views of the full Liger filter wheel assembly. There are 18 filter slots per wheel with one reserved for a clear aperture. (a): Full assembly with transparent housing to show internal components. The motors for each wheel are mounted at the top of the housing on the opposite side with individual spur gear assemblies (see Figure 4.2b) interfacing with the wheels. A stack of three detents are located in the bottom right (see Figure 4.2c). These detents will provide enough force to hold the filter wheel in a stable position during operation of the imager. Along the right side and bottom of the filter wheel are six stacks of switches which will indicate the position of each wheel. The rectangular tabs route the cables from the switches to the feedthrough at the top of the housing. (b): Photo-realistic rendering of the filter wheel model. The production version will differ in that the housing and any components in the beam path will be painted black to reduce scattered light.

the wheels have a step angle of 1.8° and a step accuracy of 3%. With the gear ratios discussed in Section 4.2.1 and filters located at a radius of 145mm, this results in a positioning accuracy of 0.2mm radially from the center of the optical beam. There then remains 3.08 mm in tolerance for the manufacturing and positioning of the wheels.

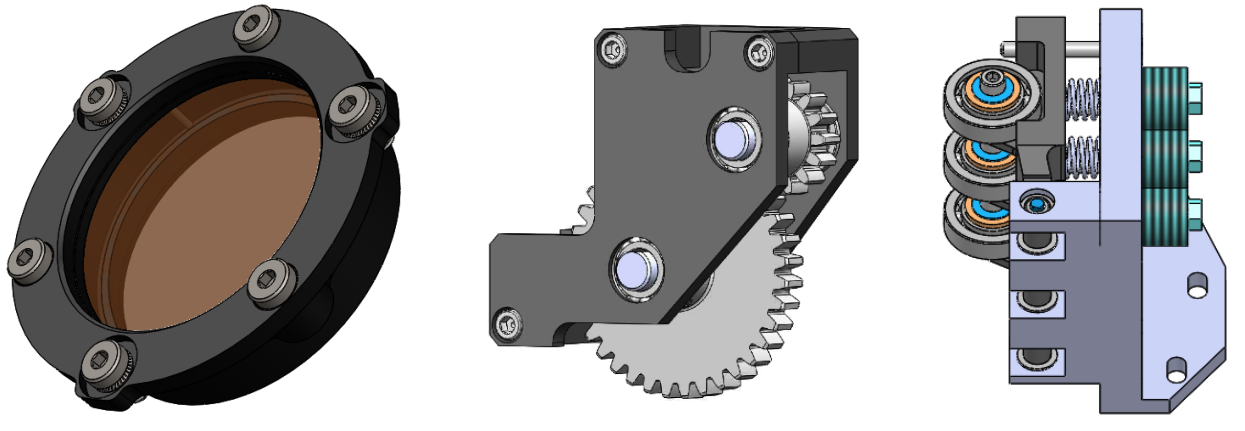

(a) (b) (c)

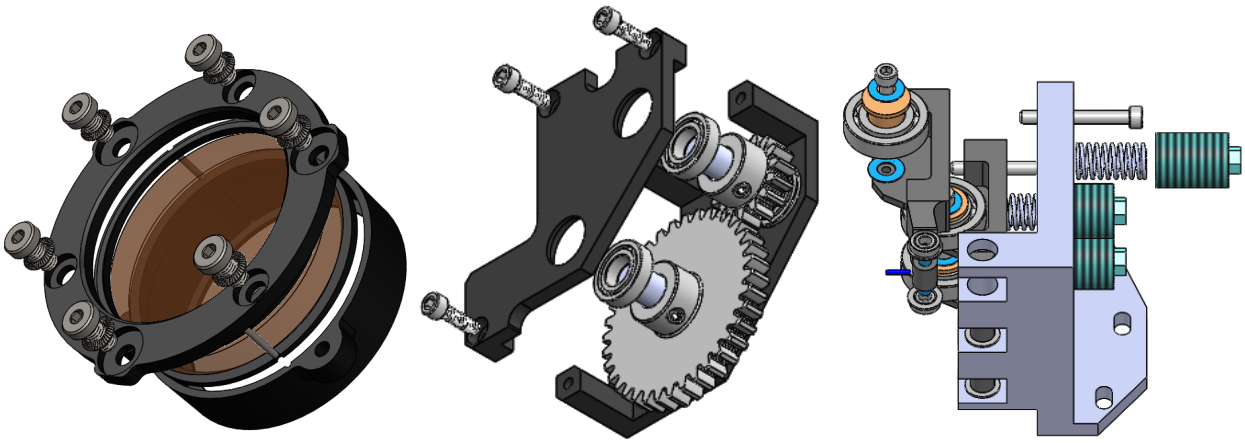

(d) Filter Assembly (e) Spur Gear Assembly (f) Detent Assembly

Figure 4.2: Close up views of key components of the Liger filter wheel. (a,d): Mounting assembly for individual filters; this is similar to the design currently used in the OSIRIS imager expanded for larger 1.5 in filters. Spacers (black) with a 3° tilt are placed on either side of the 1.5 in diameter filter (transparent orange) inside the housing. These are held in by the retainer ring which also secures the assembly in the filter wheel. The direction of the tilt is set by aligning notches cut into the spacers and retainer ring and inserting a pin to prevent rotation. (b,e): Spur gear assembly which will be the interface between the stepper motors and the filter wheels. The pinion will be directly coupled to the stepper motor shaft with the larger gear mated to the gear teeth on the filter wheel. Ball bearings are pressed into the housing (dark grey) on each side of the assembly to support the shafts. Since the three filter wheels are stacked, aluminum spacers will be used to set the height of two of these assemblies. (c,f): Detent assembly with three independent arms to maintain accurate positioning of the filter wheels. The spring connected to each detent arm will be compressed by at least 0.08 in via the threaded spring housing (dark green) on the back of the detent in order to provide the proper amount of force to prevent the wheel from slipping. The roller bearings are where contact will be made with the filter wheels so that they are able to rotate when the stepper motors are active.

4.2.1 Motor and Gearing

If we assume a filter change should be completed in 10 seconds for an initial calculation, then we would require a rotation speed of ∼6 rpm at the filter wheel. Generally, the rotation speed from the motor is dependent on the current provided and torque required, but this is a low torque application that should not put any significant strain on the motor. As a starting point to design a gear train we assume a nominal output speed of 150 rpm. This requires a significant speed reduction and gear ratio of 25:1, requiring more than a single interface. We therefore design a simple assembly making use of a 15 tooth pinion and a 36 tooth idler gear. The idler gear then interfaces with the 334 tooth filter wheel. We check for interference making use of the following equation (Budynas and Nisbett, 2011) for the minimum number of teeth needed on the pinion:

$$N_p = \frac{2k}{(1+2m)sin^2\phi}\left(m + \sqrt{m^2 + (1+2m)sin^2\phi}\right) \tag{4.1}$$

where $k = 1$ for full-depth teeth, ϕ is the pressure angle (20°), and $m = N_G/N_p$, the ratio of teeth on the gear and pinion. The interface between the pinion and idler gear gives a minimum number of teeth on the pinion of 14, so the 15 tooth pinion will not lead to interference. For the second interface between the idler gear and filter wheel the minimum number of teeth on the idler gear is 16, so the 36 tooth idler gear does not lead to interference here either. If we were to remove the idler gear, we would have $m = N_G/N_p = 334/15$ resulting in a minimum of 17 teeth on the pinion to avoid interference. Therefore, the idler gear is required to maximize the speed reduction and avoid interference. It should be noted that this achieves a gear reduction of ∼22:1, but further reduction would require a more complex mechanism to avoid interference. With this ratio the motor would need to be driven at an acceptable 140 rpm in order to achieve a wheel rotation speed of 6 rpm.

The assembly of these spur gears is shown in Figure 4.2b and included in the full filter wheel assembly of Figure 4.1. For the two wheels further from the mounting plate, simple spacers and shaft couplings are used to align and mate the gears with the motor and filter wheels.

4.2.2 Detent

In order to maintain stable positioning of the filter wheel after moving to the correct slot, as well as repeatability over time, we make use of a detent and corresponding catch ring for each filter wheel. The mechanism consists of a lever arm pinned at one end with a spring attached near the other end pushing the arm into the catch ring. A ball bearing is attached to the lever arm providing the physical interface to the catch ring in order to allow the filter wheel to rotate when the stepper motor is activated. The detent assembly consists of three lever arms and springs which independently interface with the filter wheels. In order to fit a stack of three detents without interference with the other wheels, bearings 1/4in larger in diameter were required than in the OSIRIS counterpart. This increased the space radially between the point of contact with the wheel and the rest of the detent assembly, allowing the switch activator rings of each filter wheel to pass between the separated bearings while keeping the design of the detent arms consistent with the OSIRIS imager upgrade. A model of the stacked detent is shown in Figure 4.2c, and the interface between this mechanism and the filter wheels is shown in Figure 4.3.

The spring selected for the detent mechanism must provide enough force to the filter wheel to prevent slipping but not forward driving from the motor. In order to determine the range of potential springs we first calculate the amount of torque needed to prevent the filter wheel from slipping due to mass asymmetries. Based on a solid model of the rotating components of the filter wheel the center of mass is located at a distance of $0.27\,\text{in}$ from the center. This produces a maximum torque of $29\,\text{oz}*\text{in}$ when it is at 90°.

A standard spring should not reasonably prevent the stepper motor from moving the filter wheel, but we calculate this upper limit as a sanity check. At the motor speed of $140\,\text{rpm}$ determined in Section 4.2.1, the output torque should be $\sim 31\,\text{oz}*\text{in}$. The second spur gear in the assembly described above is an idler gear so the torque transmitted to the filter wheel is simply dependent on the ratio of the filter wheel and pinion radii: $\tau_{wheel} = \frac{r_{wheel}}{r_p}\tau_{motor}$. This results in $\tau_{wheel} \sim 690\,\text{oz}*\text{in}$; setting the upper limit of the torque that could be applied by the detent while still allowing rotation of the filter wheel by the motor.

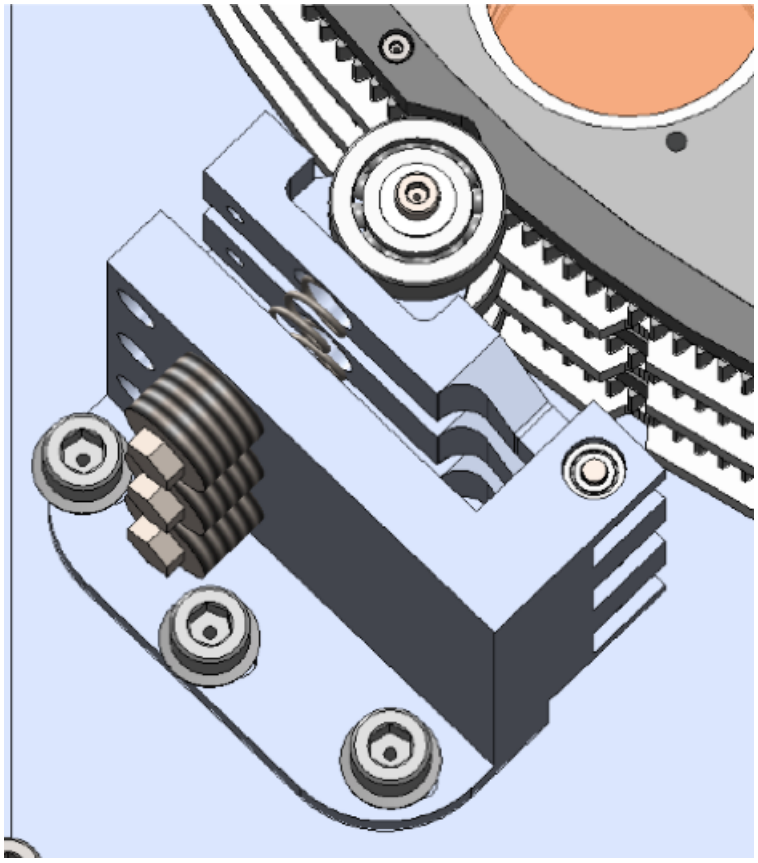

Figure 4.3: Filter wheel model showing the interface between the wheel and the detents. The detent is planar with the black catch ring which will be attached to the main wheel. This ring has notches cut into the perimeter which correspond with each filter position. The bearing on the detent arm will rest in this notch with the spring providing enough force to prevent the wheel from slipping when holding a set position.

Based on the location of the detent and a spring compression and angle of contact between the detent and wheel along with an initial assumption for the spring compression of 0.1 in, this results in a required spring constant, k, between $5.2 - 124.1\,\mathrm{lb_f\,in^{-1}}$. We therefore choose a spring with $\mathrm{k} = 18.03\,\mathrm{lb_f\,in^{-1}}$, requiring ~ 0.35 in of compression ($\sim 3\times$ the assumed minimum). As expected, this will not interfere with movement of the filter wheels when the stepper motors are active. Further, we can assume $\sim 10\%$ loss in spring constant over time. This would lower the actual spring constant to $\mathrm{k} = 16.23\,\mathrm{lb_f\,in^{-1}}$, still well within the allowed range.

4.2.3 Load Analysis

The filter wheel mounting must be able to endure not only the static load under gravity, but also an additional 4g of shock load that may be experienced during shipping and/or operation. The stress experienced in the mount was checked both analytically and computationally using the SOLIDWORKS Simulation tools.

First, during normal operating conditions with only the static load due to the weight of the filter wheels and housing, the stress throughout the filter wheel must be less than the yield strength of the material ($S_y = 276\,\text{MPa}$ for aluminum) and the deflection must be small enough that there is no vignetting of the beam. This is first checked analytically by approximating the area over which the load is experienced with the width of the bracket (160 mm) and its thickness (20 mm). The first-order approximation of the stress is then simply $\sigma = F/A$ where A is the area of the beam, and the weight of the wheel under gravity provides the load, F. This results in $\sigma = 53\,\text{kPa} << S_y$. This is a rough approximation of the stress in the aluminum bracket, but indicates the result is nowhere near the yield strength of the material. More accurate modeling is performed in SOLIDWORKS, particularly to identify areas of stress concentration such as the mounting bolts.

The second requirement for stability is that the deflection of the filter wheel and mounting bracket under its own weight is small enough that there is no vignetting of the beam. This is estimated by approximating the mounting bracket as a beam with one fixed end and a bending moment at the other. This bending moment is caused by the weight of the wheel acting at the assemblies' center of mass 23.6 mm away from the mounting bracket. The maximum deflection at the end of the beam is given by the formula $\delta_{max} = \frac{ML^2}{2EI}$, where L is the height of the bracket, $E = 68.9\,\text{GPa}$, the Modulus of Elasticity for aluminum, and I is the moment of inertia of the cross-section. This resulted in a $\delta_{max} << 1\,\text{mm}$, and therefore the design of the bracket is not a concern unless a stress concentration shows in the SOLIDWORKS Simulation or the connection between the bracket and wheel causes excessive deflection.

Next, the stress and deflection experienced throughout the filter wheel mounting is simulated with a simplified version of the model where just the mounting bracket and wheel housing

components are included. The remainder of the assembly is approximated by including the weight of the filter wheels as three remote masses located at their centers of gravity. The fasteners between the model components are included with the required pre-load for their size and the contact radius of the corresponding washer. SOLIDWORKS then evaluates both the stress and deflection under the supplied loads. This is first performed with only the static load due to the weight of the assembly (including the force input for the weight of components excluded in the simplified model). The highest stress in the model is located under the M8 bolts between the filter wheel housing and mounting bracket, but still gives $\sigma_{max} < 2S_y$, meeting the required factor of safety of 2 (Figure 4.4). The inclusion of an oversized washer under the bolt in addition to the belleville washer provides an added reduction in the stress. The deflection of the model is also evaluated in this simulation, and as can be seen in Figure 4.4, this is below 1 mm throughout.

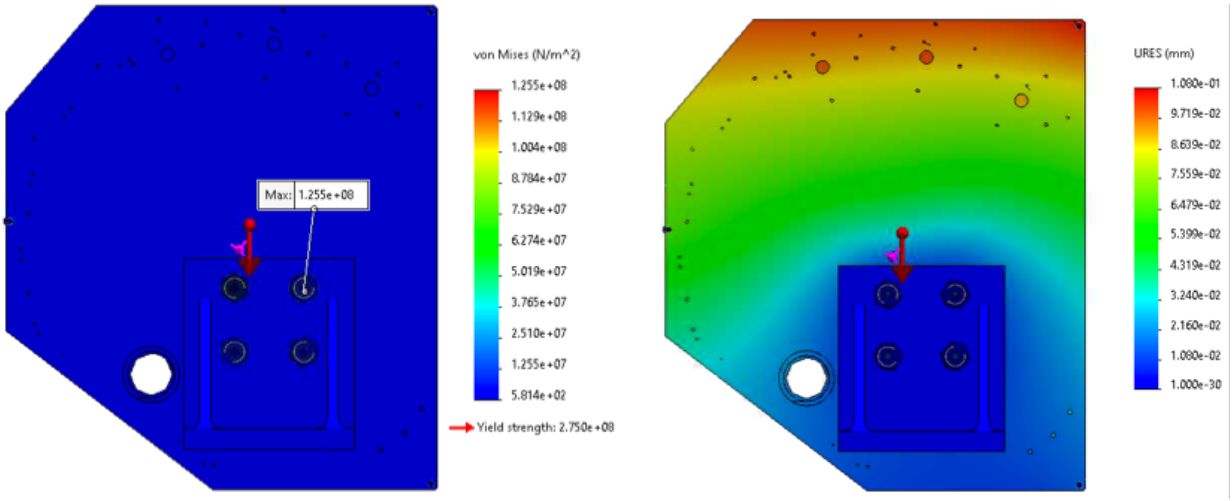

Figure 4.4: SOLIDWORKS Simulation results for stress (LEFT) and deflection (RIGHT) of the filter wheel housing and mounting bracket under static load due to gravity. The stress is below yield everywhere and the maximum deflection is < 1 mm.

The filter wheel must also be able to withstand an additional 4g load during shipping and operation. This is simulated by adding an additional source of loading to the simulations. A load of 5g was added in each direction (individually) for an additional factor of safety and to incorporate the possibility for the assembly to be oriented in different directions during shipping. With the load

added in the y-direction (adding to the weight of the filter wheel assembly), σ_{max} is still $< 2\,S_y$ (see Figure 4.5), and deflection is $< 0.1\,mm$ at the location of the filter window. The maximum stress is at the same location and amount as in the static case, meaning that the pre-load on the bolt will be the largest contributor of stress and the load of the filter wheel itself and any impact load will be well distributed and well tolerated. Adding the 5g load on the side or back of the filter wheel mounting plate results in a similar $\sigma_{max} \sim 125\,MPa$ at the M8 bolts. This is still $< 2\,S_y$ and should not result in damage to the mount.

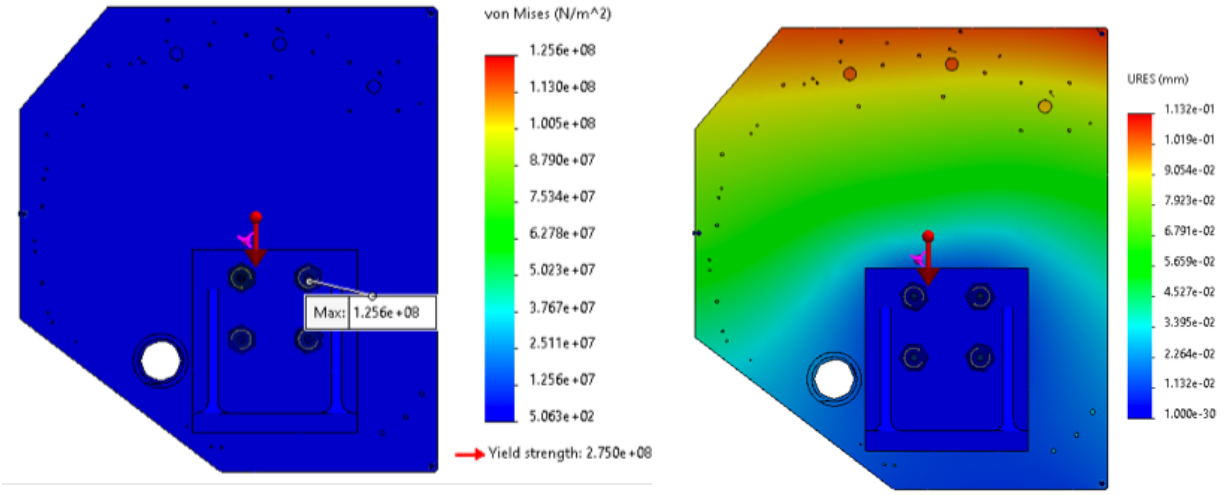

Figure 4.5: SOLIDWORKS Simulation results for stress (LEFT) and deflection (RIGHT) of the filter wheel housing and mounting bracket under a 5g impact load in addition to its own weight. The stress is below yield everywhere and the maximum deflection is $< 1\,mm$.

4.2.4 Modal Analysis

The instrument requirements from the Keck Observatory list frequencies that can be expected in the range of $10 - 40\,Hz$ during shipping and $8 - 80\,Hz$ during operation, so the resonant frequency of the mechanism should be at least $> 80\,Hz$. A frequency analysis was run in SOLIDWORKS Simulation using the same simplified model as the load analysis with only the filter wheel mounting components and housing in order to estimate the resonant frequencies. The mass of each wheel is again added as a remote load offset from the mounting point with the force of gravity included. The

simulation was run searching for the first five frequency modes with the results in Table 4.2 along with the mass participation factor for each mode.

Table 4.2: Frequencies and mass participation for the first five modes of the filter wheel mounting

Mode	Frequency (Hz)	Mass Participation (%)		
		X-direction	Y-direction	Z-direction
1	151	3	0	0
2	93	0	11	7
3	107	5	0	0
4	132	0	0.1	20
5	202	0	0	0.1

The frequencies determined in the simulations meet the requirement to be > 80 Hz. However, it should be kept in mind that this is a simplified model that leaves out the internal components mounted to the filter wheel housing, but also leaves out the rest of the instrument and cryostat which should provide a significant amount of vibration isolation for sources outside the instrument.

It can be seen in Table 4.2 that the SOLIDWORKS frequency analysis gave the somewhat unexpected result that the first modal frequency is higher than the next three. This seems to be due to the inclusion of loading in the form of gravity and remote masses for the three filter wheels. With no loads on the simplified filter wheel assembly, the first modal frequency is at 127 Hz with the next four increasing in frequency.

4.3 Pupil Wheel

Unlike our predecessor, the OSIRIS imaging camera, the Liger pupil masks will be held in a dedicated mechanism at the pupil plane rather than being included with the filter wheel. The pupil wheel contains slots for seven unique pupil masks as illustrated in Figure 4.6. The overall design of the pupil wheel will mirror that of the filter wheel; making use of the same motor and switches along with a similar detent mechanism. However, the positioning of the pupil masks requires higher precision than the filters and therefore some additional components will be needed. In addition to a detent arm keeping the wheel from slipping, the wheel will be pinched between spring loaded

bearing mechanisms at three locations in order to keep it planar (see Section 4.3.2).

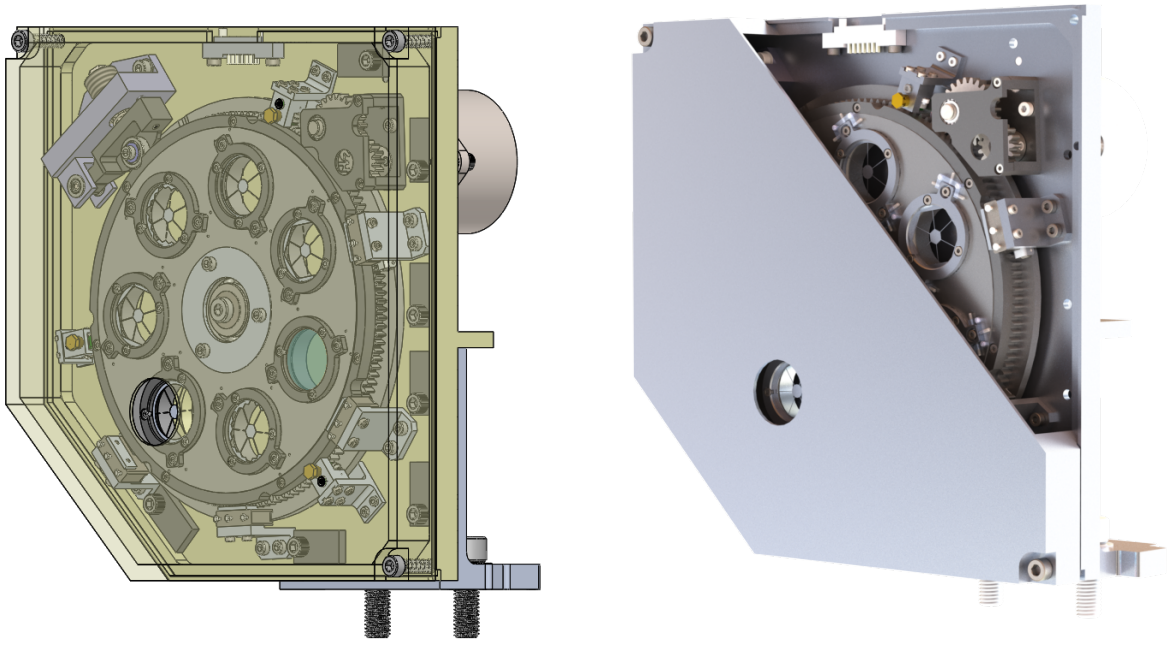

Figure 4.6: Model view of the current design for the Liger pupil wheel assembly with a photorealistic rendering on the right. The same motor as the filter wheels is mounted at the top right with a unique spur gear assembly. A single detent is located in the top left which is a more compact version of the one in the filter wheel. Four switches and the three spring loaded bearing mechanisms shown in Figure 4.10 are located around the perimeter of the wheel. The rectangular tabs route the cables from the switches to the feedthrough at the top of the housing. Potential standard pupil masks are shown in six of the seven available slots: two each of the annular, hexagonal, and matched hexagon (matched to the edges of the primary mirror) patterns, while a transparent blue aperture denotes a slot for the vector-APP coronagraph. The exact pupil masks that will be used have yet to be determined.

A set of standard masks are currently planned to be used in conjunction with the pupil wheel following the inscribed circle, hexagonal, and matched hex shapes, optimized to the short and long ends of the Liger wavelength coverage, as well as specialty masks such as a vector Apodizing Phase Plate (vector-APP) coronagraph. This unique type of coronagraph is designed for use at the pupil plane to provide an increase in contrast for directly imaging exoplanets by creating a dark hole in the point-spread-function (PSF) of the host star (Snik et al., 2012). Each of these masks will be mounted to the pupil wheel in a standalone case with two alignment tabs as shown in Figure 4.7.

These tabs will be used to perform small shifts in the position of each mask in order to meet the required 150 μm radial positioning tolerance.

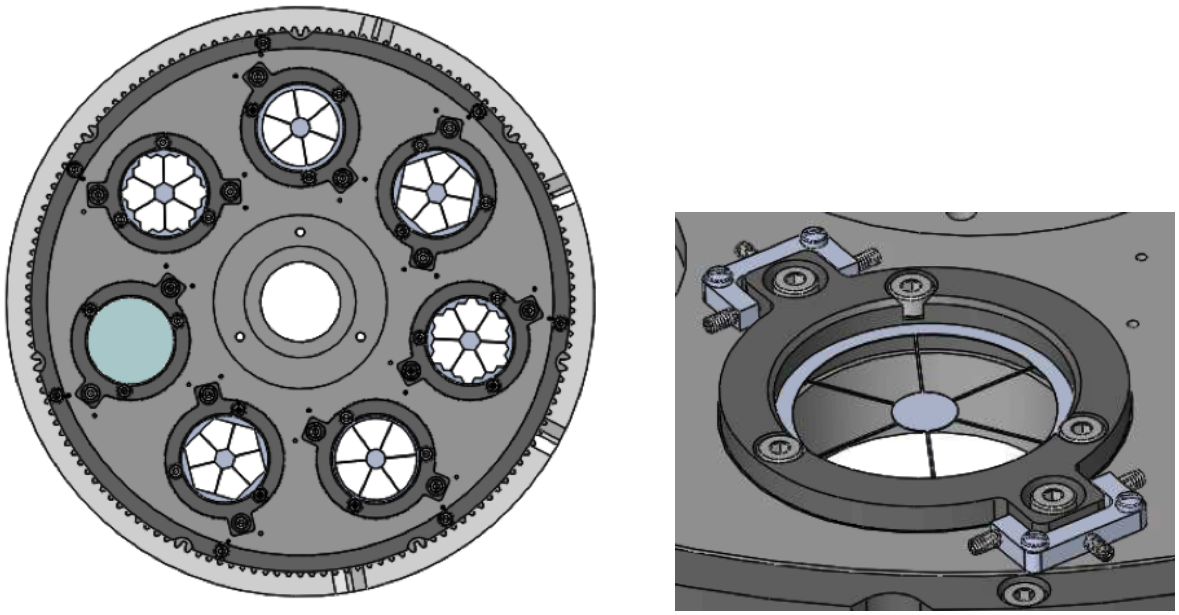

Figure 4.7: LEFT: Model view of pupil wheel components with pupil masks installed. RIGHT: close-up view of the mounting for a single pupil mask with the corresponding alignment hardware. The light gray aluminum "U"-shaped brackets on each side are fastened to the wheel and the three set screws are used to push the tab on the dark gray pupil mask holder in order to achieve the correct alignment. When each mask is aligned these brackets and set screws are removed leaving the components shown on the left.

The use of a dedicated mechanism to house the pupil masks allows the possibility of adding rotating masks rather than fixing their orientation. This would add significant complexity to the design, so we therefore performed a trade study to determine the signal-to-noise gains of this functionality.

4.3.1 Pupil Simulations

We simulate the background noise difference between using a mechanically fixed pupil mask and a rotating pupil to match the field rotation on sky. We use the Keck pupil plane simulations from Arriaga et al. (2016) which give a model of the throughput and background emission as a

function of position as the basis for this study. These models were developed using images from the pupil-viewing mode of NIRC2 with the Kp ($\lambda \sim 2.124\mu$m), PAH ($\lambda \sim 3.290\mu$m), and Br-α ($\lambda \sim 4.052\mu$m) filters; we limit this analysis to the Kp filter as PAH and Br-α fall outside the wavelength coverage of Liger.

The pixel scale was updated to the 10mas scale of the Liger Imager. Masks were generated in the large-hex, inscribed circle, and matched hex shapes to calculate the Signal-to-Noise Ratio (SNR) with different mask configurations. The dimensions of the masks were also taken from the optimization of Arriaga et al. (2016). The SNR was calculated with a mechanically fixed mask (giving relative rotation between the image pupil and the mask) as well as a rotating pupil mask which would counter this relative motion keeping the orientation of the image pupil and the mask fixed. The "signal" in these simulations is simply a value of $1\times$(exposure time) wherever the mask is not present. Therefore the relative SNR between the rotating and fixed pupils is the important parameter. In order to quantify this we evaluate the additional integration time needed with a mechanically fixed mask to reach the same SNR as a mask that rotates. This additional time is reported in Table 4.3 for a reference exposure time of 600s. In order for this to be an accurate representation of the difference between the two scenarios we take into account the affects of pupil mask misalignment and pupil nutation which we discuss in more detail below.

Table 4.3: Additional exposure time needed with a fixed mask to reach the SNR of a 600s integration with an ideal rotating pupil mask.

Mask	Elevation (°)	Additional Exposure Time (s)
inscribed circle	20	25
	30	25
	50	35
	80	25
hex	20	30
	30	30
	50	30
	80	45
matched	20	40
	30	30
	50	35
	80	65

In images taken with the NIRC2 pupil viewing camera (Figure 4.8), it is clear that there is a slight misalignment between the mask and the pupil image. This misalignment is expected to be present in any system due to the very fine precision needed to perfectly align the mask and to then keep it aligned over time while moving different masks in and out of the beam (particularly if the mask is to rotate). We add a conservative relative offset of 4.5cm at the plane of the primary mirror between the mask and the pupil image in our simulations to match that seen in Figure 4.8. This is equivalent to a 0.1mm misalignment at the pupil plane. The real system may have a larger offset than this over time after repeated cycles of changing pupil masks.

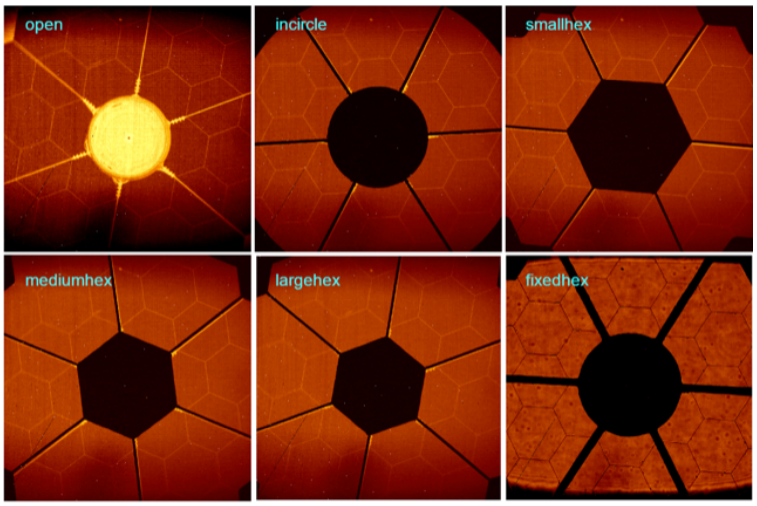

Figure 4.8: Images taken in March 2019 with the NIRC2 pupil imaging camera in the Kp filter after the most recent upgrade to the instrument showing the relative alignment between the pupil stop and the telescope pupil. All images were taken with the dome closed except for the bottom right. We match the offset seen here to define the alignment accuracy of the pupil masks in our simulations.

The other affect we incorporate into these simulations is nutation of the pupil, which is dependent on the elevation of the telescope and the AO K mirror rotation angle. This results in an offset between the pupil image and the nominal location of the pupil mask. The affect is most pronounced at large elevations where there is a higher rate of field rotation. This diminishes the effectiveness of a rotating pupil mask in the regime where it would otherwise be the most useful. In order to quantify the expected offset between the pupil and mask center, we make use of observations performed with the pupil viewing mode of the OSIRIS imager. Exposures of the telescope pupil

without masks in place were taken at a range of telescope elevation and rotator angles. The center of the telescope pupil on the OSIRIS detector is determined from these images and converted to position in cm at the plane of the primary mirror. For elevation angles above 60°, we determine an offset of (10, 8.5) cm in (x,y) at the plane of the primary mirror. For elevation angles between 45°-60° we apply an offset of (8, 7) cm, and for elevation angles between 30°-45° we apply an offset of (6.5, 6) cm. We do not apply any offset below an elevation of 30°, though there likely is some. At each elevation, the pupil offset varies with the angle of the AO K mirror, so we use a conservative estimate of the typical offset for inclusion in these simulations. Figure 4.9 shows the alignment of the "hex" mask and pupil image at each of these elevation ranges.

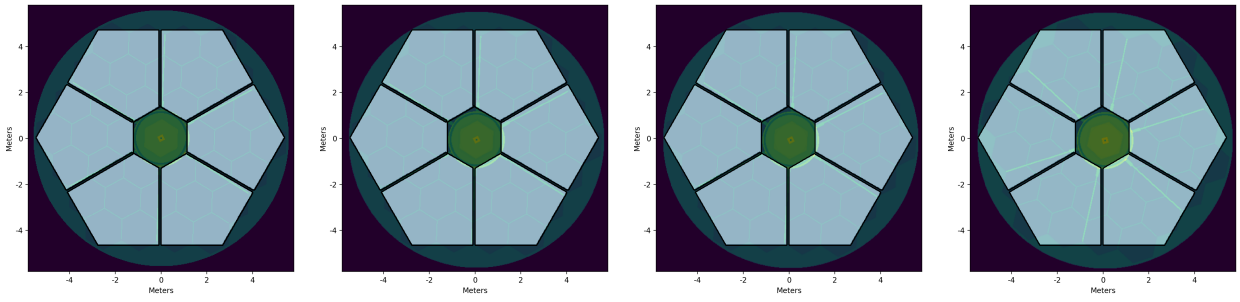

(a) 20° (b) 30° (c) 50° (d) 80°

Figure 4.9: Models of the Keck pupil and background at 4 different elevations with center offsets derived from OSIRIS imaging. The scale of the models are shown in meters projected on the plane of the primary mirror. As one can see, the deviation of pupil centers increases with higher elevation. The rotation of the pupil image after 600s (starting with the mask aligned) is also shown here. The rate of this rotation also increases with elevation.

This diminishes the difference in exposure time for the two cases being modelled to what is reported in Table 4.3 for all elevation angles. Therefore we will proceed with a pupil wheel design in which individual masks *do not* rotate. The current design of the pupil wheel with the fixed masks is shown in Figure 4.6.

4.3.2 Planarity

The alignment of the pupil masks needs to be consistent over time and between different masks. To help ensure this is met, axial bearings are added in three locations evenly spaced around

the perimeter of the wheel. As can be seen in Figure 4.10, this uses a spring in compression to pinch the wheel between two bearings. This allows the wheel to turn freely, but holds it from wobbling in/out of the plane. This spring will be adjusted in order to provide enough force to maintain planarity of the pupil wheel.

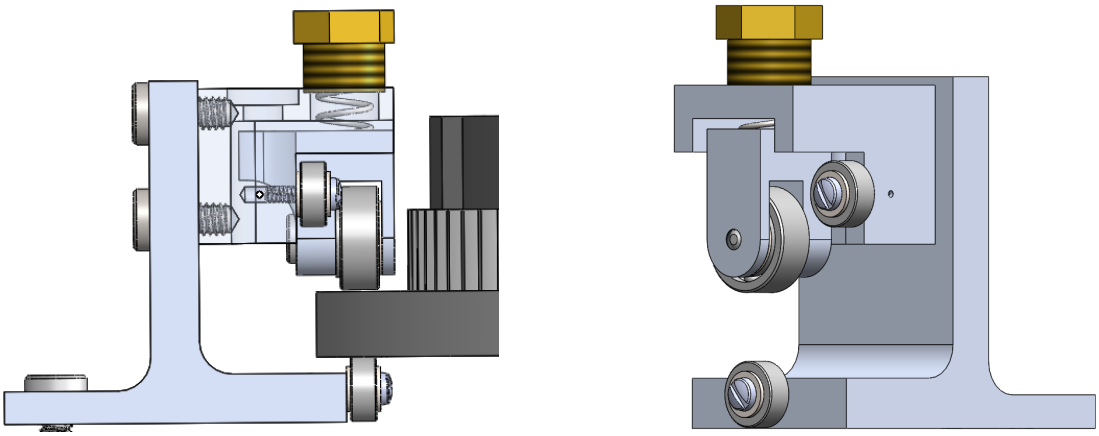

(a) (b)

Figure 4.10: Spring loaded bearing mechanism to maintain planarity of the Liger pupil wheel. The spring at the top will be compressed to provide downward force through the upper bearing to the switch activator ring (light gray) which extends radially outward from the pupil wheel (silver). Three of these mechanisms will be located symmetrically around the pupil wheel.

To determine the required load provided to the pupil wheel from each of the axial bearings, a SOLIDWORKS Simulation was performed with only the pupil wheel. The wheel was fixed where it would be mounted to the axle and loads due to gravity as well as the three bearings were applied. This was run under two conditions: 1 mm and 2 mm of compression in the axial spring to check the amount of deflection across the active pupil mask in both scenarios. The results are shown in Figure 4.11.

4.3.3 Load Analysis

The stability of the mounting bracket was verified under the static load due to the weight of the pupil wheel as a remote mass at its center of gravity ($m = 0.5\,kg$) using a simplified model of the assembly in SOLIDWORKS as in the filter wheel case described in Section 4.2.3. The maximum

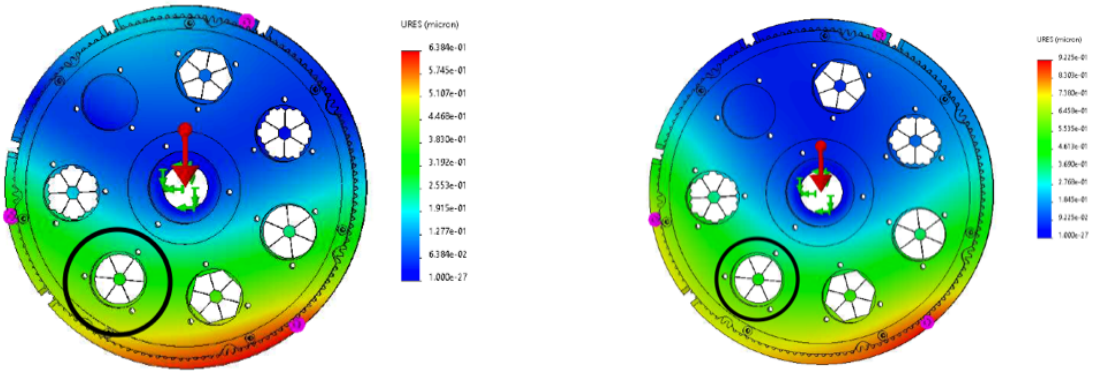

(a) 1 mm (b) 2 mm

Figure 4.11: Deflection of the pupil wheel under gravity with the load of three axial bearings (pink) with 1 mm (LEFT) and 2 mm (RIGHT) of compression in the springs. In both cases the deviation from planarity of the pupil mask in the operational position (circled in black) is $< 1\,\mu$m.

stress experienced by the bracket in the simulation was $< 1/2$ the yield strength of aluminum ($S_y = 276\,$MPa). The deflection/deformation of the mounting plate must also be small enough that no vignetting of the beam is expected to occur. The maximum deflection found in the simulation under normal load is 0.04 mm, but the deflection at the location of the active pupil mask is $\sim 8\,\mu$m (Figure 4.12).

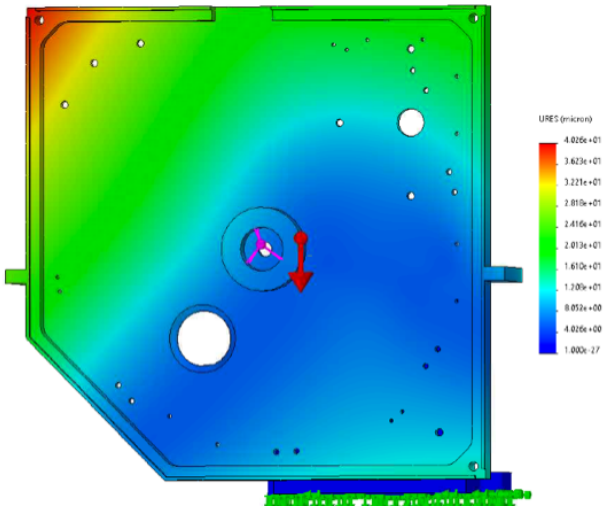

Figure 4.12: SOLIDWORKS Simulation results for deflection of the pupil wheel housing and mounting bracket under static load due to gravity. The stress is below yield everywhere and the maximum deflection is < 1 mm with the deflection at the location of the active mask $\sim 8\,\mu$m.

The addition of a 5g shock load in the same direction as the force due to gravity (y-axis) in

the SOLIDWORKS simulations does not produce a significant increase in deflection (still $\sim 8\,\mu$m at the pupil location) with the maximum stress $\sigma_{max} \sim 1/2\,S_y$ (Figure 4.13). This is therefore not expected to cause performance issues or failure at the wheel mounting. Similarly shock loads in the x and z-directions also produce $\sigma_{max} \sim 1/2\,S_y$. These loads would only be expected during shipping but the pupil wheel is still required to withstand this type of force in order to be delivered to Keck intact. It should be noted that the maximum load in all cases is directly under the bolts securing the pupil wheel to the mounting bracket meaning that even if the actual stress were to be double the simulated value failure of the mounting would not be expected as only a small area of the part would undergo deformation.

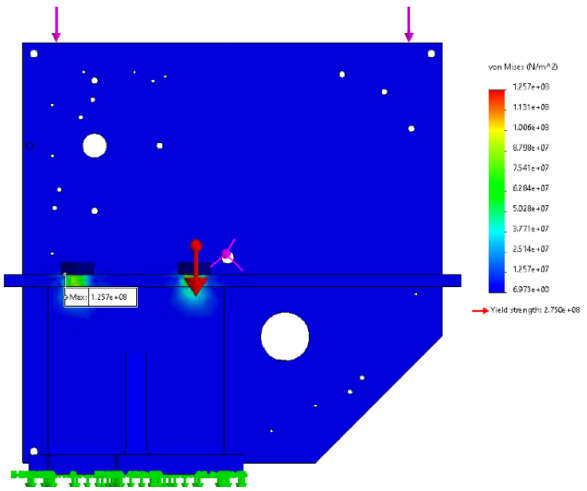

Figure 4.13: SOLIDWORKS Simulation results for stress on the pupil wheel housing and mounting bracket under static load due to gravity as well as an additional 5g shock load. The stress is below yield everywhere with the maximum located under the bolt heads.

4.3.4 Modal Analysis

Just as for the filter wheel, a frequency analysis was run in SOLIDWORKS simulation using a simplified model of the pupil wheel mounting components in order to estimate the resonant frequencies. This model is the same as the one used in the stress simulations with the pupil wheel housing added. The weight of the pupil wheel itself is accounted for in the form of a remote mass added to the simulation as in the stress calculations. The simulation was run searching for the first

five frequency modes with the results in Table 4.4. These all lie well above the frequencies to avoid $(8-80\,\text{Hz})$, and therefore resonance should not be a problem.

Table 4.4: Frequencies and mass participation for the first five modes of the pupil wheel mounting

Mode	Frequency (Hz)	Mass Participation (%)		
		X-direction	Y-direction	Z-direction
1	150	0	0	11
2	263	2	0	25
3	382	1	0	1
4	565	1	14	1
5	643	1	0	31

4.4 Summary & Future Work

We have presented the latest design of the filter and pupil wheels for the Liger imager and IFS. The full filter wheel will consist of three stacked wheels with 18 filters each (1 clear aperture). These wheels will share a common assembly but will move independently as well as having dedicated switches and detents.

A trade study was performed to determine whether adding a rotating pupil mask would provide significant enough SNR gains to justify the added design complexity. Due to the impacts of pupil nutation and mask misalignment this was determined not to be the case for Liger and we will therefore proceed with the design of a pupil wheel in which individual masks maintain a fixed orientation.

The pupil wheel contains slots for seven unique pupil masks including one slot for a specialized vAPP. The pupil wheel makes use of largely similar components to the filter wheel with a set of binary switches for positioning, the same stepper motor, and a smaller version of the filter wheel detent. Spring loaded bearings are located around the perimeter of the wheel to improve the planarity of the wheel and therefore the repeatability of mask alignment.

As demonstrated in the analysis shown here, both the filter and pupil wheels can withstand

the required loads and have resonant frequencies outside the range of expected vibrations. Both the filter and pupil wheels will be tested and assembled in a custom test chamber designed for use with Liger (Wiley et al., 2020) which will operate at a temperature below 77 K and vacuum of 10^{-5} Torr.

Acknowledgements

This research program was supported by the Heising-Simons Foundation. We would also like to thank Carlos Alvarez for providing the images of the NIRC2 pupil included in Figure 4.8.

Chapter 4, in part, is a reprint of the material as it appears in the Proceedings of the SPIE. Cosens, M., Wright, S. A., Arriaga, P., Brown, A., Fitzgerald, M., Jones, T., Kassis, M., Kress, E., Kupke, R., Larkin, J. E., Lyke, J., Wang, E., Wiley, J., & Yeh, S, *Proceedings of the SPIE*, 114474X, 2020. The dissertation author was the primary investigator and author of this paper.

Chapter 5

Liger at Keck Observatory: Imager Detector and IFS Pick-off Mirror Assembly

Abstract

Liger is a next-generation near-infrared imager and integral field spectrograph (IFS) planned for the W.M. Keck Observatory. Liger is designed to take advantage of improved adaptive optics (AO) from the Keck All-Sky Precision Adaptive Optics (KAPA) upgrade currently underway. Liger operates at 0.84-2.45 μm with spectral resolving powers of R$\sim$4,000-10,000. Liger makes use of a sequential imager and spectrograph design allowing for simultaneous observations. There are two spectrograph modes: a lenslet with high spatial sampling of 14 and 31 mas, and a slicer with 75 and 150 mas sampling with an expanded field of view. Two pick-off mirrors near the imager detector direct light to these two IFS channels. We present the design and structural analysis for the imager detector and IFS pick-off mirror mounting assembly that will be used to align and maintain stability throughout its operation. A piezoelectric actuator will be used to step through 3 mm of travel during alignment of the instrument to determine the optimal focus for both the detector and pick-off mirrors which will be locked in place during normal operation. We will demonstrate that the design can withstand the required gravitational and shipping loads and can be aligned within the positioning tolerances for the optics.

5.1 Introduction

Liger is a new integral field spectrograph (IFS) and imager in development for the W.M. Keck Observatory which will take advantage of the ongoing Keck All-Sky Precision Adaptive Optics (KAPA) upgrade. Liger (Wright et al., 2019, 2022; Cosens et al., 2020; Wiley et al., 2020) will provide a number of improvements over existing AO fed instruments including larger fields of view, finer spectral resolution (up to $R \sim 8,000 - 10,000$), and extending to bluer wavelengths ($0.84 - 2.45\,\mu$m). The Liger design draws from the heritage of two key sources: the imager component is custom designed for Liger but makes use of similar mechanisms to the Keck OSIRIS imager (Larkin et al., 2006), and the spectrograph is a clone of the design developed for the InfraRed Imaging Spectrograph IRIS (IRIS, Larkin et al., 2016, 2020; Zhang et al., 2018) — the planned first light instrument for the Thirty Meter Telescope. Like IRIS, Liger will have two spectrograph channels, a slicer and lenslet mode, which will share a common grating turret, three mirror anastigmat cameras, and detector. The Liger imager filter and pupil wheel mechanisms make use of similar gear, detent, and limit switch designs as OSIRIS, but with improvements to the number of filter slots and the presence of a dedicated pupil wheel at the pupil location (Cosens et al., 2020). For a full overview of Liger see Wright et al. (2019) and Wright et al. (2022).

Here we present the design of the assembly which will be used to mount and align the Liger imager detector as well as the pick-off mirrors which feed the two spectrograph modes. These two components require a common assembly to place the pick-off mirrors as close to the imager focal plane as possible for the best optical performance. Key requirements for the detector assembly are listed in Table 5.1.

The design of the detector-mirror assembly is outlined in Section 5.2 including the adjustability (Section 5.2.1 & 5.2.2) and baffling (Section 5.2.3) necessary to achieve the instrument requirements. In Section 5.3, structural analysis is performed to verify performance of the assembly under the loads and frequencies specified in Table 5.1.

Table 5.1: Key Requirements: Detector and Pick-off Mirrors

Parameter	Value
Operating Temperature	77 K
Operating Pressure	10^{-5} Torr
Shock Load	4g (+ gravity)
Resonant Frequency to Avoid	$8-80$ Hz
Focus Travel	3 mm
Detector	
Focus Accuracy	$100\,\mu$m
Tip-tilt Range	2°
Tip-tilt Accuracy	0.25°
Pick-off Mirrors	
Focus Offset Range	1 mm
Tip-tilt Accuracy	0.2°

5.2 Mechanism Design

The imager detector and the pick-off mirrors for the slicer and lenselt IFS are coupled to the same mounting assembly on the imager optical plate (see Figure 5.1). The pick-off mirrors for the two spectrograph channels will be made from a single piece of Zerodur. The orientation of the optics will be semi-fixed to each other; the relative z-offset (into the beam) and rotation will be independently adjustable within a small range. The alignment of the assembly in the x-direction (parallel to the optical plate and perpendicular to the beam) and y-direction (height) as well as tip-tilt for both the detector and pick-off mirrors, are adjusted manually where the assembly mounts to the optical plate. An additional tip-tilt adjustment for the detector is built into the assembly, as well as a rotation adjustment for the pick-off mirrors. The optimal z-position will be determined by moving the assembly through a range of focus positions during alignment via a piezoelectric linear actuator. This will yield the optimal offset between the detector and pick-off mirrors, that then can be adjusted via set screws. Once optimal focus is determined between the detector and pick-off mirrors the assembly is locked.

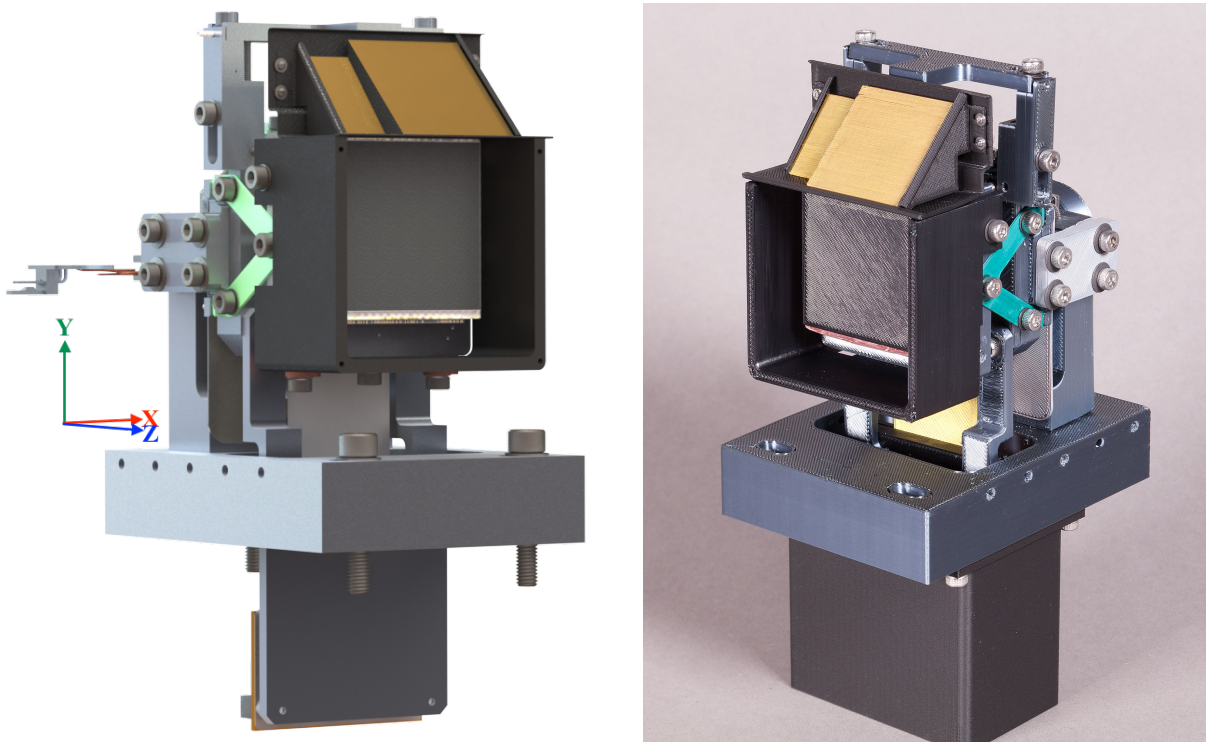

(a): rendering (b): 3D print

Figure 5.1: (a): Rendering of the Liger imager detector and pick-off mirror mounting and focus stage with all exterior baffling removed. The directional axes used throughout this paper are shown on the left hand side. The y-direction (green) is used to denote the height above the optical plate; the z-direction (blue) represents the direction of the beam path; and the x-direction (red) is parallel to the optical plate and perpendicular to the beam. The pick-off mirrors (gold) for both the lenslet and slicer IFS are made from one piece of Zerodur and are attached to the detector mounting so the two mirrors are coupled in position. A baffle snout is included around three sides of the detector which extends 12 mm in front of the detector face to block scattered light. The pick-off baffle lowers onto the top edge of this baffle snout and also extends to the same distance. The detector ASIC is held below the detector mount connected via a flexible cable. Adjustability is built into the mounting assembly in the focus position as well as the tip-tilt of the detector and pick-off mirrors. The height (y-direction) and x-direction adjustment will be made at the base of the mount. (b): A full scale 3D printed model of the same assembly with the baffling included around the ASIC. This model was built to test the planned assembly procedure.

5.2.1 Focus Alignment

The mounting assembly is designed to allow the detector and pick-off mirrors to move through a 3 mm range of possible focus positions during the alignment process. This is accomplished with the inclusion of a flexure between the mounting assembly base and the mounting points for the

detector and pick-off mirrors. The flexure is made of AISI 304 stainless steel sheet metal cut into a "U" shape that is bolted to the fixed base at the bottom and the mobile mount at the tops. As the piezoelectric linear actuator pushes on the mount, the arms of the flexure bend and extend forward as shown in Figure 5.2. To maintain planarity of the detector face throughout the travel range, two extension springs are located above the arms of the flexure connecting the fixed base to the mobile mount. The force from these springs pulls back on the top of the mount, preventing the detector face from tilting forward as the flexure bends. Two support brackets are included between the fixed base and the mobile mount. These supports have clearance slots that mate to threaded holes on the fixed base. The screws at this location will be kept loose during focus adjustment, after which the support brackets are secured to lock the assembly into place.

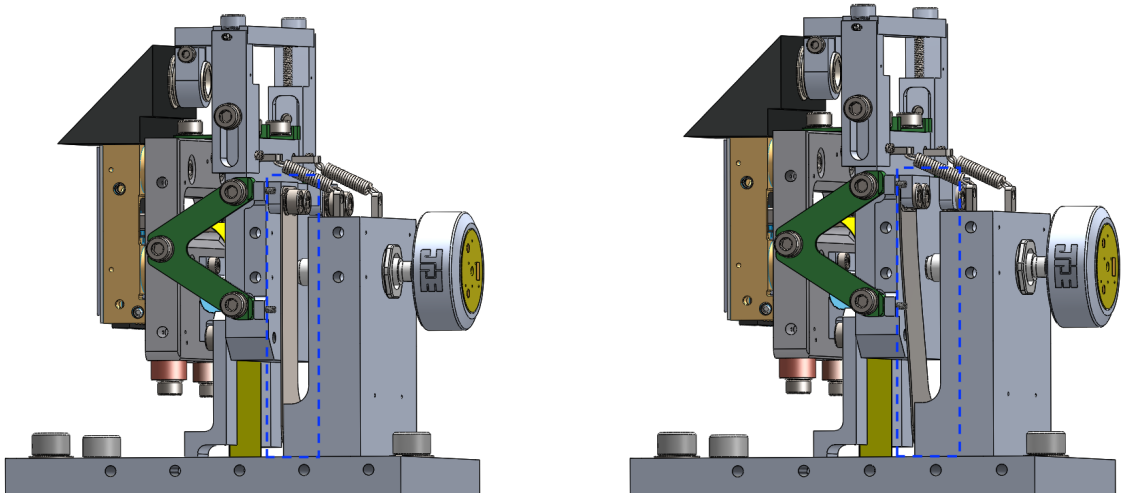

(a): neutral position (b): extended position

Figure 5.2: Side view of the detector and pick-off mirror assembly showing the AISI 304 flexure (outlined in blue) component connecting the base with the rest of the mount as well as the extension springs which maintain planarity of the system throughout the range of possible focus positions. The image on the left shows the neutral position while the right image shows the flexure and mount at the end of the 3 mm travel range. During operation support brackets will be included on each side (loosely fastened) to further maintain planarity and lock the system at the optimal focus position. The brackets are excluded from these models to show the operation of the flexure.

Both the detector and pick-off mirrors are coupled to each other as they are moved through the range of potential focus positions. There may be an offset between these best focus positions, in which case the mounting arm attaching the pick-off mirrors to the main assembly may be adjusted

by ± 0.5 mm in the z-direction with an accuracy of $100\,\mu$m.

It is important that there is no significant change in the tilt of the detector and pick-off mirrors while determining the optimal focus position. To check the planarity of the mounting block (and by extension the detector and pick-off mirrors) a simplified model is used in a static load simulation within the SolidWorks Simulation suite. The weight of the mounting assembly as well as remote masses for the detector and pick-off mirrors are included in the simulation as well as all bolts (with pre-tension) and spring parameters used in the design. The bottom of the mounting plate is designated as a fixture within the simulation. First, a baseline is determined by conducting a simulation with no force from the actuator to yield the displacement across the detector face under static load. Next a load is added at the location of the linear actuator to cause forward motion of the detector mounting. The two cases must result in a difference in the tip-tilt angles $< 0.2^\circ$ in order to meet the required tolerance. The displacement across the detector face mounting plate in both simulations are shown in Figure 5.3. As can be seen, there is a small change in the tilt of the detector mounting plane after the full 3 mm of linear motion. However, this change amounts to only 0.02°, significantly less than the 0.2° tolerance.

5.2.2 Positioning Adjustment

There are multiple adjustment points included in the detector assembly design which will allow fine-tuning during alignment. There are six degrees of freedom to the position of the pick-off mirrors and detector, although some have a limited range and/or require the use of shims at the base of the mount. Some of these adjustments cause position changes to both the detector and pick-off mirrors while others will only impact one. The separate adjustment of the detector and pick-off mirrors is particularly useful in cases where an offset is required (e.g. focus position) or when a tighter tolerance is required for one component than the other (e.g., tip-tilt).

First is the adjustment of the detector and pick-off distances in the z-direction (focus position). As discussed in the previous section, there is a flexure and actuator which allows both the detector and pick-off mirrors to be to be moved through the 3 mm focus range to find the optimal

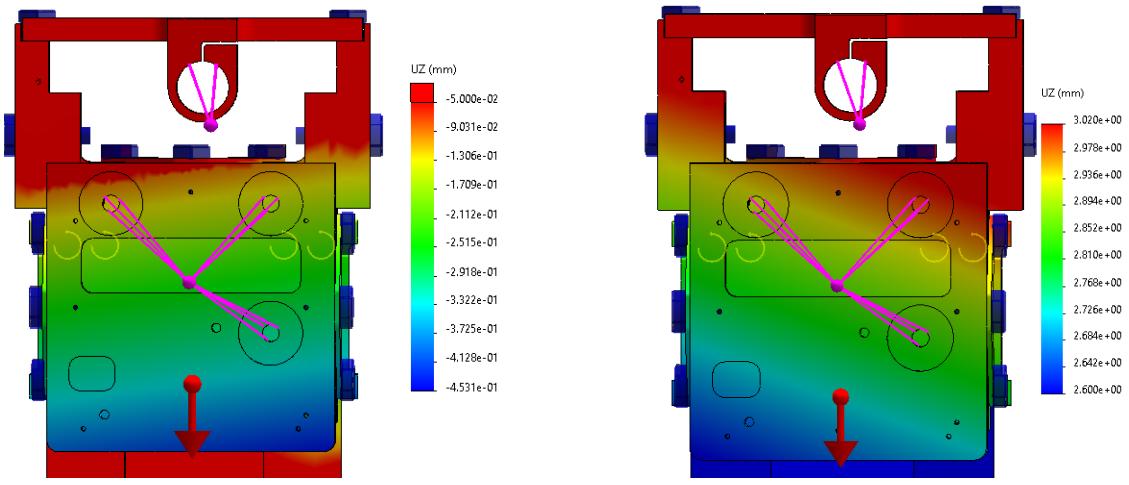

(a): neutral position

(b): extended position

Figure 5.3: Displacement from SolidWorks Simulation of static loading on detector stage at the two extremes of the focus range from 0 mm (a) to 3 mm (b). The color scales are adjusted to highlight the small deviation from planarity across the face of the front plate where the detector will mount at the three clearance holes. In (a), there is a ~ 0.4 mm difference across the face of the plate, resulting in an angle of 0.46°. At the end of the focus range shown in (b), there is a ~ 0.42 mm difference across the face of the plate, resulting in an angle of 0.48°. The change in the angle between these two extremes of the focus range is only 0.02°, much less than the tolerance in this dimension.

position. We have designed flexibility in the alignment procedure if there is an offset in the optimal position for the detector and the pick-off mirrors. If this occurs there is ± 0.5 mm over which the pick-off mirror focus position can be adjusted independently of the detector with an accuracy of $100\,\mu$m (see Figure 5.4a).

The height of the detector assembly may be adjusted by including shims between the optical plate and the mount. The height of the pick-off mirrors may be further raised above the detector in increments of as little as $100\,\mu$m using a pair of set screws. The rotation of the pick-off mirrors about the z-axis may be adjusted independently of the detector with an accuracy of 0.136° by raising either side of the frame using these same set screws. The rotation of both components can be changed by inclusion of shims on one side of the mounting plate. The position of both the detector and pick-off mirrors in the x-direction can be adjusted by pushing the assembly along clearance slots at the bolts connecting the two lowest plates shown in Figure 5.1. The pick-off mirror position can be independently adjusted in the x-direction by ± 0.25 mm with an accuracy of $75\,\mu$m using the

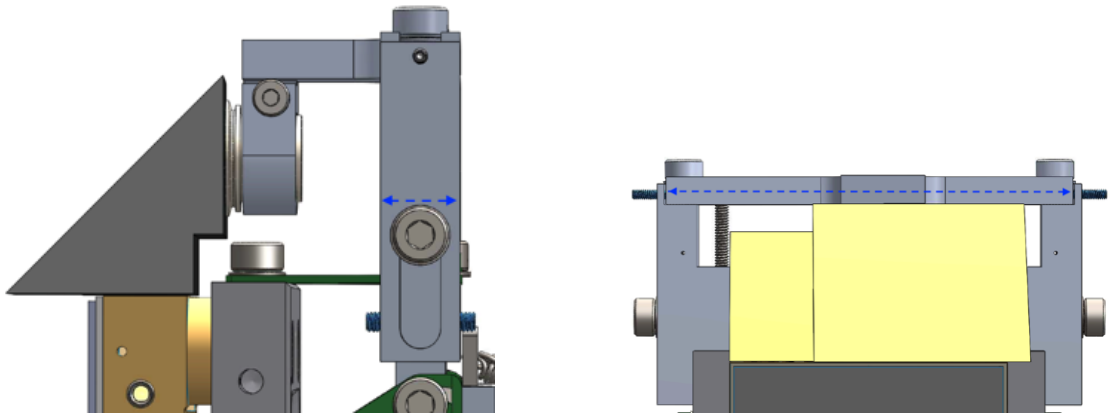

(a): focus position (b): x-position

Figure 5.4: Model views of where the pick-off mirror mounting attaches to the main assembly with baffling removed. Left: Side view; the blue arrow shows how the focus position of the pick-off mirrors can be adjusted independently of the detector using the highlighted set screws. This adjustment can be made over a range of ± 0.5 mm with an accuracy of 100 μm. Right: Front view; the blue arrow shows how the x-position of the pick-off mirrors can be adjusted independently of the detector over a range of ± 0.25 mm with an accuracy of 75 μm using the highlighted set screws. The rotation of the pick-off mirrors can be independently adjusted at the mounting location of the pick-off frame.

set screws on the side of the pick-off mounting frame (Figure 5.4b).

The tip-tilt angle may be adjusted independently for the detector and pick-off mirrors. Set screws can push the feet of the A frames which hold the detector to the main mount, allowing for a range of $\pm 1.13^\circ$ of adjustability in tip and $\pm 0.57^\circ$ in tilt (Figure 5.5). The 0.25° tolerance is met in both dimensions, with a quarter turn of the set screw giving a 0.17° change in tilt and a 0.09° change in tip. The tilt of the pick-off mirrors can be adjusted using the same set screws shown in Figure 5.4a that are used to set the focus offset. By moving one side of the pick-off frame to a closer or further offset position, slight adjustments to the tilt of the mirrors can be made with an accuracy of 0.13°. To adjust the tip angle of just the pick-off mirrors, the tip of both the mirrors and detector must be adjusted via shims between the mounting plates, while the detector can then be separately adjusted at the A-frames to compensate. The accuracy for the adjustment of the tip-tilt angle is less than the tolerance (0.2° for the pick-off mirrors and 0.25° for the detector) even when including the potential change in the tip angle at different focus positions.

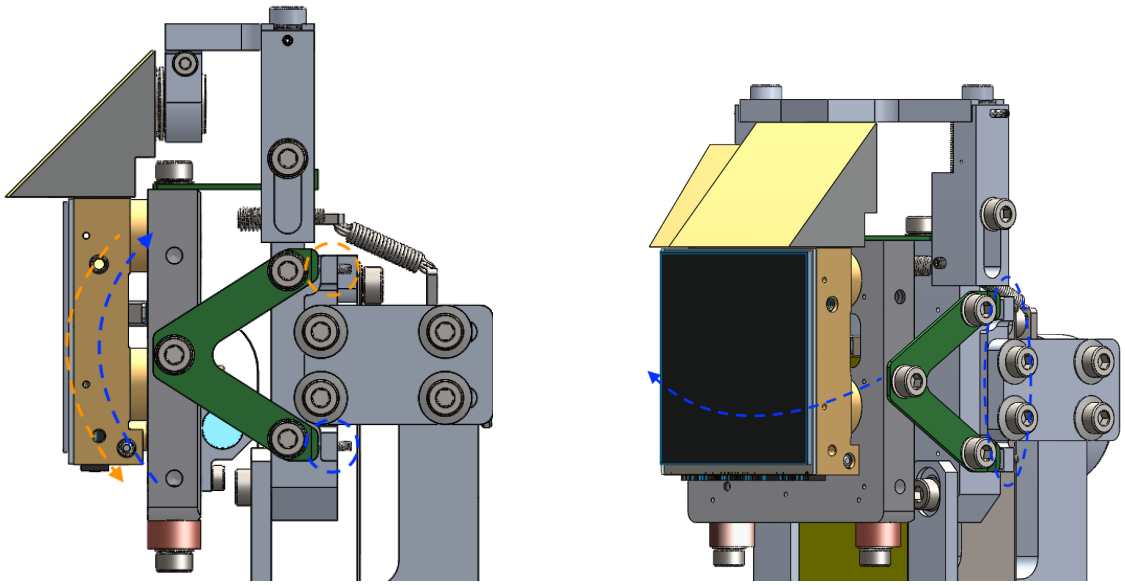

(a): tip (b): tilt

Figure 5.5: Model view of the detector mounting assembly illustrating the adjustability in tip (a) and tilt (b) via set screws at the A frame feet. Left: pushing the top foot of the A frames on the sides will result in changing the tip in the direction of the orange arrow. Likewise, pushing the bottom foot will cause a change in direction following the blue arrow. The A frame on the other side of the detector should be pushed in the same way for adjustments to the tip. Right: pushing both the top and bottom feet of the A frame shown by the same amount will cause an adjustment to the tilt of the detector following the blue arrow. Conversely, pushing the top and bottom feet of the A frame on the opposite side of the detector will cause a tilt in the opposite direction.

5.2.3 Baffling

Baffling is included directly around the detector and pick-off mirrors as well as a baffle around the entire mounting assembly for further reduction of stray light. A three-sided baffle slides over the detector, extending 12 mm in front of it. The top of this baffle is open due to the small clearance between the detector and the pick-off mirrors. Here, a sheet metal baffle made from shim stock is included that is coupled to the pick-off mirror wedge and lowered with it onto the assembly. This baffle rests on the top corners of the detector baffle and extends 12 mm past the front of the detector to prevent light from scattering off the spectrograph re-imaging optics. A small lip is folded over at each end of this baffle sheet to prevent reflections from the top and bottom corners of the pick-off mirror wedge. Two additional baffles made of shim stock will slide in the sides with a fold

to prevent reflections from pick-off mirror edges. This internal baffling setup is shown in Figure 5.6a, and the external baffling demonstrated in Figure 5.6b.

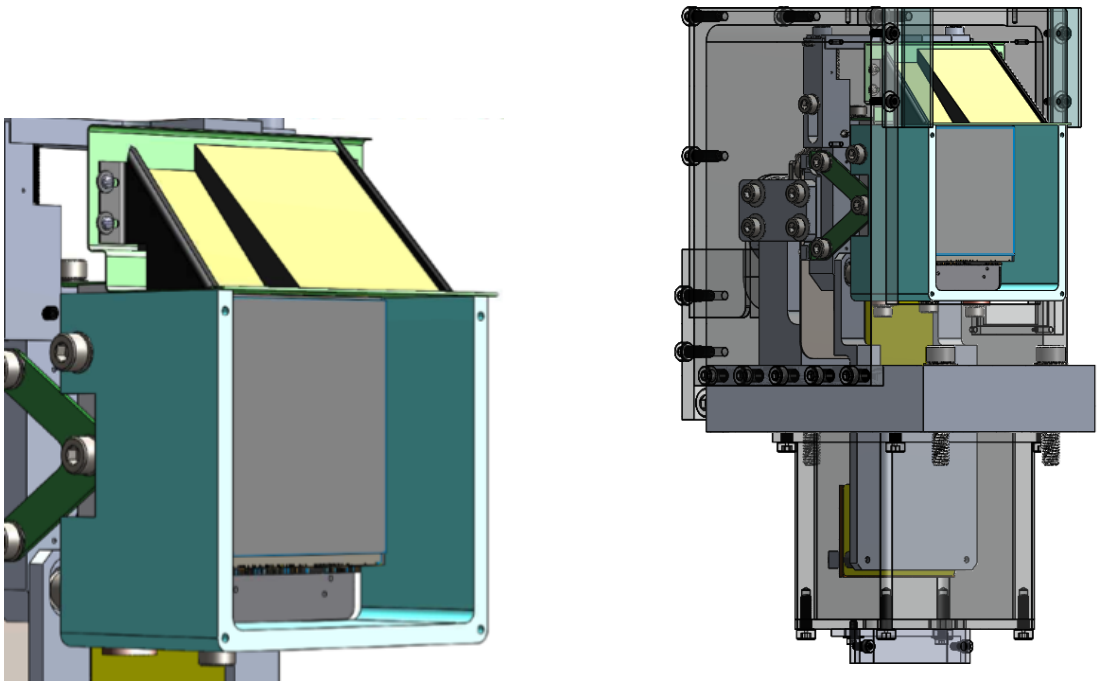

(a): internal baffling (b): external baffling

Figure 5.6: Model view showing the baffling around the detector and pick-off mirrors. Left: The three sided baffle around the detector (light blue) extends ~ 0.7 mm above its edge (< 0.1 mm above the Teledyne detector package) in order to protect this critical component while the pick-off mirrors are lowered into position. The sheet metal baffle (green) attached to the pick-off frame along with the mirror rests on this top edge and provides a roof over the detector to prevent ghosting from the re-imaging optics located after the pick-off mirrors. The silver baffles on the sides fold over the edges of the pick-off mirrors to prevent reflections off the corners. All of these baffles will be painted black; the color shown in the model is for illustrative purposes only. Right: Baffling (shown as transparent black) is also included around the full assembly including a separate box around the ASIC which extends below the optical plate.

5.3 Structural Analysis

In order to determine how the assembly will respond to loading, a simplified model with only the mounting components is analyzed within the SOLIDWORKS Simulation suite. The baffling, detector, pick-off mirrors, and all fasteners are removed in this simplified model. The weight of the detector and pick-off mirrors are accounted for in the form of remote masses, and bolted joints are

specified in the simulation with the fastener dimensions and pre-load. Like the simulation at each end of the focus range, the bottom of the mounting plate is designated as a fixture.

With only the static load due to gravity the maximum stress is $< 2/3$ the yield strength of aluminum ($S_y = 276\,\text{MPa}$). The areas of the highest stress are located under bolted connections due to pre-loading while elsewhere the stress is $< 1/2\,S_y$. The assembly is required to withstand an additional 4g's of loading during shipping and/or earthquakes. With this load applied in the vertical direction (adding to the static load due to gravity) the maximum stress in the model is still $< 2/3\,S_y$, located underneath the bolted connections between the pick-off frame and the intermediate plate (Figure 5.7). Since the 4g load may be experienced during shipping it may occur along any direction. With the shock load applied in the x- and z-directions the maximum stress is located under an A frame bolted connection instead, but is still $< 2/3\,S_y$. In all loading cases the stress outside of the bolted connections is $< 1/2\,S_y$.

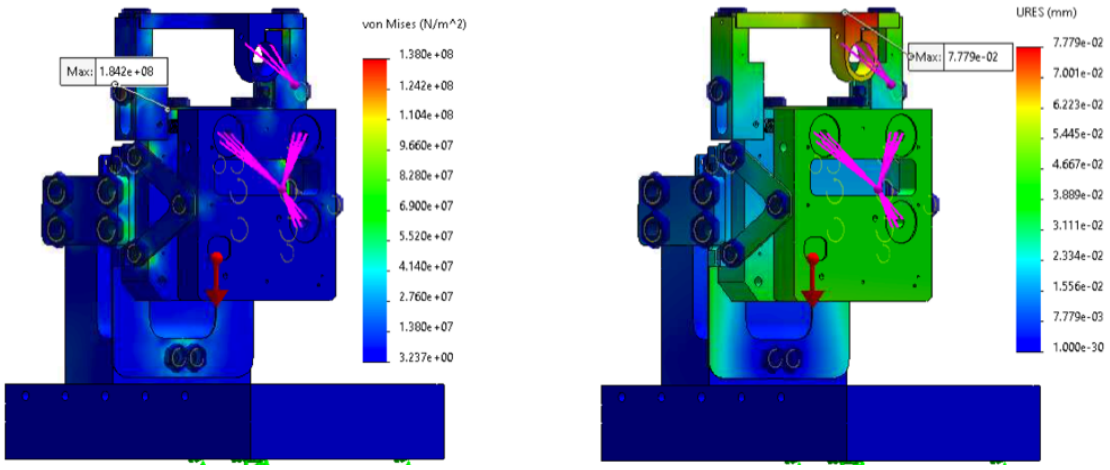

Figure 5.7: Stress (left) and deflection (right) for simulation of the detector mounting under both static and an additional 4g shock load in the vertical direction (5g total). The maximum stress determined is $< 2/3\,S_y$ underneath bolted connections and $< 1/2\,S_y$ elsewhere with negligible deflections.

If the best focus position involves full extension of the flexure, there will be a higher stress in the steel flexure itself. As shown in Figure 5.7, the mount as a whole will not fail since the support brackets will hold it up, but we also want to ensure that the flexure is not damaged so that focus

adjustments can be made later in the life of the instrument. To investigate the worst case scenario with the highest stress, the 4g shock load is simulated with a deformed flexure in the most extended configuration (with the optimal focus furthest from the starting estimate). This results in the stress throughout the flexure being well below the ultimate strength of AISI 304 steel (505MPa) except for at a single edge of the flexure. This is at the location of a modification to the deformed flexure model needed in order to create parallel surfaces for mating parts. This is likely creating an artificial stress concentration which will not be present in the fabricated part. Outside of this modified edge of the flexure, the stress is below the ultimate strength throughout, and outside of the compressive stress under fasteners, the stress is also below yield.

A frequency analysis was run in SOLIDWORKS Simulation using the simplified model in order to estimate the resonant frequencies. The mass of the detector and pick-off mirrors are again added as a remote load offset from the mounting point with the force of gravity included. The simulation was run searching for the first five frequency modes for the simplified model used in the load simulations as well as with the external baffling included (Table 5.2 & 5.3 respectively). As can be seen from the lower mass participation factors in Table 5.3, the external baffling largely does not participate in the modal response.

Table 5.2: Frequencies and mass participation for the first five modes of the imager detector and pick-off mounting without external baffling

Mode	Frequency (Hz)	Mass Participation (%)		
		X-direction	Y-direction	Z-direction
1	345	0.2	28	14
2	368	40	0.2	0
3	480	0	0	2
4	787	0	9	32
5	804	0	0.3	0.8

The instrument requirements list frequencies that can be expected in the range of $10-40\,\text{Hz}$ during shipping and $8-80\,\text{Hz}$ during operation, so the resonant frequency of the mechanism should be at least $> 80\,\text{Hz}$. The frequencies determined in the SolidWorks simulations lie well outside of

Table 5.3: Frequencies and mass participation for the first five modes of the imager detector and pick-off mounting without external baffling

Mode	Frequency (Hz)	Mass Participation (%)		
		X-direction	Y-direction	Z-direction
1	331	0.1	20	8
2	355	27	0.1	0
3	483	0	0	0.8
4	744	0	5	23
5	850	0.8	0	0

this range.

5.4 Summary

A single mounting assembly and housing will be used for the Liger imager detector and the IFS pick-off mirrors. This assembly will hold these optics < 1 mm away from each other while allowing adjustability in multiple axes. The detector and pick-off mirrors can be adjusted both together and individually, although with a smaller range of individual adjustment. Baffling is included around the individual optics as well as the full assembly to protect from scattered light and ghosting off the surfaces of other optics.

Analysis was carried out on the imager detector and IFS pick-off mirror mounting assembly to verify that the design meets the requirements. The planarity of the mounting points were evaluated throughout the range of focus positions by simulating the mechanism reaction to a force at the location of the linear actuator. The deviation from planarity across the 3 mm range of travel was 0.02°; well within the 0.25° tolerance. Next the strength of the mount was evaluated under both static and an additional 4g shock load. In both cases the maximum stress determined in the simulations is under bolt heads and is not expected to lead to failure. Modal frequencies were also determined using the SOLIDWORKS simulation tools, with all frequencies falling well above the $8 - 80$ Hz range the system is expected to be subjected to.

The detector and pick-off mirror mount will be assembled and alignment performed in a

custom cryogenic vacuum chamber designed for use with the Liger imager which will operate at a temperature below 77 K and vacuum pressure of 10^{-5} Torr (Wiley et al., 2020). The unique design of Liger allows simultaneous imaging and spectroscopy which both improves the performance of the instrument and provides useful science benefits. For example, simultaneous imaging in crowded field observations (e.g., globular clusters or the galactic center) can provide accurate astrometry and real time measurements of the telescope and instrument point-spread function. Having the light for the spectrograph modes first pass through the imager provides benefits such as improved background masking at the larger pupil located in the imager (Cosens et al., 2020). It also allows for improved AO correction in the imager without sacrificing the IFS performance. The design of the detector and IFS pick-off mirrors is critical to maintaining this performance. The closer the pick-off mirrors are to the detector, the lower the wavefront error is for both as it is best in the center and degrades with increasing radius.

Acknowledgements

The Liger instrumentation program is supported by the Heising-Simons Foundation, the Gordon and Betty Moore Foundation, University of California Observatories, and W. M. Keck Observatory.

Chapter 5, in full, is material in preparation for publication in the Proceedings of the SPIE 2022. Cosens, M., Wright, S. A., Brown, A., Fitzgerald, M., Johnson, C., Jones, T., Kassis, M., Kress, E., Kupke, R., Larkin, J. E., Magnone, K., McGurk, R., Rundquist, N., Sohn, J., Wang, E., Wiley, J., & Yeh, S, "Liger at Keck Observatory: Imager Detector and IFS Pick-off Mirror Assembly", *Proceedings of the SPIE*, *in prep*. The dissertation author is the primary investigator and author of this paper.

Chapter 6

Conclusion

Studying star forming regions is key to understanding how galaxies evolve over time. The host galaxy influences the properties of the star forming regions through environmental conditions like the availability of fuel (molecular gas) and sites of gravitational instability where star formation can begin. Likewise, as star formation progresses the energy imparted to the ISM has a profound impact on the environment. This can cause the surrounding gas to be expelled from the region or even the galaxy and is thought to be a major factor in shutting down further star formation. In order to understand the evolution of galaxies from what we observe in the distant universe to those locally we must also understand the formation and evolution of their star forming regions.

I began my thesis work in Chapter 2 with a study aiming to understand the properties of the large, kiloparsec-scale clumps of star formation observed at high redshift and how they compare to their local counterparts. To do this I gathered a comprehensive set of star forming region observations from high redshift ($1 \lesssim z \lesssim 5$), lensed and un-lensed galaxies as well as a wide range of local comparisons from regions in the Milky Way to local turbulent disk galaxies. I then developed a Bayesian MCMC code in order to fit the scaling relationships between different measured properties of the star forming regions with an emphasis on the relationship between the regions size and luminosity. The slope of this relationship can be used to differentiate between different formation modes of the regions, and previous studies had found offsets in luminosity between local and high redshift samples. The Bayesian MCMC code was a necessary and new addition in my study in order to incorporate measurement uncertainties on all dimensions independently as well as additional

fitted parameters for intrinsic scatter. Using this powerful tool and expansive observational data set I was able to perform robust fits to the sample as a whole as well as divide the data into key subsets to investigate the potential for redshift evolution in the scaling relationships or selection biases between types of observations. I found no evidence of an evolution in the size-luminosity relationship with redshift, nor a bias in sample selection between high redshift lensed and unlensed galaxies. What I did find was evidence of a break based on $\Sigma_{\rm SFR}$, with high and low $\Sigma_{\rm SFR}$ star forming regions exhibiting different slopes in the relationship between size and luminosity. The high $\Sigma_{\rm SFR}$ subset exhibit a slope $L \sim r^3$, consistent with Jeans collapse, while the low $\Sigma_{\rm SFR}$ subset exhibit a slope $L \sim r^2$ which can be explained by collapse due to Toomre instability. However, both of these slopes can also be explained without the need for differing formation modes and can simply be explained as Strömgren spheres impacted by the geometry of the host galaxy disk.

In the course of this investigation I identified key areas of the parameter space in need of observational constraints. In particular, observations of small, low luminosity star forming regions which set the intercept of the scaling relationships were missing. There was also a limited number of observations taken with IFS, limiting the feasibility of investigating the impact of kinematics as a third parameter in the scaling relationship fits. In order to address both these areas simultaneously, in Chapter 3, I sought to observe a new sample of star forming regions in IC 10, the nearest starburst galaxy to the Milky Way. The starburst nature of IC 10 provided a large sample of star forming H II regions to observe, and its close proximity allowed for extremely high spatial resolution when combined with the 10-m diameter Keck telescope and the KCWI IFS. With these high spatial and spectral resolution observations covering ~ 1.25 sq. deg. of IC 10, I identified 46 individual H II regions with an average radius of only ~ 4 pc, and SFR $\sim 1.3 \times 10^{-4}$ $M_\odot$ yr^{-1}.

The goals of these KCWI observations were two-fold: first to better constrain the scaling relationships through the intercept of the size-luminosity relation and multi-parameter fits; and second to study the detailed internal ionization state and kinematic properties of local H II regions in order to better understand their formation and evolution. Instead of constraining the intercept of the scaling relations however, I discovered that with the improved resolution of KCWI over prior

imaging, the H II regions of IC 10 are actually offset to higher luminosity and velocity dispersion for a given size. I found that this is likely due to these regions being young and undergoing active expansion rather than being virialized. From measurements of the H II region luminosities and gas velocities I estimated the balance of outward pressure from star formation feedback against inward pressure from gravity and surrounding turbulent gas. This results in 89% of the H II regions showing greater outward than inward sources of pressure. The dominant contribution to this outward pressure comes from thermal pressure in gas that has been heated by the young stars in the H II region, providing a ~ 3 orders of magnitude greater contribution than direct radiation pressure. I also found five H II regions with bordering turbulent gas volumes which can be supported by energy originating from the star forming region. In two of these regions the turbulence is most likely supported by energy from stellar winds while the other three are consistent with the energy which would be provided by champagne flows in which neutral gas is heated causing an area of overpressure and rapid gas expansion. The estimates of pressure and energy in IC 10's H II regions provide interesting insights into the effectiveness of star formation feedback in young, compact H II regions. Most notably, implying that pressure from warm gas may be more effective than it was expected to be when the ionizing cluster has a low stellar mass.

The observational work in my thesis and the studies that will advance our understanding of star forming regions in the future are made possible by the development of new telescopes and instruments. This instrumentation work provides improvements in sensitivity, resolution, field of view, and wavelength coverage necessary to push our understanding of the universe forward. With the need for these improvements in instrumentation in mind, I have also worked extensively on the design of the new Liger imager and IFS for Keck Observatory. Liger will take advantage of an adaptive optics upgrade at Keck and provide coverage of bluer wavelengths, larger fields of view, and higher spectral resolution than current IFSs. For example, the wavelength coverage of Liger will allow for observations of near-IR emission lines in nearby galaxies which can be used to provide constraints on the excitation mechanisms and ages of star-forming regions (e.g., Paβ, Brγ; Dale et al., 2004). As these lines are emitted at longer wavelengths, they are less sensitive to dust

obscuration than Hβ and Hα. The high spectral resolution will also mean the [FeII] and Paβ lines will be deblended, and the ratio can be used as a probe of the excitation mechanism. As described in Chapters 4 & 5, I have designed three major opto-mechanical components of the Liger imager and sequential spectrograph: the filter wheel, pupil wheel, and imager detector focus stage. The filter wheel consists of three independent wheels which can hold up to 51 different filters used to select the desired wavelength range of the observations. The pupil wheel contains seven slots for unique pupil masks which block the background light. The imager detector focus stage holds the detector as well as pick-off mirrors for the two unique spectrograph channels. The stage will move these optics through a 3 mm range of travel during initial alignment and then be fixed at the optimal position. Proper operation of these components are critical to the performance of Liger and the ability to achieve the amazing science planned for this instrument.

6.1 Looking Ahead

As discussed in Chapter 3, supplementary observations of the same field in IC 10 were carried out with the "large slicer, R$\sim$900" configuration in order to expand the wavelength coverage and obtain an estimate of the extinction correction and metallicity. However, due to time constraints these observations were shallow, giving only indirect metallicity estimates from strong line calibrations in the highest signal-to-noise regions. In order to more fully understand the conditions of the ionized gas and the impact feedback may have on the H II regions and diffuse gas metallicity a follow-up study utilizing deeper observations in this mode are underway. This will enable not only metallicity estimates from the strong line method throughout the HII regions and diffuse gas, but also more accurate direct metallicity measurements from the faint auroral [OIII]4363Å line in bright regions. Measurements of the metallicity throughout IC 10 will provide insight into variations between H II regions and diffuse gas and allow the investigation of chemical enrichment at the locations of potential outflows, which if present would provide evidence that the turbulent outflows are due to the mass loss in stellar winds rather than champagne flows.

Another interesting finding in Chapter 3 was that the compact H II regions of IC 10 do

not appear to be virialized and are offset from the typical scaling relationships between measured properties. The question remains whether this is typical with the improved resolution of modern IFSs or is an effect of the recent starburst in IC 10. To answer this, a larger sample of H II regions measured in a similar way across a range of star-forming environments is needed. Further, there are a limited number of studies like that of Chapter 3 which observationally characterize the effectiveness of different feedback mechanisms, making it difficult to broadly asses the regimes in which different mechanisms are effective at clearing gas from the surroundings and potentially quenching further star formation. The Local Volume Mapper (LVM), as part of the next generation of the Sloan Digital Sky Survey (SDSS), is designed to address this observational limitation by providing IFS observations mapping the Milky Way midplane, the Magellanic Clouds, and other local volume galaxies (Kollmeier et al., 2017). This survey will provide < 1 pc resolution observations within the Milky Way and ~ 10 pc resolution in the Magellanic Clouds, similar to our KCWI observations of IC 10. The wide wavelength coverage ($3,600 - 10,000$Å) and R $\sim 4,000$ spectral resolution planned for LVM will allow measurement of photoionization rates, ionized gas kinematics, and oxygen abundance measurements in a large sample of star forming regions and ISM gas. This will allow for a similar study as Chapter 3 of the impact of different mechanisms of star formation feedback on a much larger scale with which environmental trends can potentially be discovered.

Perhaps the most exciting new observatory for astronomers is the *James Webb Space Telescope* (JWST), which was successfully launched on December 25, 2021 and will begin science operations soon. JWST has two on-board IFSs with the Near Infrared Spectrograph (NIRSPEC) operating between $0.6 - 5$ microns and the Mid-Infrared Instrument (MIRI) covering longer wavelengths between $5 - 28$ microns. These long wavelengths are — for the most part — not accessible from the ground due to the presence of the atmosphere so we need space based telescopes to conduct observations in this regime. There are many observing programs planned with JWST that will advance our understanding of how star formation interacts with and influences the host galaxy, including some early release programs which will be among the first observations taken in the next few months. One early release science program from the GOALS team will target the nuclei of

local galaxies with the NIRSPEC and MIRI IFS modes to observe the conditions and kinematics of the ISM at $50-100$ pc scales (Armus et al., 2017). These observations cover infrared wavelengths allowing detailed mapping of features such as the dust continuum and emission from molecular hydrogen. The longer wavelengths covered by JWST will also allow observations of the obscured component of star formation at $z \sim 1-3$ that is missed with Hα. At even higher redshift, the optical emission lines used locally to measure H II region and ISM conditions like metallicity will be shifted into the wavelength bands of JWST. Single slit spectroscopy with NIRSPEC will measure emission lines originating from the ionized gas in galaxies out to $z \sim 10$ enabling studies of the ISM conditions (e.g., ionization parameter and metallicity) in some of the earliest galaxies (e.g., Finkelstein et al., 2017).

Looking further ahead, the next generation of ground based optical and near-IR observatories with primary mirror diameters of 25- to 40-m (known as ELTS) will allow for significant advances in the observational study of resolved star forming region properties. This class of telescopes, which includes the European Extremely Large Telescope (e-ELT; 39 m), the Giant Magellan Telescope (GMT; 25 m), and the Thirty Meter Telescope (TMT; 30 m), will provide spatial resolution better than 100 pc when observing Hα emission at $z = 1$ and operating at the diffraction limit. This significant improvement in resolution will help to bridge the gap in the level of detail that can be observed in local versus high-z star forming regions. This will allow astronomers to probe whether there are more compact substructures within high-z clumps visible in emission line maps, and the kinematic details of individual clumps can be probed with greater accuracy to test the presence of rotating or expanding gas. The larger primary mirror also provides greater sensitivity as the $3\times$ greater diameter gives a $9\times$ greater collecting area. This not only means that exposure times can be shorter to achieve the same signal to noise as current telescopes, but also that fainter emission lines can be detected in sources where it is currently not possible. For example, the faint auroral [OIII]4363Å emission line will not only be detectable at high-z, but the IFSs planned for the ELTs should be able to perform resolved observations of this emission line throughout the galaxy for direct measurements of metallicity gradients.

With the new optical and near-infrared instruments and observatories on the horizon we will be able to greatly improve our understanding of the interplay between star-forming regions and their host galaxies. In this thesis I have shown that there is not a simple redshift evolution to the scaling relationships between star-forming region properties (and therefore the region formation mechanism and evolution). Instead, I have shown that there is evidence of a break into distinct samples of high and low Σ_{SFR} with differences in either formation mechanism or geometry relative to the host galaxy disk that is independent of redshift. In studying the local starburst galaxy IC 10, I have shown that the H II regions around these low mass star clusters are likely expanding due to active feedback from the ionizing cluster. The dominant contribution to outward expansion of the ionized gas appears to be due to warm gas pressure, a mode of feedback previously thought to be less effective in these low mass environments.

These observations provide a key stepping stone to fully utilizing the next generation of telescopes and surveys. The analysis techniques and methodology used for the KCWI observations of IC 10 can be extended to a larger sample of star forming regions from more expansive observing campaigns and surveys like SDSS/LVM in order to consistently estimate the effectiveness of different feedback mechanisms across a range of environments (i.e., metallicity, age, stellar mass). The observations of local H II regions in this thesis are also highly complimentary to the capabilities we will soon have with JWST. The longer wavelength coverage of JWST will probe the dust and molecular gas phase of the ISM locally for another view of the physical conditions and impact of the energy from star formation feedback. JWST will also allow astronomers to observe the same optical emission lines at high redshift which are used to estimate the ionization state and metallicity of the gas, providing clues to the evolution of galaxy environments over time. The ELTs will not only be able to measure these emission lines at intermediate redshift, but they will be able to resolve them throughout the galaxies, differentiating between gas in the star forming clumps and the ISM. They will also allow astronomers to resolve more details of the clump substructure and internal kinematics. This will allow the cause of the Σ_{SFR} break I found in the size-luminosity scaling relationship to be probed with greater detail in this regime. These new observational tools, and

others which will be developed in the future, will help to better answer key questions such as how the star forming environment changes over cosmic time and what impact that star formation has on shaping the host galaxy.

Bibliography

J. Allington-Smith. Basic principles of integral field spectroscopy. *New Astronomy Reviews*, 50(4):244–251, 2006. ISSN 1387-6473. doi: https://doi.org/10.1016/j.newar.2006.02.024. URL https://www.sciencedirect.com/science/article/pii/S1387647306000157. Integral Field Spectroscopy: Techniques and Data Production.

P. Ambrocio-Cruz, E. Le Coarer, M. Rosado, D. Russeil, P. Amram, A. Laval, B. Epinat, M. Ramírez, M. Odonne, and G. Goldes. The kinematical properties of superbubbles and H II regions of the Large Magellanic Cloud derived from the 3D Hα Survey. *MNRAS*, 457(2):2048–2067, Apr. 2016. doi: 10.1093/mnras/stw054.

L. D. Anderson, T. M. Bania, D. S. Balser, and R. T. Rood. The Green Bank Telescope H II Region Discovery Survey. II. The Source Catalog. *ApJS*, 194(2):32, June 2011. doi: 10.1088/0067-0049/194/2/32.

W. P. Armentrout, L. D. Anderson, T. V. Wenger, D. S. Balser, and T. M. Bania. A VLA Census of the Galactic H II Region Population. *ApJS*, 253(1):23, Mar. 2021. doi: 10.3847/1538-4365/abd5c0.

L. Armus, A. S. Evans, P. N. Appleton, L. Barcos-Munoz, V. Charmandaris, T. Diaz-Santos, J. H. Howell, H. Inami, K. L. Larson, S. Linden, M. A. Malkan, J. Marshall, J. M. Mazzarella, A. Medling, E. J. Murphy, G. Privon, J. A. S. Rich, D. B. Sanders, S. Stierwalt, J. A. Surace, and V. U. A JWST Study of the Starburst-AGN Connection in Merging LIRGs. JWST Proposal ID 1328. Cycle 0 Early Release Science, Nov. 2017.

P. Arriaga, M. P. Fitzgerald, J. E. Lyke, R. D. Campbell, P. L. Wizinowich, S. M. Adkins, and K. Y. Matthews. Modeling the transmission and thermal emission in a pupil image behind the Keck II adaptive optics system. In C. J. Evans, L. Simard, and H. Takami, editors, *Ground-based and Airborne Instrumentation for Astronomy VI*, volume 9908 of *Society of Photo-Optical Instrumentation Engineers (SPIE) Conference Series*, page 990835, Aug. 2016. doi: 10.1117/12.2233068.

P. Arriaga, M. Fitzgerald, C. Johnson, J. Weiss, and J. E. Lyke. Upgrade and characterization of the OSIRIS imager detector. In C. J. Evans, L. Simard, and H. Takami, editors, *Ground-based and Airborne Instrumentation for Astronomy VII*, volume 10702 of *Society of Photo-Optical Instrumentation Engineers (SPIE) Conference Series*, page 107022U, July 2018. doi: 10.1117/12.2313101.

S. Arribas, L. Colina, E. Bellocchi, R. Maiolino, and M. Villar-Martín. Ionized gas outflows and global kinematics of low-z luminous star-forming galaxies. *A&A*, 568:A14, Aug. 2014. doi: 10.1051/0004-6361/201323324.

R. Arsenault and J. R. Roy. Correlations between integrated parameters and H-alpha velocity widths in giant extragalactic HII regions : a new appraisal. *A&A*, 201:199–207, Aug. 1988.

R. Arsenault, J. R. Roy, and J. Boulesteix. Large-scale formation of massive stars in the spiral galaxy NGC 4321. *A&A*, 234:23, Aug. 1990.

T. Ashley, B. G. Elmegreen, M. Johnson, D. L. Nidever, C. E. Simpson, and N. R. Pokhrel. The H I Chronicles of LITTLE THINGS BCDs II: The Origin of IC 10's H I Structure. *AJ*, 148(6):130, Dec 2014. doi: 10.1088/0004-6256/148/6/130.

Astropy Collaboration, T. P. Robitaille, E. J. Tollerud, P. Greenfield, M. Droettboom, E. Bray, T. Aldcroft, M. Davis, A. Ginsburg, A. M. Price-Whelan, W. E. Kerzendorf, A. Conley, N. Crighton, K. Barbary, D. Muna, H. Ferguson, F. Grollier, M. M. Parikh, P. H. Nair, H. M. Unther, C. Deil, J. Woillez, S. Conseil, R. Kramer, J. E. H. Turner, L. Singer, R. Fox, B. A. Weaver, V. Zabalza, Z. I. Edwards, K. Azalee Bostroem, D. J. Burke, A. R. Casey, S. M. Crawford, N. Dencheva, J. Ely, T. Jenness, K. Labrie, P. L. Lim, F. Pierfederici, A. Pontzen, A. Ptak, B. Refsdal, M. Servillat, and O. Streicher. Astropy: A community Python package for astronomy. *A&A*, 558:A33, Oct. 2013. doi: 10.1051/0004-6361/201322068.

R. Bacon, G. Adam, A. Baranne, G. Courtes, D. Dubet, J. P. Dubois, E. Emsellem, P. Ferruit, Y. Georgelin, G. Monnet, E. Pecontal, A. Rousset, and F. Say. 3D spectrography at high spatial resolution. I. Concept and realization of the integral field spectrograph TIGER. *A&AS*, 113:347, Oct. 1995.

R. Bacon, M. Accardo, L. Adjali, H. Anwand, S. Bauer, I. Biswas, J. Blaizot, D. Boudon, S. Brau-Nogue, J. Brinchmann, P. Caillier, L. Capoani, C. M. Carollo, T. Contini, P. Couderc, E. Daguisé, S. Deiries, B. Delabre, S. Dreizler, J. Dubois, M. Dupieux, C. Dupuy, E. Emsellem, T. Fechner, A. Fleischmann, M. François, G. Gallou, T. Gharsa, A. Glindemann, D. Gojak, B. Guiderdoni, G. Hansali, T. Hahn, A. Jarno, A. Kelz, C. Koehler, J. Kosmalski, F. Laurent, M. Le Floch, S. J. Lilly, J. L. Lizon, M. Loupias, A. Manescau, C. Monstein, H. Nicklas, J. C. Olaya, L. Pares, L. Pasquini, A. Pécontal-Rousset, R. Pelló, C. Petit, E. Popow, R. Reiss, A. Remillieux, E. Renault, M. Roth, G. Rupprecht, D. Serre, J. Schaye, G. Soucail, M. Steinmetz, O. Streicher, R. Stuik, H. Valentin, J. Vernet, P. Weilbacher, L. Wisotzki, and N. Yerle. The MUSE second-generation VLT instrument. In I. S. McLean, S. K. Ramsay, and H. Takami, editors, *Ground-based and Airborne Instrumentation for Astronomy III*, volume 7735 of *Society of Photo-Optical Instrumentation Engineers (SPIE) Conference Series*, page 773508, July 2010. doi: 10.1117/12.856027.

N. Bastian, E. Emsellem, M. Kissler-Patig, and C. Maraston. Young star cluster complexes in NGC 4038/39. Integral field spectroscopy using VIMOS-VLT. *A&A*, 445(2):471–483, Jan. 2006. doi: 10.1051/0004-6361:20053793.

J. E. Beckman, M. Rozas, A. Zurita, R. A. Watson, and J. H. Knapen. Populations of High-Luminosity Density-bounded H II Regions in Spiral Galaxies: Evidence and Implications. *AJ*, 119(6):2728–2744, June 2000. doi: 10.1086/301380.

F. Belfiore, R. Maiolino, C. Tremonti, S. F. Sánchez, K. Bundy, M. Bershady, K. Westfall, L. Lin, N. Drory, M. Boquien, D. Thomas, and J. Brinkmann. SDSS IV MaNGA - metallicity and nitrogen abundance gradients in local galaxies. *MNRAS*, 469(1):151–170, July 2017. doi: 10.1093/mnras/stx789.

J. O. Berger. *Statistical decision theory and Bayesian analysis; 2nd ed.* Springer series in statistics. Springer, New York, 1985. doi: 10.1007/978-1-4757-4286-2. URL https://cds.cern.ch/record/1327974.

M. Betancourt and L. C. Stein. The Geometry of Hamiltonian Monte Carlo. *arXiv e-prints*, art. arXiv:1112.4118, Dec. 2011.

A. D. Bolatto, A. K. Leroy, E. Rosolowsky, F. Walter, and L. Blitz. The Resolved Properties of Extragalactic Giant Molecular Clouds. *ApJ*, 686(2):948–965, Oct. 2008. doi: 10.1086/591513.

L. Bottinelli, L. Gouguenheim, G. Paturel, and G. de Vaucouleurs. HI line studies of galaxies. III. Distance moduli of 822 disk galaxies. *A&AS*, 56:381–413, June 1984.

F. Bournaud, B. G. Elmegreen, and D. M. Elmegreen. Rapid Formation of Exponential Disks and Bulges at High Redshift from the Dynamical Evolution of Clump-Cluster and Chain Galaxies. *ApJ*, 670(1):237–248, Nov. 2007. doi: 10.1086/522077.

F. Bournaud, V. Perret, F. Renaud, A. Dekel, B. G. Elmegreen, D. M. Elmegreen, R. Teyssier, P. Amram, E. Daddi, P.-A. Duc, D. Elbaz, B. Epinat, J. M. Gabor, S. Juneau, K. Kraljic, and E. Le Floch'. The Long Lives of Giant Clumps and the Birth of Outflows in Gas-rich Galaxies at High Redshift. *ApJ*, 780(1):57, Jan. 2014. doi: 10.1088/0004-637X/780/1/57.

L. Bradley, B. Sipőcz, T. Robitaille, E. Tollerud, Z. Vinícius, C. Deil, K. Barbary, T. J. Wilson, I. Busko, H. M. Günther, M. Cara, S. Conseil, M. Droettboom, A. Bostroem, E. M. Bray, L. A. Bratholm, P. L. Lim, M. Craig, G. Barentsen, S. Pascual, A. Donath, J. Greco, G. Perren, W. Kerzendorf, M. de Val-Borro, N. Dencheva, L. de Albernaz Ferreira, H. Souchereau, F. D'Eugenio, and B. A. Weaver. astropy/photutils: v0.7.2, Dec. 2019. URL https://doi.org/10.5281/zenodo.3568287.

F. Bresolin, L. Rizzi, I. T. Ho, R. Terlevich, E. Terlevich, E. Telles, R. Chávez, S. Basilakos, and M. Plionis. Internal kinematics of giant H II regions in M101 with the Keck Cosmic Web Imager. *MNRAS*, 495(4):4347–4365, July 2020. doi: 10.1093/mnras/staa1472.

R. G. Budynas and J. K. Nisbett. *Shigley's Mechanical Engineering Design*. McGraw-Hill, ninth edition, 2011.

F. Buitrago, C. J. Conselice, B. Epinat, A. G. Bedregal, R. Grützbauch, and B. J. Weiner. SINFONI/VLT 3D spectroscopy of massive galaxies: evidence of rotational support at z $\sim$ 1.4. *MNRAS*, 439(2):1494–1521, Apr. 2014. doi: 10.1093/mnras/stu034.

K. Bundy, M. A. Bershady, D. R. Law, R. Yan, N. Drory, N. MacDonald, D. A. Wake, B. Cherinka, J. R. Sánchez-Gallego, A.-M. Weijmans, D. Thomas, C. Tremonti, K. Masters, L. Coccato, A. M. Diamond-Stanic, A. Aragón-Salamanca, V. Avila-Reese, C. Badenes, J. Falcón-Barroso, F. Belfiore, D. Bizyaev, G. A. Blanc, J. Bland-Hawthorn, M. R. Blanton, J. R. Brownstein, N. Byler, M. Cappellari, C. Conroy, A. A. Dutton, E. Emsellem, J. Etherington, P. M. Frinchaboy, H. Fu, J. E. Gunn, P. Harding, E. J. Johnston, G. Kauffmann, K. Kinemuchi, M. A. Klaene, J. H. Knapen, A. Leauthaud, C. Li, L. Lin, R. Maiolino, V. Malanushenko, E. Malanushenko, S. Mao, C. Maraston, R. M. McDermid, M. R. Merrifield, R. C. Nichol, D. Oravetz, K. Pan, J. K. Parejko, S. F. Sanchez, D. Schlegel, A. Simmons, O. Steele, M. Steinmetz, K. Thanjavur, B. A. Thompson, J. L. Tinker, R. C. E. van den Bosch, K. B. Westfall, D. Wilkinson, S. Wright, T. Xiao, and K. Zhang. Overview of the SDSS-IV MaNGA Survey: Mapping nearby Galaxies at Apache Point Observatory. *ApJ*, 798(1):7, Jan. 2015. doi: 10.1088/0004-637X/798/1/7.

D. Calzetti, G. Liu, and J. Koda. Star Formation Laws: The Effects of Gas Cloud Sampling. *ApJ*, 752(2):98, June 2012. doi: 10.1088/0004-637X/752/2/98.

J. A. Cardelli, G. C. Clayton, and J. S. Mathis. The Relationship between Infrared, Optical, and Ultraviolet Extinction. *ApJ*, 345:245, Oct. 1989. doi: 10.1086/167900.

N. Castro, P. A. Crowther, C. J. Evans, J. Mackey, N. Castro-Rodriguez, J. S. Vink, J. Melnick, and F. Selman. Mapping the core of the Tarantula Nebula with VLT-MUSE. I. Spectral and nebular content around R136. *A&A*, 614:A147, June 2018. doi: 10.1051/0004-6361/201732084.

A. Cava, D. Schaerer, J. Richard, P. G. Pérez-González, M. Dessauges-Zavadsky, L. Mayer, and V. Tamburello. The nature of giant clumps in distant galaxies probed by the anatomy of the cosmic snake. *Nature Astronomy*, 2:76–82, Nov. 2018. doi: 10.1038/s41550-017-0295-x.

D. Ceverino, A. Dekel, N. Mandelker, F. Bournaud, A. Burkert, R. Genzel, and J. Primack. Rotational support of giant clumps in high-z disc galaxies. *MNRAS*, 420(4):3490–3520, Mar. 2012. doi: 10.1111/j.1365-2966.2011.20296.x.

G. Chabrier. Galactic Stellar and Substellar Initial Mass Function. *PASP*, 115(809):763–795, July 2003. doi: 10.1086/376392.

L. Cortese, L. M. R. Fogarty, I. T. Ho, K. Bekki, J. Bland-Hawthorn, M. Colless, W. Couch, S. M. Croom, K. Glazebrook, J. Mould, N. Scott, R. Sharp, C. Tonini, J. T. Allen, J. Bloom, J. J. Bryant, M. Cluver, R. L. Davies, M. J. Drinkwater, M. Goodwin, A. Green, L. J. Kewley, I. S. Kostantopoulos, J. S. Lawrence, S. Mahajan, A. M. Medling, M. Owers, S. N. Richards, S. M. Sweet, and O. I. Wong. The SAMI Galaxy Survey: Toward a Unified Dynamical Scaling Relation for Galaxies of All Types. *ApJL*, 795(2):L37, Nov. 2014. doi: 10.1088/2041-8205/795/2/L37.

M. Cosens, S. A. Wright, E. Mieda, N. Murray, L. Armus, T. Do, J. E. Larkin, K. Larson, G. Martinez, G. Walth, and A. Vayner. Size-Luminosity Scaling Relations of Local and Distant Star-forming Regions. *ApJ*, 869(1):11, Dec. 2018. doi: 10.3847/1538-4357/aaeb8f.

M. Cosens, S. A. Wright, P. Arriaga, A. Brown, M. Fitzgerald, T. Jones, M. Kassis, E. Kress, R. Kupke, J. E. Larkin, J. Lyke, E. Wang, J. Wiley, and S. Yeh. Liger for next-generation Keck AO: filter wheel and pupil design. In *Ground-based and Airborne Instrumentation for Astronomy VIII*, volume 11447 of *Society of Photo-Optical Instrumentation Engineers (SPIE) Conference Series*, page 114474X, Dec. 2020. doi: 10.1117/12.2561837.

G. Cresci, F. Mannucci, and M. Curti. Fundamental metallicity relation in CALIFA, SDSS-IV MaNGA, and high-z galaxies. *A&A*, 627:A42, July 2019. doi: 10.1051/0004-6361/201834637.

S. M. Croom, J. S. Lawrence, J. Bland-Hawthorn, J. J. Bryant, L. Fogarty, S. Richards, M. Goodwin, T. Farrell, S. Miziarski, R. Heald, D. H. Jones, S. Lee, M. Colless, S. Brough, A. M. Hopkins, A. E. Bauer, M. N. Birchall, S. Ellis, A. Horton, S. Leon-Saval, G. Lewis, Á. R. López-Sánchez, S.-S. Min, C. Trinh, and H. Trowland. The Sydney-AAO Multi-object Integral field spectrograph. *MNRAS*, 421(1):872–893, Mar. 2012. doi: 10.1111/j.1365-2966.2011.20365.x.

P. A. Crowther. Physical Properties of Wolf-Rayet Stars. *ARA&A*, 45(1):177–219, Sept. 2007. doi: 10.1146/annurev.astro.45.051806.110615.

D. A. Dale, H. Roussel, A. Contursi, G. Helou, H. L. Dinerstein, D. A. Hunter, D. J. Hollenbach, E. Egami, K. Matthews, J. Murphy, Thomas W., C. E. Lafon, and R. H. Rubin. Near-Infrared Integral Field Spectroscopy of Star-forming Galaxies. *ApJ*, 601(2):813–830, Feb. 2004. doi: 10.1086/380753.

R. D. Davies, K. H. Elliott, and J. Meaburn. The nebular complexes of the Large and Small Magellanic Clouds. , 81:89, Jan. 1976.

A. Dekel and M. R. Krumholz. Steady outflows in giant clumps of high-z disc galaxies during migration and growth by accretion. *MNRAS*, 432(1):455–467, June 2013. doi: 10.1093/mnras/stt480.

A. Dekel, R. Sari, and D. Ceverino. Formation of Massive Galaxies at High Redshift: Cold Streams, Clumpy Disks, and Compact Spheroids. *ApJ*, 703(1):785–801, Sept. 2009. doi: 10.1088/0004-637X/703/1/785.

N. Don, M. Matt, and M. Chris. KCWI data reduction pipeline, June 2018. URL https://github.com/Keck-DataReductionPipelines/KcwiDRP/releases/tag/v1.1.0.

S. L. Ellison, S. F. Sánchez, H. Ibarra-Medel, B. Antonio, J. T. Mendel, and J. Barrera-Ballesteros. Star formation is boosted (and quenched) from the inside-out: radial star formation profiles from MaNGA. *MNRAS*, 474(2):2039–2054, Feb. 2018. doi: 10.1093/mnras/stx2882.

B. G. Elmegreen. Star Formation in Disks: Spiral Arms, Turbulence, and Triggering Mechanisms. In J. Andersen, Nordströara, B. m, and J. Bland-Hawthorn, editors, *The Galaxy Disk in Cosmological Context*, volume 254, pages 289–300, Mar. 2009. doi: 10.1017/S1743921308027713.

B. G. Elmegreen, F. Bournaud, and D. M. Elmegreen. Bulge Formation by the Coalescence of Giant Clumps in Primordial Disk Galaxies. *ApJ*, 688(1):67–77, Nov. 2008. doi: 10.1086/592190.

D. M. Elmegreen, B. G. Elmegreen, and A. C. Hirst. Discovery of Face-on Counterparts of Chain Galaxies in the Tadpole Advanced Camera for Surveys Field. *ApJL*, 604(1):L21–L23, Mar. 2004a. doi: 10.1086/383312.

D. M. Elmegreen, B. G. Elmegreen, and C. M. Sheets. Chain Galaxies in the Tadpole Advanced Camera for Surveys Field. *ApJ*, 603(1):74–81, Mar. 2004b. doi: 10.1086/381357.

B. Epinat, T. Contini, O. Le Fèvre, D. Vergani, B. Garilli, P. Amram, J. Queyrel, L. Tasca, and L. Tresse. Integral field spectroscopy with SINFONI of VVDS galaxies. I. Galaxy dynamics and mass assembly at 1.2 ¡ z ¡ 1.6. *A&A*, 504(3):789–805, Sept. 2009. doi: 10.1051/0004-6361/200911995.

B. Epinat, L. Tasca, P. Amram, T. Contini, O. Le Fèvre, J. Queyrel, D. Vergani, B. Garilli, M. Kissler-Patig, J. Moultaka, L. Paioro, L. Tresse, F. Bournaud, C. López-Sanjuan, and V. Perret. MASSIV: Mass Assembly Survey with SINFONI in VVDS. II. Kinematics and close environment classification. *A&A*, 539:A92, Mar. 2012. doi: 10.1051/0004-6361/201117711.

C. Espinosa-Ponce, S. F. Sánchez, C. Morisset, J. K. Barrera-Ballesteros, L. Galbany, R. García-Benito, E. A. D. Lacerda, and D. Mast. H ii regions in the CALIFA survey: I. catalogue presentation. *MNRAS*, 494(2):1622–1646, Mar. 2020. doi: 10.1093/mnras/staa782.

S. M. Fall, M. R. Krumholz, and C. D. Matzner. Stellar Feedback in Molecular Clouds and its Influence on the Mass Function of Young Star Clusters. *ApJL*, 710(2):L142–L146, Feb. 2010. doi: 10.1088/2041-8205/710/2/L142.

G. J. Ferland, M. Chatzikos, F. Guzmán, M. L. Lykins, P. A. M. van Hoof, R. J. R. Williams, N. P. Abel, N. R. Badnell, F. P. Keenan, R. L. Porter, and P. C. Stancil. The 2017 Release Cloudy. , 53: 385–438, Oct. 2017.

S. L. Finkelstein, M. Dickinson, H. C. Ferguson, A. Grazian, N. Grogin, J. Kartaltepe, L. Kewley, D. D. Kocevski, A. M. Koekemoer, J. Lotz, C. Papovich, L. Pentericci, P. G. Perez-Gonzalez, N. Pirzkal, S. Ravindranath, R. S. Somerville, J. R. Trump, and S. M. Wilkins. The Cosmic Evolution Early Release Science (CEERS) Survey. JWST Proposal ID 1345. Cycle 0 Early Release Science, Nov. 2017.

D. B. Fisher, K. Glazebrook, I. Damjanov, R. G. Abraham, D. Obreschkow, E. Wisnioski, R. Bassett, A. Green, and P. McGregor. DYNAMO-HST survey: clumps in nearby massive turbulent discs and the effects of clump clustering on kiloparsec scale measurements of clumps. *MNRAS*, 464(1):

491–507, Jan. 2017. doi: 10.1093/mnras/stw2281.

N. M. Förster Schreiber, R. Genzel, M. D. Lehnert, N. Bouché, A. Verma, D. K. Erb, A. E. Shapley, C. C. Steidel, R. Davies, D. Lutz, N. Nesvadba, L. J. Tacconi, F. Eisenhauer, R. Abuter, A. Gilbert, S. Gillessen, and A. Sternberg. SINFONI Integral Field Spectroscopy of z ~2 UV-selected Galaxies: Rotation Curves and Dynamical Evolution. *ApJ*, 645(2):1062–1075, July 2006. doi: 10.1086/504403.

N. M. Förster Schreiber, R. Genzel, N. Bouché, G. Cresci, R. Davies, P. Buschkamp, K. Shapiro, L. J. Tacconi, E. K. S. Hicks, S. Genel, A. E. Shapley, D. K. Erb, C. C. Steidel, D. Lutz, F. Eisenhauer, S. Gillessen, A. Sternberg, A. Renzini, A. Cimatti, E. Daddi, J. Kurk, S. Lilly, X. Kong, M. D. Lehnert, N. Nesvadba, A. Verma, H. McCracken, N. Arimoto, M. Mignoli, and M. Onodera. The SINS Survey: SINFONI Integral Field Spectroscopy of z ~2 Star-forming Galaxies. *ApJ*, 706(2): 1364–1428, Dec. 2009. doi: 10.1088/0004-637X/706/2/1364.

N. M. Förster Schreiber, A. E. Shapley, R. Genzel, N. Bouché, G. Cresci, R. Davies, D. K. Erb, S. Genel, D. Lutz, S. Newman, K. L. Shapiro, C. C. Steidel, A. Sternberg, and L. J. Tacconi. Constraints on the Assembly and Dynamics of Galaxies. II. Properties of Kiloparsec-scale Clumps in Rest-frame Optical Emission of z ~2 Star-forming Galaxies. *ApJ*, 739(1):45, Sept. 2011. doi: 10.1088/0004-637X/739/1/45.

J. Freundlich, F. Combes, L. J. Tacconi, M. C. Cooper, R. Genzel, R. Neri, A. Bolatto, F. Bournaud, A. Burkert, P. Cox, M. Davis, N. M. Förster Schreiber, S. Garcia-Burillo, J. Gracia-Carpio, D. Lutz, T. Naab, S. Newman, A. Sternberg, and B. Weiner. Towards a resolved Kennicutt-Schmidt law at high redshift. *A&A*, 553:A130, May 2013. doi: 10.1051/0004-6361/201220981.

J. S. Gallagher and D. A. Hunter. Gas kinematics and the structure of extragalactic giant and supergiant H II regions. *ApJ*, 274:141–151, Nov. 1983. doi: 10.1086/161432.

Y. Gao and P. M. Solomon. The Star Formation Rate and Dense Molecular Gas in Galaxies. *ApJ*, 606(1):271–290, May 2004. doi: 10.1086/382999.

R. Genzel, L. J. Tacconi, F. Eisenhauer, N. M. Förster Schreiber, A. Cimatti, E. Daddi, N. Bouché, R. Davies, M. D. Lehnert, D. Lutz, N. Nesvadba, A. Verma, R. Abuter, K. Shapiro, A. Sternberg, A. Renzini, X. Kong, N. Arimoto, and M. Mignoli. The rapid formation of a large rotating disk galaxy three billion years after the Big Bang. *Nature*, 442(7104):786–789, Aug. 2006. doi: 10.1038/nature05052.

R. Genzel, A. Burkert, N. Bouché, G. Cresci, N. M. Förster Schreiber, A. Shapley, K. Shapiro, L. J. Tacconi, P. Buschkamp, A. Cimatti, E. Daddi, R. Davies, F. Eisenhauer, D. K. Erb, S. Genel, O. Gerhard, E. Hicks, D. Lutz, T. Naab, T. Ott, S. Rabien, A. Renzini, C. C. Steidel, A. Sternberg, and S. J. Lilly. From Rings to Bulges: Evidence for Rapid Secular Galaxy Evolution at z ~2 from Integral Field Spectroscopy in the SINS Survey. *ApJ*, 687(1):59–77, Nov. 2008. doi: 10.1086/591840.

R. Genzel, F. Eisenhauer, and S. Gillessen. The Galactic Center massive black hole and nuclear star cluster. *Reviews of Modern Physics*, 82(4):3121–3195, Oct. 2010. doi: 10.1103/RevModPhys.82.3121.

R. Genzel, S. Newman, T. Jones, N. M. Förster Schreiber, K. Shapiro, S. Genel, S. J. Lilly, A. Renzini, L. J. Tacconi, N. Bouché, A. Burkert, G. Cresci, P. Buschkamp, C. M. Carollo, D. Ceverino, R. Davies, A. Dekel, F. Eisenhauer, E. Hicks, J. Kurk, D. Lutz, C. Mancini, T. Naab, Y. Peng, A. Sternberg, D. Vergani, and G. Zamorani. The Sins Survey of z ~2 Galaxy Kinematics: Properties of the Giant Star-forming Clumps. *ApJ*, 733(2):101, June 2011. doi: 10.1088/0004-637X/733/2/101.

A. M. Ghez, B. L. Klein, M. Morris, and E. E. Becklin. High Proper-Motion Stars in the Vicinity of Sagittarius A*: Evidence for a Supermassive Black Hole at the Center of Our Galaxy. *ApJ*, 509 (2):678–686, Dec. 1998. doi: 10.1086/306528.

A. M. Ghez, S. Salim, N. N. Weinberg, J. R. Lu, T. Do, J. K. Dunn, K. Matthews, M. R. Morris, S. Yelda, E. E. Becklin, T. Kremenek, M. Milosavljevic, and J. Naiman. Measuring Distance and Properties of the Milky Way's Central Supermassive Black Hole with Stellar Orbits. *ApJ*, 689(2): 1044–1062, Dec. 2008. doi: 10.1086/592738.

P. Girichidis, S. S. R. Offner, A. G. Kritsuk, R. S. Klessen, P. Hennebelle, J. M. D. Kruijssen, M. G. H. Krause, S. C. O. Glover, and M. Padovani. Physical Processes in Star Formation. , 216 (4):68, June 2020. doi: 10.1007/s11214-020-00693-8.

K. Glazebrook. The Dawes Review 1: Kinematic Studies of Star-Forming Galaxies Across Cosmic Time. *PASA*, 30:e056, Nov. 2013. doi: 10.1017/pasa.2013.34.

R. M. González Delgado, R. García-Benito, E. Pérez, R. Cid Fernandes, A. L. de Amorim, C. Cortijo-Ferrero, E. A. D. Lacerda, R. López Fernández, N. Vale-Asari, S. F. Sánchez, M. Mollá, T. Ruiz-Lara, P. Sánchez-Blázquez, C. J. Walcher, J. Alves, J. A. L. Aguerri, S. Bekeraité, J. Bland-Hawthorn, L. Galbany, A. Gallazzi, B. Husemann, J. Iglesias-Páramo, V. Kalinova, A. R. López-Sánchez, R. A. Marino, I. Márquez, J. Masegosa, D. Mast, J. Méndez-Abreu, A. Mendoza, A. del Olmo, I. Pérez, A. Quirrenbach, and S. Zibetti. The CALIFA survey across the Hubble sequence. Spatially resolved stellar population properties in galaxies. *A&A*, 581:A103, Sept. 2015. doi: 10.1051/0004-6361/201525938.

N. A. Grogin, D. D. Kocevski, S. M. Faber, H. C. Ferguson, A. M. Koekemoer, A. G. Riess, V. Acquaviva, D. M. Alexander, O. Almaini, M. L. N. Ashby, M. Barden, E. F. Bell, F. Bournaud, T. M. Brown, K. I. Caputi, S. Casertano, P. Cassata, M. Castellano, P. Challis, R.-R. Chary, E. Cheung, M. Cirasuolo, C. J. Conselice, A. Roshan Cooray, D. J. Croton, E. Daddi, T. Dahlen, R. Davé, D. F. de Mello, A. Dekel, M. Dickinson, T. Dolch, J. L. Donley, J. S. Dunlop, A. A. Dutton, D. Elbaz, G. G. Fazio, A. V. Filippenko, S. L. Finkelstein, A. Fontana, J. P. Gardner, P. M. Garnavich, E. Gawiser, M. Giavalisco, A. Grazian, Y. Guo, N. P. Hathi, B. Häussler, P. F. Hopkins, J.-S. Huang, K.-H. Huang, S. W. Jha, J. S. Kartaltepe, R. P. Kirshner, D. C. Koo, K. Lai, K.-S. Lee, W. Li, J. M. Lotz, R. A. Lucas, P. Madau, P. J. McCarthy, E. J. McGrath,

D. H. McIntosh, R. J. McLure, B. Mobasher, L. A. Moustakas, M. Mozena, K. Nandra, J. A. Newman, S.-M. Niemi, K. G. Noeske, C. J. Papovich, L. Pentericci, A. Pope, J. R. Primack, A. Rajan, S. Ravindranath, N. A. Reddy, A. Renzini, H.-W. Rix, A. R. Robaina, S. A. Rodney, D. J. Rosario, P. Rosati, S. Salimbeni, C. Scarlata, B. Siana, L. Simard, J. Smidt, R. S. Somerville, H. Spinrad, A. N. Straughn, L.-G. Strolger, O. Telford, H. I. Teplitz, J. R. Trump, A. van der Wel, C. Villforth, R. H. Wechsler, B. J. Weiner, T. Wiklind, V. Wild, G. Wilson, S. Wuyts, H.-J. Yan, and M. S. Yun. CANDELS: The Cosmic Assembly Near-infrared Deep Extragalactic Legacy Survey. *ApJS*, 197(2):35, Dec. 2011. doi: 10.1088/0067-0049/197/2/35.

M. Y. Grudić, D. Guszejnov, S. S. R. Offner, A. L. Rosen, A. N. Raju, C.-A. Faucher-Giguère, and P. F. Hopkins. The dynamics and outcome of star formation with jets, radiation, winds, and supernovae in concert. *MNRAS*, 512(1):216–232, May 2022. doi: 10.1093/mnras/stac526.

Q. Guo, E. Tempel, and N. I. Libeskind. Galaxies in Filaments have More Satellites: The Influence of the Cosmic Web on the Satellite Luminosity Function in the SDSS. *ApJ*, 800(2):112, Feb. 2015a. doi: 10.1088/0004-637X/800/2/112.

Y. Guo, H. C. Ferguson, E. F. Bell, D. C. Koo, C. J. Conselice, M. Giavalisco, S. Kassin, Y. Lu, R. Lucas, N. Mandelker, D. H. McIntosh, J. R. Primack, S. Ravindranath, G. Barro, D. Ceverino, A. Dekel, S. M. Faber, J. J. Fang, A. M. Koekemoer, K. Noeske, M. Rafelski, and A. Straughn. Clumpy Galaxies in CANDELS. I. The Definition of UV Clumps and the Fraction of Clumpy Galaxies at 0.5 ¡ z ¡ 3. *ApJ*, 800(1):39, Feb. 2015b. doi: 10.1088/0004-637X/800/1/39.

S. Hannon, J. C. Lee, B. C. Whitmore, R. Chandar, A. Adamo, B. Mobasher, A. Aloisi, D. Calzetti, M. Cignoni, D. O. Cook, D. Dale, S. Deger, L. Della Bruna, D. M. Elmegreen, D. A. Gouliermis, K. Grasha, E. K. Grebel, A. Herrero, D. A. Hunter, K. E. Johnson, R. Kennicutt, H. Kim, E. Sacchi, L. Smith, D. Thilker, J. Turner, R. A. M. Walterbos, and A. Wofford. H α morphologies of star clusters: a LEGUS study of H II region evolution time-scales and stochasticity in low-mass clusters. *MNRAS*, 490(4):4648–4665, Dec. 2019. doi: 10.1093/mnras/stz2820.

E. Harper-Clark and N. Murray. One-Dimensional Dynamical Models of the Carina Nebula Bubble. *ApJ*, 693(2):1696–1712, Mar. 2009. doi: 10.1088/0004-637X/693/2/1696.

C. R. Harris, K. J. Millman, S. J. van der Walt, R. Gommers, P. Virtanen, D. Cournapeau, E. Wieser, J. Taylor, S. Berg, N. J. Smith, R. Kern, M. Picus, S. Hoyer, M. H. van Kerkwijk, M. Brett, A. Haldane, J. Fernández del Río, M. Wiebe, P. Peterson, P. Gérard-Marchant, K. Sheppard, T. Reddy, W. Weckesser, H. Abbasi, C. Gohlke, and T. E. Oliphant. Array programming with NumPy. *Nature*, 585:357–362, 2020. doi: 10.1038/s41586-020-2649-2.

M. Heyer and T. M. Dame. Molecular Clouds in the Milky Way. *ARA&A*, 53:583–629, Aug. 2015. doi: 10.1146/annurev-astro-082214-122324.

A. M. Hidalgo-Gámez. Physical conditions in the dwarf local irregular galaxy IC 10. I. Diffuse ionized gas. *A&A*, 442(2):443–453, Nov. 2005. doi: 10.1051/0004-6361:20041663.

P. Hodge and M. G. Lee. The H II Regions of IC 10. *PASP*, 102:26, Jan. 1990. doi: 10.1086/132603.

P. Hodge, M. G. Lee, and J. Kennicutt, Robert C. The H II Regions of NGC 6822. II. The Luminosity Function and Size Distribution. *PASP*, 101:32, Jan. 1989. doi: 10.1086/132401.

D. W. Hogg, J. Bovy, and D. Lang. Data analysis recipes: Fitting a model to data. *arXiv e-prints*, art. arXiv:1008.4686, Aug. 2010.

K. Hollyhead, N. Bastian, A. Adamo, E. Silva-Villa, J. Dale, J. E. Ryon, and Z. Gazak. Studying the YMC population of M83: how long clusters remain embedded, their interaction with the ISM and implications for GC formation theories. *MNRAS*, 449(1):1106–1117, May 2015. doi: 10.1093/mnras/stv331.

A. M. Hopkins. On the Evolution of Star-forming Galaxies. *ApJ*, 615(1):209–221, Nov. 2004. doi: 10.1086/424032.

A. M. Hopkins and J. F. Beacom. On the Normalization of the Cosmic Star Formation History. *ApJ*, 651(1):142–154, Nov. 2006. doi: 10.1086/506610.

P. F. Hopkins, E. Quataert, and N. Murray. Stellar feedback in galaxies and the origin of galaxy-scale winds. *MNRAS*, 421(4):3522–3537, Apr. 2012. doi: 10.1111/j.1365-2966.2012.20593.x.

P. F. Hopkins, D. Kereš, J. Oñorbe, C.-A. Faucher-Giguère, E. Quataert, N. Murray, and J. S. Bullock. Galaxies on FIRE (Feedback In Realistic Environments): stellar feedback explains cosmologically inefficient star formation. *MNRAS*, 445(1):581–603, Nov. 2014. doi: 10.1093/mnras/stu1738.

W. K. Huchtmeier. The giant H I-envelope of the irregular galaxy IC 10. *A&A*, 75:170–175, May 1979.

D. A. Hunter. The Stellar Population and Star Clusters in the Unusual Local Group Galaxy IC 10. *ApJ*, 559(1):225–242, Sept. 2001. doi: 10.1086/322399.

J. D. Hunter. Matplotlib: A 2D Graphics Environment. *Computing in Science and Engineering*, 9 (3):90–95, May 2007. doi: 10.1109/MCSE.2007.55.

F. P. Israel. H II regions and CO clouds: the blister model. *A&A*, 70:769–775, Dec. 1978.

T. L. Johnson, J. R. Rigby, K. Sharon, M. D. Gladders, M. Florian, M. B. Bayliss, E. Wuyts, K. E. Whitaker, R. Livermore, and K. T. Murray. Star Formation at z = 2.481 in the Lensed Galaxy SDSS J1110+6459: Star Formation Down to 30 pc Scales. *ApJL*, 843(2):L21, July 2017. doi: 10.3847/2041-8213/aa7516.

T. A. Jones, A. M. Swinbank, R. S. Ellis, J. Richard, and D. P. Stark. Resolved spectroscopy of gravitationally lensed galaxies: recovering coherent velocity fields in subluminous z ~2-3 galaxies. *MNRAS*, 404(3):1247–1262, May 2010. doi: 10.1111/j.1365-2966.2010.16378.x.

J. Kennicutt, R. C. and P. W. Hodge. H II Regions and Star Formation in the Magellanic Clouds. *ApJ*, 306:130, July 1986. doi: 10.1086/164326.

J. Kennicutt, Robert C. The Integrated Spectra of Nearby Galaxies: General Properties and Emission-Line Spectra. *ApJ*, 388:310, Apr. 1992. doi: 10.1086/171154.

J. Kennicutt, Robert C. Star Formation in Galaxies Along the Hubble Sequence. *ARA&A*, 36: 189–232, Jan. 1998a. doi: 10.1146/annurev.astro.36.1.189.

J. Kennicutt, Robert C. The Global Schmidt Law in Star-forming Galaxies. *ApJ*, 498(2):541–552, May 1998b. doi: 10.1086/305588.

J. Kennicutt, Robert C., L. Armus, G. Bendo, D. Calzetti, D. A. Dale, B. T. Draine, C. W. Engelbracht, K. D. Gordon, A. D. Grauer, G. Helou, D. J. Hollenbach, T. H. Jarrett, L. J. Kewley, C. Leitherer, A. Li, S. Malhotra, M. W. Regan, G. H. Rieke, M. J. Rieke, H. Roussel, J.-D. T. Smith, M. D. Thornley, and F. Walter. SINGS: The SIRTF Nearby Galaxies Survey. *PASP*, 115 (810):928–952, Aug. 2003. doi: 10.1086/376941.

C. R. Kerton, G. Wolf-Chase, K. Arvidsson, C. J. Lintott, and R. J. Simpson. The Milky Way Project: What are Yellowballs? *ApJ*, 799(2):153, Feb. 2015. doi: 10.1088/0004-637X/799/2/153.

L. J. Kewley and S. L. Ellison. Metallicity Calibrations and the Mass-Metallicity Relation for Star-forming Galaxies. *ApJ*, 681(2):1183–1204, July 2008. doi: 10.1086/587500.

L. J. Kewley, M. J. Geller, and R. A. Jansen. [O II] as a Star Formation Rate Indicator. *AJ*, 127(4): 2002–2030, Apr. 2004. doi: 10.1086/382723.

L. J. Kewley, D. C. Nicholls, and R. S. Sutherland. Understanding Galaxy Evolution Through Emission Lines. *ARA&A*, 57:511–570, Aug. 2019. doi: 10.1146/annurev-astro-081817-051832.

M. Kim, E. Kim, N. Hwang, M. G. Lee, M. Im, H. Karoji, J. Noumaru, and I. Tanaka. Reddening and Distance of the Local Group Starburst Galaxy IC 10. *ApJ*, 703(1):816–828, Sep 2009. doi: 10.1088/0004-637X/703/1/816.

H. A. Kobulnicky and L. J. Kewley. Metallicities of 0.3¡z¡1.0 Galaxies in the GOODS-North Field. *ApJ*, 617(1):240–261, Dec. 2004. doi: 10.1086/425299.

J. A. Kollmeier, G. Zasowski, H.-W. Rix, M. Johns, S. F. Anderson, N. Drory, J. A. Johnson, R. W. Pogge, J. C. Bird, G. A. Blanc, J. R. Brownstein, J. D. Crane, N. M. De Lee, M. A. Klaene, K. Kreckel, N. MacDonald, A. Merloni, M. K. Ness, T. O'Brien, J. R. Sanchez-Gallego, C. C. Sayres, Y. Shen, A. R. Thakar, A. Tkachenko, C. Aerts, M. R. Blanton, D. J. Eisenstein, J. A. Holtzman, D. Maoz, K. Nandra, C. Rockosi, D. H. Weinberg, J. Bovy, A. R. Casey, J. Chaname, N. Clerc, C. Conroy, M. Eracleous, B. T. Gänsicke, S. Hekker, K. Horne, J. Kauffmann, K. B. W. McQuinn, E. W. Pellegrini, E. Schinnerer, E. F. Schlafly, A. D. Schwope, M. Seibert, J. K. Teske, and J. L. van Saders. SDSS-V: Pioneering Panoptic Spectroscopy. *arXiv e-prints*, art.

arXiv:1711.03234, Nov. 2017.

N. Krieger, A. D. Bolatto, E. W. Koch, A. K. Leroy, E. Rosolowsky, F. Walter, A. Weiß, D. J. Eden, R. C. Levy, D. S. Meier, E. A. C. Mills, T. Moore, J. Ott, Y. Su, and S. Veilleux. The Turbulent Gas Structure in the Centers of NGC 253 and the Milky Way. *ApJ*, 899(2):158, Aug. 2020. doi: 10.3847/1538-4357/aba903.

P. Kroupa. On the variation of the initial mass function. *MNRAS*, 322(2):231–246, Apr. 2001. doi: 10.1046/j.1365-8711.2001.04022.x.

M. R. Krumholz. The big problems in star formation: The star formation rate, stellar clustering, and the initial mass function. , 539:49–134, June 2014. doi: 10.1016/j.physrep.2014.02.001.

M. R. Krumholz and T. A. Thompson. Direct Numerical Simulation of Radiation Pressure-driven Turbulence and Winds in Star Clusters and Galactic Disks. *ApJ*, 760(2):155, Dec. 2012. doi: 10.1088/0004-637X/760/2/155.

M. R. Krumholz and T. A. Thompson. Numerical simulations of radiatively driven dusty winds. *MNRAS*, 434(3):2329–2346, Sept. 2013. doi: 10.1093/mnras/stt1174.

M. R. Krumholz, M. R. Bate, H. G. Arce, J. E. Dale, R. Gutermuth, R. I. Klein, Z. Y. Li, F. Nakamura, and Q. Zhang. Star Cluster Formation and Feedback. In H. Beuther, R. S. Klessen, C. P. Dullemond, and T. Henning, editors, *Protostars and Planets VI*, page 243, Jan. 2014. doi: 10.2458/azu_uapress_9780816531240-ch011.

M. R. Krumholz, A. Adamo, M. Fumagalli, A. Wofford, D. Calzetti, J. C. Lee, B. C. Whitmore, S. N. Bright, K. Grasha, D. A. Gouliermis, H. Kim, P. Nair, J. E. Ryon, L. J. Smith, D. Thilker, L. Ubeda, and E. Zackrisson. Star Cluster Properties in Two LEGUS Galaxies Computed with Stochastic Stellar Population Synthesis Models. *ApJ*, 812(2):147, Oct. 2015. doi: 10.1088/0004-637X/812/2/147.

M. R. Krumholz, C. F. McKee, and J. Bland-Hawthorn. Star Clusters Across Cosmic Time. *ARA&A*, 57:227–303, Aug. 2019. doi: 10.1146/annurev-astro-091918-104430.

E. A. D. Lacerda, R. Cid Fernandes, G. S. Couto, G. Stasińska, R. García-Benito, N. Vale Asari, E. Pérez, R. M. González Delgado, S. F. Sánchez, and A. L. de Amorim. Diffuse ionized gas in galaxies across the Hubble sequence at the CALIFA resolution. *MNRAS*, 474(3):3727–3739, Mar. 2018. doi: 10.1093/mnras/stx3022.

C. J. Lada, M. Lombardi, and J. F. Alves. On the Star Formation Rates in Molecular Clouds. *ApJ*, 724(1):687–693, Nov. 2010. doi: 10.1088/0004-637X/724/1/687.

H. J. Lamers and E. M. Levesque. Stellar winds and mass loss. In *Understanding Stellar Evolution*, 2514-3433, pages 15–1 to 15–12. IOP Publishing, 2017. ISBN 978-0-7503-1278-3. doi: 10.1088/978-0-7503-1278-3ch15. URL http://dx.doi.org/10.1088/978-0-7503-1278-3ch15.

J. Larkin, M. Barczys, A. Krabbe, S. Adkins, T. Aliado, P. Amico, G. Brims, R. Campbell, J. Canfield, T. Gasaway, A. Honey, C. Iserlohe, C. Johnson, E. Kress, D. LaFreniere, J. Lyke, K. Magnone, N. Magnone, M. McElwain, J. Moon, A. Quirrenbach, G. Skulason, I. Song, M. Spencer, J. Weiss, and S. Wright. OSIRIS: a diffraction limited integral field spectrograph for Keck. In I. S. McLean and M. Iye, editors, *Society of Photo-Optical Instrumentation Engineers (SPIE) Conference Series*, volume 6269 of *Society of Photo-Optical Instrumentation Engineers (SPIE) Conference Series*, page 62691A, June 2006. doi: 10.1117/12.672061.

J. E. Larkin, A. M. Moore, S. A. Wright, J. E. Wincentsen, D. Anderson, E. M. Chisholm, R. G. Dekany, J. S. Dunn, B. L. Ellerbroek, Y. Hayano, A. C. Phillips, L. Simard, R. Smith, R. Suzuki, R. W. Weber, J. L. Weiss, and K. Zhang. The Infrared Imaging Spectrograph (IRIS) for TMT: instrument overview. In C. J. Evans, L. Simard, and H. Takami, editors, *Ground-based and Airborne Instrumentation for Astronomy VI*, volume 9908 of *Society of Photo-Optical Instrumentation Engineers (SPIE) Conference Series*, page 99081W, Aug. 2016. doi: 10.1117/12.2232212.

J. E. Larkin, S. A. Wright, E. M. Chisholm, D. Andersen, R. G. Dekany, J. S. Dunn, Y. Hayano, R. Kupke, R. Smith, R. Suzuki, R. W. Weber, and K. Zhang. The Infrared Imaging Spectrograph (IRIS) for TMT: instrument overview. In *Ground-based and Airborne Instrumentation for Astronomy VIII*, volume 11447 of *Society of Photo-Optical Instrumentation Engineers (SPIE) Conference Series*, page 114471Y, Dec. 2020. doi: 10.1117/12.2561184.

K. L. Larson, T. Díaz-Santos, L. Armus, G. C. Privon, S. T. Linden, A. S. Evans, J. Howell, V. Charmandaris, V. U, D. B. Sanders, S. Stierwalt, L. Barcos-Muñoz, J. Rich, A. Medling, D. Cook, A. Oklopĉić, E. J. Murphy, and P. Bonfini. Star-forming Clumps in Local Luminous Infrared Galaxies. *ApJ*, 888(2):92, Jan. 2020. doi: 10.3847/1538-4357/ab5dc3.

R. B. Larson. Turbulence and star formation in molecular clouds. *MNRAS*, 194:809–826, Mar. 1981. doi: 10.1093/mnras/194.4.809.

D. R. Law, C. C. Steidel, D. K. Erb, J. E. Larkin, M. Pettini, A. E. Shapley, and S. A. Wright. Integral Field Spectroscopy of High-Redshift Star-forming Galaxies with Laser-guided Adaptive Optics: Evidence for Dispersion-dominated Kinematics. *ApJ*, 669(2):929–946, Nov. 2007a. doi: 10.1086/521786.

D. R. Law, C. C. Steidel, D. K. Erb, M. Pettini, N. A. Reddy, A. E. Shapley, K. L. Adelberger, and D. J. Simenc. The Physical Nature of Rest-UV Galaxy Morphology during the Peak Epoch of Galaxy Formation. *ApJ*, 656(1):1–26, Feb. 2007b. doi: 10.1086/510357.

D. R. Law, C. C. Steidel, D. K. Erb, J. E. Larkin, M. Pettini, A. E. Shapley, and S. A. Wright. The Kiloparsec-scale Kinematics of High-redshift Star-forming Galaxies. *ApJ*, 697(2):2057–2082, June 2009. doi: 10.1088/0004-637X/697/2/2057.

V. Lebouteiller, G. C. Sloan, M. A. T. Groenewegen, M. Matsuura, D. Riebel, D. G. Whelan, J. Bernard-Salas, P. Massey, and E. Bayet. Oxygen-rich dust production in IC 10. *A&A*, 546: A94, Oct 2012. doi: 10.1051/0004-6361/201220087.

N. Leethochawalit, T. A. Jones, R. S. Ellis, D. P. Stark, J. Richard, A. Zitrin, and M. Auger. A Keck Adaptive Optics Survey of a Representative Sample of Gravitationally Lensed Star-forming Galaxies: High Spatial Resolution Studies of Kinematics and Metallicity Gradients. *ApJ*, 820(2): 84, Apr. 2016. doi: 10.3847/0004-637X/820/2/84.

J. Lequeux, M. Peimbert, J. F. Rayo, A. Serrano, and S. Torres-Peimbert. Chemical composition and evolution of irregular and blue compact galaxies. *A&A*, 500:145–156, Dec. 1979.

R. C. Livermore, T. Jones, J. Richard, R. G. Bower, R. S. Ellis, A. M. Swinbank, J. R. Rigby, I. Smail, S. Arribas, J. Rodriguez Zaurin, L. Colina, H. Ebeling, and R. A. Crain. Hubble Space Telescope Hα imaging of star-forming galaxies at z 1-1.5: evolution in the size and luminosity of giant H II regions. *MNRAS*, 427(1):688–702, Nov. 2012. doi: 10.1111/j.1365-2966.2012.21900.x.

R. C. Livermore, T. A. Jones, J. Richard, R. G. Bower, A. M. Swinbank, T. T. Yuan, A. C. Edge, R. S. Ellis, L. J. Kewley, I. Smail, K. E. K. Coppin, and H. Ebeling. Resolved spectroscopy of gravitationally lensed galaxies: global dynamics and star-forming clumps on $\sim$100 pc scales at 1 ¡ z ¡ 4. *MNRAS*, 450(2):1812–1835, June 2015. doi: 10.1093/mnras/stv686.

L. A. Lopez, M. R. Krumholz, A. D. Bolatto, J. X. Prochaska, and E. Ramirez-Ruiz. What Drives the Expansion of Giant H II Regions?: A Study of Stellar Feedback in 30 Doradus. *ApJ*, 731(2): 91, Apr. 2011. doi: 10.1088/0004-637X/731/2/91.

L. A. Lopez, M. R. Krumholz, A. D. Bolatto, J. X. Prochaska, E. Ramirez-Ruiz, and D. Castro. The Role of Stellar Feedback in the Dynamics of H II Regions. *ApJ*, 795(2):121, Nov. 2014. doi: 10.1088/0004-637X/795/2/121.

M. J. Lundquist, H. A. Kobulnicky, M. J. Alexander, C. R. Kerton, and K. Arvidsson. An All-sky Sample of Intermediate-mass Star-forming Regions. *ApJ*, 784(2):111, Apr. 2014. doi: 10.1088/0004-637X/784/2/111.

J. Lyke, T. Do, A. Boehle, R. Campbell, S. Chappell, M. Fitzgerald, T. Gasawy, C. Iserlohe, A. Krabbe, J. Larkin, K. Lockhart, J. Lu, E. Mieda, M. McElwain, M. Perrin, A. Rudy, B. Sitarski, A. Vayner, G. Walth, J. Weiss, T. Wizanski, and S. Wright. OSIRIS Toolbox: OH-Suppressing InfraRed Imaging Spectrograph pipeline, Oct. 2017.

P. Madau and M. Dickinson. Cosmic Star-Formation History. *ARA&A*, 52:415–486, Aug. 2014. doi: 10.1146/annurev-astro-081811-125615.

L. Magrini and D. R. Gonçalves. IC10: the history of the nearest starburst galaxy through its Planetary Nebula and HII region populations. *MNRAS*, 398(1):280–292, Sep 2009. doi: 10.1111/j.1365-2966.2009.15124.x.

C. Mancini, N. M. Förster Schreiber, A. Renzini, G. Cresci, E. K. S. Hicks, Y. Peng, D. Vergani, S. Lilly, M. Carollo, L. Pozzetti, G. Zamorani, E. Daddi, R. Genzel, C. Maraston, H. J. McCracken, L. Tacconi, N. Bouché, R. Davies, P. Oesch, K. Shapiro, V. Mainieri, D. Lutz, M. Mignoli,

and A. Sternberg. The zCOSMOS-SINFONI Project. I. Sample Selection and Natural-seeing Observations. *ApJ*, 743(1):86, Dec. 2011. doi: 10.1088/0004-637X/743/1/86.

N. Mandelker, A. Dekel, D. Ceverino, D. Tweed, C. E. Moody, and J. Primack. The population of giant clumps in simulated high-z galaxies: in situ and ex situ migration and survival. *MNRAS*, 443(4):3675–3702, Oct. 2014. doi: 10.1093/mnras/stu1340.

N. Mandelker, A. Dekel, D. Ceverino, C. DeGraf, Y. Guo, and J. Primack. Giant clumps in simulated high- z Galaxies: properties, evolution and dependence on feedback. *MNRAS*, 464(1):635–665, Jan. 2017. doi: 10.1093/mnras/stw2358.

R. A. Marino, F. F. Rosales-Ortega, S. F. Sánchez, A. Gil de Paz, J. Vílchez, D. Miralles-Caballero, C. Kehrig, E. Pérez-Montero, V. Stanishev, J. Iglesias-Páramo, A. I. Díaz, A. Castillo-Morales, R. Kennicutt, A. R. López-Sánchez, L. Galbany, R. García-Benito, D. Mast, J. Mendez-Abreu, A. Monreal-Ibero, B. Husemann, C. J. Walcher, B. García-Lorenzo, J. Masegosa, A. Del Olmo Orozco, A. M. Mourão, B. Ziegler, M. Mollá, P. Papaderos, P. Sánchez-Blázquez, R. M. González Delgado, J. Falcón-Barroso, M. M. Roth, G. van de Ven, and Califa Team. The O3N2 and N2 abundance indicators revisited: improved calibrations based on CALIFA and T_e-based literature data. *A&A*, 559:A114, Nov. 2013. doi: 10.1051/0004-6361/201321956.

F. Martins, D. Schaerer, and D. J. Hillier. A new calibration of stellar parameters of Galactic O stars. *A&A*, 436(3):1049–1065, June 2005. doi: 10.1051/0004-6361:20042386.

P. Massey and S. Holmes. Wolf-Rayet Stars in IC 10: Probing the Nearest Starburst. *ApJL*, 580(1): L35–L38, Nov. 2002. doi: 10.1086/345405.

M. Mayor and D. Queloz. A Jupiter-mass companion to a solar-type star. *Nature*, 378(6555): 355–359, Nov. 1995. doi: 10.1038/378355a0.

C. F. McKee and E. C. Ostriker. Theory of Star Formation. *ARA&A*, 45(1):565–687, Sept. 2007. doi: 10.1146/annurev.astro.45.051806.110602.

A. F. McLeod, J. E. Dale, C. J. Evans, A. Ginsburg, J. M. D. Kruijssen, E. W. Pellegrini, S. K. Ramsay, and L. Testi. Feedback from massive stars at low metallicities: MUSE observations of N44 and N180 in the Large Magellanic Cloud. *MNRAS*, 486(4):5263–5288, July 2019. doi: 10.1093/mnras/sty2696.

A. F. McLeod, A. A. Ali, M. Chevance, L. Della Bruna, A. Schruba, H. F. Stevance, A. Adamo, J. M. D. Kruijssen, S. N. Longmore, D. R. Weisz, and P. Zeidler. The impact of pre-supernova feedback and its dependence on environment. *MNRAS*, 508(4):5425–5448, Dec. 2021. doi: 10.1093/mnras/stab2726.

E. Mieda, S. A. Wright, J. E. Larkin, L. Armus, S. Juneau, S. Salim, and N. Murray. IROCKS: Spatially Resolved Kinematics of z $\sim$ 1 Star-forming Galaxies. *ApJ*, 831(1):78, Nov. 2016. doi: 10.3847/0004-637X/831/1/78.

J. Molina, E. Ibar, A. M. Swinbank, D. Sobral, P. N. Best, I. Smail, A. Escala, and M. Cirasuolo. SINFONI-HiZELS: the dynamics, merger rates and metallicity gradients of 'typical' star-forming galaxies at z = 0.8-2.2. *MNRAS*, 466(1):892–905, Apr. 2017. doi: 10.1093/mnras/stw3120.

I. G. Momcheva, J. C. Lee, C. Ly, S. Salim, D. A. Dale, M. Ouchi, R. Finn, and Y. Ono. Nebular Attenuation in Hα-selected Star-forming Galaxies at z = 0.8 from the NewHα Survey. *AJ*, 145 (2):47, Feb. 2013. doi: 10.1088/0004-6256/145/2/47.

A. Monreal-Ibero, L. Colina, S. Arribas, and M. García-Marín. Search for tidal dwarf galaxy candidates in a sample of ultraluminous infrared galaxies. *A&A*, 472(2):421–433, Sept. 2007. doi: 10.1051/0004-6361:20066760.

P. Morrissey, M. Matuszewski, D. C. Martin, J. D. Neill, H. Epps, J. Fucik, B. Weber, B. Darvish, S. Adkins, S. Allen, R. Bartos, J. Belicki, J. Cabak, S. Callahan, D. Cowley, M. Crabill, W. Deich, A. Delecroix, G. Doppman, D. Hilyard, E. James, S. Kaye, M. Kokorowski, S. Kwok, K. Lanclos, S. Milner, A. Moore, D. O'Sullivan, P. Parihar, S. Park, A. Phillips, L. Rizzi, C. Rockosi, H. Rodriguez, Y. Salaun, K. Seaman, D. Sheikh, J. Weiss, and R. Zarzaca. The keck cosmic web imager integral field spectrograph. *ApJ*, 864(1):93, sep 2018. doi: 10.3847/1538-4357/aad597. URL https://doi.org/10.3847%2F1538-4357%2Faad597.

J. Moustakas, J. Kennicutt, Robert C., and C. A. Tremonti. Optical Star Formation Rate Indicators. *ApJ*, 642(2):775–796, May 2006. doi: 10.1086/500964.

J. Moustakas, J. Kennicutt, Robert C., C. A. Tremonti, D. A. Dale, J.-D. T. Smith, and D. Calzetti. Optical Spectroscopy and Nebular Oxygen Abundances of the Spitzer/SINGS Galaxies. *ApJS*, 190(2):233–266, Oct. 2010. doi: 10.1088/0067-0049/190/2/233.

E. J. Murphy, J. J. Condon, E. Schinnerer, R. C. Kennicutt, D. Calzetti, L. Armus, G. Helou, J. L. Turner, G. Aniano, P. Beirão, A. D. Bolatto, B. R. Brandl, K. V. Croxall, D. A. Dale, J. L. Donovan Meyer, B. T. Draine, C. Engelbracht, L. K. Hunt, C. N. Hao, J. Koda, H. Roussel, R. Skibba, and J. D. T. Smith. Calibrating Extinction-free Star Formation Rate Diagnostics with 33 GHz Free-free Emission in NGC 6946. *ApJ*, 737(2):67, Aug. 2011. doi: 10.1088/0004-637X/737/2/67.

N. Murray, E. Quataert, and T. A. Thompson. The Disruption of Giant Molecular Clouds by Radiation Pressure & the Efficiency of Star Formation in Galaxies. *ApJ*, 709(1):191–209, Jan. 2010. doi: 10.1088/0004-637X/709/1/191.

T. Nagao, R. Maiolino, and A. Marconi. Gas metallicity diagnostics in star-forming galaxies. *A&A*, 459(1):85–101, Nov. 2006. doi: 10.1051/0004-6361:20065216.

B. Namumba, C. Carignan, T. Foster, and N. Deg. H I observations of IC 10 with the DRAO synthesis telescope. *MNRAS*, 490(3):3365–3377, Dec. 2019. doi: 10.1093/mnras/stz2737.

S. F. Newman, R. Genzel, N. M. Förster Schreiber, K. Shapiro Griffin, C. Mancini, S. J. Lilly, A. Renzini, N. Bouché, A. Burkert, P. Buschkamp, C. M. Carollo, G. Cresci, R. Davies, F. Eisen-

hauer, S. Genel, E. K. S. Hicks, J. Kurk, D. Lutz, T. Naab, Y. Peng, A. Sternberg, L. J. Tacconi, S. Wuyts, G. Zamorani, and D. Vergani. The SINS/zC-SINF Survey of z ~2Galaxy Kinematics: The Nature of Dispersion-dominated Galaxies. *ApJ*, 767(2):104, Apr. 2013. doi: 10.1088/0004-637X/767/2/104.

Q. Nguyen-Luong, H. V. V. Nguyen, F. Motte, N. Schneider, M. Fujii, F. Louvet, T. Hill, P. Sanhueza, J. O. Chibueze, and P. Didelon. The Scaling Relations and Star Formation Laws of Mini-starburst Complexes. *ApJ*, 833(1):23, Dec. 2016. doi: 10.3847/0004-637X/833/1/23.

D. L. Nidever, T. Ashley, C. T. Slater, J. Ott, M. Johnson, E. F. Bell, S. Stanimirović, M. Putman, S. R. Majewski, C. E. Simpson, E. Jütte, T. A. Oosterloo, and W. Butler Burton. Evidence for an Interaction in the Nearest Starbursting Dwarf Irregular Galaxy IC 10. *ApJL*, 779(2):L15, Dec. 2013. doi: 10.1088/2041-8205/779/2/L15.

C. R. O'Dell, G. J. Ferland, and M. Peimbert. Structure and physical conditions in the Huygens region of the Orion nebula. *MNRAS*, 464(4):4835–4857, Feb. 2017. doi: 10.1093/mnras/stw2713.

M. S. Oey, G. R. Meurer, S. Yelda, E. J. Furst, S. M. Caballero-Nieves, D. J. Hanish, E. M. Levesque, D. A. Thilker, G. L. Walth, J. Bland-Hawthorn, M. A. Dopita, H. C. Ferguson, T. M. Heckman, M. T. Doyle, M. J. Drinkwater, K. C. Freeman, J. Kennicutt, R. C., V. A. Kilborn, P. M. Knezek, B. Koribalski, M. Meyer, M. E. Putman, E. V. Ryan-Weber, R. C. Smith, L. Staveley-Smith, R. L. Webster, J. Werk, and M. A. Zwaan. The Survey for Ionization in Neutral Gas Galaxies. III. Diffuse, Warm Ionized Medium and Escape of Ionizing Radiation. *ApJ*, 661(2):801–814, June 2007. doi: 10.1086/517867.

A. Oklopčić, P. F. Hopkins, R. Feldmann, D. Kereš, C.-A. Faucher-Giguère, and N. Murray. Giant clumps in the FIRE simulations: a case study of a massive high-redshift galaxy. *MNRAS*, 465(1): 952–969, Feb. 2017. doi: 10.1093/mnras/stw2754.

D. E. Osterbrock. *Astrophysics of gaseous nebulae and active galactic nuclei*. 1989.

D. E. Osterbrock and G. J. Ferland. *Astrophysics of gaseous nebulae and active galactic nuclei*. 2006.

B. E. J. Pagel, M. G. Edmunds, D. E. Blackwell, M. S. Chun, and G. Smith. On the composition of H II regions in southern galaxies - I. NGC 300 and 1365. *MNRAS*, 189:95–113, Oct. 1979. doi: 10.1093/mnras/189.1.95.

E. W. Pellegrini, J. A. Baldwin, and G. J. Ferland. Structure and Feedback in 30 Doradus. II. Structure and Chemical Abundances. *ApJ*, 738(1):34, Sept. 2011. doi: 10.1088/0004-637X/738/1/34.

E. Pérez, R. Cid Fernandes, R. M. González Delgado, R. García-Benito, S. F. Sánchez, B. Husemann, D. Mast, J. R. Rodón, D. Kupko, N. Backsmann, A. L. de Amorim, G. van de Ven, J. Walcher, L. Wisotzki, C. Cortijo-Ferrero, and CALIFA Collaboration. The Evolution of Galaxies Resolved

in Space and Time: A View of Inside-out Growth from the CALIFA Survey. *ApJL*, 764(1):L1, Feb. 2013. doi: 10.1088/2041-8205/764/1/L1.

F. Perez and B. E. Granger. Ipython: A system for interactive scientific computing. *Computing in Science & Engineering*, 9(3):21–29, 2007.

L. S. Pilyugin and T. X. Thuan. Oxygen Abundance Determination in H II Regions: The Strong Line Intensities-Abundance Calibration Revisited. *ApJ*, 631(1):231–243, Sept. 2005. doi: 10.1086/432408.

Planck Collaboration, P. A. R. Ade, N. Aghanim, C. Armitage-Caplan, M. Arnaud, M. Ashdown, F. Atrio-Barandela, J. Aumont, C. Baccigalupi, A. J. Banday, R. B. Barreiro, J. G. Bartlett, E. Battaner, K. Benabed, A. Benoît, A. Benoit-Lévy, J. P. Bernard, M. Bersanelli, P. Bielewicz, J. Bobin, J. J. Bock, A. Bonaldi, J. R. Bond, J. Borrill, F. R. Bouchet, M. Bridges, M. Bucher, C. Burigana, R. C. Butler, E. Calabrese, B. Cappellini, J. F. Cardoso, A. Catalano, A. Challinor, A. Chamballu, R. R. Chary, X. Chen, H. C. Chiang, L. Y. Chiang, P. R. Christensen, S. Church, D. L. Clements, S. Colombi, L. P. L. Colombo, F. Couchot, A. Coulais, B. P. Crill, A. Curto, F. Cuttaia, L. Danese, R. D. Davies, R. J. Davis, P. de Bernardis, A. de Rosa, G. de Zotti, J. Delabrouille, J. M. Delouis, F. X. Désert, C. Dickinson, J. M. Diego, K. Dolag, H. Dole, S. Donzelli, O. Doré, M. Douspis, J. Dunkley, X. Dupac, G. Efstathiou, F. Elsner, T. A. Enßlin, H. K. Eriksen, F. Finelli, O. Forni, M. Frailis, A. A. Fraisse, E. Franceschi, T. C. Gaier, S. Galeotta, S. Galli, K. Ganga, M. Giard, G. Giardino, Y. Giraud-Héraud, E. Gjerløw, J. González-Nuevo, K. M. Górski, S. Gratton, A. Gregorio, A. Gruppuso, J. E. Gudmundsson, J. Haissinski, J. Hamann, F. K. Hansen, D. Hanson, D. Harrison, S. Henrot-Versillé, C. Hernández-Monteagudo, D. Herranz, S. R. Hildebrandt, E. Hivon, M. Hobson, W. A. Holmes, A. Hornstrup, Z. Hou, W. Hovest, K. M. Huffenberger, A. H. Jaffe, T. R. Jaffe, J. Jewell, W. C. Jones, M. Juvela, E. Keihänen, R. Keskitalo, T. S. Kisner, R. Kneissl, J. Knoche, L. Knox, M. Kunz, H. Kurki-Suonio, G. Lagache, A. Lähteenmäki, J. M. Lamarre, A. Lasenby, M. Lattanzi, R. J. Laureijs, C. R. Lawrence, S. Leach, J. P. Leahy, R. Leonardi, J. León-Tavares, J. Lesgourgues, A. Lewis, M. Liguori, P. B. Lilje, M. Linden-Vørnle, M. López-Caniego, P. M. Lubin, J. F. Macías-Pérez, B. Maffei, D. Maino, N. Mandolesi, M. Maris, D. J. Marshall, P. G. Martin, E. Martínez-González, S. Masi, M. Massardi, S. Matarrese, F. Matthai, P. Mazzotta, P. R. Meinhold, A. Melchiorri, J. B. Melin, L. Mendes, E. Menegoni, A. Mennella, M. Migliaccio, M. Millea, S. Mitra, M. A. Miville-Deschênes, A. Moneti, L. Montier, G. Morgante, D. Mortlock, A. Moss, D. Munshi, J. A. Murphy, P. Naselsky, F. Nati, P. Natoli, C. B. Netterfield, H. U. Nørgaard-Nielsen, F. Noviello, D. Novikov, I. Novikov, I. J. O'Dwyer, S. Osborne, C. A. Oxborrow, F. Paci, L. Pagano, F. Pajot, R. Paladini, D. Paoletti, B. Partridge, F. Pasian, G. Patanchon, D. Pearson, T. J. Pearson, H. V. Peiris, O. Perdereau, L. Perotto, F. Perrotta, V. Pettorino, F. Piacentini, M. Piat, E. Pierpaoli, D. Pietrobon, S. Plaszczynski, P. Platania, E. Pointecouteau, G. Polenta, N. Ponthieu, L. Popa, T. Poutanen, G. W. Pratt, G. Prézeau, S. Prunet, J. L. Puget, J. P. Rachen, W. T. Reach, R. Rebolo, M. Reinecke, M. Remazeilles, C. Renault, S. Ricciardi, T. Riller, I. Ristorcelli, G. Rocha, C. Rosset, G. Roudier, M. Rowan-Robinson, J. A. Rubiño-Martín, B. Rusholme, M. Sandri, D. Santos, M. Savelainen, G. Savini, D. Scott, M. D. Seiffert, E. P. S. Shellard, L. D. Spencer, J. L. Starck, V. Stolyarov, R. Stompor, R. Sudiwala, R. Sunyaev, F. Sureau, D. Sutton, A. S. Suur-Uski, J. F. Sygnet, J. A. Tauber, D. Tavagnacco, L. Terenzi, L. Toffolatti, M. Tomasi,

M. Tristram, M. Tucci, J. Tuovinen, M. Türler, G. Umana, L. Valenziano, J. Valiviita, B. Van Tent, P. Vielva, F. Villa, N. Vittorio, L. A. Wade, B. D. Wandelt, I. K. Wehus, M. White, S. D. M. White, A. Wilkinson, D. Yvon, A. Zacchei, and A. Zonca. Planck 2013 results. XVI. Cosmological parameters. *A&A*, 571:A16, Nov. 2014. doi: 10.1051/0004-6361/201321591.

F. L. Polles, S. C. Madden, V. Lebouteiller, D. Cormier, N. Abel, F. Galliano, S. Hony, O. Ł. Karczewski, M. Y. Lee, M. Chevance, M. Galametz, and S. Lianou. Modeling ionized gas in low-metallicity environments: the Local Group dwarf galaxy IC 10. *A&A*, 622:A119, Feb. 2019. doi: 10.1051/0004-6361/201833776.

A. M. Price-Whelan, B. M. Sipőcz, H. M. Günther, P. L. Lim, S. M. Crawford, S. Conseil, D. L. Shupe, M. W. Craig, N. Dencheva, A. Ginsburg, J. T. VanderPlas, L. D. Bradley, D. Pérez-Suárez, M. de Val-Borro, P. Paper Contributors, T. L. Aldcroft, K. L. Cruz, T. P. Robitaille, E. J. Tollerud, A. Coordination Committee, C. Ardelean, T. Babej, Y. P. Bach, M. Bachetti, A. V. Bakanov, S. P. Bamford, G. Barentsen, P. Barmby, A. Baumbach, K. L. Berry, F. Biscani, M. Boquien, K. A. Bostroem, L. G. Bouma, G. B. Brammer, E. M. Bray, H. Breytenbach, H. Buddelmeijer, D. J. Burke, G. Calderone, J. L. Cano Rodríguez, M. Cara, J. V. M. Cardoso, S. Cheedella, Y. Copin, L. Corrales, D. Crichton, D. D'Avella, C. Deil, É. Depagne, J. P. Dietrich, A. Donath, M. Droettboom, N. Earl, T. Erben, S. Fabbro, L. A. Ferreira, T. Finethy, R. T. Fox, L. H. Garrison, S. L. J. Gibbons, D. A. Goldstein, R. Gommers, J. P. Greco, P. Greenfield, A. M. Groener, F. Grollier, A. Hagen, P. Hirst, D. Homeier, A. J. Horton, G. Hosseinzadeh, L. Hu, J. S. Hunkeler, Ž. Ivezić, A. Jain, T. Jenness, G. Kanarek, S. Kendrew, N. S. Kern, W. E. Kerzendorf, A. Khvalko, J. King, D. Kirkby, A. M. Kulkarni, A. Kumar, A. Lee, D. Lenz, S. P. Littlefair, Z. Ma, D. M. Macleod, M. Mastropietro, C. McCully, S. Montagnac, B. M. Morris, M. Mueller, S. J. Mumford, D. Muna, N. A. Murphy, S. Nelson, G. H. Nguyen, J. P. Ninan, M. Nöthe, S. Ogaz, S. Oh, J. K. Parejko, N. Parley, S. Pascual, R. Patil, A. A. Patil, A. L. Plunkett, J. X. Prochaska, T. Rastogi, V. Reddy Janga, J. Sabater, P. Sakurikar, M. Seifert, L. E. Sherbert, H. Sherwood-Taylor, A. Y. Shih, J. Sick, M. T. Silbiger, S. Singanamalla, L. P. Singer, P. H. Sladen, K. A. Sooley, S. Sornarajah, O. Streicher, P. Teuben, S. W. Thomas, G. R. Tremblay, J. E. H. Turner, V. Terrón, M. H. van Kerkwijk, A. de la Vega, L. L. Watkins, B. A. Weaver, J. B. Whitmore, J. Woillez, V. Zabalza, and A. Contributors. The Astropy Project: Building an Open-science Project and Status of the v2.0 Core Package. *AJ*, 156:123, Sept. 2018. doi: 10.3847/1538-3881/aabc4f.

M. Relaño, J. E. Beckman, A. Zurita, M. Rozas, and C. Giammanco. The internal dynamical equilibrium of H II regions: A statistical study. *A&A*, 431:235–251, Feb. 2005. doi: 10.1051/0004-6361:20040483.

T. Robitaille, C. Deil, and A. Ginsburg. reproject: Python-based astronomical image reprojection, Nov. 2020.

B. Rodríguez del Pino, S. Arribas, J. Piqueras López, M. Villar-Martín, and L. Colina. Properties of ionized outflows in MaNGA DR2 galaxies. *MNRAS*, 486(1):344–359, June 2019. doi: 10.1093/mnras/stz816.

H. Rogers and J. M. Pittard. Feedback from winds and supernovae in massive stellar clusters - I. Hydrodynamics. *MNRAS*, 431(2):1337–1351, May 2013. doi: 10.1093/mnras/stt255.

E. Rosolowsky and A. Leroy. Bias-free Measurement of Giant Molecular Cloud Properties. *PASP*, 118(842):590–610, Apr. 2006. doi: 10.1086/502982.

E. W. Rosolowsky, J. E. Pineda, J. Kauffmann, and A. A. Goodman. Structural Analysis of Molecular Clouds: Dendrograms. *ApJ*, 679(2):1338–1351, June 2008. doi: 10.1086/587685.

M. Rozas, N. Sabalisck, J. E. Beckman, and J. H. Knapen. Internal turbulence, viriality, and density bounding of the most luminous H II regions in the spiral galaxy M 100. *A&A*, 338:15–26, Oct. 1998.

M. Rozas, M. G. Richer, J. A. López, M. Relaño, and J. E. Beckman. Hα line profiles for a sample of supergiant HII regions. I. The main spectral component. *A&A*, 455(2):539–547, Aug. 2006. doi: 10.1051/0004-6361:20054388.

S. C. Russell and M. A. Dopita. Abundances of the Heavy Elements in the Magellanic Clouds. II. H II Regions and Supernova Remnants. *ApJS*, 74:93, Sept. 1990. doi: 10.1086/191494.

S. Sakai, B. F. Madore, and W. L. Freedman. Cepheid and Tip of the Red Giant Branch Distances to the Dwarf Irregular Galaxy IC 10. *ApJ*, 511(2):671–679, Feb. 1999. doi: 10.1086/306716.

E. E. Salpeter. The Luminosity Function and Stellar Evolution. *ApJ*, 121:161, Jan. 1955. doi: 10.1086/145971.

S. F. Sánchez, R. C. Kennicutt, A. Gil de Paz, G. van de Ven, J. M. Vílchez, L. Wisotzki, C. J. Walcher, D. Mast, J. A. L. Aguerri, S. Albiol-Pérez, A. Alonso-Herrero, J. Alves, J. Bakos, T. Bartáková, J. Bland-Hawthorn, A. Boselli, D. J. Bomans, A. Castillo-Morales, C. Cortijo-Ferrero, A. de Lorenzo-Cáceres, A. Del Olmo, R. J. Dettmar, A. Díaz, S. Ellis, J. Falcón-Barroso, H. Flores, A. Gallazzi, B. García-Lorenzo, R. González Delgado, N. Gruel, T. Haines, C. Hao, B. Husemann, J. Iglésias-Páramo, K. Jahnke, B. Johnson, B. Jungwiert, V. Kalinova, C. Kehrig, D. Kupko, Á. R. López-Sánchez, M. Lyubenova, R. A. Marino, E. Mármol-Queraltó, I. Márquez, J. Masegosa, S. Meidt, J. Mendez-Abreu, A. Monreal-Ibero, C. Montijo, A. M. Mourão, G. Palacios-Navarro, P. Papaderos, A. Pasquali, R. Peletier, E. Pérez, I. Pérez, A. Quirrenbach, M. Relaño, F. F. Rosales-Ortega, M. M. Roth, T. Ruiz-Lara, P. Sánchez-Blázquez, C. Sengupta, R. Singh, V. Stanishev, S. C. Trager, A. Vazdekis, K. Viironen, V. Wild, S. Zibetti, and B. Ziegler. CALIFA, the Calar Alto Legacy Integral Field Area survey. I. Survey presentation. *A&A*, 538:A8, Feb. 2012a. doi: 10.1051/0004-6361/201117353.

S. F. Sánchez, F. F. Rosales-Ortega, R. A. Marino, J. Iglesias-Páramo, J. M. Vílchez, R. C. Kennicutt, A. I. Díaz, D. Mast, A. Monreal-Ibero, R. García-Benito, J. Bland -Hawthorn, E. Pérez, R. González Delgado, B. Husemann, Á. R. López-Sánchez, R. Cid Fernand es, C. Kehrig, C. J. Walcher, A. Gil de Paz, and S. Ellis. Integral field spectroscopy of a sample of nearby galaxies. II. Properties of the H ii regions. *A&A*, 546:A2, Oct. 2012b. doi: 10.1051/0004-6361/201219578.

S. F. Sánchez, F. F. Rosales-Ortega, B. Jungwiert, J. Iglesias-Páramo, J. M. Vílchez, R. A. Marino, C. J. Walcher, B. Husemann, D. Mast, A. Monreal-Ibero, R. Cid Fernandes, E. Pérez, R. González Delgado, R. García-Benito, L. Galbany, G. van de Ven, K. Jahnke, H. Flores, J. Bland-Hawthorn, A. R. López-Sánchez, V. Stanishev, D. Miralles-Caballero, A. I. Díaz, P. Sánchez-Blazquez, M. Mollá, A. Gallazzi, P. Papaderos, J. M. Gomes, N. Gruel, I. Pérez, T. Ruiz-Lara, E. Florido, A. de Lorenzo-Cáceres, J. Mendez-Abreu, C. Kehrig, M. M. Roth, B. Ziegler, J. Alves, L. Wisotzki, D. Kupko, A. Quirrenbach, D. Bomans, and Califa Collaboration. Mass-metallicity relation explored with CALIFA. I. Is there a dependence on the star-formation rate? *A&A*, 554:A58, June 2013. doi: 10.1051/0004-6361/201220669.

S. F. Sánchez, E. Pérez, F. F. Rosales-Ortega, D. Miralles-Caballero, A. R. López-Sánchez, J. Iglesias-Páramo, R. A. Marino, L. Sánchez-Menguiano, R. García-Benito, D. Mast, M. A. Mendoza, P. Papaderos, S. Ellis, L. Galbany, C. Kehrig, A. Monreal-Ibero, R. González Delgado, M. Mollá, B. Ziegler, A. de Lorenzo-Cáceres, J. Mendez-Abreu, J. Bland-Hawthorn, S. Bekeraitė, M. M. Roth, A. Pasquali, A. Díaz, D. Bomans, G. van de Ven, and L. Wisotzki. Imprints of galaxy evolution on H II regions. Memory of the past uncovered by the CALIFA survey. *A&A*, 574:A47, Jan. 2015. doi: 10.1051/0004-6361/201424873.

D. J. Schlegel, D. P. Finkbeiner, and M. Davis. Maps of Dust Infrared Emission for Use in Estimation of Reddening and Cosmic Microwave Background Radiation Foregrounds. *ApJ*, 500 (2):525–553, June 1998. doi: 10.1086/305772.

K. L. Shapiro, R. Genzel, N. M. Förster Schreiber, L. J. Tacconi, N. Bouché, G. Cresci, R. Davies, F. Eisenhauer, P. H. Johansson, D. Krajnović, D. Lutz, T. Naab, N. Arimoto, S. Arribas, A. Cimatti, L. Colina, E. Daddi, O. Daigle, D. Erb, O. Hernandez, X. Kong, M. Mignoli, M. Onodera, A. Renzini, A. Shapley, and C. Steidel. Kinemetry of SINS High-Redshift Star-Forming Galaxies: Distinguishing Rotating Disks from Major Mergers. *ApJ*, 682(1):231–251, July 2008. doi: 10.1086/587133.

A. E. Shapley, C. C. Steidel, M. Pettini, and K. L. Adelberger. Rest-Frame Ultraviolet Spectra of z~3 Lyman Break Galaxies. *ApJ*, 588(1):65–89, May 2003. doi: 10.1086/373922.

G. S. Shostak and E. D. Skillman. Neutral hydrogen observations of the irregular galaxy IC 10. *A&A*, 214:33–42, Apr. 1989.

E. D. Skillman, R. C. Kennicutt, and P. W. Hodge. Oxygen Abundances in Nearby Dwarf Irregular Galaxies. *ApJ*, 347:875, Dec 1989. doi: 10.1086/168178.

L. J. Smith, R. P. F. Norris, and P. A. Crowther. Realistic ionizing fluxes for young stellar populations from 0.05 to 2 Z_{solar}. *MNRAS*, 337(4):1309–1328, Dec. 2002. doi: 10.1046/j.1365-8711.2002.06042.x.

F. Snik, G. Otten, M. Kenworthy, M. Miskiewicz, M. Escuti, C. Packham, and J. Codona. The vector-APP: a broadband apodizing phase plate that yields complementary PSFs. In R. Navarro, C. R. Cunningham, and E. Prieto, editors, *Modern Technologies in Space- and Ground-based*

Telescopes and Instrumentation II, volume 8450 of *Society of Photo-Optical Instrumentation Engineers (SPIE) Conference Series*, page 84500M, Sept. 2012. doi: 10.1117/12.926222.

P. M. Solomon, A. R. Rivolo, J. Barrett, and A. Yahil. Mass, Luminosity, and Line Width Relations of Galactic Molecular Clouds. *ApJ*, 319:730, Aug. 1987. doi: 10.1086/165493.

L. Spitzer. *Physical processes in the interstellar medium*. 1978. doi: 10.1002/9783527617722.

Stan Development Team. PyStan: the Python interface to Stan, 2017. URL http://mc-stan.org.

W. Steffen, N. Koning, S. Wenger, C. Morisset, and M. Magnor. Shape: A 3D Modeling Tool for Astrophysics. *IEEE Transactions on Visualization and Computer Graphics*, 17(4):454–465, Apr. 2011. doi: 10.1109/TVCG.2010.62.

J. P. Stott, D. Sobral, A. M. Swinbank, I. Smail, R. Bower, P. N. Best, R. M. Sharples, J. E. Geach, and J. Matthee. A relationship between specific star formation rate and metallicity gradient within z $\sim$ 1 galaxies from KMOS-HiZELS. *MNRAS*, 443(3):2695–2704, Sept. 2014. doi: 10.1093/mnras/stu1343.

J. P. Stott, A. M. Swinbank, H. L. Johnson, A. Tiley, G. Magdis, R. Bower, A. J. Bunker, M. Bureau, C. M. Harrison, M. J. Jarvis, R. Sharples, I. Smail, D. Sobral, P. Best, and M. Cirasuolo. The KMOS Redshift One Spectroscopic Survey (KROSS): dynamical properties, gas and dark matter fractions of typical z $\sim$ 1 star-forming galaxies. *MNRAS*, 457(2):1888–1904, Apr. 2016. doi: 10.1093/mnras/stw129.

J. Sun, A. K. Leroy, E. C. Ostriker, A. Hughes, E. Rosolowsky, A. Schruba, E. Schinnerer, G. A. Blanc, C. Faesi, J. M. D. Kruijssen, S. Meidt, D. Utomo, F. Bigiel, A. D. Bolatto, M. Chevance, I.-D. Chiang, D. Dale, E. Emsellem, S. C. O. Glover, K. Grasha, J. Henshaw, C. N. Herrera, M. J. Jimenez-Donaire, J. C. Lee, J. Pety, M. Querejeta, T. Saito, K. Sandstrom, and A. Usero. Dynamical Equilibrium in the Molecular ISM in 28 Nearby Star-forming Galaxies. *ApJ*, 892(2): 148, Apr. 2020. doi: 10.3847/1538-4357/ab781c.

A. M. Swinbank, T. M. Webb, J. Richard, R. G. Bower, R. S. Ellis, G. Illingworth, T. Jones, M. Kriek, I. Smail, D. P. Stark, and P. van Dokkum. A spatially resolved map of the kinematics, star formation and stellar mass assembly in a star-forming galaxy at z = 4.9. *MNRAS*, 400(3): 1121–1131, Dec. 2009. doi: 10.1111/j.1365-2966.2009.15617.x.

A. M. Swinbank, I. Smail, D. Sobral, T. Theuns, P. N. Best, and J. E. Geach. The Properties of the Star-forming Interstellar Medium at z = 0.8-2.2 from HiZELS: Star Formation and Clump Scaling Laws in Gas-rich, Turbulent Disks. *ApJ*, 760(2):130, Dec. 2012a. doi: 10.1088/0004-637X/760/2/130.

A. M. Swinbank, D. Sobral, I. Smail, J. E. Geach, P. N. Best, I. G. McCarthy, R. A. Crain, and T. Theuns. The properties of the star-forming interstellar medium at z = 0.84-2.23 from HiZELS: mapping the internal dynamics and metallicity gradients in high-redshift disc galaxies. *MNRAS*,

426(2):935–950, Oct. 2012b. doi: 10.1111/j.1365-2966.2012.21774.x.

K. Tehrani, P. A. Crowther, and I. Archer. Revealing the nebular properties and Wolf-Rayet population of IC10 with Gemini/GMOS. *MNRAS*, 472(4):4618–4633, Dec 2017. doi: 10.1093/mnras/stx2124.

G. Tenorio-Tagle. The gas dynamics of H II regions. I. The champagne model. *A&A*, 71:59–65, Jan. 1979.

H. I. Teplitz, M. A. Malkan, C. C. Steidel, I. S. McLean, E. E. Becklin, D. F. Figer, A. M. Gilbert, J. R. Graham, J. E. Larkin, N. A. Levenson, and M. K. Wilcox. Measurement of [O III] Emission in Lyman-Break Galaxies. *ApJ*, 542(1):18–26, Oct. 2000. doi: 10.1086/309539.

The Pandas Development Team. pandas-dev/pandas: Pandas, Dec. 2016. URL https://pandas.pydata.org/pandas-docs/version/0.19.2/.

R. Thomas, B. Chris, M. Braden, and R. Erik. astrodendro, 2013. URL http://www.dendrograms.org/.

J. C. Thurow and E. M. Wilcots. The Kinematics of the Ionized Gas in IC 10. *AJ*, 129(2):745–767, Feb. 2005. doi: 10.1086/426751.

L. Tierney. Markov Chains for Exploring Posterior Distributions. *The Annals of Statistics*, 22(4): 1701 – 1728, 1994. doi: 10.1214/aos/1176325750. URL https://doi.org/10.1214/aos/1176325750.

W. G. Tifft and W. J. Cocke. Uncertainties in 21 centimeter Redshifts. I. Data. *ApJS*, 67:1, May 1988. doi: 10.1086/191265.

A. Toomre. On the gravitational stability of a disk of stars. *ApJ*, 139:1217–1238, May 1964. doi: 10.1086/147861.

W. D. Vacca, C. D. Sheehy, and J. R. Graham. Imaging of the Stellar Population of IC 10 with Laser Guide Star Adaptive Optics and the Hubble Space Telescope. *ApJ*, 662(1):272–283, June 2007. doi: 10.1086/516725.

M. Valdez-Gutiérrez, M. Rosado, I. Puerari, L. Georgiev, J. Borissova, and P. Ambrocio-Cruz. Unveiling the Kinematics and Dynamics of Ionized Gas in the Nearby Irregular Galaxy NGC 4449. *AJ*, 124(6):3157–3178, Dec. 2002. doi: 10.1086/344304.

C. Vanderriest. A fiber-optics dissector for spectroscopy of nebulosities around quasars and similar objects. *PASP*, 92:858–862, Dec. 1980. doi: 10.1086/130764.

S. Veilleux, G. Cecil, and J. Bland-Hawthorn. Galactic Winds. *ARA&A*, 43(1):769–826, Sept. 2005. doi: 10.1146/annurev.astro.43.072103.150610.

G. L. Walth, E. Egami, B. Clément, T. D. Rawle, M. Rex, J. Richard, P. Pérez-González, F. Boone, M. Dessauges-Zavadsky, J. Portouw, B. Weiner, I. McGreer, and E. Schneider. Infrared Galaxies in the Field of the Massive Cluster Abell S1063: Discovery of a Luminous Kiloparsec-sized H II Region in a Gravitationally Lensed Infrared-luminous Galaxy at z = 0.6. *ApJ*, 877(1):7, May 2019. doi: 10.3847/1538-4357/ab16d8.

Q. D. Wang, K. E. Whitaker, and R. Williams. An XMM-Newton and Chandra study of the starburst galaxy IC 10. *MNRAS*, 362(3):1065–1077, Sept. 2005. doi: 10.1111/j.1365-2966.2005.09379.x.

L. Weitzel, A. Krabbe, H. Kroker, N. Thatte, L. E. Tacconi-Garman, M. Cameron, and R. Genzel. 3D: The next generation near-infrared imaging spectrometer. *A&AS*, 119:531–546, Nov. 1996.

Wes McKinney. Data Structures for Statistical Computing in Python. In Stéfan van der Walt and Jarrod Millman, editors, *Proceedings of the 9th Python in Science Conference*, pages 56 – 61, 2010. doi: 10.25080/Majora-92bf1922-00a.

H. A. White, D. B. Fisher, N. Murray, K. Glazebrook, R. G. Abraham, A. D. Bolatto, A. W. Green, E. Mentuch Cooper, and D. Obreschkow. Gas Content and Kinematics in Clumpy, Turbulent Star-forming Disks. *ApJ*, 846(1):35, Sept. 2017. doi: 10.3847/1538-4357/aa7fbf.

E. M. Wilcots and B. W. Miller. The Kinematics and Distribution of H I in IC 10. *AJ*, 116(5): 2363–2394, Nov. 1998. doi: 10.1086/300595.

J. Wiley, K. Mathur, A. Brown, S. Wright, M. Cosens, J. Maire, T. Fitzgerald, Michael amd Jones, M. Kassis, E. Kress, R. Kupke, J. E. Larkin, J. Lyke, E. Wang, and S. Yey. Liger for Next-Generation Keck Adaptive Optics: Cryogenic Chamber for the Imaging Camera. In J. Shields, editor, *Ground-based and Airborne Instrumentation for Astronomy VI*, volume 11447 of *Society of Photo-Optical Instrumentation Engineers (SPIE) Conference Series*, pages 11447–311, Dec. 2020.

J. P. Williams, L. Blitz, and C. F. McKee. The Structure and Evolution of Molecular Clouds: from Clumps to Cores to the IMF. In V. Mannings, A. P. Boss, and S. S. Russell, editors, *Protostars and Planets IV*, page 97, May 2000.

E. Wisnioski, K. Glazebrook, C. Blake, G. B. Poole, A. W. Green, T. Wyder, and C. Martin. Scaling relations of star-forming regions: from kpc-sized clumps to H II regions. *MNRAS*, 422(4): 3339–3355, June 2012. doi: 10.1111/j.1365-2966.2012.20850.x.

E. Wisnioski, N. M. Förster Schreiber, S. Wuyts, E. Wuyts, K. Bandara, D. Wilman, R. Genzel, R. Bender, R. Davies, M. Fossati, P. Lang, J. T. Mendel, A. Beifiori, G. Brammer, J. Chan, M. Fabricius, Y. Fudamoto, S. Kulkarni, J. Kurk, D. Lutz, E. J. Nelson, I. Momcheva, D. Rosario, R. Saglia, S. Seitz, L. J. Tacconi, and P. G. van Dokkum. The KMOS^{3D} Survey: Design, First Results, and the Evolution of Galaxy Kinematics from 0.7 ¡= z ¡= 2.7. *ApJ*, 799(2):209, Feb. 2015. doi: 10.1088/0004-637X/799/2/209.

S. Wright, J. E. Larkin, T. Jones, R. Kupke, M. Fitzgerald, M. Kassis, M. Cosens, E. Chisholm, T. Do, C. Fassnacht, D. Fisher, A. Ghez, C. Johnson, J. Keane, E. Kirby, E. Kress, Q. Konopacky, J. R. Lu, J. Maire, J. O'Meara, N. Reddy, R. Sanders, K. Sandstrom, A. Shapley, J.-M. Sohn, A. Surya, T. Treu, R. Weber, J. Wiley, P. Wizinowich, M. Wong, and A. Zonca. Liger: Next Generation Imager and Spectrograph for Keck Observatory Adaptive Optics. In *Bulletin of the American Astronomical Society*, volume 51, page 201, Sept. 2019.

S. Wright, A. Brown, M. Fitzgerald, T. Jones, M. Kassis, R. Kupke, J. E. Larkin, M. Cosens, C. Johnson, E. Kress, K. Magnone, R. McGurk, N.-E. Rundquist, J.-M. Sohn, E. Wang, J. Wiley, and S. Yey. Liger at Keck Observatory: Overall Design Specifications and Science Drivers. In *Ground-based and Airborne Instrumentation for Astronomy IX*, volume 12184 of *Society of Photo-Optical Instrumentation Engineers (SPIE) Conference Series*, pages 12184–10, June 2022.

S. A. Wright, J. E. Larkin, M. Barczys, D. K. Erb, C. Iserlohe, A. Krabbe, D. R. Law, M. W. McElwain, A. Quirrenbach, C. C. Steidel, and J. Weiss. Integral Field Spectroscopy of a Candidate Disk Galaxy at z ~1.5 Using Laser Guide Star Adaptive Optics. *ApJ*, 658(1):78–84, Mar. 2007. doi: 10.1086/511632.

S. A. Wright, J. E. Larkin, D. R. Law, C. C. Steidel, A. E. Shapley, and D. K. Erb. Dynamics of Galactic Disks and Mergers at z ~1.6: Spatially Resolved Spectroscopy with Keck Laser Guide Star Adaptive Optics. *ApJ*, 699(1):421–440, July 2009. doi: 10.1088/0004-637X/699/1/421.

S. A. Wright, J. E. Larkin, T. Jones, T. Aliado, L. Armus, A. Brown, E. Chisholm, M. Cosens, R. Dekaney, T. Do, C. Fassanacht, D. Fisher, M. Fitzgerald, A. Ghez, J. Hirtenstein, C. Johnson, M. Kassis, J. Keane, P. Kelley, E. Kirby, Q. Konopacky, E. Kress, R. Kupke, J. Lu, J. Lyke, M. Marley, A. Medling, M. Millar-Blanchaer, R. Nash, A. Nierenberg, N. Reddy, M. Rich, J.-B. Ruffio, N.-E. Rundquist, D. Sand, R. Sanders, K. Sandstrom, A. Shapley, J.-M. Sohn, A. Surya, T. Treu, E. Wang, B. Weber, J. Wiley, P. Wizinowich, M. Wong, S. Yeh, and A. Zonca. Liger for Next-Generation Keck Adaptive Optics: Overall Design and Status. In J. Shields, editor, *Ground-based and Airborne Instrumentation for Astronomy VI*, volume 11447 of *Society of Photo-Optical Instrumentation Engineers (SPIE) Conference Series*, pages 11447–331, Dec. 2020.

J. Wu, I. Evans, Neal J., Y. Gao, P. M. Solomon, Y. L. Shirley, and P. A. Vanden Bout. Connecting Dense Gas Tracers of Star Formation in our Galaxy to High-z Star Formation. *ApJL*, 635(2): L173–L176, Dec. 2005. doi: 10.1086/499623.

H. Yang and E. D. Skillman. A Nonthermal Superbubble in the Irregular Galaxy IC 10. *AJ*, 106: 1448, Oct. 1993. doi: 10.1086/116738.

M. Zamora-Avilés, E. Vázquez-Semadeni, R. F. González, J. Franco, S. N. Shore, L. W. Hartmann, J. Ballesteros-Paredes, R. Banerjee, and B. Körtgen. Structure and expansion law of H II regions in structured molecular clouds. *MNRAS*, 487(2):2200–2214, Aug. 2019. doi: 10.1093/mnras/stz1235.

J. Zaragoza-Cardiel, J. E. Beckman, J. Font, B. García-Lorenzo, A. Camps-Fariña, K. Fathi, P. A. James, S. Erroz-Ferrer, J. Barrera-Ballesteros, and M. Cisternas. Comparative internal kinematics of the H II regions in interacting and isolated galaxies: implications for massive star formation modes. *MNRAS*, 451(2):1307–1330, Aug. 2015. doi: 10.1093/mnras/stv1024.

J. Zaragoza-Cardiel, J. Beckman, J. Font, M. Rosado, A. Camps-Fariña, and A. r. Borlaff. Kinematics of the ionized and molecular gas in nearby luminous infrared interacting galaxies. *MNRAS*, 465(3):3461–3474, Mar. 2017. doi: 10.1093/mnras/stw2963.

K. Zhang, Y. Zhou, A. M. Moore, E. Chisholm, J. E. Larkin, S. Wright, Y. Zhu, D. J. Reiley, and Z. Hu. The infrared imaging spectrograph (IRIS) for TMT: design of image slicer. In C. J. Evans, L. Simard, and H. Takami, editors, *Ground-based and Airborne Instrumentation for Astronomy VII*, volume 10702 of *Society of Photo-Optical Instrumentation Engineers (SPIE) Conference Series*, page 107029A, July 2018. doi: 10.1117/12.2312700.